Radio Science Bulletin

ISSN 1024-4530

INTERNATIONAL
UNION OF
RADIO SCIENCE

UNION
RADIO-SCIENTIFIQUE
INTERNATIONALE

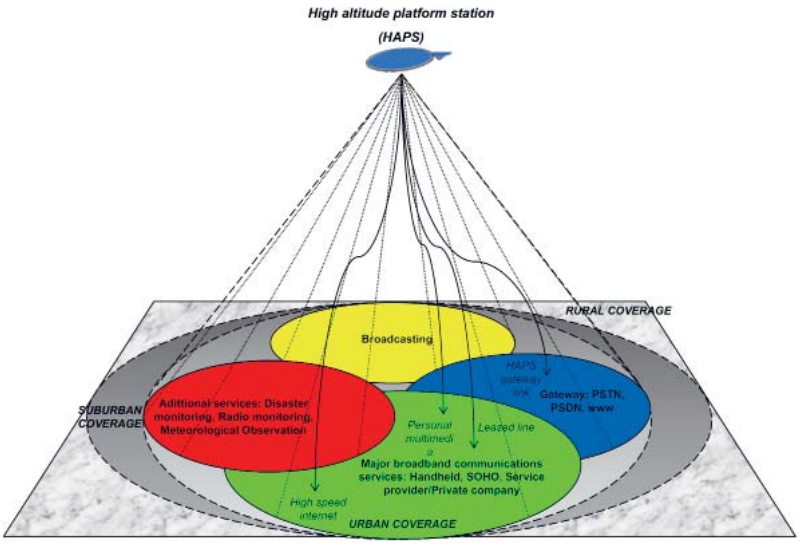

No 332
March 2010

URSI, c/o Ghent University (INTEC)
St.-Pietersnieuwstraat 41, B-9000 Gent (Belgium)

Contents

Front cover: The exploratory technology for deploying commercial wireless communications and other services using HAPS. See paper by I.R. Palma-Lázgare and J.A. Delgado-Penín pp. 50-66.

For information, please contact :
The URSI Secretariat
c/o Ghent University (INTEC)
Sint-Pietersnieuwstraat 41, B-9000 Gent, Belgium
Tel.: (32) 9-264 33 20, Fax: (32) 9-264 42 88
E-mail: info@ursi.org
http://www.ursi.org

Editorial

Special Sections

This issue contains the first of two special sections on High-Altitude Platforms (HAPs). Such platforms – which may take the form of a lighter-than-air craft, or manned or unmanned aircraft – hold exciting potential for providing a variety of types of future communications. The first special section is in this issue of the *Radio Science Bulletin*; the second special section will appear in the June issue. The Guest Editors for these special sections, David Grace, Jacob Gavan, and Ryszard Struzak, have provided a separate introduction, including an introduction to each of the five papers for the special section in this issue. Their efforts, and the work of the authors who have provided the papers, are greatly appreciated.

Our *Reviews*

We also have two invited *Reviews of Radio Science* in this issue. The first, by U. G. Wannberg and 35 other authors from the EISCAT Scientific Association, describes EISCAT_3D. EISCAT_3D is a European Union initiative to design and build the next-generation radar system for upper-atmospheric and geospace research. This incoherent-scattering radar will provide simultaneous three-dimensional measurements over the entire three-dimensional extent of the ionosphere. It will have a tenfold improvement in the temporal and spatial resolution compared to existing EISCAT systems, and will allow measurement of electron density with better than 10% accuracy over a range of 100 km to 300 km altitude, in one second or less. Measurements of the full vector ionospheric drift velocities over the entire altitude range will be possible. In addition, EISCAT_3D will have full imaging capabilities, with a horizontal resolution of less than 20 m at an altitude of 100 km. The authors first describe the performance targets, and then explain the details of the system configuration. They then describe the imaging capabilities, including a detailed discussion of the imaging algorithm to be used. They discuss Faraday rotation, and how the receiver system will adaptively track the polarization of the received signal. They explain the method to be used for beam steering, and the timing system. EISCAT_3D will quite literally generate more data than can be reasonably stored. The methods for recording, storing, and accessing such huge amounts of data are described. The paper finishes with details of the Demonstrator array and receiver. The conclusion explains the next steps planned for the program.

The efforts of John Mathews, Associate Editor for Commission G, and of Phil Wilkinson in bringing us this *Review* are gratefully acknowledged.

The Virtual Wave Observatory (VWO) is a heliophysics virtual observatory being developed by NASA as part of the Heliophysics Data Environment (HPDE). The VWO will make a huge quantity of heliophysics plasma wave and radiation data available online in readily useable forms. Shing Fung has provided an in-depth description of the VWO in this invited *Review of Radio Science* from Commission H. This paper has two purposes: while it provides a detailed description of the VWO program, it also serves as a call for participation in the program to the heliphysics community. The paper begins with a description of the NASA virtual observatory program, and the reasons behind the development of the VWO. This includes consideration of the unique characteristics of wave data, and how such data are used in heliophysics research. A description of the heliophysics data environments being developed by NASA follows. This is followed by a description of Space Physics Archive Search and Extract (SPASE), the standard data model that has been adopted by the virtual observatory community. The description of the VWO begins with a discussion of the goal of the program, followed by the design objectives. The architecture of VWO is described. The VWO user interface and functions are then explained in detail. Several examples illustrating potential scientific uses of VWO are then given. Ways in which the heliophysics community can participate in the VWO program are described, along with a call for participation. The paper concludes with a look at the status of the program.

The efforts of Ondrej Santolik, Associate Editor for Commission H, and Phil Wilkinson in bringing us this paper are gratefully acknowledged.

Our Other Contributions

Kristian Schlegel has provided a review of a new book on the Earth's ionosphere. If you have a suggestion for a book to be reviewed, or would like to serve as a reviewer, please contact Kristian via e-mail at ks-ursi@email.de.

Peter Watson has brought us another doctoral dissertation abstract in radio science. If you or one of your students has recently completed a dissertation in our field, please send a copy of the abstract to Peter via e-mail at

peter.watson43@btinternet.com. This is an excellent opportunity to share your work and interests with the radio science community.

In his Radio-Frequency Radiation Safety and Health column, Jim Lin looks at a recent study that showed some interesting correlations among cell-phone use and changes in cognitive behavior in children. You should read this: the results were not entirely what some people expected!

Finally, we have a report on an interesting workshop, and announcements of several important meetings.

XXX URSI General Assembly and Scientific Symposium

The call for papers for the XXX URSI General Assembly and Scientific Symposium, to be held August 13-20, 2011, in Istanbul, Turkey appears in this issue. There is also an announcement of the Young Scientist program for the General Assembly and Scientific Symposium. *Now* is the time to start making plans to submit a paper, and to attend. I hope to see you there!

XXX General Assembly and Scientific Symposium of the International Union of Radio Science

Union Radio Scientifique Internationale

August 13-20, 2011 Lütfi Kırdar Convention and Exhibition Centre, Istanbul, TURKEY

Call for Papers

The XXX General Assembly and Scientific Symposium of the International Union of Radio Science (Union Radio Scientifique Internationale: URSI) will be held at the Lütfi Kırdar Convention and Exhibition Centre in the beautiful historical center of Istanbul, Turkey, August 13-20, 2011.

The XXX General Assembly and Scientific Symposium will have a scientific program organized around the ten Commissions of URSI and consisting of plenary lectures, public lectures, tutorials, posters, invited and contributed papers. In addition, there will be workshops, short courses, special programs for young scientists, student paper competition, programs for accompanying persons, and industrial exhibits. More than 1,500 scientists from more than fifty countries are expected to participate in the Assembly. The detailed program, the link to an electronic submission site, the registration form, and hotel information will be available on the General Assembly Web site: **http://www.ursigass2011.org**

Information for all authors -*Submission information*
All contributions (four pages full paper and up to 100 words abstract) should be submitted electronically via the link provided on the General Assembly Web site. Please consult the symposium Web site, **http://www.ursigass2011.org**, for the latest instructions, templates, and sample formats.

Important Deadlines

Paper submission	February 11, 2011
Notification of acceptance	April 30, 2011

Topics of Interest

Commission A : Electromagnetic Metrology Commission B : Fields and Waves Commission C : Radiocommunication Systems and Signal Processing Commission D : Electronics and Photonics Commission E : Electromagnetic Environments and Interference Commission F : Wave Propagation and Remote Sensing Commission G : Ionospheric Radio and Propagation Commission H : Waves in Plasmas Commission J : Radio Astronomy Commission K : Electromagnetics in Biology and Medicine

Student Paper Competition
A student must be first author of the paper. The student's advisor should attach a statement that his/her contribution is primarily advisory. All other submission requirements and instructions can be found at symposium Web site.

Special Sessions
Individuals interested in organizing special sessions should request permission from the Chair of the appropriate URSI Commission.

Contact
For any questions related to the XXX General Assembly, please contact the Chair of the Conference: Prof. Hamit Serbest Department of Electrical and Electronics Engineering Cukurova University, Adana, Turkey
E-mail: ursigass2011@ursigass2011.org

FIRST ANNOUNCEMENT

The XXX General Assembly and Scientific Symposium of the International Union of Radio Science (Union Radio Scientifique Internationale-URSI) will be held at the Lütfi Kırdar Convention & Exhibition Centre, Istanbul, Turkey on August 13-20, 2011.

The General Assemblies and Scientific Symposia of URSI are held at intervals of plans for future research and special projects in all areas of radio science, especially where international cooperation is desirable. The first Assembly was held in Brussels, Belgium in 1922 and the latest in Chicago, IL, USA in 2008.

The XXX General Assembly and Scientific Symposium will have a scientific program organized around the ten Commissions of URSI and consisting of plenary lectures, public lectures, tutorials, invited and contributed papers. In addition, there will be workshops, short courses, special programs for young scientists, student paper competition, and programs for accompanying persons. More than 1,500 scientists from more than fifty countries are expected to participate in the Assembly and Scientific Symposium.

The Call for Papers will be issued in mid 2010, will be published in the Radio Science Bulletin and in the IEEE Antennas and Propagation Magazine, and will be posted on the URSI website. It is expected that all papers should be received by the beginning of February 2011, that Authors will be notified of the disposition of their submissions by the end of April 2011.

Preliminary information

Detailed information on the scientific program and on abstract submissions will be available toward the end of March 2010. A web site with current information on the XXX General Assembly is available at: **www.ursigass2011.org** and all abstracts will be received electronically.

Organizing Committee

Chair	A. Hamit Serbest, *Cukurova University, Turkey*; hamitserbest@gmail.com
Vice Chair	Ayhan Altıntaş, *Bilkent University, Turkey,* altintas@ee.bilkent.edu.tr
Finance	Sedef Kent, *Technical University of Istanbul, Turkey*, kents@itu.edu.tr
Publications	Erdem Yazgan, *Hacettepe University, Turkey,* yazgan@hacettepe.edu.tr
Young Scientists	Özlem Aydın Çivi, *Middle East Technical University, Turkey,* ozlem@metu.edu.tr
Student Paper Competition	Birsen Saka, *Hacettepe University, Turkey,* birsen@hacettepe.edu.tr
Workshops/Short Courses	Vakur B. Ertürk, *Bilkent University, Turkey,* vakur@ee.bilkent.edu.tr
Exhibits	Şimşek Demir, *Middle East Technical University*, *Turkey*, simsek@metu.edu.tr
Fundraising	Erdal Panayırcı, *Kadir Has University, Turkey,* eepanay@khas.edu.tr
Registration	Tour Select Ltd, organization@ursigass2011.org
Social activities	Tour Select Ltd, organization@ursigass2011.org
Hotel Reservation	Tour Select Ltd, organization@ursigass2011.org
Contact with URSI	P. Van Daele, peter.vandaele@intec.ugent.be W. Ross Stone, r.stone@ieee.org

Scientific Program Committee

Coordinator	P.L.E. Uslenghi *(U.S.A)*
Associate Coordiator	A. Hamit Serbest *(Turkey)*
Commission A	Chair: P. Banerjee *(National Physical Laboratory, New Delhi, India)* Vice Chair: W. A. Davis *(Virginia Tech, Blacksburg, VA, USA)*
Commission B	Chair: Karl J. Langenberg *(University of Kassel, Germany)* Vice-Chair: Giuliano Manara *(Università di Pisa, Italy)*
Commission C	Chair: Prof. Takashi Ohira *(Toyohashi University of Technology, Japan)* Vice-Chair: Prof. Marco Luise *(University of Pisa-Dip. Ingegneria Informazione, Italy)*
Commission D	Chair: Franz Kaertner *(USA)* Vice Chair: Mr. S. Tedjini *(INPG-ESISAR, France)*
Commission E	Chair: Professor Christos Christopoulos *(University of Nottingham, UK)* Vice-Chair: Professor A P J van Deursen *(Technische Universiteit Eindhoven, Netherlands)*
Commission F	Chair: Madhu Chandra *(Germany)* Vice Chair: Dr R.H. Lang *(George Washington University, USA)*
Commission G	Chair: Dr Michael T Rietveld *(EISCAT Scientific Association, Norway)* Vice Chair: Prof John D Mathews *(Pennsylvania State University, USA)*
Commission H	Chair: Yoshiharu Omura *(Japan)* Vice Chair: Dr. O. Santolik *(Academy of Sciences of the Czech Republic, Czech Republic)*
Commission J	Chair: Subra Anathakrishnan *(India)* Vice Chair: Dr. D.C. BACKER, *(University of California, USA)*
Commission K	Chair: Guglielmo D'Inzeo *(Italy)* Vice Chair: Prof. M. TAKI, *(Tokyo Metropolitan University, JAPAN)*

www.ursigass2011.org

AWARDS FOR YOUNG SCIENTISTS

CONDITIONS

A limited number of awards are available to assist young scientists from both developed and developing countries to attend the General Assembly and Scientific Symposium of URSI.

To qualify for an award the applicant:

1. must be less than 35 years old on September 1 of the year of the URSI General Assembly and Scientific Symposium;

2. should have a paper, of which he or she is the principal author, submitted and accepted for oral or poster presentation at a regular session of the General Assembly and Scientific Symposium.

Applicants should also be interested in promoting contacts between developed and developing countries. Applicants from all over the world are welcome, also from regions that do not (yet) belong to URSI. All successful applicants are expected to participate fully in the scientific activities of the General Assembly and Scientific Symposium. They will receive free registration, and financial support for board and lodging at the General Assembly and Scientific Symposium. A basic accommodation is provided by the assembly organizers permitting the Young Scientists from around the world to collaborate and interact. Young scientists may arrange alternative accommodation, but such arrangements are entirely at their own expense. Limited funds will also be available as a contribution to the travel costs of young scientists from developing countries.

The application needs to be done electronically by going to the same website used for the submission of abstracts/papers. This website is www.papers-GASS2011.ursi.org. The deadline for paper submission for the URSI GASS2011 in Istanbul is 07 February 2011.
A web-based form will appear when applicants check "Young Scientist paper" at the time they submit their paper. All Young Scientists must submit their paper(s) and this application together with a CV and a list of publications in PDF format to the GA submission Web site.

Applications will be assessed by the URSI Young Scientist Committee taking account of the national ranking of the application and the technical evaluation of the abstract by the relevant URSI Commission. Awards will be announced on the URSI Web site in April 2011.

For more information about URSI, the General Assembly and Scientific Symposium and the activities of URSI Commissions, please look at the URSI Web site at: http://www.ursi.org or the GASS 2011 website at http://www.ursigass2011.org/

If you need more information concerning the Young Scientist Program, please contact:

The URSI Secretariat
c/o Ghent University / INTEC
Sint-Pietersnieuwstraat 41
B-9000 GENT
BELGIUM
fax: +32 9 264 42 88
E-mail: ingeursi@intec.ugent.be

URSI Forum 2010

PALACE OF THE ACADEMIES

Hertogstraat 1, B-1000, Brussel| Rue Ducale, 1, B-1000, Bruxelles

Tuesday, 18 May 2008

Announcement and Call for Papers

Objective:

The 16th. URSI Forum ("Cross-Border Radio Science") is offering a meeting opportunity to all European researchers preparing a PhD in the different scientific fields covered by URSI (*International Union of Radio Science - Union Radioscientifique Internationale*). Researchers with a PhD are also welcome to present significant advances in their postdoctoral research. The meeting offers to them and to the academic and scientific staff of universities and institutes a unique opportunity to be informed about the different research programmes in Radio Science.

Organisation:

Following evaluation of previous editions of the URSI Forum, the structure of the Forum will mainly consist of Poster Sessions (contributions will be placed in the relevant URSI session). Some formal presentations of a keynote speaker, other invited speakers and final year doctorandi are also planned.

Submission of abstracts:

The contributions will be evaluated by the Scientific Program Committee. For a final year PhD project or a follow up project, the evaluation will be based on a summary (maximum 3 pages) of the project to be submitted by the applicant. For an ongoing PhD project a 1 page abstract must be submitted. **Submission is required by March 26 2010**.
Electronic submission of abstracts prepared in MS Word according to the attached rules is mandatory (RTF (Rich Text Format) file is also acceptable).
An area of 1m (wide) x 2m (high) will be available for all selected posters.

Proceedings:

The proceedings of the URSI Forum will consist of a collection of submitted abstracts and summaries and will be distributed at the Forum to all participants.

Registration:

Registration is required before **8 March 2010** by returning the enclosed form (by fax, mail or E-mail).
Registration is free for authors of URSI-affiliated institutions and all academy members. Non-authors from universities or research institutions must pay a fee of 75 Euro's to cover expenses (proceedings, lunch, coffee breaks and reception).
Industrial attendees must pay a fee of 150 Euro's.

Final Programme:

The final programme, including, titles of sessions and poster presentations, time schedule and directions to the palace of the academies, will be sent by E-mail. The Forum is open to an international audience, and will hence have the status of an international conference. This contact Forum is sponsored by the Belgian academy KVAB.

Organisation & Contact:

Prof. E. Stijns
Prof. I. Veretinicoff
VUB; div. TONA,

Pleinlaan 10, bus 2444; B-1018 Brussel
Tel: +32-(0)2-321063, Fax: +32-(0)2-321986,
E-mail: Ann.Deforce@VUB.ac.Be

Scientific Program Committee:

Prof. M. Blondel, Fac. Polytechn. de Mons
Prof. A. Franchois, UGent
Prof. I. Huynen, UCL
Prof. P. Lagasse, UGent
Prof. V. Pierrard, IASB
Prof. B. Nauwelaers, K.U.Leuven
Prof. H. Rogier, UGent
Prof. S. Prohoroff, ULB
Prof. E. Schweicher, ERM
Prof. P. Sobieski, UCL
Prof. E. Stijns, VUB
Prof. R. Strom, NFRA & UvA
Prof. A. Van Ardenne, Astron & Chalmers
Prof. L. Van Biesen, VUB
Prof. A. Van de Capelle, K.U.Leuven
Ir. F. van den Bogaart, FEL/TNO
Prof. E. Van Lil, K.U.Leuven
Prof. C. Vloeberghs, KMS
Dr. R. Warnant, KSB-ORB
Prof. A. Yarovoy, TUD

URSI Accounts 2009

URSI continues to survive the global economic crisis in good financial shape. This is due to 3 factors. Firstly the income URSI has received from the US National Committee for the 2008 Chicago General Assembly has put URSI in a strong financial position before the crisis struck. Secondly an ongoing effort to reduce the administrative costs has kept the spending well under control. Thirdly having invested the reserves in a very conservative manner allowed URSI to suffer practically no financial losses.

The year after the General Assembly is a year in which we need to have a significant profit so as to allow for a larger expenditure that will be incurred during the preparation of the following General Assembly. Having realized this goal in 2009 URSI is now in a strong position to help ensure the success of the 2011 Istanbul GASS and to take new initiatives, such as Student Paper competitions, that should further the development of Radio Science and help Radio Scientists worldwide in their research activities.

Paul Lagasse
Secretary General

BALANCE SHEET: 31 DECEMBER 2009

ASSETS	EURO	EURO
Dollars		
Merrill Lynch WCMA	1,357.28	
BNP Paribas Fortis	0.00	
Smith Barney Shearson	4,531.26	
		5,888.54
Euros		
Banque Degroof	5.79	
PNB Paribas Fortis zichtrekening	117,378.82	
PNB Paribas Fortis zichtrekening	374,855.23	
		492,239.84
Investments		
Demeter Sicav Shares	22,681.79	
Rorento Units	111,414.88	
Aqua Sicav	63,785.56	
Merrill-Lynch Low Duration (304 units)	3,268.17	
Massachusetts Investor Fund	251,387.65	
Provision for (not realised) less value	(27,906.96)	
Provision for (not realised) currency differences	(78,491.74)	
	346,139.35	
684 Rorento units on behalf of van der Pol Fund	12,414.34	
		358,553.69
Short Term Deposito	0.00	
Petty Cash	215.33	
Total Assets		856,897.40
Less Creditors		
IUCAF	7,703.08	
ISES	6,555.36	
		(14,258.44)
Balthasar van der Pol Medal Fund		(12,414.34)
NET TOTAL OF URSI ASSETS		**830,224.62**

The net URSI Assets are represented by:	EURO	EURO
Closure of Secretariat		
Provision for Closure of Secretariat		90,000.00
Scientific Activities Fund		
Scientific Activities in 2009	45,000.00	
Publications in 2009	40,000.00	
Young Scientists in 2009	0.00	
Administration Fund in 2009	85,000.00	
Scientific paper submission software in 2009	0.00	
I.C.S.U. Dues in 2009	5,000.00	
		175,000.00
XXIX General Assembly 2008/2011 Fund:		
During 2009 (GA 2008)		0.00
During 2009 - 2010 - 2011 (GA 2011)		100,000.00
Total allocated URSI Assets		365,000.00
Unallocated Reserve Fund		465,224.62
		830,224.62

Statement of Income and expenditure for the year ended 31 December 2009

I. INCOME	EURO	EURO
Grant from ICSU Fund and US National		
Academy of Sciences	0.00	
Allocation from UNESCO to ISCU Grants Programme	0.00	
UNESCO Contracts	0.00	
Contributions from National Members (year -1)	21,890.00	
Contributions from National Members (year)	168,982.00	
Contributions from National Members (year +1)	8,120.00	
Contributions from Other Members	0.00	
Special Contributions	0.00	
Contracts	0.00	
Sales of Publications, Royalties	1,380.00	
Sales of scientific materials	0.00	
Bank Interest	5,676.08	
Other Income	(1,000.00)	
Total Income		**205,048.08**
II. EXPENDITURE		
A1) Scientific Activities		17,757.43
General Assembly 2005/2008/2011	714.14	
Scientific meetings: symposia/colloqiua	17,043.29	
Working groups/Training courses	0.00	
Representation at scientific meetings	0.00	
Data Gather/Processing	0.00	
Research Projects	0.00	
Grants to Individuals/Organisations	0.00	
Other	0.00	
Loss covered by UNESCO Contracts	0.00	

		EURO	EURO
A2)	Routine Meetings		10,323.23
	Bureau/Executive committee	10,323.23	
	Other	0.00	
A3)	Publications		19,616.07
B)	Other Activities		22,358.84
	Contribution to ICSU	18,358.84	
	Contribution to other ICSU bodies	4,000.00	
	Activities covered by UNESCO Contracts	0.00	
C)	Administrative Expenses		59,610.00
	Salaries, Related Charges	78,226.77	
	General Office Expenses	2,905.07	
	Travel and representation	5,775.06	
	Office Equipment	2,720.55	
	Accountancy/Audit Fees	10,603.11	
	Bank Charges/Taxes	1,737.24	
	Loss on Investments (realised/unrealised)	(42,357.80)	
	Total Expenditure:		**129,665.57**
Excess of Income over Expenditure			75,382.51
Currency translation difference (USD => EURO) - Bank Accounts			(50.98)
Currency translation difference (USD => EURO) - Investments			(1,525.23)
Currency translation difference (USD => EURO) - others			15,148.12
Accumulated Balance at 1 January 2009			741,270.20
			830,224.62

Rates of exchange:

January 1, 2009	$ 1 = 0.6990 EUR
December 31, 2009	$ 1 = 0.6930 EUR

Balthasar van der Pol Fund	
684 Rorento Shares: market value on December 31	
(Aquisition Value: USD 12.476,17/EUR 12.414,34)	30,602.16
Book Value on December 31, 2009/2008/2007	12,414.34
Market Value of investments on December 31, 2009-2007	
Demeter Sicav	68,993.10
Rorento Units (1)	581,620.00
Aqua-Sicav	88,781.48
M-L Low Duration	2,039.30
Massachusetts Investor Fund	146,213.07
	887,646.95
Book Value on December 31, 2009/2008/2007	346,139.35

(1) Including the 684 Rorento Shares of the van der Pol Fund

APPENDIX: Detail of Income and Expenditure

	EURO	EURO
I. INCOME		
Other Income		
Income General Assembly 2005	0.00	
Income General Assembly 2008	0.00	
Young Scientist Support (Japan)	0.00	
Support Koga Medal	0.00	
Closure Radio Science Press	0.00	
Commission B + C	(1,000.00)	
Mass Investors Growth Stock Fund	0.00	
Other	0.00	
		(1,000.00)
II . EXPENDITURE		
General Assembly 2008		
Organisation	815.19	
Vanderpol Medal	0.00	
Young Scientists	139.80	
Expenses officials	(416.34)	
Student Support	(419.40)	
General Assembly 2011		
Organisation	594.89	
		714.14
Symposia/Colloquia/Working Groups:		
Commission A	500.00	
Commission B	0.00	
Commission C	1,800.00	
Commission D	1,000.00	
Commission E	1,000.00	
Commission F	1,200.00	
Commission G	3,500.00	
Commission H	4,500.00	
Commission J	1,000.00	
Commission K	500.00	
Central Fund	2,043.29	
		17,043.29
Contribution to other ICSU bodies		
UNESCO-ICTP	0.00	
FAGS	2,000.00	
IUCAF	2,000.00	
		4,000.00
Publications:		
Printing ‘The Radio Science Bulletin’	8,290.05	
Mailing ‘The Radio Science Bulletin’	11,326.02	
URSI Leaflet	0.00	
		19,616.07

IUCAF Annual Report for 2009

1. Introduction

The Scientific Committee on Frequency Allocations for Radio Astronomy and Space Science, IUCAF, was formed in 1960 by its sponsoring Scientific Unions, COSPAR, the IAU, and URSI. Its brief is to study and coordinate the requirements of radio frequency allocations for passive (i.e. non-emitting or receive-only) radio sciences, such as radio astronomy, space research and remote sensing, in order to make these requirements known to the national administrations and international bodies that allocate frequencies. IUCAF operates as a standing inter-disciplinary committee under the auspices of ICSU, the International Council for Science. IUCAF is a Sector Member of the International Telecommunication Union (ITU).

2. Membership

At the end of 2009 the membership for IUCAF was:

URSI	S. Ananthakrishnan (Com J)	India
	S. Reising (Com F)	USA
	I. Häggström (Com G)	Sweden
	A. Tzioumis (Com J)	Australia
	W. van Driel (Com J)	France
IAU	H. Chung	Korea (RO)
	H.S. Liszt	USA
	M. Ohishi (Chair)	Japan
	K.F. Tapping	Canada
	A. Tiplady	South Africa
COSPAR	Y. Murata	Japan
at large:	W.A. Baan	the Netherlands
	K. Ruf	Germany
	D.T. Emerson	USA

IUCAF also has a group of Correspondents, in order to improve its global geographic representation and for issues on spectrum regulation concerning astronomical observations in the optical and infrared domains.

3. International Meetings

During the period of January to December 2009, its Members and Correspondents represented IUCAF in the following international meetings:

February	ITU-R Working Party 7D (radio astronomy)
June	Space Frequency Coordination Group meeting (SFCG-29)
August	XXVII IAU General Assembly
September	ITU-R Working Party 7D (radio astronomy)
	ITU-R Study Group 7 (Science Services)
	ITU-R Working Party 1A (spectrum management)

Additionally, many IUCAF members and Correspondents participated in numerous national or regional meetings (including CORF, CRAF, RAFCAP, the FCC etc.), dealing with spectrum management issues, such as the preparation of input documents to various ITU fora.

4. IUCAF Business Meetings

During 2009 IUCAF had face-to-face committee meetings before each of the ITU-R WP 7D meetings and the IAU General Assembly listed above, with the purpose of discussing issues on the agenda of the meetings in preparation for the public sessions. During these ITU sessions ad-hoc meetings of IUCAF were held to discuss further its strategy. Also discussed was other IUCAF business, such as hand-over of the IUCAF chairman from Wim van Driel to Masatoshi Ohishi, action plans for future workshops and summer schools or initiatives and future contributions to international spectrum management meetings.

Although such face-to-face meetings have been convenient and effective, throughout the year much IUCAF business is undertaken via e-mail communications between the members and correspondents.

5. Contact with the Sponsoring Unions and ICSU

IUCAF maintains regular contact with its supporting Scientific Unions and with ICSU. The Unions play a strong supporting role for IUCAF and the membership is greatly encouraged by their support.

Pursuing its brief, IUCAF continued its activities towards strengthening its links with other passive radio science communities, in particular in space science, and defining a concerted strategy in common spectrum management issues.

At the 27th IAU General Assembly in Rio de Janeiro, Brazil, IUCAF organized two science sessions: Working Group on Radio Frequency Interference Mitigation, chaired by A. Tzioumis, and Working Group on Astrophysically Important Spectral Lines chaired by M. Ohishi. The

Working Group on Astrophysically Important Spectral Lines successfully approved a new list of important spectral lines in the frequency range between 1000 and 3000 GHz. IUCAF also organized its business session jointly with IAU Commission 50 on the Protection of Existing and Potential Observatory Sites.

IUCAF member, W. van Driel, has been appointed president of IAU Commission 50. Two IUCAF members, A. Tzioumis and M. Ohishi, have joined the Organising Committee of IAU Commission 50. IUCAF member, A. Tzioumis, was Chair of the Working Group on Radio Frequency Interference Mitigation of IAU Division X (radio astronomy) until August 2009, and IUCAF member, W.A. Baan, has been appointed as the new chair of this Working Group. IUCAF chair, M. Ohishi, chairs the Working Group on Astrophysically Important Spectral Lines of Division X. The IUCAF chair, M. Ohishi, has also been appointed president of IAU Commission 5 on Documentation and Astronomical Data.

The preparation towards the next URSI General Assembly in 2011 has been ongoing, led by the president of Commission J (radio astronomy), S. Ananthakrishnan (IUCAF member). Several session proposals, including a session on the mitigation of radio frequency interference, have been sent to URSI, and some IUCAF members are nominated as SOC members. In 2009, IUCAF members also actively participated in national URSI meetings.

6. Protecting the Passive Radio Science Services

At the ITU, the work in the various Working Parties of interest to IUCAF was focused on the relevant agenda items that were adopted in 2007 for the ITU World Radiocommunication Conference in 2012 (WRC-12), as well as on creation and maintenance of various ITU-R Recommendations and ITU-R Reports.

A WRC-12 agenda item that is most relevant to radio astronomy concerns is the use of the radio spectrum between 275 and 3000 GHz. No frequency allocations for the use of this frequency band will be made at WRC-12, however the radio astronomy community has to identify a list of specific bands of interest. This list was established in close collaboration with the IAU Working Group of Important Spectral Lines, and a new ITU-R Recommendation RA.1860 (Preferred frequency bands for radio astronomical measurements in the range 1-3 THz) was published on February 25th, 2010. IUCAF members actively participated in the drafting and approval process of this important Recommendation.

Work has proceeded towards a new ITU-R Report on "The essential role and global importance of radio spectrum use for Earth observations and for other related science applications", which contains a description of benefits from spectrum use by radio astronomy and space research.

IUCAF members submitted several contribution papers towards a new ITU-R Report on "Characteristics of Radio Quiet Zones" for radio astronomy.

Power Line Communications utilizing the High Frequency range (2-30 MHz) is a technology that sends electrical signals for communication purposes through the power lines. This technology aims to enable broadband Internet access and home LAN by means of the "existing" power lines. Since the power lines are designed and installed to carry current at 50/60Hz only, there has been serious concern that the electromagnetic field radiated from the power lines may cause harmful interferences to radio communication services such as broadcasting, communication, and radio astronomy observations. In this regard IUCAF members submitted to ITU-R Working Party 1A (spectrum management) several contributions containing measurement results of actual harmful interference and theoretical analyses. These study results were welcomed by the ITU-R Working Party 1A, and were adopted as part of the ITU-R Report SM.2158 (Impact of power line telecommunication systems on radiocommunication systems operating in the LF, MF, HF and VHF bands below 80 MHz).

IUCAF member, M. Ohishi, was the Chair of ITU-R Working Party 7D (radio astronomy) until September, 2009, and his position was succeeded by another IUCAF member, A. Tzioumis. And IUCAF member, H. Chung, is the vice-chairman of ITU-R Study Group 7 (Science Services). IUCAF member, S. Ananthakrishnan, is the president of URSI Commission J (radio astronomy).

7. IUCAF-Sponsored Meetings

In our report for the year 2008, it was mentioned that the third Summer School on Spectrum Management for Passive Radio Sciences had been in preparation to be held in the Republic of Korea in early summer of 2009. However, the world-wide economic crisis affected the government of Korea, and it was unfortunately decided to postpone the Summer School to 2010. Last year IUCAF worked towards the organization of its third Summer School, which has been decided to be held in Tokyo, Japan in June 2010. The preparation is going well, and the first circular has already been distributed to all the relevant groups around the world.

The increased sensitivity of passive instruments in radio astronomy and remote sensing and the intensifying active use of the spectrum have led to an increasing influence of the active services on the passive use of the spectrum. Advances in technology and computing have opened up new possibilities for mitigating the effects of certain classes of interference. Interference in allocated bands always leads to data loss for the passive users of the spectrum even if interference mitigation is applied. However, interference mitigation in non-allocated spectral bands may facilitate partial use of this spectrum for passive observations. There is no generic method to mitigate every

class of interference, so a multi-layered approach may be advisable to reduce detrimental effects of several types of radio interference. IUCAF member, W.A. Baan, has been leading the preparation for the RFI2010 workshop to address the radio interference mitigation techniques, which will be held from 29th to 31st of March, 2010, in the Netherlands. See the details at http://www.astron.nl/rfiworkshop/.

8. Publications and Reports

IUCAF has a permanent website at http://www.iucaf.org, that is currently in the process of being updated. All contributions to IUCAF-sponsored meetings are made available on this website.

9. Conclusion

IUCAF interests and activities range from preserving what has been achieved through regulatory measures or mitigation techniques, to looking far into the future of high frequency use and giant radio telescope use. Current priorities, which will certainly keep us busy through the next years, include the use of satellite down-links close in frequency to the radio astronomy bands, the coordination of the operation in shared bands of radio observatories and powerful transmissions from downward-looking satellite radars, the possible detrimental effects of ultra-wide band (UWB) transmissions, high-frequency power line communications (HF-PLC) and cognitive radio systems on all passive services, the scientific use of the 275 to 3000 GHz frequency range, and studies on the operational conditions that will allow the successful operation of future giant radio telescopes.

IUCAF is grateful for the moral and financial support that has been given for these continuing efforts by ICSU, COSPAR, the IAU, and URSI during the recent years. IUCAF also recognizes the support given by radio astronomy observatories, universities and national funding agencies to individual members in order to participate in the work of IUCAF.

Masatoshi Ohishi, IUCAF Chair
IUCAF website: http://www.iucaf.org
IUCAF contact: iucafchair@iucaf.org

Introduction to the Special Section on High-Altitude Platforms

Today, wireless communication systems are becoming ubiquitous, requiring ever-greater resources and flexible deployments. This trend is set to continue, meaning that existing terrestrial and satellite systems will need to be enhanced by new types of systems and architectures. One such possibility could be the use of High-Altitude Platforms (HAPs)[1] These are stratospheric quasi-stationary platforms that will operate at heights of from 17 to 24 km, where wind velocity is minimal, for significant periods of time. HAPs will be a useful new complement – and even in several cases, an alternative – to actual geo-stationary (GEO) and low-Earth-orbit (LEO) satellite systems. The most important applications of HAPs are for military and commercial radio communication, remote sensing, intelligence, surveillance, reconnaissance (ISR), differential GPS, and other wireless applications. HAPs radio systems may also be an advantageous alternative for the numerous terrestrial and satellite radio systems.

The purpose of this first of two special sections is to examine new research findings in the area of wireless deployments from HAPs, in particular looking at the challenges, constraints and solutions of this rapidly emerging field.

The first paper, "Circularly Polarized Homogeneous Lens Antenna System Providing Multi-Beam Radiation Pattern for HAPS," presents a design for a multi-feed lens based antenna operating at 30 GHz for use on a stationary HAP at 21 km altitude. This design will help to solve one of the critical problems of the deployments of multibeam antenna systems. Each feed is delivered using small horns connected to circular waveguides. The authors show that this system can deliver an optimum circularly polarized beam of 21 dBi directivity, with an impedance bandwidth of 19% at −10 dB.

The second paper, "Inter-High Altitude Platform Handoff for Communications Systems with Directional Antennas," presents a strategy to enable a fleet of short-duration manned HAPs to maintain long-duration continuous service to groups of wireless users, using inter-HAP handoff. A crucial issue in the design of such platforms is the minimum separation distance of the existing and incoming HAPs, which is taken in the paper to be the Civil Aviation Authority (CAA) cylinder, and also the user antenna's beamwidth. It is shown that incoming HAPs should aim to minimize the vertical separation with the existing HAP (subject to the CAA cylinder constraints), prior to taking over the communications provision

The third paper, "Low-Latency MAC-Layer Handoff for a High-Altitude Platform Delivering Broadband Communications," presents a novel rapid inter-cell handoff scheme. The primary aim of this is to cope with the effects of HAP movement, while minimizing the changes required to conventional terrestrial user equipment operating IEEE 802.16-like protocols. This is achieved by exploiting the collocation of base stations on the HAP, and inherent cell overlap, enabling tight coordination of transmissions sent to the different footprints. The paper proposes various HAP mobility models as way of assessing the performance of the schemes.

The fourth paper, "WIMAX HAPS-Based Downlink Performance Employing Geometrical and Statistical Channel Propagation Characteristics," presents a new L-band downlink broadband channel model for HAPS communication to fixed terrestrial terminals located in urban areas. The model exploits both the geometrical properties of the paths as well as simple diffraction theory, and is able to model both the direct path and specular multipath properties of the channel. Performance is evaluated by taking into account the IEEE 802.16 physical-layer system specifications.

The final paper, "ITU's Regulatory Framework, Technical Studies in ITU-R, and Future Activities in Relation to High-Altitude-Platform Stations (HAPS)," presents an overview of the development of HAPS from the global standardization and regulation viewpoint. The authors summarize various ITU-R Recommendations dealing with the choice of frequencies for HAPS, and discuss the relevant ITU Radio Regulations and Conference Resolutions that impose regulatory/legal restrictions imposed on that technology. To extend these over and above what is now set in the current Radio Regulations, one should take an active part in the preparations for the next ITU Radio Conference, WRC-12, the agenda of which foresees discussions on HAPS.

The guest editors would like to thank the authors for their contributions, and also the reviewers who have provided useful feedback in the form of suggestions and corrections to help improve the quality of the manuscripts. We would also like to thank Dr. Ross Stone, the Editor of the URSI *Radio Science Bulletin*, for giving us this opportunity to put together these special sections. Finally, we hope that the *Radio Science Bulletin*'s readers will find the articles inspiring and helpful to their future research.

David Grace, Jacob Gavan, and Ryszard Struzak

David Grace is with the Department of Electronics, the University of York, York, YO10 5DD, UK; e-mail: dg6@ohm.york.ac.uk. Jacob Gavan is with the Sami Shamoon College of Engineering, Jabutinsky 84, Ashdod, Israel; e-mail: gavan@hit.ac.il. Ryszard Struzak is with the National Institute of Telecommunications, Swojczycka 38, 51-501, Wroclaw, Poland; e-mail: struzak@gmail.com.

[1] The more narrowly defined High-Altitude-Platform Station (HAPS) is similar to a HAP. Such terminology is often used by regulatory bodies, such as the International Telecommunications Union (ITU)

Circularly Polarized Homogeneous Lens Antenna System Providing Multibeam Radiation Pattern for HAPS

M. Letizia
B. Fuchs
A. Skrivervik
J.R. Mosig

Abstract

In this paper, a 30 GHz multibeam antenna design is described that has been developed for high-altitude-platform station (HAPS) applications. When mounted on a HAPS at the stationary altitude of 21 km, this antenna provides cellular coverage on the ground. The antenna consists of a dielectric lens, fed by circular waveguides terminated with small horns. Circular polarization was achieved by integrating a polarizer into the waveguide feed. Each beam presents the same radiation pattern due to the symmetry of the lens. The global antenna system was designed and realized. The prototype fulfilled the initial specifications. It showed a directivity of 21 dBi and an impedance bandwidth at −10 dB of 19%. Moreover, an axial ratio lower than 2 dB was achieved within this bandwidth.

1. Introduction

In recent years, an impressive quantity of work has been carried out on high-altitude-platform stations (HAPS) and their related telecommunication systems (see, for instance, the recent survey in [1]). From an antenna point of view, HAPS antenna models have been used [2] to analyze the performance of a HAPS-based wireless telecommunication system. Theoretical antenna radiation patterns have been employed to perform useful system analysis.

Many wireless services, such as GPS and TV broadcasting, need circular polarization to reach high performance. Since these services can be furnished and improved by using HAPS, a circularly polarized antenna system is a basic onboard element. However, and to the knowledge of the authors, a functional prototype of a circularly polarized compact multibeam antenna, suitable for HAPS applications, has not yet been fully described in the literature. This paper puts together well-known solutions for individual components (waveguide/horn feed, inner circular polarizer, dielectric lens). It presents the design, realization, and preliminary characterization of a Ka-band circularly polarized multibeam antenna for HAPS applications. Although the practical demonstrator included only a reduced number of feeds (seven), all of the antenna's technology and topology have been developed to easily allow increasing of the number of beams without redesigning the full antenna system.

Multibeam antennas are a standard in telecommunication satellites. They are currently being used to provide the downlink and uplink coverage for mobile communication satellites, direct broadcast satellites, and personal communication services. These antennas typically provide contiguous coverage over a specified area by using high-gain overlapping spot beams. For effective utilization of the frequency spectrum of these satellite systems, the frequency is reused on a number of beams. This is done by dividing the available bandwidth into a number of subbands, typically using either a three-cell or a four-cell frequency-reuse scheme [3]. The relevant point here is that these considerations are applicable not only to low-Earth-orbit (LEO) satellites, but also to high-altitude-platform stations (HAPS).

Designs suitable and frequently used for multibeam antennas include (a) a single-aperture design with a single feed element per beam, (b) a single aperture design with overlapping feed clusters, (c) a direct radiating array, and (d) a multiple-aperture design with a single element per beam. In the satellite realm, the apertures are usually offset-parabolic reflector antennas. Here, we selected the use of dielectric lenses as an alternative solution for HAPS. Indeed, a multibeam radiation pattern is easily achievable by feeding a dielectric lens with several apertures that will generate *N* spot beams on the ground [4].

The proposed antenna system was realized by feeding a lens with circular waveguides terminated by small horns. To achieve the desired circular polarization, blade or septum polarizers were integrated into these feeds.

T M. Letizia, B. Fuchs, A. Skrivervik, and J. R. Mosig are with the Laboratory of Electromagnetics and Acoustics (LEMA), Ecole Polytechnique Fédérale de Lausanne (EPFL), EPFL Station 11, CH-1015, Lausanne, Switzerland; E-mail: marco.letizia@epfl.ch.

After a presentation of the scenario in Section 2, the lens-feed design is described in Section 3. Section 4 then discusses the dielectric lens design and the antenna's performance. Section 5 shows the prototype realization, together with the first measurement results. Finally, Section 6 concludes and summarizes the paper.

2. Scenario

In this section, a set of antenna specifications is introduced based on a possible scenario suitable for wireless communications via HAPS. The selected challenge corresponds to a concept currently under investigation in Switzerland. It consists of a Ka-band (27.5-31.3 GHz) multibeam antenna, mounted on a balloon platform at the standard height of $H_{HAPS} = 21$ km, and providing seven spot beams on the ground [5]. This antenna should allow for multi-cell architecture and for spectrum reuse [6-9].

From global system considerations, it was determined that the spot beams should be arranged in an overlapping hexagonal grid, and that every beam should guarantee an effective ground coverage in the form of a 5 km diameter circular cell (Figure 1, with $2R_{cell} = 5$ km). Typical beam overlaps used for multibeam antenna designs are -3 dB for two adjacent beams, and -4 dB for three adjacent beams, as explained in [3]. Since in this scenario the beams were arranged in a hexagonal grid, the beam-overlap level was chosen to be -4 dB. The circular cell boundary on the ground therefore corresponded to a -4 dB beam aperture. The field of view (FoV) angle associated with this cell diameter was simply given by (Figure 1)

$$FoV = 2\arctan\left(R_{cell}/H_{HAPS}\right) = 13.6° \qquad (1)$$

This value could also be considered to be an external specification for our antenna. Finally, it must be mentioned that in this particular project, global budget link considerations called for a minimum antenna gain of $G = 19$ dB.

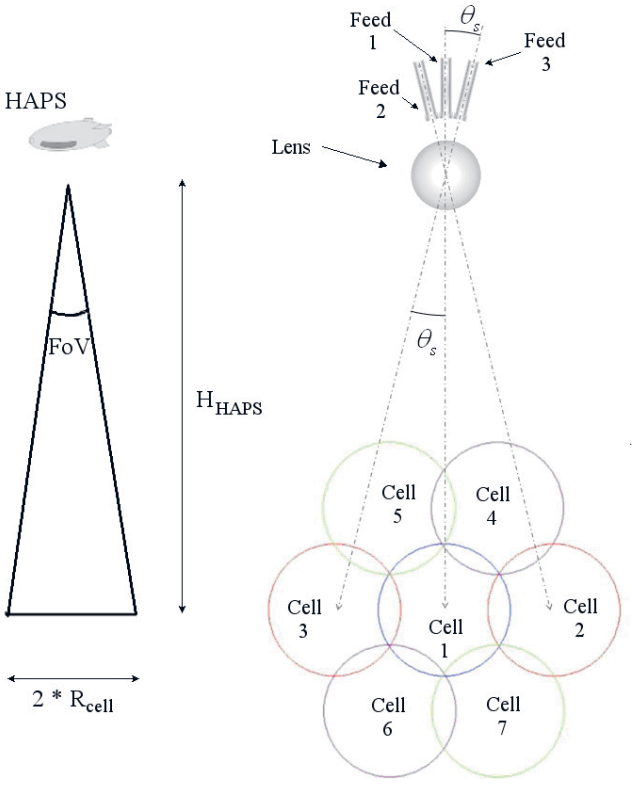

Figure 1. The HAPS downlink geometry applied to seven cells arranged in a hexagonal grid with a simplified antenna system.

The feasibility of the gain requirement from an antenna point of view can be very quickly checked. Standard antenna theory [10] provides an upper value for the theoretical directivity of a antenna having a conical main beam with no sidelobes as

$$D_{max} = 4\pi/\Omega_{beam}\ , \qquad (2)$$

where Ω_{beam} is the main beam's solid angle. This angle is usually estimated as [10]

$$\Omega_{beam} = \left(\theta_{3\text{dB}}\right)^2, \qquad (3)$$

where $\theta_{3\text{dB}}$ is the half-power beamwidth angle (radians) in any cut of the conical beam. From our specifications, the 4 dB angle is given, as it corresponds to the field-of-view angle. The 3 dB angle is obviously a trifle smaller, and can be estimated with the usual cosine-squared assumption for the pattern, yielding

$$\theta_{3\text{dB}} = 0.88\theta_{4\text{dB}} = 0.88FoV\ . \qquad (4)$$

Introducing the value of $\theta_{3\text{dB}} = 12.0° = 0.2094$ rad obtained from using Equation (4) in Equations (2) and (3), the maximum theoretical achievable directivity was found to be around 25.4 dBi. This gives a comfortable margin for including losses and efficiencies of real antennas, and still achieving the sought-after gain of 19 dB.

The specifications of the final link scenario are summarized in Table 1. Although those are key parameters for the antenna's design, the proposed concept can successfully be applied in other different realistic scenarios.

Frequency	27.5 to 31.3 GHz
Bandwidth	3.8 GHz (≈13%)
R_{cell}	2.5 km
H_{HAPS}	21 km
FoV	13.6°
G	19 dB

Table 1. The HAPS link scenario

In order to produce seven cells on the ground (as shown in Figure 1), seven independent beams have to be radiated by the lens. By placing seven feeds at the same distance from the surface of the lens, seven identical beams are generated. Each feed radiates broadside and properly illuminates the lens. The lens focuses the radiation coming from every feed and shapes it into a directive beam. Each feed has to be positioned around the lens in such a way that each beam points to the corresponding cell's center on the ground, and all the feeds' longitudinal axes intersect at the center of the lens. From geometrical considerations, the distance between adjacent cell centers is given by

$$d = 2R_{cell}\cos 30° = 4.33\,\text{km}. \qquad (5)$$

In turn, this distance determines the angular position of the feeds around the lens, guaranteeing adequate coverage of the ground. The angle between adjacent feeds must be

$$\theta_s = \arctan\left(4.33/H_{HAPS}\right) = 12° . \qquad (6)$$

A last word must be said about the ground shape of external cells. Obvious geometrical considerations demonstrate that the external cells of the cluster (cells number 2-7) are slightly deformed, and exhibit an elliptical shape with axes of 5.24 km and 5 km. This ellipticity of 5% could be corrected by acting on the corresponding feed. However, this is out of the scope and the interests of this paper.

3. Feed Design Analysis

For many reasons, waveguide technology is appropriate for feeding the lens for HAPS applications. Indeed, as shown in [11-14],

- The use of waveguide feeds allows handling high power.
- Interaction with the lens can be controlled by designing a proper horn.
- By using waveguide technologies, each feed is mechanically independent from the others. This usually leads to a weak electromagnetic coupling between feeds (on the other hand, if printed feeds were used, they would typically share the same substrate, thus increasing the chances of mutual coupling through surface waves, for instance).
- Waveguide feeds can be accurately and inexpensively realized in aluminum or brass by using digital milling machines
- Circular polarization is easily achievable by combining circular waveguides and internal polarizers.

Figure 2 is a schematic view of a circular waveguide feed that illuminates the lens. The coaxial-to-waveguide transition allows exciting the fundamental mode in the circular waveguide. This transition determines the bandwidth of not only the waveguide feed, but also of the whole lens antenna. Since the fundamental mode in a circular waveguide is linearly polarized, a polarizer is necessary to achieve circular polarization (section AB of Figure 2). Finally, since the waveguide's open end constitutes a strong discontinuity for the propagating waves, a horn is needed to provide a smooth transition to free space, matching the impedance while avoiding internal reflections. Moreover, the horn helps to properly illuminate the lens.

3.1 Coaxial to Waveguide Transition

The coaxial connector played an important role in the waveguide feed design. A 2.4 mm bulkhead connector assembly (see Figure 3a) was used to feed the waveguide: it allowed good performance up to 60 GHz. The most efficient way to excite the fundamental mode in circular waveguides via a coaxial connector is shown in Figure 3b. The structure in Figure 3 was modeled using CST *Microwave Studio*®. The dimensions *M*, *C*, and *P* were then optimized to work in Ka band. With the optimized values in Table 2, a return loss lower than −25 dB was achieved over the whole frequency band (27.5 GHz - 31.3 GHz).

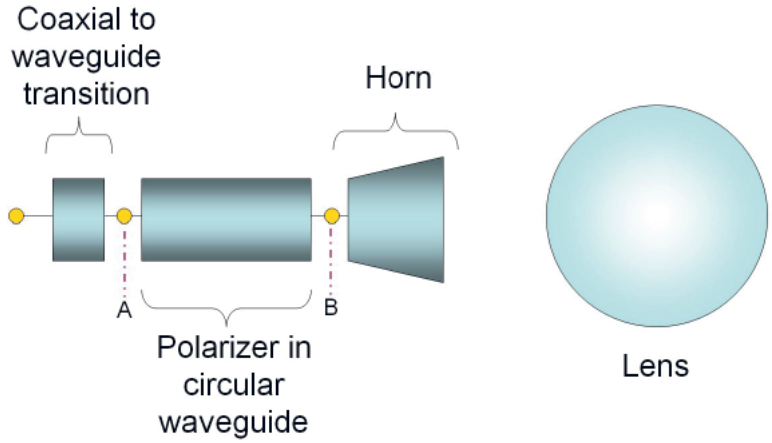

Figure 2. The antenna system configuration.

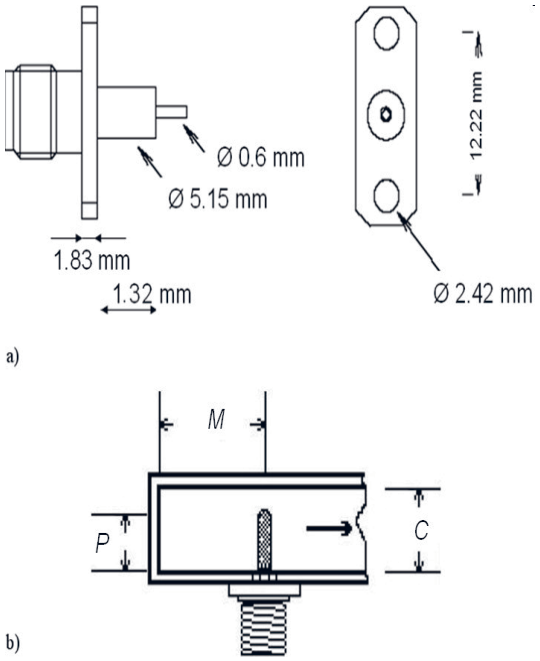

Figure 3. a) The dimensions of the coaxial connector, and b) the coaxial-to-waveguide transition.

M	3.72 mm
P	2.05 mm
C	7.30 mm

Table 2. The dimensions of the coaxial-to-waveguide transition.

3.2 Dielectric Septum Polarizer

A polarizer is needed to convert linear polarization into circular polarization. If wideband behavior is needed, a dielectric septum polarizer is a good candidate [15]. Such a polarizer can be designed [16, 17] by placing a metallic or dielectric slab (septum) in the center plane of the waveguide where the electric fields are strongest. A typical circular polarizer with a dielectric septum is illustrated in Figure 4a. A vertically incident field, E_i, which is inclined 45° with respect to the septum, is composed of two orthogonal components, E_h and E_v. E_h and E_v have the same magnitude and phase, and are respectively parallel and perpendicular to the dielectric septum. When the wave propagates through the septum region, $E_{h,o}$ (the horizontal component of the outgoing wave) is delayed by 90° with respect to $E_{v,o}$ by passing through the polarizer, and thus the outgoing wave is circularly polarized. A right-hand circular polarization or a left-hand circular polarization is produced depending on the direction of the incident field, E_i, as illustrated in Figure 4.

To improve the impedance matching, the rectangular-shaped dielectric septum of Figure 4 was smoothly modified and transformed into the tapered shape shown in Figure 5. The tapering at both ends of the dielectric septum was optimized for matching the impedance in both polarization states.

3.3 Design of a Ka-Band Circular Polarizer with Dielectric Septum

In order to compute the differential phase shift between the two polarizations, the structure has to be analyzed for both polarizations. From these two full-wave analyses, we recovered the scattering transmission parameters, $S_{21,h}$ and $S_{21,v}$, from which the differential phase, $\Delta\phi$, was computed as $\Delta\phi = \angle S_{21,h} - \angle S_{21,v}$. The polarizer design procedure started by considering the relevant specifications over the operating bandwidth, which, in this typical case, were

- the center frequency;
- the differential phase error with respect to 90°; and
- the return-loss lower bound.

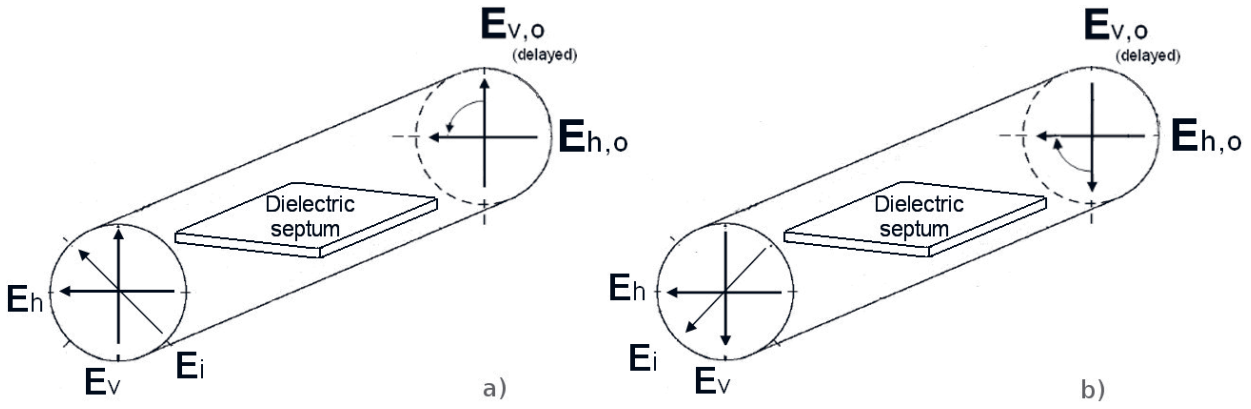

Figure 4. A schematic representation of the dielectric-septum circular waveguide polarizer. a) A vertically incident field produces left-hand circular polarization, and b) a horizontally incident field produces right-hand circular polarization.

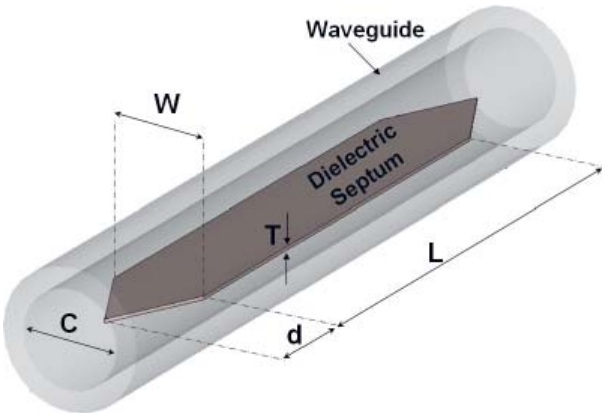

Figure 5. The polarizer model with the notation used for the design.

The following dimensions remained fixed during the polarizer-optimization design process:

- the polarizer diameter, *D*;
- the septum width, *W*;
- the septum dielectric constant, ε_r ; and
- the septum thickness, *T*.

The obvious choice was to use the same diameter for all of the circular waveguide's sections (the central part containing the polarizer, and the end parts making the connections with the coaxial feed and with the horn). This avoided step discontinuities, and ensured a perfect surface continuity for the entire lens feed. For mechanical reasons, the septum had to touch the internal waveguide wall, so the septum width, *W*, remained constant during the design. A width $W = 7.20$ mm ensured good mechanical contact between septum and waveguide wall. Rogers RT5870 substrate ($\varepsilon_r = 2.33$, $\tan\delta = 0.0012$) was used to design the septum.

L	6.20 mm
d	10.67 mm
C	7.30 mm
T	1.02 mm
W	7.20 mm

Table 3. The dimensions of the polarizer.

The relevant parameters for the optimization (see Figure 5) were the dielectric septum length, *L*, and the dielectric septum end extension (taper length), *d*. The initial values and bounds of *L* and *d* were chosen according to the recommendations found in [18]. The septum length, *L*, was taken to be in the range $[\lambda/2, \lambda]$, whereas the dielectric septum end extension, *d*, was selected to be in the range $[\lambda/4, \lambda/2]$. The differential phase shift was controlled by adjusting the septum length, *L*. By optimizing *d*, both the frequency center and return-loss specifications were met. Table 3 reports all of the final polarizer dimensions.

3.4 Complete Feed Design

The feed was completed by terminating both sides of the polarizer with a coaxial-to-waveguide transition (described in Section 3.1) and a small horn (see Figure 6). The distance between the dielectric slab and the coaxial connector pin was optimized to improve the return loss while keeping the quality of the circular polarization. Since the polarizer was designed to work in mono-modal conditions, its distance to the coaxial pin had to be larger than $\lambda_g/4$, because the fundamental mode was strongly perturbed around the coaxial pin.

The aperture of the horn and its length were optimized to improve both the axial ratio and the reflection coefficient of the structure. A big aperture improves the matching

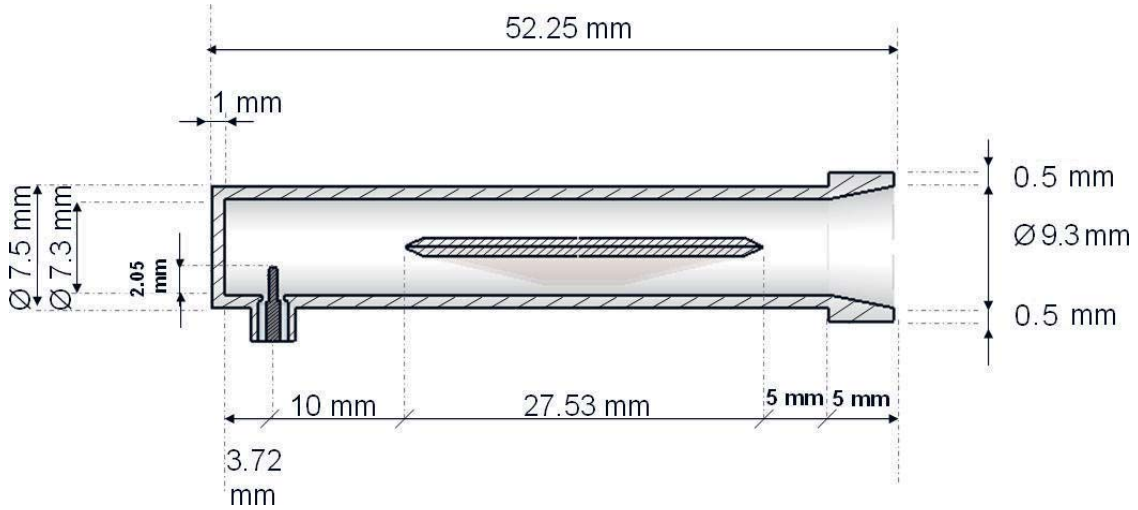

Figure 6. A cross-sectional view of the feed model, and its dimensions.

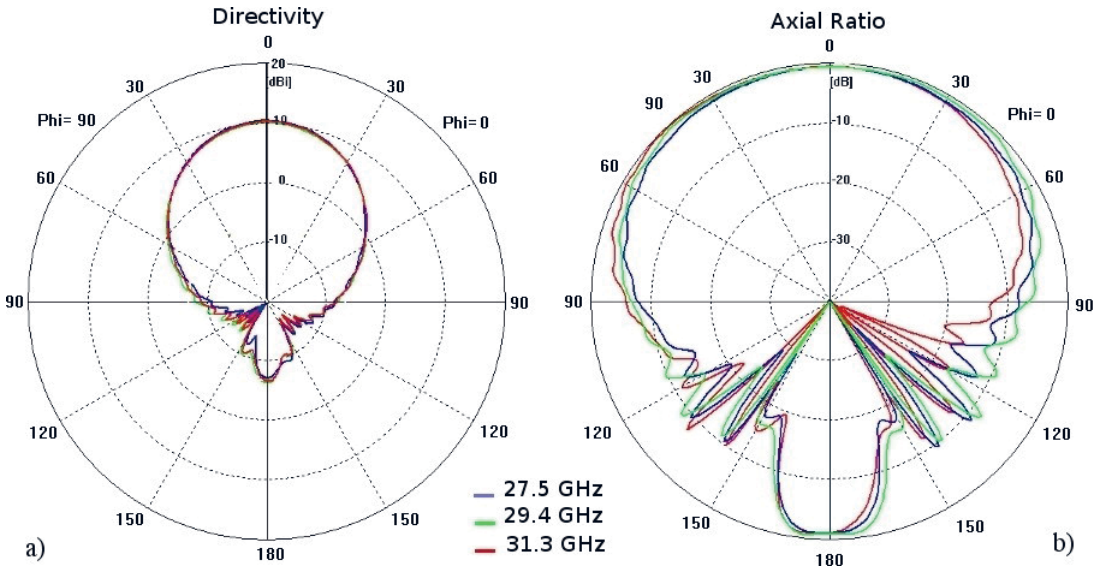

Figure 7. The feed radiation patterns: a) The directivity [dBi] and b) the axial ratio [dB].

between waveguide and free space, but also increases the feed's directivity. In a multi-feed scenario, large apertures would also result in restrictions concerning the angular distances between feeds. Moreover, the lens needed to be illuminated by a moderately directive primary source. It was therefore not convenient to design a large, highly-directive horn aperture. Figure 6 shows a single feed with its final dimensions. The scattering parameters of this structure were evaluated with CST *Microwave Studio*®. Figures 7 and 8 show the radiation patterns of the complete feed (no lens), and the excellent quality of the circular polarization achieved for different frequencies. The half-power beamwidth of the feed was about 60°, and its radiation pattern was symmetric and stable within the frequency band of interest.

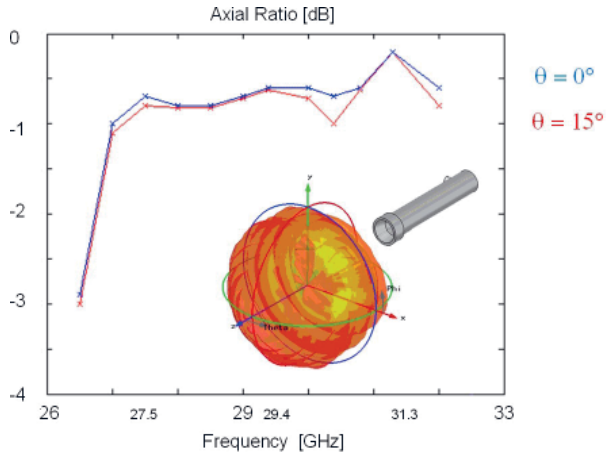

Figure 8. The feed radiation pattern: axial ratio as a function of frequency. The primary source axial ratio was higher than –2 dB within the frequency band (27.5 GHz to 31.3 GHz)

4. Homogeneous Teflon Lens Fed by Circular Waveguide

To focus the radiation of the primary source designed in the previous section, a homogeneous Teflon spherical lens was selected. Spherical dielectric lenses indeed exhibit a good tradeoff among performance, robustness, and ease of manufacturing.

The whole lens antenna structure was analyzed with CST *Microwave Studio*®. A dense mesh was used to model the feed polarizer, in order to have enough accuracy for the circular-polarization prediction, whereas a coarser mesh was used to model the homogeneous lens. The model of the whole structure (Figure 13) was meshed with more than 6.2×10^6 hexahedrals, which took around 12 hours to be simulated using a 2.66 GHz quad-core CPU.

In order to efficiently design the lens antenna, the degree of complexity of the analyzed structure was increased step by step:

1. First, the waveguide aperture (horn only) was associated with the lens to roughly find the best lens diameter and the best feed-lens distance, looking at the far field and the reflection coefficient. At this stage, only the linear polarizer source was considered.
2. The complete feed (with polarizer) and lens were then considered to compute the far field, the reflection coefficient, and the axial ratio.
3. Finally, the seven feeds and lens were simulated to determine the far field, the reflection coefficient, the axial ratio, and the coupling between feeds.

The results are now detailed for each step.

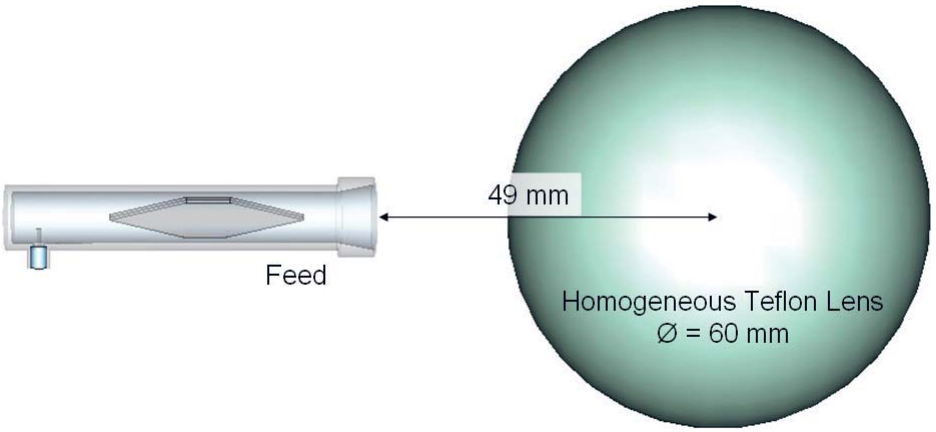

Figure 9. The single-beam antenna model with relevant dimensions.

4.1 The Lens Fed by One Waveguide

The lens radius, R, and the distance, F, between the center of the lens and the feed aperture, are obviously the most critical parameters influencing the beam pattern. They were optimized to find the best tradeoff among maximum directivity, field of view, and the best reflection coefficient. F can be roughly approximated by the homogeneous dielectric lens' focal-point distance, given by [19]

$$F \approx \frac{nR}{2(n-1)}, \tag{7}$$

where n is the refractive index of the lens material ($n \approx 1.44$ for Teflon). This value was used as a starting point to speed up the numerical optimization, which finally yielded $F = 49$ mm and $R = 30$ mm as optimized values.

The complete feed and the lens were included in a global numerical model (Figure 9). The performance of the full antenna system was as follows.

The reflection coefficient was lower than -15 dB within the frequency band of interest (Figure 10), and the antenna bandwidth was more than 13%. The feed worked in a mono-modal condition within 26.8 GHz and 32.5 GHz. The presence of the lens did not significantly alter the return loss of the feed.

The far-field patterns of the lens antenna are plotted in Figure 11 for frequencies of 27.5 GHz and 29.4 GHz. A directivity of 21 dBi was reached, and the main-beam half-power beamwidth was equal to 12°, for a field of view of 13.4°. The sidelobe level, *SLL*, was 18 dB. As expected, the pattern was identical for both the $\phi = 0°$ and $\phi = 90°$ planes. Furthermore, it was stable within the frequency band of interest. The lens increased the directivity of the feed alone by 10 dB.

The aperture efficiency of a lens antenna is defined by [10]

$$\eta_{ap} = D/D_{ap}\,, \tag{8}$$

where D is the maximum directivity of the lens and D_{ap} is the directivity of a constant-field circular aperture with the same lens diameter. Since the lens directivity was computed to be 21 dBi, we easily obtained an aperture efficiency given by

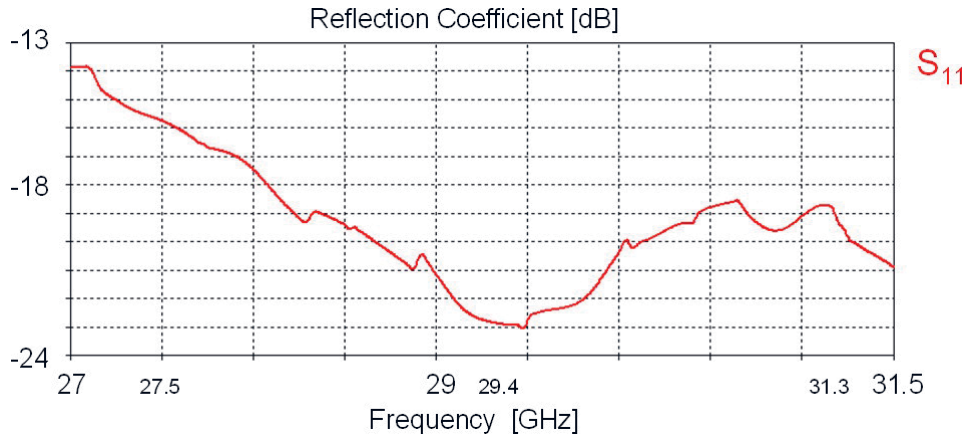

Figure 10. The reflection coefficient of the Teflon lens fed by one primary source.

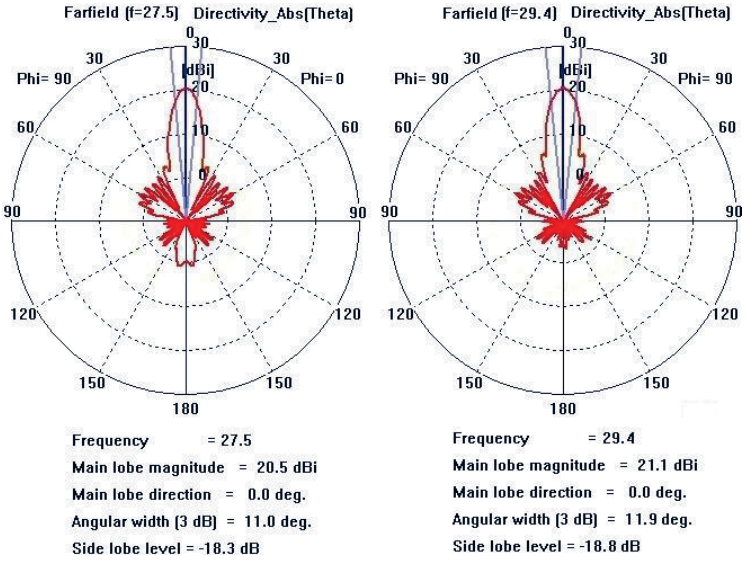

Figure 11. The single beam radiation patterns: directivity

$$\eta_{ap} = \frac{10^{(21/10)}}{(2\pi R/\lambda)^2} \approx 37\% \,. \qquad (9)$$

Loses were not taken into account in Equation (9). η_{ap} could be considered too low, but the design goal here was not to maximize the directivity, but rather to meet footprint and axial-ratio specifications. Indeed, the quality of the circular polarization is shown in Figure 12 for different frequencies and for $\theta = 0°$ and $\theta = 15°$. The axial ratio of the complete antenna system (Figure 9) was better than –2 dB. According to Figures 8 and 12, the lens degraded the primary source polarization quality by only 0.8 dB in the worst case.

Simulations confirmed that the polarization of the antenna system shown in Figure 9 could be easily changed from right-hand circular polarization to left-hand circular polarization by rotating the polarizer septum 90° along its major axis. The antenna's performance for right-hand circular polarization and left-hand circular polarization was identical, as expected.

The antenna's single-beam performance is summarized in Table 4. All of the initial scenario specifications given in Table 1 were achieved. The antenna covered all the expected frequencies, and indeed showed a frequency bandwidth broader than required (19% instead of 13%). The directivity of 21 dBi gave a 2 dB difference to meet the gain requirement of 19 dB. This means that the ohmic and dielectric losses of the real antenna had to be lower than 2 dB. Both the sidelobe level and axial ratio were within the specifications.

Working Frequency Band	26.8-32.5 GHz
Bandwidth	5.7 GHz (≈19%)
Directivity	21 dBi
Beamwidth at –4 dB (FoV)	13.4°
Sidelobe level (SLL)	< –18 dB
Circular polarization quality (AR): RHCP and LHCP	< 2 dB

Table 4. The performance of the Teflon lens fed by a circular waveguide feed.

4.2 Lens Fed by Seven Waveguides

In the next step, the full multibeam antenna system was modeled by positioning seven feeds around the lens, as shown in Figure 13. The angle between two adjacent beams was $\theta_s = 12°$, as explained in Section 2. The distance between the center of the lens and each horn aperture was kept at 49 mm. The polarizers were positioned within each feed in order to radiate a right-hand-circular-polarized field.

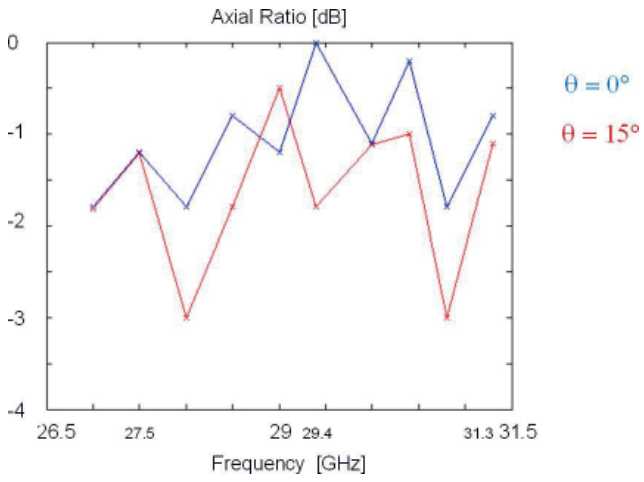

Figure 12. The single beam radiation patterns: axial ratio [dB] as a function of frequency. The antenna system's axial ratio was higher than –2 dB within the frequency band.

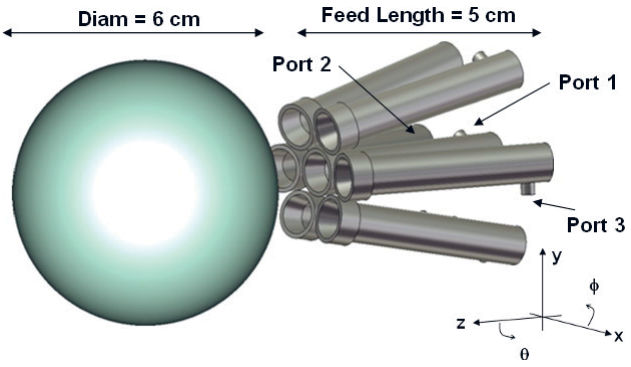

Figure 13. The multibeam antenna model

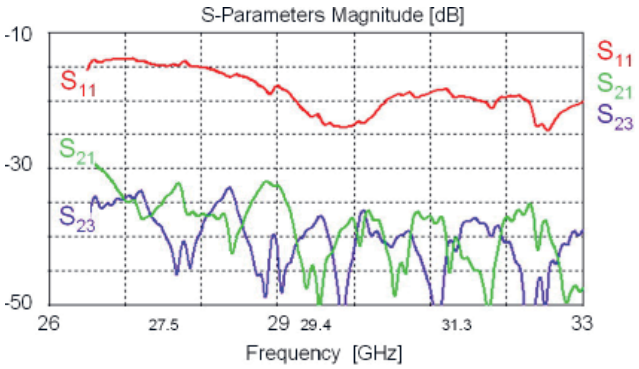

Figure 14. The scattering parameters: the reflection coefficient and the transmission coefficients

The active reflection coefficient of the central feed in the presence of the other six (S_{11} in Figure 14) was quite similar to that of the single-feed antenna (Figure 10). This anticipated weak coupling between feeds, and promised quite identical results for all the S_{ii} in the multi-feed simulation. Indeed, the coupling between adjacent feeds was lower than -32 dB within the working frequency band. This is shown in Figure 14, where for symmetrical reasons only S_{21} and S_{23} are depicted. Ports 1, 2, and 3 were defined as in Figures 1 and 13. Again, the single-beam radiation pattern (Figure 15) of the multibeam antenna (embedded radiation pattern) did not change significantly compared to the radiation pattern of the single-feed antenna (Figure 11). Since the performance of one waveguide feed was not influenced by the presence of the others, the multibeam antenna could be easily designed focusing attention on only one feed.

Since in the proposed antenna system each radiated beam can have both right-hand circular polarization and left-hand circular polarization, depending on the position of the polarizer, the coupling between feed 1 and feed 2 (see Figure 13) was compared for the two following cases:

- feeds 1 and 2 both radiated a right-hand circular polarization field;

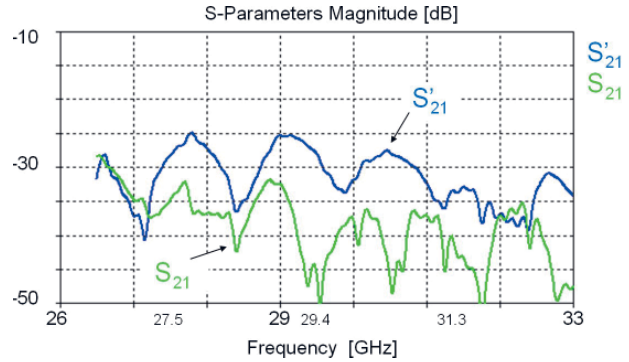

Figure 16. The scattering parameters, showing the coupling of the feeds coupling. S'_{21} : feed 1 radiated a right-hand circularly polarized field and feed 2 radiated a left-hand circularly polarized field; S_{21} : both feeds radiated right-hand circularly polarized fields.

- feed 1 radiated right-hand circular polarization and feed 2 radiated left-hand circular polarization

.

Figure 16 shows that the coupling between adjacent feeds increased when the two primary sources radiated with opposite polarization. This phenomenon was probably due to partial reflections in the lens' surfaces, reversing the wave polarization. Although of minor relevance (the coupling

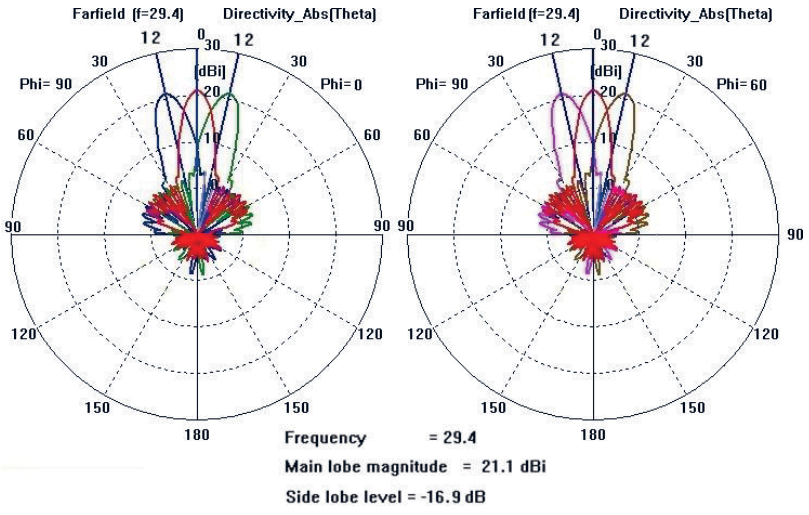

Figure 15. The multibeam radiation patterns: directivity [dBi]; $\phi = 0°$ and $\phi = 60°$ were the most interesting planes due to the antenna system's geometry.

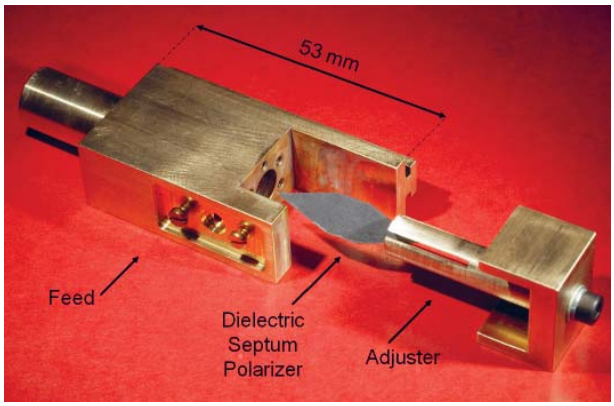

Figure 17. A single feed realization: the dielectric polarizer was introduced into the waveguide structure by using a proper adjuster

increased from −32 dB to −25 dB at some frequencies), these considerations had to be taken into account when the performance of the cluster was evaluated.

5. Initial Prototype

Primary sources, dielectric polarizers, and Teflon lens were realized by using milling-machine techniques with a nominal tolerance of 50 μm. A metal adjuster tool (Figure 17) was machined to align the dielectric septum inside the waveguide before mounting the connector. Thanks to this tool, few operations were needed to change the antenna's polarization. Figure 18 is a picture of a single-feed prototype with a mounted coaxial connector. The dielectric-slab polarizer was inside the waveguide, and the horn shape was integrated into the waveguide's inner profile. A plastic frame (Figure 19) kept the lens and the feeds in place for anechoic-chamber measurements. Preliminary measurements of a feed reflection coefficient (Figure 20) showed the validity of the global optimization procedure, as the matching improved in the presence of the other antenna parts (polarizer and lens).

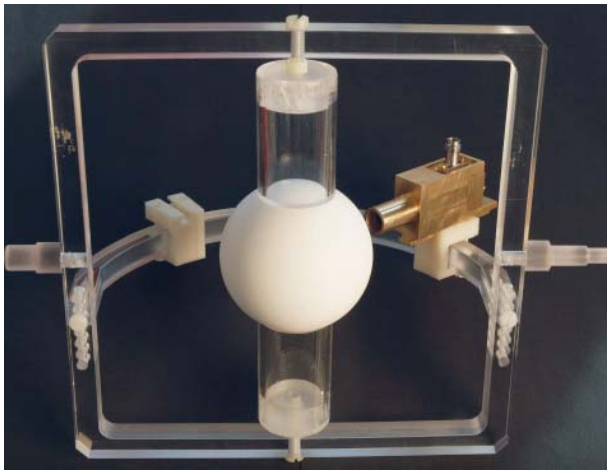

Figure 19. The 60 cm diameter Teflon lens realization with the primary source.

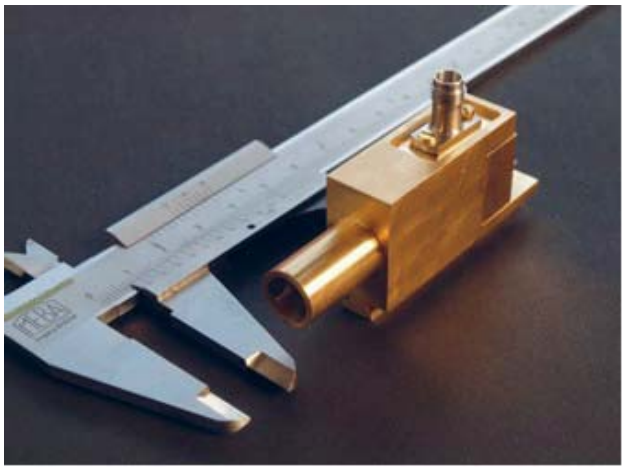

Figure 18. The single feed prototype with a mounted coaxial connector: the dielectric slab polarizer was inside the waveguide, and the horn shape was integrated in the waveguide's inner profile.

6. Conclusion

This paper has presented a 30 GHz multibeam antenna suitable for HAPS wireless applications. A set of well-known elements (coaxial excitation, circular waveguide, septum polarizer, circular horn, and homogeneous dielectric lens) has been carefully optimized, in order to produce a functional concept, demonstrated by a preliminary prototype.

The antenna was based on seven identical elementary radiators that feed a dielectric lens. Every elementary radiator consisted of a circular waveguide internally supporting a dielectric septum polarizer and terminated with a short horn. These elementary radiators can handle relatively high powers, while providing excellent circular polarization and a reasonable bandwidth meeting the system specifications. Moreover, computer simulations showed that the mutual coupling between adjacent elementary radiators (and hence, between adjacent beams) could be easily mastered and kept

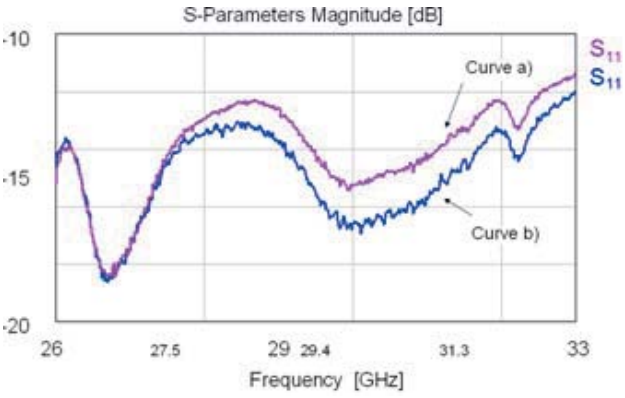

Figure 20. Preliminary measurements of the single primary source. Curve a is the reflection coefficient without the polarizer (empty waveguide), and curve b is the reflection coefficient with the polarizer embedded in the waveguide. The feed radiator was better matched with the polarizer.

at low levels. With a relatively easy fabrication process and excellent mechanical robustness, these radiators are the best possible candidates for the antenna's feed system.

The analysis of the complete antenna, including the lens, was also full of promise. According to our simulations, the lens only slightly degraded (about 0.8 dB in the broadside direction, and 2 dB at 15° from the broadside direction) the good quality of the feed's circular polarization (always below 3 dB within the aperture angle, lower than 2 dB in the main direction of the beam). The complete antenna showed excellent performance, with a symmetric radiation pattern stable across the 27 to 32 GHz frequency band. Return loss (lower than −15 dB within the working frequency band) and sidelobes (lower than −18 dB) also met the specifications. With overall dimensions of only 12 cm × 6 cm × 6 cm, this antenna concept is an excellent solution for wireless systems that require high RF power, circular polarization, high antenna gain, and multibeam behavior. Preliminary measurements confirmed the validity of the performed synthesis, as individual elements improved their performance when included into the global antenna system.

7. Acknowledgements

This research was initiated within the European COST Action 297 "HAPCOS," and performed thanks to the financial support of the Swiss CTI Project 9301.1 "FEASANT." The authors also wish to thank Mr. J.-F. Zurcher (EPFL-LEMA) for invaluable help with the prototype construction and measurement, and the staff of CSEM and StratXX, partners in the CTI project, for helpful discussions and support.

8. References

1. J. Gavan, S. Tapuchi and D. Grace, "Concepts and Main Applications of High-Altitude-Platform Radio Relays," *Radio Science Bulletin*, No. 330, September 2009.

2. J. Thornton, D. Grace, M. H. Capstick and T. C. Tozer, "Optimising an Array of Antennas for Cellular Coverage from a High Altitude Platform," *IEEE Transactions on Wireless Communications*, **2**, 3, 2003, pp. 484-492.

3. S. K. Rao, "Design and Analysis of Multiple-Beam Reflector Antennas," *IEEE Transactions on Antennas and Propagation*, **AP-41**, 4, April 1999, pp. 53-54.

4. D. Gray, J. Thornton, H. Tsuji and Y. Fujinos, "Scalar Feeds for 8 Wavelength Diameter Homogeneous Lenses," IEEE International Symposium on Antennas and Propagation, Charleston, USA, 2009.

5. T. C. Tozer and D. Grace, "High-Altitude Platforms for Wireless Communications," *IEE Electronics and Communications Engineering Journal*, **13**, June 2001, pp. 127-137.

6. J. Thornton, "Properties of Spherical Lens Antennas for High Altitude Platform Communications," 6th European Workshop on Mobile/Personal Satcoms and 2nd Advanced Satellite Mobile Systems (EMPS & ASMS), September 21-22, 2004, ESTEC, European Space Agency.

7. J. Thornton, D. Grace, C. Spillard, T. Konefal and T. C. Tozer, "Broadband Communications from a High Altitude Platform – The European HeliNet Programme," *IEE Electronic Communication Engineering Journal*, **13**, June 2001, pp. 138-144.

8. M. A. Mitchell, J. R. Sanford, L. E. Corey, R. A. Moore and V. P. Pusateri, "A Multiple-Beam Multiple-Frequency Spherical Lens Antenna System Providing Hemispherical Coverage," *ICAP 89*, 1989, pp. 394-398.

9. J. Thornton, "Antenna Technologies for Communications Services from Stratospheric Platforms," 4th International Airship Convention and Exhibition, Cambridge, UK, July 2002.

10. C. A. Balanis, *Antenna Theory, Second Edition*, New York, John Wiley and Sons, 1997, pp. 45-86, 609.

11. J. Sanford and H. Schrank, "A Luneberg-lens Update," *IEEE Transactions on Antennas and Propagation*, **AP-37**, 1, January 1995, pp. 76-79.

12. J. Sanford, "Scattering by Spherically Stratified Microwave Lenses," *IEEE Transactions on Antennas and Propagation*, **AP-42**, 5, May 2006, pp. 690-698.

13. B. Fuchs, *Lentilles Stratifiees et Sources Reelles Associees – Analyses Theoriques et Validations Experimentales en ondes Millimetriques*, PhD dissertation, Universite de Rennes I, Rennes, November 2007.

14. B. Fuchs, S. Palud, L. L. Coq, O. Lafond, M. Himdi and S. Rondineau, "Scattering of Spherically and Hemispherically Stratified Lenses Fed by Any Real Source," *IEEE Transactions on Antennas and Propagation*, **AP-56**, 2, February 2008, pp. 450-460.

15. S. W. Wang, C. H. Chien and C. L. Wang, "A Circular Polarizer Designed with a Dielectric Septum Loading," *IEEE Transactions on Microwave Theory and Techniques*, **52**, 2004, pp. 1719-1723.

16. J. Bornemann and V. A. Labay, "Ridge Waveguide Polarizer with Finite and Stepped-Thickness Septum," *IEEE Transactions on Microwave Theory and Techniques*, **MTT-4352**, 1995, pp. 1782-1787.

17. J. Esteban and J. M. Rebollar, "Field Theory Cad of Septum OMT-Polarizers," IEEE International Symposium on Antennas and Propagation *Digest*, 1992, pp. 2146-2149.

18. T. Zhang and Z. Yan, "A Ka Dual-Band Circular Waveguide Polarizer," National Laboratory of Antennas and Microwave Technology, Xidian University, Xi'an, 710071, China (CIE).

19. B. Schoenlinner, W. Xidong, J. P. Ebling, G. V. Eleftheriades, G. M. Rebeiz, "Wide-Scan Spherical-Lens Antennas for Automotive Radars," *IEEE Transactions on Microwave Theory and Techniques*, **50**, 9, 2002, pp. 2166-2175.

Inter-High-Altitude-Platform Handoff for Communications Systemswith Directional Antennas

K. Katzis
D. Grace

Abstract

In this paper, we examine a number of issues relating to the inter-HAP handoff process for broadband communications that operate with fixed or steerable directional antennas, allowing a platform to be replaced either for maintenance or periodic replacement in the case of short-term manned HAPs. Handoff performance was evaluated for both types of antennas based on a number of criteria, such as the antenna's beamwidth, the platforms' height, the position cylinder, and the civil aviation authority (CAA) cylinder. Results showed that for users employing fixed antennas pointing towards the center of the position cylinder, handoff can take place as soon as the new platform enters the cylinder. Users from the center of the service area are required to employ the widest-beamwidth antenna (29°), whereas users at the edge of the service area can employ a narrower beamwidth. Users employing steerable antennas can employ a much narrower beamwidth. However, connections will be dropped for any beamwidth less than 5°, unless users employ two antennas, or the new platform follows a complex flight path, preferably as close as possible (±305 m vertical separation) to the current serving platform.

1. Introduction

High altitude platforms (HAPs) are either airships or aircraft [1-5] that will operate in the stratosphere, 17 to 22 km above the ground. Such platforms have been suggested for the delivery of both broadband fixed wireless access (BFWA) services [6] and 3G mobile [7]. HAPs will have a rapid rollout capability and the ability to serve a large number of users, using considerably less communications infrastructure than required by a terrestrial network [8]. To aid the eventual deployment of HAPs, the International Telecommunications Union – Radiocommunications sector (ITU-R) has allocated spectrum in the mm-wave bands. This is around 48 GHz worldwide [8] and 31/28 GHz for forty countries worldwide, including parts of Asia and the Americas [10], with spectrum in the 3G bands also allocated for use with HAPs [11].

Early designs for HAPs were focused on unmanned long-endurance craft that would stay aloft for months or even years at a time, delivering services in a manner similar to satellites [8]. This vision is still some way off, due to both technical and regulatory reasons. To bypass these difficulties, a reexamination has been undertaken of the fundamental requirements for HAPs to be able to provide continuous communications and other services. This has led to the conclusion that the same range of services can be delivered from a fleet of short-endurance manned HAPs, equipped with a suitable handoff strategy that can be devised to provide service continuity. Solving this problem is likely to be much more straightforward in the short term, allowing the potential of this new means of delivery to be exploited, rather than trying to solve the more-difficult issues associated with the unmanned vehicles.

To achieve service continuity, a minimum of two HAPs are required. One will fly over the service area providing the connectivity. When it is nearing the end of its mission, the second HAP will take off and arrive on station over the service area. Services will then be handed over to the newly arrived HAP and the original HAP will then return to the ground, with this cycle continuously repeating. Manned HAPs have been available for some time, e.g., there are the Proteus, M55 Geophysica [12], and the model range from Grob, the G520: Strato 1, and HALE G600, with the G850: Strato 2C under development [13].

K. Katzis is with the Department of Computer Engineering, European University Cyprus,6 Diogenes Str. Engomi, 1516, Nicosia, Cyprus; Tel: +357 22 713296; Fax: +357 22 590539; E-mail: K.Katzis@euc.ac.cy. D. Grace is with the Communications Research Group, Department of Electronics, University of York, Heslington, York, YO10 5DD, United Kingdom; Tel: +44 (0) 1904 432396;Fax: +44 (0) 1904 432335; E-mail: dg@ohm.york.ac.uk.

Handoff is widely used in cellular communications in order to maintain service continuity when mobile users move between cells provided by a fixed-base-station infrastructure, with the protocols specified in mobile standards such as 3G. Until recently, the most popular wireless broadband standards, e.g., Wi-Fi (IEEE802.11 [14]) and WiMAX (IEEE802.16), did not contain built-in handoff. This has recently been remedied for WiMAX with the development of IEEE802.16e-2005 [15] and IEEE802.16g-2007 [16]. One important difference with all of these standards is that it is the user that is moving, and not the base station. The main implication in our scenario is that the platform itself is moving, whereas the users are fixed. This makes the handoff process more deterministic, with the total user population requiring handoff in a short period of time. The proposed HAP handoff scenario has some similarities to commercial low-Earth-orbit satellites, except that satellite movements are highly predictable, and handoff strategies are intended to deal with users with wide-beamwidth antennas [17], [18]. The intended broadband data rates for HAPs are also significantly higher.

Handoff requirements for a cellular architecture with mobile users delivered from a long-endurance HAP have already been studied by a number of researchers. For example, the requirements for geographical locations requiring handoff when subject to HAP lateral drift was studied [19], along with corresponding payload stabilization strategies, with earlier work carried out by El-Jabu and Steele [20]. An integrated handoff/radio-resource management strategy that copes with platform movement has been developed to operate transparently with fixed broadband users [21]. The effects of platform instability on UMTS [22] and platform motion on IMT-2000 soft handover [23] have also been addressed. Foo et al. [24] modeled conventional 3G handoff for mobile users, assuming stationary HAPs. Nofal et al. [25] also examined handoff for HAPs, for a ring-shaped beam that was designed to cope better with circling platforms. However, none of the above addresses this fundamentally different problem.

The purpose of this paper is to examine a number of issues relating to the inter-HAP handoff process, of greatest benefit to short-endurance HAPs for broadband communications that operate with fixed and steerable directional antennas. The paper will first describe the HAP communications architecture, along with the station-keeping and regulatory constraints affecting the movement of HAPs in close proximity to one another. Section 2 will then discuss the effect of cell overlap and the implications of a handoff process on existing broadband communications standards. Section 3 will then develop possible handoff strategies, and present the necessary analytical models and equations in order to determine the handoff performance. Following this, Section 4 will present the performance results, and discuss their impact on the way handoff should operate with the HAP architecture. Finally, conclusions will be presented.

2. Cell Overlap and Handoff Techniques

Cell overlap and handoff techniques together have become an essential mechanism for HAP communication systems. In [21, 26-28], it was shown that by employing handoff, it is possible to maintain uninterrupted connectivity when the aerial platform moves. Furthermore, it is possible to redirect existing traffic from one cell to another in order to improve capacity on a cell-by-cell basis [29, 30]. For this scenario, handoff is employed when a platform needs to be replaced, either for maintenance or because it has to be replaced according to the time schedule (manned airplanes).

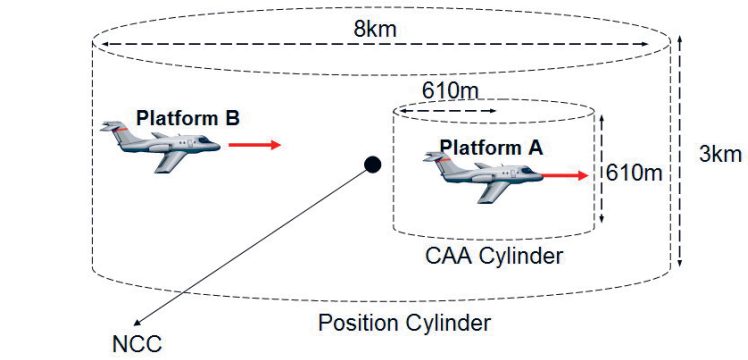

Figure 1. The high-altitude short-endurance (HASE) handoff scenario.

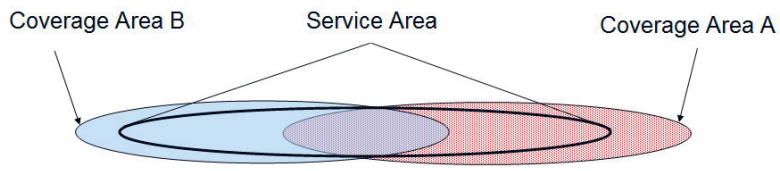

2.1 High-Altitude Short-Endurance Platforms

Broadband services using aerial platforms can be delivered through three different types of platforms. These are the unmanned aerial vehicles (UAVs), unmanned airships, and manned airplanes. Manned airplanes are possibly the most realistic option at the moment, as they are legally and financially viable. Manned airplanes can provide long-endurance service with a fleet of platforms operating for a short period of time, interchanging at regular intervals.

G520 Strato 1, G850 Strato 2C, and HALE are aircraft designed by GROB [13] specifically for short-term stratospheric missions. The G520 aircraft has a pressurized cockpit for the pilot, and a wingspan of 33 m. It is capable of carrying a payload of 1,000 kg. The aircraft has a range of 4,000 km, an endurance of 13 hr, and can operate up to 15.5 km. On the other hand, the G850 Strato 2C has the ability to remain airborne for up to 50 hr. During a typical mission, the aircraft can carry a crew of four people in a reasonably roomy pressurized cabin, flying at an altitude between 15 km and 23 km for over 8 hr. HALE is a high-altitude surveillance aircraft, designed specifically for high-altitude and long-endurance surveillance missions. The aircraft is capable of flying nonstop as far as 21,000 km with a flight endurance of 33 hr, remaining aloft at altitudes of up to 18 km for over 18.6 hr [13].

2.2 Long-Term Missions Using Short-Duration Platforms

HAP movements during service operation are constrained by two cylinders. One is the position cylinder, which determines the actual limit of movement during correct operation. The second cylinder is the Civil Aviation Authority (CAA) cylinder, which defines the limit of which two planes can get close together. According to [31], a plane serving as a HAP should be stationed within a position cylinder for 99% of the time to ensure constant service availability. As seen in Figure 1, the position cylinder must have a radius of 4 km and a height of 3 km [31]. The nominal center of connectivity (NCC), which is the center of the position cylinder, is a fixed point. It is ideally located at the center of the specified service area at 17 km height. Platform A, the current serving platform, must be located at any time within the position cylinder until the new coming platform B takes complete control of the services.

During the transition time, part of the service area is served by the coverage area of platform A and part from platform B, until platform B takes position, ideally near the nominal center-of-connectivity point. These platforms will be operating for limited time durations, depending on the type of the platform And/or the arrangement with the crew. They will fly above the service area, and provide WiMAX (IEEE 802.16) or 3G connectivity. The handoff should gradually take place, which means that the coverage area will be gradually served by the new platform while the existing one will retire. For manned planes operating in the service area, the planes – according to the Civil Aviation Authority (CAA) in the UK [32], and the Federal Aviation Authority (FAA) in the US [33], and the Reduced Vertical Separation Minimum regulation – must have at least 305 m (1000 ft) vertical separation. This is provided that both airplanes are equipped with height-keeping systems, which enable them to maintain the prescribed height-keeping performance capability. In the case were the two aircraft are separated by less than the vertical separation minimum, then some form of horizontal separation must exist.

For this work, we assume that a 610 m (2000 ft) horizontal separation distance is required, provided that a procedural separation is employed by the pilots. Figure 1 illustrates the flying zone of platform A as a cylinder (CAA cylinder). The new platform, platform B, cannot enter this cylinder, as this will breach the CAA/FAA regulations. It will thus have to either fly above or underneath platform A. Ground-user customer premises equipment (CPE) antennas will be pointing somewhere within the position cylinder, depending whether their antennas are fixed or steerable.

3. Inter-High-Altitude Platform Handoff Strategies

For users to perform handoff, both platforms must be situated within the range for which the user's antenna is set to operate (either fixed or steerable). That is when the minimum specified channel-to-interference noise ratio (CINR) level between a user and both platforms is met. This depends primarily on the antenna beamwidth employed, which is equivalent to the angle subtended with the edge of the cell optimally set at −4.5 dB [34].

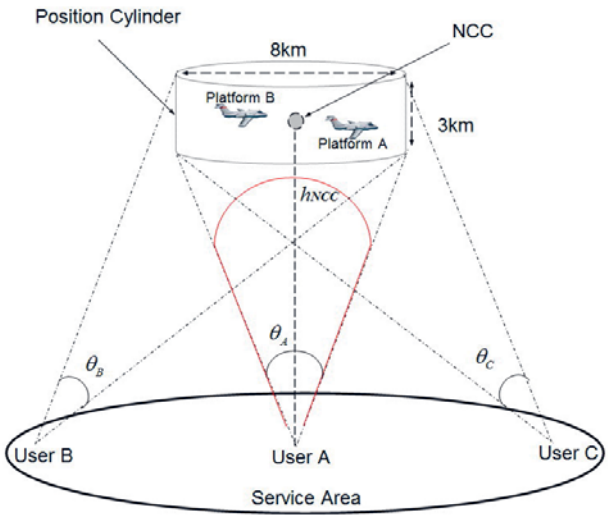

Figure 2. Customer-premises-equipment antenna beamwidths and subtended angles for users employing fixed antennas

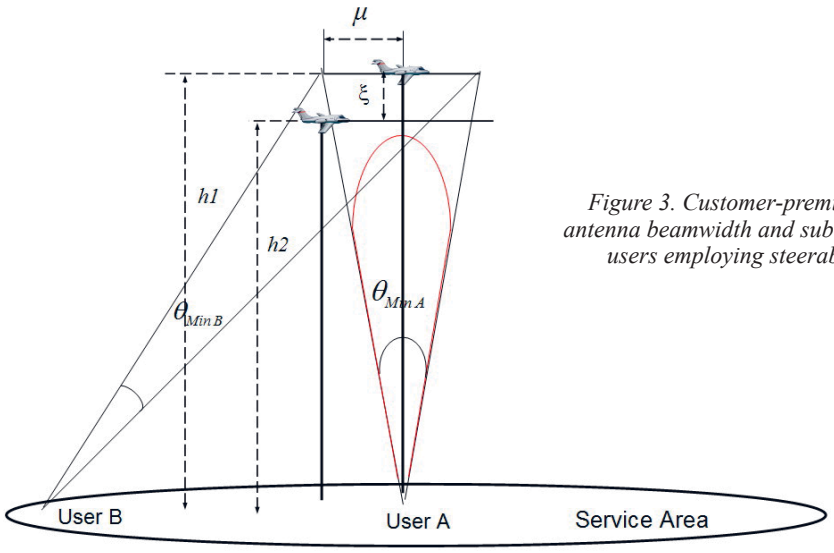

Figure 3. Customer-premises-equipment antenna beamwidth and subtended angles for users employing steerable antennas.

3.1 CPE Antenna Beamwidth

Based on the dimensions of the CAA cylinder illustrated in Figure 1, it is possible to define the minimum antenna beamwidth for the ground users, assuming a fixed or steerable antenna. The beamwidth in both cases must be wide enough to be able to track the current platform within the position cylinder, as well as be able to cope with the handoff procedure.

As shown in Figure 2, for a fixed antenna pointing towards the nominal center-of-connectivity point, the beamwidth must be wide enough to track the platform whilst it moves through the position cylinder [31]. The platform must be located at any time within the cylinder. The beamwidth of the customer-premises-equipment antenna is thus wide enough to cope with any of the horizontal and vertical separation distances between the platforms during the change of shift.

The beamwidth of the customer-premises-equipment fixed antenna must be wide enough (approximately 29°), assuming that the minimum height of the platform can be set at 15.5 km (derived from range 17 km ± 1.5 km) and the user is located at the center of the service area. On the other hand, if steerable antennas are employed, then the beamwidth can be smaller than 29°. In this case, users located directly under the position cylinder (see Figure 3, nominal center-of-connectivity point) will have to employ wider beamwidth than other users, since they will be closer to the platform. They will thus be required to be able to cope with the handoff procedure during which the two platforms will be close to each other based on the CAA cylinder. As platform B flies within the position cylinder, all customer-premises-equipment antennas will continue to be steered to point at platform A. Platform B can be located as close to platform A as possible, provided that the CAA cylinder restrictions are met. Based on these restrictions (horizontal and vertical separation), it is possible to define the minimum beamwidth that the steerable antennas must employ.

As explained before, the minimum beamwidth, θ_{min}, can be set based on how close the platforms can get before we can perform the handoff. This can be achieved in two ways. These are to have platform B either horizontally or vertically aligned with platform A.

If platform B is horizontally aligned with platform A at a distance μ, then the beamwidth for user A, which is mostly subjected to platform movements, can be defined as

$$\theta_{min} = 2\arctan\left(\frac{\mu}{h_1}\right), \text{ when } \xi = 0, \qquad (1)$$

where μ is the minimum horizontal separation distance between the two platforms. Since ξ is 0, then μ must be equal to 610 m. In the case where the beamwidth is required to be made narrower (to achieve higher data rates), the two platforms must be vertically aligned when changing shift, with a vertical separation that is greater or equal to 305 m. The two platforms can thus be (ideally) vertically aligned with each other without risking an air collision. Making the beamwidth of the user's antenna narrower has a direct impact on the time period in which a handoff is permitted. This effectively decreases the amount of time that the user has to switch from one platform to the other. On the other hand, it provides higher connection speeds, due to an improved link budget.

3.2 Handoff Opportunity Period and Antenna Beamwidth

The handoff-opportunity period (HOP) is defined as the time period in which a user can perform handoff from one platform to the other. During this time, both users and base stations are required to be ready for the handoff. This handoff-opportunity period is defined according to the location of the user, the beamwidth, and the positions and the speeds of the platforms. The analysis here is based on the following assumptions:

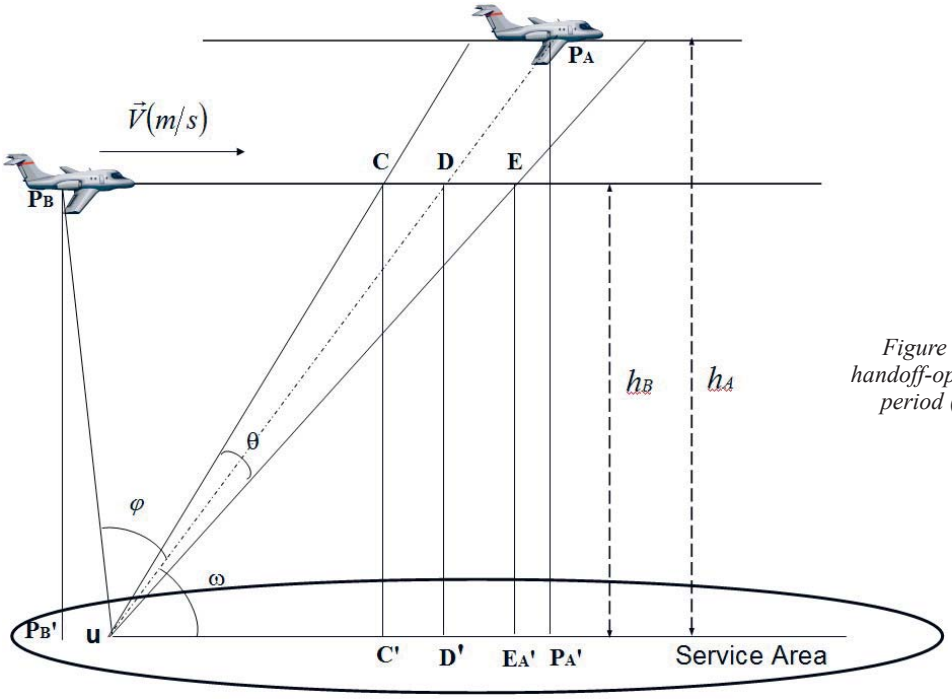

Figure 4. The handoff-opportunity period (HOP)

- Platform A is located at the nominal center of connectivity
- Platform B is traveling along a vector of constant height and along the *x* axis

User *u* can be located at any point within the service area.

In order to calculate the handoff-opportunity period, it is important to calculate the distance at which platform B (P_B) crosses the beam of user (*u*) when the boresight of the antenna belonging to user (*u*) is constantly pointing at platform A (P_A) (see Figure 4). The flying path of platform B intersects the beam at two points (*C* and *E*), and this forms the window in which the user can "see" both platforms. For calculating the distance *CE*, the following equations have been derived, using vector notation:

$$\sin(\omega) = \left(\frac{|\mathbf{P_A P'_A}|}{|\mathbf{uP_A}|} \right), \tag{2}$$

$$|\mathbf{uD'}| = \frac{|\mathbf{uP_A}| \bullet |\mathbf{P}_B \mathbf{P'}_B|}{|\mathbf{P_A P'_A}|}, \tag{3}$$

$$|\mathbf{uC}| = \frac{|\mathbf{P_B P'_B}|}{\sin\left(\omega + \frac{\theta}{2}\right)}, \tag{4}$$

$$|\mathbf{uE}| = \frac{|\mathbf{P_B P'_B}|}{\sin\left(\omega - \frac{\theta}{2}\right)}, \tag{5}$$

$$|\mathbf{CE}|^2 = |\mathbf{uC}|^2 + |\mathbf{uE}|^2 - 2|\mathbf{uC}| \bullet |\mathbf{uE}| \cos(\theta), \tag{6}$$

$$|\mathbf{CE}|^2 = \left[\frac{|\mathbf{P_B P'_B}|}{\sin\left(\omega + \frac{\theta}{2}\right)} \right]^2 + \left[\frac{|\mathbf{P_B P'_B}|}{\sin\left(\omega - \frac{\theta}{2}\right)} \right]^2$$

$$-2\left[\frac{|\mathbf{P_B P'_B}|^2 \cos(\theta)}{\sin\left(\omega + \frac{\theta}{2}\right)\sin\left(\omega - \frac{\theta}{2}\right)} \right]. \tag{7}$$

Platform B will be visible to the user's antenna when angle ϕ is less or equal to the angle $\theta/2$. Angle ϕ can be expressed as follows:

$$\phi = \arccos\left(\frac{\mathbf{uP_A} \bullet \mathbf{uP_B}}{|\mathbf{uP_A}| \bullet |\mathbf{uP_B}|} \right). \tag{8}$$

The time duration for which platform B is visible to customer premises equipment can be calculated using the distance CE and the speed of the platform:

$$HOP = \left(\frac{|\mathbf{CE}|}{|\mathbf{V}|} \right), \qquad (9)$$

where $\mathbf{V}$ is the relative velocity (ground speed) of platform B (with respect to platform A) in km/h. It is now possible to derive the equation for calculating the number of handoffs that can occur when platform B enters the position cylinder. It is possible for an immediate handoff to take place as soon as $\phi = \theta/2$. Assuming that U is the set of all test users located in the service area, the users U_H comprise the set of all users located in the service area that can be handed off to the new platform. On the other hand, U_{NH} is the set of all users located in the service area that are out of range of the new platform, and they remain connected to platform A. The set of users that can be handed off (U_H) can therefore be defined as

$$NU_H = \left\{ U_H \in U : U_H(\phi) \le \theta/2 \right\}, \qquad (10)$$

where

$$U = U_H + U_{NH}. \qquad (11)$$

3.3 Long-Duration and Short-Duration Handoff

Depending on the position and the speed of the two platforms, as well as on the location of the users within the service area, it is possible to calculate the time window for which both platforms are available for handoff. A short-duration handoff ensures a fast shifting of traffic between platforms, and therefore a fast exit for the platform in service. All new connections and existing connections will be gradually directed from platform A to platform B. This implies that platform B must cope with the large number of handoff requests, as well as new-connection requests. On the other hand, a long-duration handoff can be advantageous, as many of the connections that may require handoff to platform B will terminate naturally on platform A. This is provided that all users are informed of the presence of the new platform, so that all new calls are directed to the new platform. As a result, fewer handoff requests will take place, thus reducing the number of dropped connections (connection loss), and thereby ensuring a higher quality of service (QoS).

4. Performance of Handoff Strategies

4.1 Fixed Antennas

Here, we assume that users are uniformly distributed around the service area. The radius of the service area is 30 km long. The beamwidth of every user customer-premises-equipment antenna is calculated based on the angle subtended by the position cylinder, as defined in [31]. Users that are directly below the cylinder have their beamwidth calculated based on the base of the position cylinder (user A in Figure 2). The rest of the users (users B and C in Figure 2) in the service area have a beamwidth that must contain the whole position cylinder.

The results in Figure 5 illustrate the calculated beamwidth required by the users as a function of their distance from the center of the service area. This was irrespective of their location within the service area, as there is symmetry with respect to the center of the service area. From the results, it can be seen that users directly under the position cylinder were required to employ the highest beamwidth, which was about 29°. On the other hand, the users at the edge of the service area were required to employ a much narrower beamwidth, since they were situated further away from the platform than the users at the center. User antennas can therefore be manufactured and installed, based on the user's position and the position

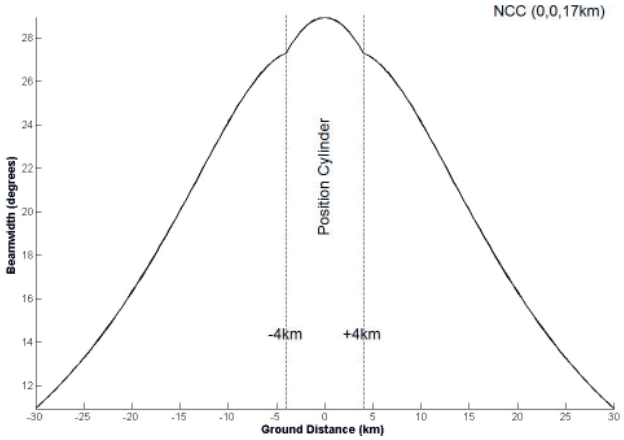

Figure 5. The minimum Antenna beamwidth for a fixed antenna system based on position cylinder.

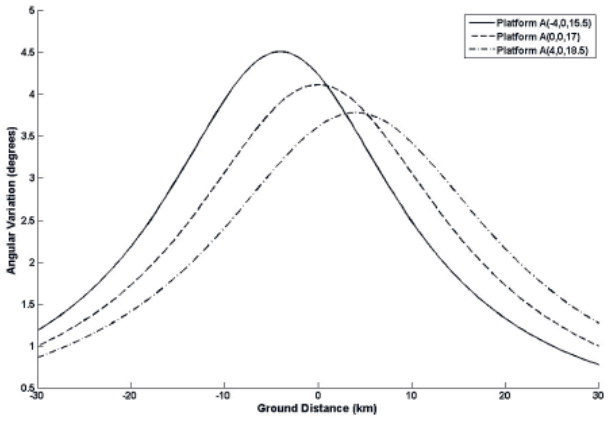

Figure 6. The angular variation on the ground (x axis) as a function of the horizontal displacement.

cylinder, so that the beamwidth is adequate to cope with station keeping.

4.2 Steerable Antennas

The minimum beamwidth for users employing steerable antennas is based on the angle subtended by the CAA cylinder. More specifically, it is calculated based on the diagonal enclosed by the cylinder, which has a length of 1.36 km (assuming a diameter of 1220 m and a height of 610 m, as seen in Figure 1). This length ensures that the user-steerable antennas will be wide enough to allow the two platforms to fly as closely as possible, as well as cope with the handoff. This is irrespective of the user's location and platform(s)' position within the position cylinder.

The results in Figure 6 illustrate the angular variation, as seen at a specific ground distance along the *x* axis, when platform A moved diagonally from one side of the position cylinder (–4, 0, 15.5) to the upper side (4, 0, 18.5). From this plot, it can be seen that as the platform moved closer to the users, the angular variation became greater. The highest variation defines the beamwidth that a user must have in order to cope with the worst-case scenario. That is when platform A is as close as possible to the user, while at the same time assuming the beamwidth is wide enough to hand off connections when platform B will be at its closest possible position with respect to platform A.

4.3 Handoff Permissible Distance

We can define the handoff permissible distance (HPD) as the distance through which the new HAP can fly and accept handoffs. The handoff permissible distance is equal to length CE shown in Figure 4. As platform B (the new platform) is vertically below/above platform A (the current platform), users that are currently connected to platform A will have the opportunity to perform handoff. Figure 7 illustrates the worst case, where platform B is vertically below platform A at a height of 15.5 km: the minimum possible height at which a platform can fly, according to the position cylinder. On the other hand, Platform A is situated at an altitude of 15.805 km (305 m above Platform B, according to the CAA cylinder). From the results in Figure 7, it can be seen that the handoff permissible distance becomes smaller for the users that are closer to the platforms. On the other hand, when platform B flies above platform A, the handoff permissible distance increases.

Users that experience a handoff permissible distance above 8 km may employ fixed antennas, instead of steerable antennas. In the cases examined here, this applied only for the users employing 20° beamwidth antennas, and with a distance of at least approximately 12 km from the nominal center-of-connectivity point.

On the other hand, users that experience a handoff permissible distance below 305 m will be unable to track the new platform coming in with their steerable antenna. This is because the new platform has to be less than 305 m away from platform A to become visible to these users, thus entering the CAA cylinder. To overcome this problem, users are required to employ a secondary antenna to be able to track Platform B when entering the position cylinder. Alternatively, platform B can employ a more-complicated flight path, rather than just fly in the position cylinder following a straight path.

4.4 Handoff-Opportunity Period

The handoff-opportunity period (HOP) determines the time period over which a handoff can occur between the two platforms. This is important, as platforms will only be able to process handoffs at a certain rate. The time specified by the handoff-opportunity period is of critical importance,

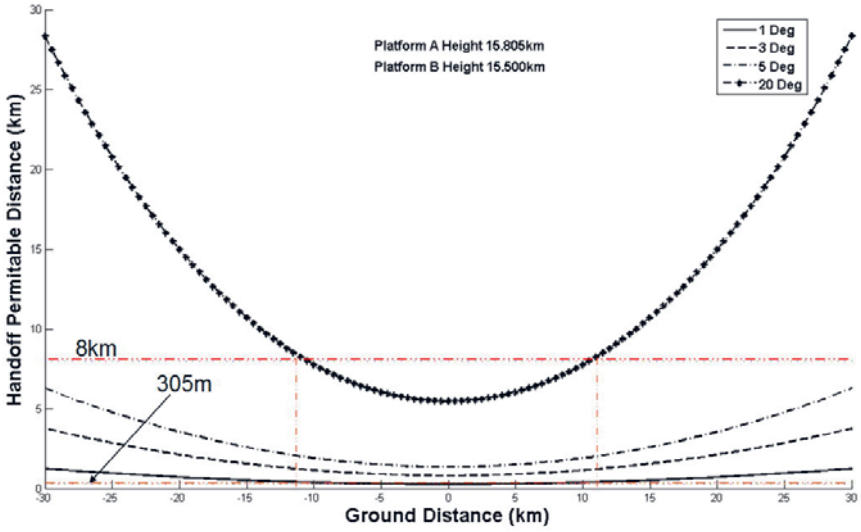

Figure 7. The handoff permissible distance as a function of user position (with platform B height at 15.5 km).

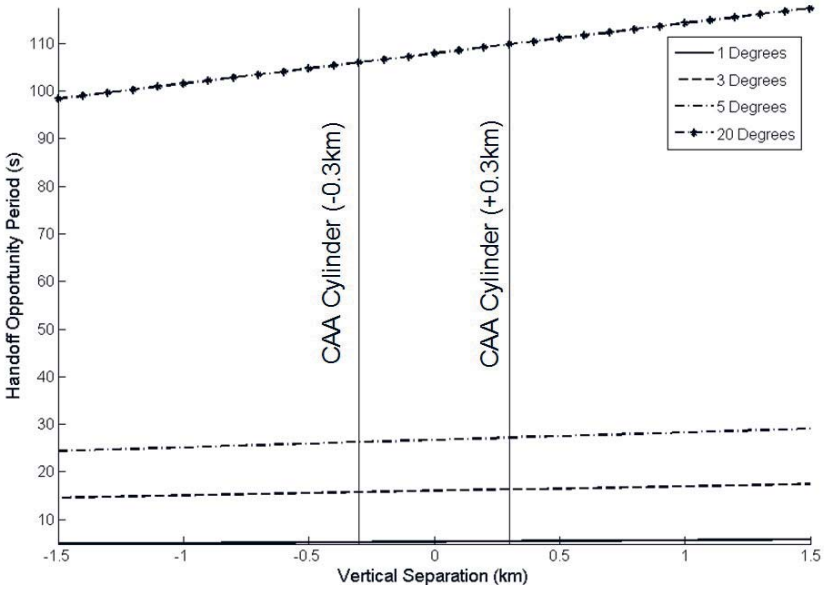

Figure 8. The shortest handoff-opportunity period across the coverage area.

given that all users (potentially, a large number) need to be handed off from one platform to another during this period. The handoff-opportunity period is a function of the antenna's beamwidth, the vertical HAP separation, and the user's location. To investigate the handoff-opportunity period, the vertical separation between the two platforms was varied. Platform A was considered to be stationary at position (0, 0, 17 km), whereas platform B was set to fly along the x axis at a speed of 200 km/h. This was repeated for a different set of heights. Users were uniformly distributed within the service area, of 30 km radius. Results were generated for different levels of beamwidth, ranging form 1° to 20°. Figure 8 illustrates that the narrower the beamwidth, the shorter the handoff-opportunity period will be for the users, as the antenna must be able to track both HAPs. The value of the minimum time illustrated in this plot is the smallest time duration across the coverage area. Of course, the platforms cannot get closer than the vertical separation distance (305 m) which the CAA cylinder specifies.

4.5 The Percentage of Successful Handoffs

We now examine the percentage of users that can successfully hand off within the coverage area, when platform B enters the position cylinder. Results have been generated for different vertical separation distances. We first looked at the case where platform B entered the position cylinder at 305 m below platform A. We then looked at the extreme case, were platform B entered the position cylinder at the minimum possible height of 15.5 km.

For the first case, platform A was set at 17 km height, whereas platform B was set at 16.695 km. Platform B was set to move with a speed of 200 km/h along the x axis towards the center of the service area ($x = 0$). On the other hand, Platform A was assumed to remain stationary above the center of the service area, at (0, 0, 17 km). Users were

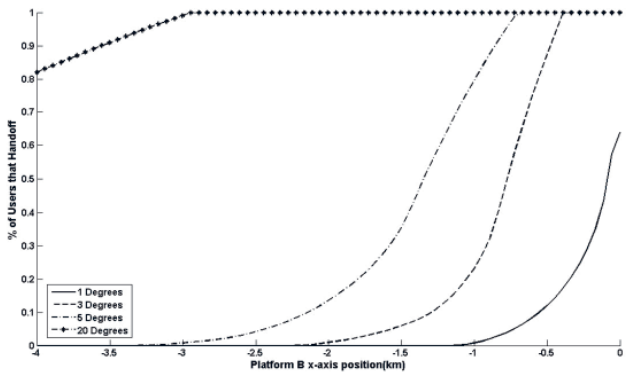

Figure 9a. The number of handoffs as a function of the position of platform B when platform A is set at a height of 17 km, with platform B at a height of 16.695 km.

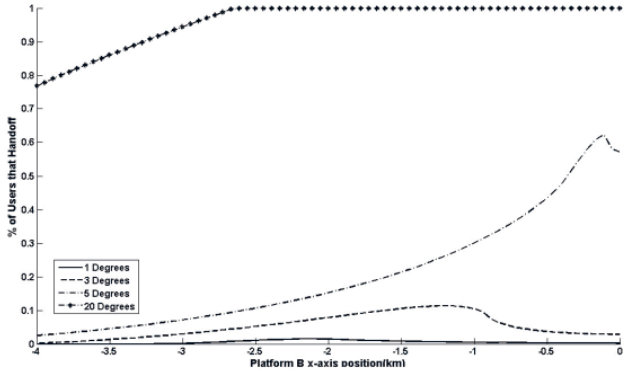

Figure 9b. The number of handoffs as a function of the position of platform B when platform A is set at a height of 17 km, with platform B at a height of 15.5 km.

uniformly distributed within a radius of 30 km, and they were spaced apart by 500 m. All users were set to point towards platform A. As platform B moved along the *x* axis, some of the users were able to perform a handoff, and some others were not. This depended primarily on their location, their beamwidth, and the height at which the platform flew.

Figure 9a illustrates the percentage of users that handed off successfully to platform B for various beamwidths. From the results, it could be seen that the wider the beamwidth, the earlier the users could perform handoff. However, for the case where the beamwidth was narrow (e.g., 1° beamwidth), a high percentage of the users could not perform a handoff, as platform B did not cross their antenna beam that was currently pointing at platform A. These users were located in the service area horizontally tangential to the flight path. This was expected, as the diameter of the base of the cone (where the customer-premises-equipment antenna forms the tip) for many of the users was less than the vertical separation distance of 305 m at which platform B had to fly. This is directly related to the results presented in Figure 7, showing that users with a handoff-permissible distance below 305 m would be unable to connect to platform B unless it also flew on additional flight paths over the service area, or users employed two antennas.

In Figure 9b, we present the case where platform B flew at a much lower height (15.5 km) than before. From the results, it could be seen that handoff for most of the users employing 1°, 3°, and 5° beamwidths could not be performed, except for users that employed a 20° beamwidth. From Figures 9a and 9b, it could be concluded that a greater percentage of users performing handoff is achieved when platform B flies as close as possible to platform A. It is therefore preferable that the new platform enters the position cylinder ideally as close as possible to platform A (with a ±305 m vertical separation).

5. Conclusions

In this paper, we have examined a number of issues relating to the inter-HAP handoff process for broadband communications that operate with fixed and steerable directional antennas, which is seen as the most challenging of the communications applications. For this work, handoff has been employed to allow a platform to be replaced, either for maintenance or because it has to be replaced according to the time schedule (manned airplanes).

For fixed users pointing towards the center of the position cylinder, handoff can take place as soon as the new platform enters the cylinder. Users from the center of the service area are required to employ the highest beamwidth, which is about 29°, whereas users at the edge of the service area are required to employ a much narrower beamwidth. This is because the distance between the users at the edge of the service area and the platform is greater than for the users at the center.

In the case where steerable antennas are employed by the users, it is possible to use a narrower beamwidth. The size of the angle depends primarily on the position of the user, the position cylinder, as well as the Civil Aviation Authority (CAA) cylinder, which defines the minimum separation distance between the two platforms. From the results, it has been shown that the wider the beamwidth, the earlier the users can perform handoff. However, for the case where the beamwidth was below 5° degrees in this typical scenario, the majority of users could not perform a handoff. The percentage of the users that are able to perform handoff is significantly decreased when platform B flies at extreme cases, such as when Platform B flies at the minimum possible height of 15.5 km. It is therefore preferable that the new platform enter the position cylinder ideally as close as possible to platform A (with a ±305 m vertical separation), or that platform B flies additional flight paths to cover those users that have been located in the service area horizontally tangential to the flight path.

6. Acknowledgments

This work was supported through a Short Term Scientific Mission (STSM) for Dr. K. Katzis (European University of Cyprus) at the University of York, sponsored by COST 297 – HAPCOS (http://www.hapcos.org), during the summers of 2007 and 2008.

7. References

1. D. Grace, N. E. Daly, T. C. Tozer, A. G. Burr, and D. A. J. Pearce, "Providing Multimedia Communications from High Altitude Platforms," *International Journal of Satellite Communications*, No. 19, November 2001, pp. 559-580.

2. R. Steele, "Guest Editorial: An Update on Personal Communications," *IEEE Communications Magazine*, **30**, 12, December 1992, pp. 30-31.

3. R. Miura and M. Oodo, "Wireless Communications System Using Stratospheric Platforms," *Journal of the Communication Research Laboratory*, **48**, 4, 2001 pp. 33-48.

4. J.-M. Park, B.-J. Ku, Y.-S. Kim, and D.-S. Ahn, "Technology Development for Wireless Communications System Using Stratospheric Platform in Korea," IEEE PIMRC 2002, **4**, Lisbon, Portugal, September 2002, pp. 1596-600.

5. J. Thornton, D. Grace, C. Spillard, T. Konefal, and T. C. Tozer, "Broadband Communications from a High Altitude Platform – The European HeliNet Programme," *IEE Electronics and Communications Engineering Journal*, **13**, 3, June 2001, pp. 138-144.

6. G. M. Djuknic, J. Freidenfelds, and Y. Okunev, "Establishing Wireless Communications Services via High-Altitude Aeronautical Platforms: A Concept Whose Time Has Come?," *IEEE Communications Magazine*, September 1997, pp. 128-135.

7. S. Masumura and M. Nakagawa, "Joint System of Terrestrial and High Altitude Platform Stations (HAPS) Cellular for W-CDMA Mobile Communications," *IEICE Trans. Commun.*, **E85-B**, 10, October 2002, pp. 2051-2058.

8. T. C. Tozer and D. Grace, "High-Altitude Platforms for Wireless Communications," *IEE Electronics and Communications Engineering Journal*, June 2001, pp. 127-137.

9. Recommendation ITU-R F.1500, "Preferred Characteristics of Systems in the FS Using High Altitude Platforms Operating in the Bands 47.2-47.5 GHz and 47.9-48.2 GHz," International Telecommunications Union, 2000.

10. Footnote 5.537A and 5.543A, Article 5, Chapter II, Radio Regulations, ITU and Potential Use of the Bands 27.5-28.35 GHz and 31-31.3 GHz by High Altitude Platform Stations (HAPS) in the Fixed Service, Resolution 145 (WRC-03), Radio Regulations, International Telecommunication Union, 2007.

11. Recommendation ITU-R M.1456, Minimum Performance Characteristics and Operational Conditions for High Altitude Platform Stations providing IMT-2000 in the Bands 1885-1980 MHz, 2010-2025 MHz and 2110-2170 MHz in the Regions 1 and 3 and 1885-1980 MHz and 2110-2160 MHz in Region 2, International Telecommunications Union, 2000.

12. D. Grace and P. Likitthanasate, "A Business Modelling Approach for Broadband Services from High Altitude Platforms," International Conference on Telecommunications (ICT'06), Madeira, Portugal, May 2006.

13. Grob Aerospace, http://www.grob-aerospace.net, accessed September 2007.

14. IEEE 802.11, Part 11: Wireless LAN Medium Access Control (MAC) and Physical Layer (PHY) Specifications, IEEE Computer Society, 1999.

15. IEEE 802.16e-2005 and IEEE 802.16-2004/Cor1-2005, Part 16: Air Interface for Fixed and Mobile Broadband Wireless Access Systems – Amendment 2: Physical and Medium Access Control Layers for Combined Fixed and Mobile Operation in Licensed Bands and Corrigendum 1, IEEE, February 28, 2006.

16. IEEE 802.16g-2007, Part 16: Air Interface for Fixed and Mobile Broadband Wireless Access Systems Amendment 3: Management Plane Procedures and Services, IEEE, September 27, 2007.

17. Y.-W. Chang and E. Geraniotis, "Optimal Policies for Handoff and Channel Assignment in Networks of LEO Satellites Using CDMA," *Wireless Networks*, **4**, 2, 1998, pp. 181-187.

18. S. Kalyanasundaram, E. K. P. Chong, and N. B. Shroff, "An Efficient Scheme to Reduce Handoff Dropping in LEO Satellite Systems," *Wireless Networks*, **7**, 2001, pp. 75-85.

19. J. Thornton and D. Grace, "Effect of Lateral Displacement of a High Altitude Platform on Cellular Interference and Handover," *IEEE Trans. on Wireless Comm.*, **4**, 4, July 2005, pp. 1483-90.20. B. El-Jabu and R. Steele, "Cellular Communications Using Aerial Platforms," *IEEE Trans. Veh. Technol.*, **50**, May 2001, pp. 686-700.

21. D. Grace, K. Katzis, D. A. J. Pearce, P. D. Mitchell, "Low Latency MAC Layer Handoff for a High Altitude Platform delivering Broadband Communications," *URSI Radio Science Bulletin*, No. 332, March 2010, to be published.

22. D. I. Axiotis, M. E. Theologou, and E. D. Sykas, "The Effect of Platform Instability on the System Level Performance of HAPS UMTS," *IEEE Communications Letters*, **8**, 2, February 2004, pp. 111-113.

23. S. Liu, Z. Niu, and Y. Wu, "Impact of Platform Motion on Soft Handover in High Altitude Platform IMT-2000 System," *IEEE VTC Spring*, **3**, April 2003, pp. 1964-1968.

24. W. L. Lim, Y. C. Foo, and R. Tafazolli, "Adaptive Softer Handover Algorithm for High Altitude Platform Station UMTS with Onboard Power Resource Sharing," *Wireless Multimedia Communications 2002*, **1**, October 2002, pp. 52-56.

25. M. Nofal, M. Hadhood, M. Dessouky, and Y. Albagory, "A Novel Cellular Structure for Stratospheric Platform Mobile Communications," Proceedings of the Nineteenth National Radio Science Conference (19th NRSC 2002), March 2002, pp. 354-362.

26. K. Katzis, D. A. J. Pearce, and D. Grace, "Impact of High Altitude Platform Movements on Cellular Handover," First International Workshop on High Altitude Platform Systems, Athens, Greece, September 2005.

27. CAPANINA Report D23A, "Resource Allocation and Handoff Techniques for High Altitude Platforms," FP6-IST-2003-506745, July 2006, http:// www.capanina.org/documents/CAP-D23a-WP24-UOY-PUB-01.pdf, accessed June 17, 2008.

28. K. Katzis, *Resource Allocation Techniques for High Altitude Platforms*, PhD dissertation, University of York, BLDSC NO. DXN095323, October 2005.

29. D. Everitt, "Traffic Capacity of Cellular Mobile Communications Systems," *Computer Networks ISDN Sys.*, **20**, 1990, pp. 447-454.

30. T. Fujii, S. Nishioka, "Selective Handover for Traffic Balance in Mobile Communications," IEEE/ Supercomm ICC92, 1992.

31. D. Grace, J. Thornton, T. Konefal, C. Spillard, and T. C. Tozer, "Broadband Communications from High Altitude Platforms – The HeliNet Solution," Wireless Personal Mobile Conference, Aalborg, Denmark, 2001.

32. "Reduced Vertical Separation Minimum," Civil Aviation Authority, http://www.caa.co.uk, accessed August 15, 2007.

33. "Reduced Vertical Separation Minimum," Federal Aviation Authority, http://www.faa.gov/, accessed August 15, 2007.

34. J. Thornton, D. A. J. Pearce, D. Grace, M. Oodo, K. Katzis, and T. C. Tozer, "Effect of Antenna Beam Pattern and Layout on Cellular Performance in High Altitude Platform Communications," *International Journal of Wireless Personal Communications*, **35**, 1, October 2005, pp. 35-51.

Low-Latency MAC-Layer Handoff for a High-Altitude Platform Delivering Broadband Communications

D. Grace
K. Katzis
D.A.J. Pearce
P.D. Mitchell

Abstract

This paper presents a low-latency handoff algorithm that exploits the unique characteristics of a high-altitude platform (HAP) multi-cell system payload to significantly reduce the need for payload stabilization. The handoff algorithm incorporates a novel time reuse Time-Division Multiplex/Time-Division Multiple Access (TDM/TDMA) frame structure, similar to that available with IEEE 802.16. Single- and multiple-frequency variants have been developed, with the intention of keeping the handoff process transparent to the user. The multiple-frequency variant is designed to increase system capacity by using a sequence of frequencies in different parts of the frame. Performance of the single-frequency-band handoff scheme is assessed using a generic pitch model. It has been shown to perform robustly, offering low-latency handoff, even with very short cell dwell times. Using a number of developed HAP mobility models – such as bounce, random walk, and rotation – the worst-case handoff performance is also quantified for a distribution of fixed users within a coverage area. It is shown that local user traffic hotspots are the dominant factor affecting performance, but that mitigation strategies are available.

1. Introduction

High-altitude platforms (HAPs) are either airships or aircraft [1-5] that will operate in the stratosphere, 17 to 22 km above the ground. Such platforms have been suggested for the delivery of both broadband fixed wireless access (BFWA) services [6] and 3G mobile [7]. HAPs will have a rapid rollout capability and the ability to serve a large number of users, using considerably less communications infrastructure than required by a terrestrial network [8]. To aid the eventual deployment of HAPs, the International Telecommunications Union Radiocommunications sector (ITU-R) has allocated spectrum in the millimeter-wave bands, around 48 GHz worldwide [9] and 31/28 GHz for forty countries worldwide including parts of Asia and the Americas [10], with spectrum in the 3G bands also allocated for use with HAPs [11].

Efficient spectrum reuse is required to ensure that such deployments can deliver high spectral efficiencies and high aggregate data rates. To achieve this, millimeter-wave cellular solutions were examined in [12], specifically addressing the antenna beam characteristics required to produce an efficient cellular structure on the ground, and the effect of antenna sidelobe levels on channel-reuse plans. Cells can be regularly spaced, as their area and location are substantially unaffected by geography and terrain. Since they all originate from the same HAP, this centralization can be additionally exploited by the resource-management strategy, as shown in [13]. Spectrum efficiency can be further enhanced by exploiting the antenna directionality of the user, and employing multiple HAPs to serve the same coverage area [14]. For the purposes of this paper, we define a cell as being a fixed geographic location on the ground, with each cell being served by a footprint (or beam) generated by an antenna on the HAP, i.e., the footprints move across the cells.

The requirements for geographical locations requiring handoff when subject to HAP lateral drift have previously been investigated [15], along with corresponding payload stabilization strategies, with earlier work carried out by El-Jabu and Steele [16]. The effects of platform instability on UMTS [17] and platform motion on IMT-2000 soft handover [18] have also been addressed. Foo et al. [19] modeled conventional 3G handoff for mobile users assuming stationary HAPs. Nofal et al. [20] also examined handoff for HAPs, for a ring-shaped beam that was designed to cope better with circling platforms. However, none of the above considered the specific millimeter-wave broadband situation addressed in this paper. This centralized HAP

D. Grace, D. A. J. Pearce, and P .D. Mitchell are with the Communications Research Group, Department of Electronics, University of York, Heslington, York, YO10 5DD, UK; Tel: +44 (0) 1904 432396; Fax: +44 (0) 1904 432335; E-mail: {dg, dajp, pdm106}@ohm.york.ac.uk.

K. Katzis is with the Department of Computer Science and Engineering, European University Cyprus, 6 Diogenes Str. Engomi, 1516, Nicosia, Cyprus; Tel: +357 22 713296; Fax: +357 22 590539; E-mail: K.Katzis@euc.ac.cy.

architecture is similar to that seen by multi-spot-beam satellites. However, in the case of geostationary satellites, the footprints do not move appreciably on the ground. In the case of low-Earth-orbit satellites, movement of beams is highly predictable, allowing handoff requirements between beams and satellites to be predicted well in advance, ensuring that traffic streams remain practically contiguous [21-23]. The proposed data rates for HAPs are also significantly higher.

Handoff is widely used in cellular communications in order to maintain service continuity when mobile users move between cells provided by a fixed-base-station infrastructure, with the protocols specified in mobile standards such as GSM, 3G, etc. IEEE 802.16-SC [24, 25] is seen as the most promising standard on which to base HAP broadband millimeter-wave communications, with modifications being largely confined to the base station in order to cope with HAP mobility and the centralized cell structure. The standard was developed for frequency bands from 10-66 GHz, and assumes fixed users with highly directional antennas. This standard has a variant based on a frequency-division duplex (FDD) TDM(A) frame structure that is capable of delivering up to 155 Mbit/s per cell. IEEE 802.16e [24], intended for frequency bands below 10 GHz, is a recent update. It amends the original standard for mobile-user scenarios, with the handoff process operating in a manner similar to other standards. These mobile users will operate in general with lower data rates using wide-beamwidth or omnidirectional antennas, using them to communicate with multiple base stations with control information passing between base station(s) and mobile to initiate the handoff process. IEEE802.16e is also likely to operate in a time-division duplex (TDD) mode, making it inefficient for the long transmission links required for HAPs, due to the roundtrip time being a significant proportion of the frame duration. Thus, IEEE802.16e-based equipment is less than suitable for HAPs use.

The purpose of this paper is to examine a number of issues relating to the HAP communications architecture, along with the station-keeping and operational constraints affecting the movement of HAP. The purpose is to devise a latency handoff algorithm that exploits the unique characteristics of a high-altitude platform (HAP) multi-cell system payload to significantly reduce the need for payload stabilization. In Section 2, we first of all introduce the HAP architecture, station keeping, and the various HAP mobility models. The combined resource-allocation and handoff protocol will then be explained in Section 3, along with several options for processing the handoff information. In Section 4, this is followed by simulation results for the scheme, assessing the speed and reliability of handoff as a function of cell dwell time, backed up by mathematical analysis. The worst-case performance of HAP handoff is then assessed, taking into account a random distribution of users and different HAP mobility models. This is followed by conclusions.

2. HAP Station-Keeping and Mobility Models

The configuration of the payload on board a HAP is highly dependent on weight, available space, and power, which in turn affects the range of system architectures available. It is assumed that the HAP payload is capable of serving a number of cells on the ground. The more cells within the footprint, the greater the number of beams. This leads to a higher payload weight and an increased requirement to perform handoff, owing to shorter dwell times. A payload-stabilization mechanism is one way of removing the need for intra-HAP handoff, but this adds to the payload requirements. The purpose of this paper is to illustrate that it is possible to largely eliminate the need for some forms of payload stabilization by providing a rapid handoff algorithm that will work with time-division

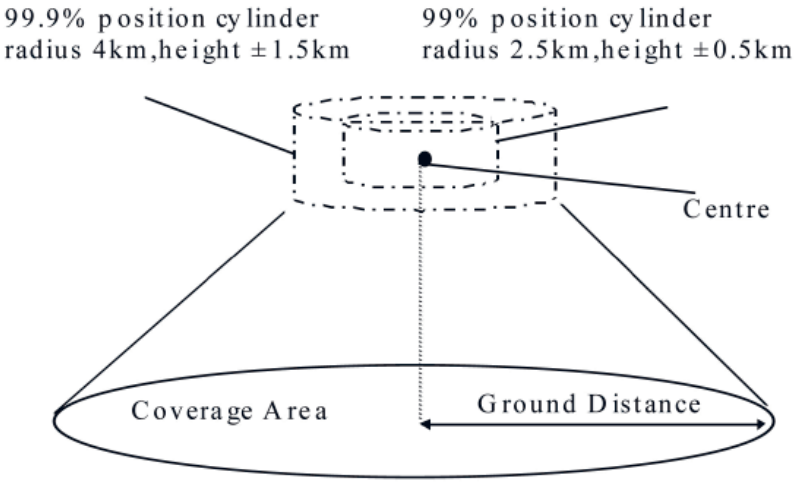

Figure 1. The HAP position cylinder for 99% and 99.9% of the time.

multiplex/time-division multiple access (TDM/TDMA), based on broadband fixed wireless access (FWA) schemes such as IEEE802.16-SC.

The ITU-R has specified that platforms should be kept within a circle of radius 400 m, with height variations of ±700 m [9]. Alternatively, the HALO project has suggested that its platform will remain within a toroid of 4 to 6 km [26], and the HeliNet project has specified two position cylinders that depend on platform availability [27], as shown in Figure 1. This is somewhat more relaxed than the ITU-R specification, but is intended to be realistic for a plane-based application. The size of the position envelopes largely controls whether the highly directional user antennas need to be steered to track the HAP, or whether they can be fixed, but does not significantly affect the intra-beam handoff requirements. This is mainly governed by the motion characteristics of the HAPs, and is currently largely an unknown, as there are no representative HAPs flying at the moment. To remove this problem in this paper, we develop a set of generic models that can be used to characterize the pertinent movements of HAPs, as seen from a handoff perspective.

The models can be separated into three groups, allowing each important feature to be modeled separately:

- *Rotation*, assuming HAP payloads are not stabilized, achieved using two different types of rotation: rotation about a *fixed axis*, and a *fixed radius of rotation*.
- *Yaw, pitch, and roll*, modeling changes in motion about the HAP center of gravity.
- *Linear motion* within the position cylinder using the *random walk* and *bounce* models, where we assume that the payload is stabilized against rotation, but not against drift.

In practice, it is likely that each type of HAP will be subject to a combination of the three basic types of mobility mentioned above. These generic models are thus intended to describe the movement of either airship or plane-based HAPs, but the specific combination of movements will be vehicle dependent. The models can be defined by specifying the six degrees of freedom defined using the basis vectors **i**, **j**, **k**, θ_i, θ_j, θ_j. The first three denote movement in a specific direction, and the latter three denote rotations, with the subscript denoting the axis of rotation.

2.1 Rotation

The first rotation model assumes that the HAP is in the center of the position envelope and rotates with angular velocity ω about the vertical (**k**) axis, i.e.,

$$r_t = r_{t-\Delta t} + \omega \Delta t \theta_k . \quad (1)$$

This is the most basic model to be developed, and it is intended to be used with other models below to more fully describe the motion of the platforms.

The second rotation model assumes that the HAP is circling about the center of the position envelope at a distance radius, *r*, with constant radial velocity, *v*. There are no changes in height. Such movements are likely to be especially common with fuel-based manned HAPs. We assume that the current position vector, $\mathbf{r}_t$, is dependent on the vector ($\mathbf{r}_t - \Delta \mathbf{t}$) generated Δt seconds previously:

$$r_t = r_{t-\Delta t} + r\cos\left(\frac{v\Delta t}{r}\right)i + r\sin\left(\frac{v\Delta t}{r}\right)j + \left(\frac{v\Delta t}{r}\right)\theta_k . \quad (2)$$

With this second model, there is thus both a positional variation in **i** and **j**, as well as the rotation in θ_k

2.2 Yaw, Pitch, and Roll

Yaw, pitch, and roll will be present in differing degrees with all types of HAPs. These models can be considered together as the effect of moving the footprints past the cells with an effective ground speed that is governed by the frequency of oscillation (f_o) and the maximum angular variation, γ, in degrees. (This approach can also be used to characterize HAP vibration.) It is assumed that the vehicle is located at its nominal position, *A*, and is traveling in direction **i**. The pitch, yaw, and roll can be expressed mathematically at a time *t* (based on a triangle wave [28]), using the same vector notation respectively, as

$$r_t = \frac{2\gamma}{\pi}\arcsin\left[\sin\left(2\pi f_o t\right)\right]\theta_j , \quad (3)$$

$$r_t = \frac{2\gamma}{\pi}\arcsin\left[\sin\left(2\pi f_o t\right)\right]\theta_k , \quad (4)$$

$$r_t = \frac{2\gamma}{\pi}\arcsin\left[\sin\left(2\pi f_o t\right)\right]\theta_i . \quad (5)$$

2.3 Random Walk

This model characterizes random movements of the HAP within the position cylinder, and is intended to represent the effects of wind on the HAP. It will be especially important for solar-plane and airship-based HAPs. Assuming the HAP starts from position *A*, the movement of the HAP can be broken down into horizontal and vertical components. It is assumed that the HAP continues on the same vector over the update interval Δt, with velocity v_h. The new horizontal component of position

is therefore anywhere on a circle of radius r at a randomly distributed angle θ. The decent/ascent rate is assumed to be uniformly distributed between $\pm v_v$. The new locus of the new position, A', is therefore an ellipsoid centered on point A (assuming it does not hit the edge of the position envelope). Mathematically, this can be represented as

$$\mathbf{r}_t = \mathbf{r}_{t-\Delta t} + \Delta t\left[v_h \cos(\theta)\mathbf{i} + v_h \sin(\theta)\mathbf{j} + v_v\mathbf{k}\right]. \quad (6)$$

2.4 Bounce

This model is intended to characterize certain linear movements of plane-based HAPs within the position cylinder. In some situations, it may be more energy efficient for planes to fly straight (rather than in a circle) within the bounds of the position cylinder. With this mobility model, a starting point, A, is assumed (e.g., the center of the position envelope). A point A_F is selected anywhere within the position envelope, according to a random uniform distribution. The HAP then heads towards this point with constant velocity v. The positions along this path, A'_n, are then calculated every update interval, Δt. On reaching the point A_F, the process is repeated. Mathematically, this can be represented as

$$\mathbf{r}_t = \mathbf{r}_{t-\Delta t} + v\Delta t\hat{\mathbf{a}}', \quad (7)$$

where

$$\hat{\mathbf{a}}' = \frac{\mathbf{a}_f - \mathbf{a}_{f-1}}{\left|\mathbf{a}_f - \mathbf{a}_{f-1}\right|},$$

with $\mathbf{a}_f$ representing the vector corresponding to point A_F, and $\mathbf{a}_{f-1}$ corresponding to the vector of the point of the previous-point update.

3. The Handoff Algorithm

Intra-HAP handoff, i.e., to new cells served by the same HAP, can exploit the centralized architecture and collocated base stations. The important issue is to control which spot-beam transmissions are sent, and at what time. This can be aided by messages sent on the uplink from the user terminal, identifying the most-appropriate beams to receive and transmit messages, using criteria such as received signal strength (RSS) and carrier-to-interference ratio (CIR). It is then the choice of the HAP to allocate the resources to the most-appropriate beam, taking into account the user terminals' received signal strength, received signal strength, and traffic loading on the eligible cells. Handoff can be controlled at the MAC layers and need not complicate higher OSI layers, with handoff appearing transparent to layers 3 and above.

The IEEE802.16-SC standard adopts a TDM(A)/TDM-based frame structure. Control information is delivered using the downlink map (DL-MAP) and uplink map (UL-MAP) fields, with each cell responsible for its own TDM(A) frame(s). The standard defines the physical (PHY) and MAC layers of the transmission channel, and is intended to operate with multiple higher-layer standards, such as IPv4 and IPv6. Here, we use this standard as a basis for the handoff technique. We also exploit the fact that all base stations are collocated on the HAP and can be perfectly synchronized. We use this to significantly simplify the handoff process for the user. This is achieved through a novel integrated beam-frame structure, where neighboring beams occupy different sections of the TDM(A) frame, with the transmissions in the TDM(A) frame being distributed across a beam of interest and its immediate neighbors. This can also enable users to connect to more than one beam simultaneously, exploiting the beam overlap available with the HAP architecture [15]. Handoff can therefore be made largely transparent to the user, because now the handoff process is fully integrated with the frame-by-frame resource allocation controlled by the respective base stations, with each user synchronized to only one composite TDM(A) frame. Thus, HAP movement appears as another factor affecting the temporal reallocation of resources at the base stations, which is already required to efficiently cope with variable-bit-rate broadband traffic.

In contrast, conventional mobile-user handoff techniques all tend to rely on message transfer between mobile, old, and new base stations to achieve the handoff. Here, message transfer associated with handoff is restricted to messages between new and old base stations, reducing the latency. This approach ensures that the handoff process can cope with the large and frequent number of handoffs that will be seen with a HAP payload with only limited stabilization.

3.1 Time-Reuse Frame Structure: Single Frequency

The time-reuse structure used by the HAP architecture is shown in Figure 2. Each frame contains a series of control and data slots (channels). It is assumed that each cell has its own control and data slot. It is assumed that these will be different from immediate neighbors, and that its spatial reuse distance will be determined by the cluster size. The control field may contain only entries relating to a specific beam, or may also include information relating to neighboring beams.

The example shown in Figure 2 assumes a cluster size of seven, with control and data transmissions for each cell shown shaded and labeled A (ignore time slots B to G). This basic seven-cell structure would then be repeated for all cells in the footprint. A similar approach can be taken with different cluster sizes or dynamic channel assignment, but these extensions are beyond the scope of the paper. Time

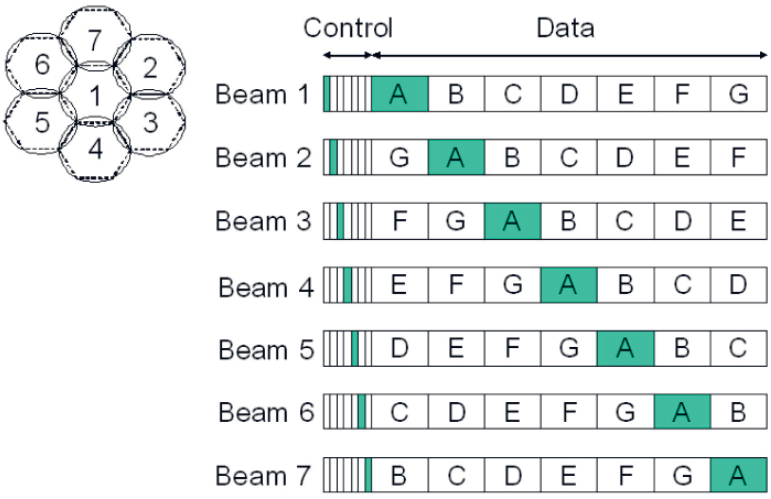

Figure 2. The frame structure used to implement handoffs.

reuse for data and control can be different if it is necessary to better protect the control information. Dynamic time reuse would allow more/fewer slots to be allocated to a beam, depending on loading.

The transmission channel (a single-frequency channel), as seen by the user, will behave in a manner similar to a conventional IEEE 802.16 channel. The difference will be which HAP beam originates and receives the transmissions. Downlink (HAP-to-user) transmissions will originate from different spot beams in different slots, depending on the destination user terminal. The reverse will happen for the uplink (user-to-HAP) transmissions. Control of transmission slots will be carried out at the HAP (as is also done in IEEE 802.16 by the base station), using the DL-MAP/UL-MAP fields. The HAP will also choose the most-appropriate beam to receive the transmission from a time slot; this will be dependent on the channel-allocation scheme in operation. The most-appropriate beam will depend on the resource-allocation scheme, but can be the beam delivering the highest received signal strength or CINR.

3.1.1 Handoff Algorithm

Figure 3 shows the uplink and downlink signaling associated with the handoff algorithm, which operates as follows:

- The user terminal transmits the carrier-to-interference ratio/received signal strength levels of beams one to seven on the uplink, in the control slot associated with the currently allocated beam. The received signal-strength levels are determined from listening to the control information sent on a frame-by-frame basis on the downlink, which contains the beam allocations (or, alternatively, the base station (BS) can determine the carrier-to-interference ratio/received signal strength levels directly, through knowledge of the location of all user terminals, plus the location of beams
- The base station uses the carrier-to-interference ratio/ received signal strength information received on the uplink to allocate resources for the next frame (on a frame-by-frame basis) in the most-appropriate beam. The new allocation is signaled to the user in the appropriate beam, using the associated control slot on the downlink.
- The base station signals a cleardown in the current beam, if necessary (if handoff has occurred).
- The user terminal listens to the control information and any relevant data on the current downlink beam.
- The user terminal transmits on the uplink in the appropriate time slot(s), obtained from the control information received on the downlink.
- The base station receives the user's transmission(s) in the appropriate beam.

It is useful to consider how the scheme operates as seen by a user terminal. Assuming that the user terminal has achieved frame synchronization from additional control information present, it will be able to decode parts of the frame that have both adequate received signal strength and carrier-to-interference ratio. These transmissions will belong to the beam it is currently occupying, or, if it is moving towards a beam boundary, those of several other neighboring cells. Control transmissions of neighboring beams will be transmitted at different time periods within the frame. The handoff algorithm described above ensures that information destined/originating at the user's terminal is redirected to the appropriate time slots to maintain the link on the ground. In this paper, "appropriate" means the beam corresponding to the closest antenna boresight (highest received signal strength). However, as discussed above, due to the extensive overlap, different criteria can

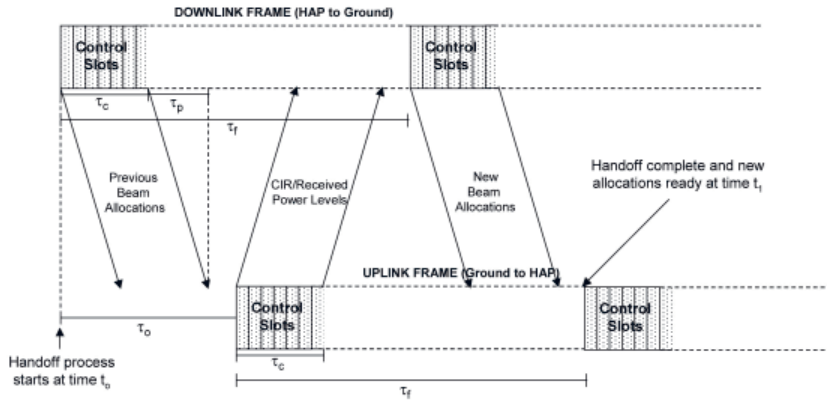

Figure 3. The uplink and downlink signaling associated with the handoff algorithm

be adopted – linked to the resource-allocation scheme – by exploiting the centralized nature of the multibeam, time-synchronized transmissions, and diverting resources from beam to beam on a frame-by-frame basis. Such a scheme does not necessarily require full centralized processing of all the beams on the HAP, only the current beam and surrounding neighbors.

In order to determine how well the handoff algorithm can perform when subject to rapid movements, we can calculate the probability that a wanted packet is not transmitted/received in the best beam (slot), defined as the not-best-slot (NBS) probability. In these circumstances, the not-best-slot probability provides a measure of the latency of the handoff process, since we assume that there are always free resources available in the new beam (the effect of limited resources in the new beam will be considered later).

The not-best-slot probability can be defined analytically as

$$P_{nbs} = \frac{\text{latency}}{\text{dwell time}} = \frac{T_l}{T_d}. \qquad (8)$$

The latency is defined as the time elapsed from the instant it becomes appropriate to hand off to the next cell until the handoff is complete and the new assignment becomes ready in the most-appropriate beam. Handoff may be required at any point in the frame, so a period of a half-frame duration will elapse (on average) prior to commencement of the handoff process. Figure 3 shows the signaling associated with the subsequent measurement and reallocation process, which starts at time t_0. A period of τ_0 seconds elapses until the carrier-to-interference ratio/received signal strength levels are transmitted on the uplink, where τ_0 represents the fixed time offset between the uplink and downlink frames. The reallocation process takes place once the measurement information has been received on the uplink, and the new beam allocations can be used in the following frame, introducing a further delay of τ_f seconds, where τ_f corresponds to the duration of the uplink and downlink frames. The overall and average latency in the handoff process is therefore given by

$$T_l = \frac{\tau_f}{2} + \tau_0 + \tau_f = \tau_0 + \frac{3}{2}\tau_f. \qquad (9)$$

The time offset between the uplink and downlink frames is required to ensure that the control information sent on the downlink is received in time for the carrier-to-interference ratio/received signal strength levels to be determined prior to transmission at the start of the uplink frame. The offset time should be minimized to reduce the average latency, but needs to allow for the transmission duration of the control information, τ_c, and the propagation delay, τ_p. Therefore,

$$\tau_{0\_min} = \tau_c + \tau_p. \qquad (10)$$

The cell dwell time (T_d) is the time it takes to travel across a single cell. It is given by multiplying one over the normalized effective ground speed (S_g) by the frame duration (τ_f), where S_g is specified in the number of cells per frame:

$$T_d = \frac{1}{S_g}\tau_f. \qquad (11)$$

It is important to note that whenever a handoff is initiated, the user's terminal has not transmitted in the best slot, since handoff occurs when the carrier-to-interference ratio/received signal strength level in one or more beams is greater than the beam currently in use. The handoff probability is therefore equivalent to the not-best-slot probability, and is given by

$$P_{handoff} = P_{nbs} = \frac{\text{latency}}{\text{dwell time}} = \frac{T_l}{T_d} = \frac{\left(\tau_0 + \frac{3}{2}\tau_f\right)}{\frac{1}{S_g}\tau_f}$$

. (12)

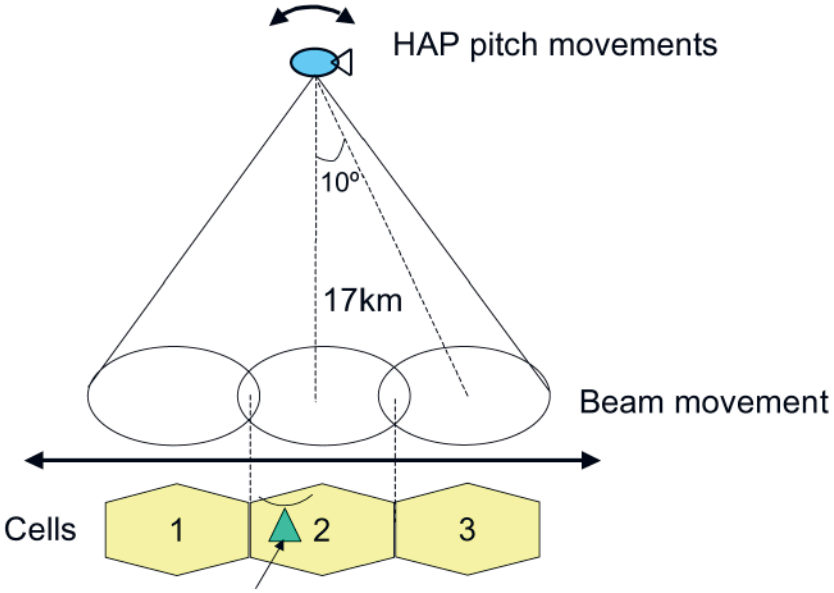

Figure 4. The scenario used to test handoff performance.

3.2 Multiple-Frequency Extension

The drawback of this scheme is that the capacity is shared amongst a cluster of beams, whereas with a conventional terrestrial IEEE802.16-based deployment, the whole of the capacity within the frame is available across a single cell. Using multiple frequencies would allow for the increase of either uplink or downlink capacity. This would ensure that all parts of the frame can carry traffic in every cell, as shown in Figure 2. This is achieved by time-reusing multiple frequencies. Using again the seven-cell reuse example, we fill the remaining parts of the frame in each beam with six additional frequencies (B-G). Across these seven cells, each frequency is continually in use, with the beam carrying each frequency changing on a time-reuse basis, such that only one beam in the seven-cell cluster uses the frequency at any one time.

The user terminals over the whole system would use all seven frequencies, assuming even loading is required. However, each terminal need only listen on one frequency for the duration of a connection (or time period), just as with the single-frequency case. More-sophisticated user terminals can exploit additional frequencies if required to increase their burst data rate.

4. Results

The worst-case HAP mobility is likely to be pitch/roll/yaw vibrations or wobble, which will give rise to rapid beam movement if antenna stabilization is not employed on the HAP. From a power/weight/cost perspective, it would be beneficial to use as little stabilization as possible. The performance of the single-frequency handoff scheme has been assessed for its ability to cope with these movements and to ascertain the maximum frequency and amplitude of oscillation the system can cope with using a three-cell structure, as shown in Figure 4. It is assumed that the beams track parallel with the centers.

Therefore, to examine the robustness of the handoff algorithm in worst-case conditions, a simulated pitch movement was used. The angle was $\pm 10°$, and the rate varied between 0 and 0.4 cells/frame, corresponding to a frequency of oscillation range of 0 to 70 Hz (an effective ground speed of 0 to 800 km/s). Note that this tangential movement did not result in any changes of link length, which would normally occur when a user moves towards or away from a conventional terrestrial base station. In this latter case, this rate of change of link length can have serious effects on timing of the TDM. The maximum supported velocities of IEEE802.16 are hence much lower than those tested here, but such maxima cannot be applied directly to this scenario. Doppler shifts similarly do not occur due to these tangential movements. In the case of position changes (arising from any other types of HAP movement), any component in the direction of the user is extremely small, so, again, will have minimal effect on the performance of the IEEE802.16 example protocol. These movements, particularly the amplitude-frequency combination, are likely to be well in excess of those predicted for real HAPs, but they were designed to demonstrate the robustness of the algorithm. Table 1 presents a list of simulation parameters and their values.

Figure 5 shows the analytical and simulated results for the not-best-slot probability for high- and low-speed cases. The not-best-slot probability was obtained from the simulation by recording all packets that were not received in the best slot, and dividing by the total number of packets received. In a more-sophisticated simulation or real implementation, handoff cannot be initiated as soon as it becomes favorable, since measurements are only taken on a frame-by-frame basis. As a result, the probability

Simulation Parameters	Value
Number of cells	3
Effective Ground speed (S_g)	0-0.4 cells/frame
Effective trajectory length along ground	8 km
Platform height	17 km
Spot beam antenna separation	10°
Nominal 3dB spot beam antenna beamwidth	5°
Frame duration (τ_f)*	1 ms
Uplink/downlink frame offset (τ_0)	0.5 ms
Control slot duration	2 μs
Slot duration*	10 μs
Packet size*	500 bits
Transmission rate*	155 Mbit/s
Number of slots per frame	100

*Table 1. Miscellaneous simulation parameters used in the handoff simulation (*IEEE802.16 compliant [25])*

of a packet not being transmitted/received in the best slot is dependent on the latency of the handoff process from the instant the measurement process starts (when the handoff is actually identified as being favorable). In order to effectively compare the simulation results to the analysis (see Equation (12)), it was necessary to neglect the component of latency corresponding to the time that elapses prior to commencement of the handoff process ($\tau_f/2$). The modified analytical equation is

$$P_{handoff} = P_{nbs} = \frac{\text{latency}}{\text{dwell time}} = \frac{\left(\tau_o + \tau_f\right)}{\frac{1}{S_g}\tau_f}. \quad (13)$$

The high-speed case was obtained from the scenario described above. It can be seen from Figure 5 that at these very high effective ground speeds, there is a high probability that transmissions will not occur in the best slot. The simulated results indicated that even at these speeds, the handoff process remained stable, with the measurement process still managing to keep up with the effective speed, and not losing track of the best cell. There was also good agreement with the analytical predictions, providing a means of verification for the development process behind the scheme. In the case of the low-speed scenario, which corresponds to a situation much more likely to arise with a HAP system, the simulated and analytical results were in close agreement, but it could be seen that the not-best-slot probability was extremely low (< 0.006). The not-best-slot probability will result in packets being dropped in the worst case if cell overlap is not exploited. However, because of the gradual roll-off in antenna-beam pattern, giving rise to beam overlap, the difference in the received signal strength of the best and next best slot in these cases will be very low [5]. Given this behavior, it will be the resource-allocation scheme and availability of resources on the platform that will determine the overall performance of the HAP system.

To examine the worst-case handoff performance, it was necessary to model a distribution of users requiring continuous-bit-rate (CBR) services. The low-latency scheme above assumed that there was always sufficient capacity in the new beam to accommodate the request for resources. In practice, users are likely to be randomly distributed over the coverage area, and will give rise to varying user densities per unit cell area, in some cases creating traffic hotspots comparable to the resources available in a single beam. These hotspots will become a problem if users are admitted to the system when two beams are serving the hotspot. This will become a problem if the HAP movement causes the hotspot to be served only by a single beam. In these circumstances, users admitted to the system over and above those that can be served by a single beam must be dropped. Such a scenario is shown in Figure 6. A Poisson point process can be used to determine the probability an active user is within a radius of any specified location [29], and can be used to determine the dropping probability for a given cell size, connection duration, and dwell time.

A similar situation was modeled in a LEO satellite case [22], but in this situation, only lateral drift of the beams across the cell were present. In a HAP situation, the mobility mechanisms are much more complex and less deterministic.

Connection dropping and handoff performance were assessed using different HAP mobility models for continuous-bit-rate traffic with exponentially distributed service times and arrival rates, with specific parameters given in Table 1 and general system parameters presented in Table 2. For the handoff to be successful, it was assumed (pessimistically) that resources must be found in the beam with the closest boresight, otherwise the service was dropped. This is the worst-case performance, because it will be possible to delay handoff until resources become free in practice, due to beam overlap, and also alternative strategies to improve performance include pre-reservation of

Parameter	Value	Unit
Number of cells	19	
Channels per cell	240	
Mean connection duration	300	s
Total offered traffic	742.34	Erlangs
Cluster size	7	
Cell radius	3.15	km
HAP initial position	(0,0,17)	km
User area radius	9	km
HAP speed	0-200	km/h

Table 2. The handoff scenario simulation parameters

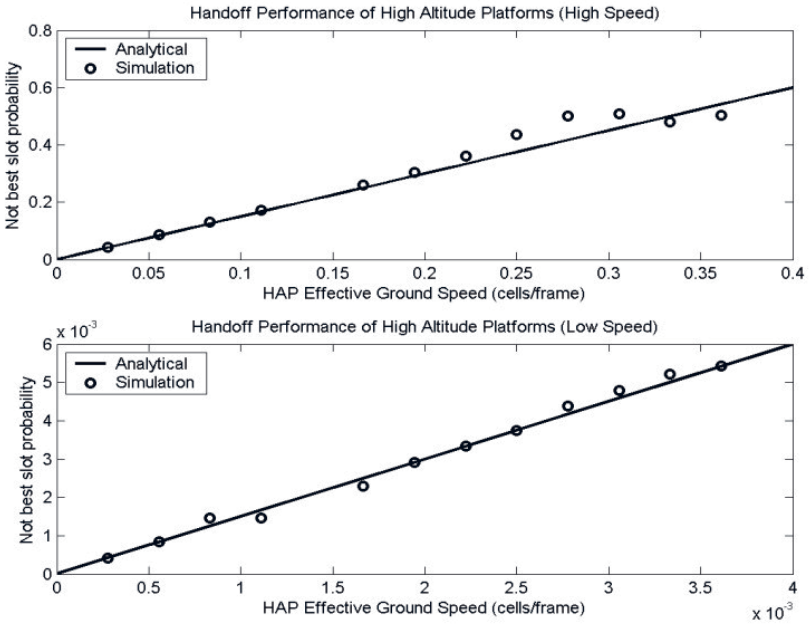

Figure 5. The performance of the handoff algorithm at high and low effective ground speeds.

channels within the new cell. Investigation of these strategies is beyond the scope of this paper. Performance was thus assessed specifically using handoff probability, defined here as the probability that a connection undergoes at least one handoff over its lifetime, and dropping probability, defined as the probability that a connection undergoing handoff fails to obtain resources in the new beam and has to terminate.

The simulation performed was based on a 19-cell hexagonal layout, delivering an uninterrupted coverage area of 11.36 km radius. The users were uniformly randomly distributed within a service area of 9 km radius, e.g., modeling a broadband service over a center of population. The coverage area was purposely made larger than the service area to ensure continuous coverage, removing the need for lateral payload stabilization, assuming that the HAP was restricted to moving in the 2.36 km position cylinder, similar to Figure 1. HAP mobility models such as bounce, rotation, and random walk (discussed earlier) were used to examine handoff and dropping probability as a function of the distance from the center of the coverage area. In the case of the rotation-mobility model, the rotational movement was quantified in terms of the two rings that form the coverage area. Figure 7 illustrates the behavior of all three mobility models with respect to the distance from the center of the coverage area. For the case of the bounce mobility model, the further the users were located away from the center of the coverage, the higher the handoff probability they would experience. The handoff probability decreased slightly at the center of the first ring. This is because some of the users were centrally located within a cell (of the first ring), and thus there was a lower probability of them requiring handoff. The handoff probability decreased steadily away from the center to become zero in second ring at 9 km, which was the limit of the user deployment. The bounce mobility model caused the highest dropping probability. However, for both bounce and random-walk mobility models, the dropping probability increased towards the edges of the cells. For example, for the edges of the cells of the center ring in Figure 7, the dropping probability decreased towards the edge of the coverage area because the second ring was less congested.

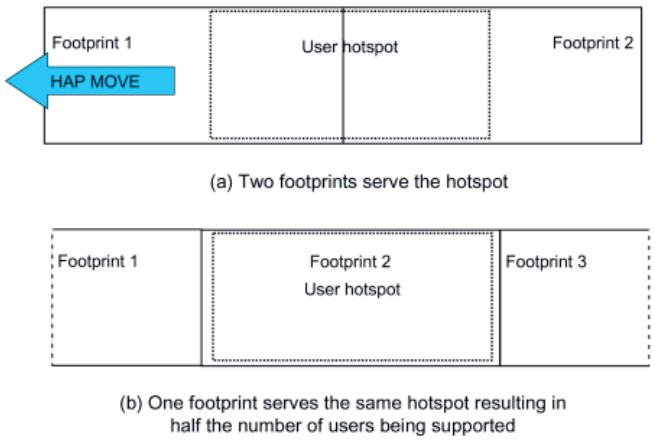

Figure 6. Local-user hotspot location and the ability to accommodate users in more than one footprint

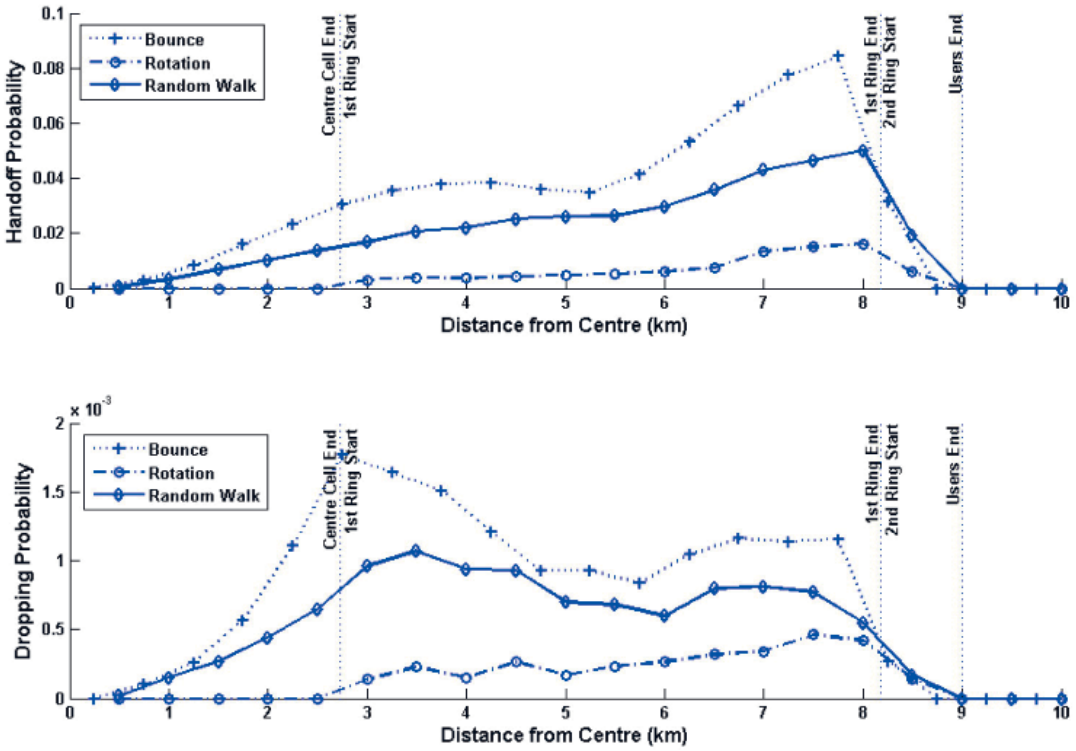

Figure 7. The handoff and dropping probabilities as a function of distance from the center of the coverage area

5. Conclusions

This paper has presented a low-latency handoff algorithm that exploits the unique characteristics of the high-altitude platform multi-cell payload to ensure that little or no payload stabilization against HAP motion is required. The handoff algorithm is based on a time-reuse TDM/TDMA frame structure that is similar to that available with IEEE 802.16. A single-frequency variant has been suggested, where the HAP transmits from/receives to different spot beams in different portions of the frame. This process remains transparent to the user, requiring only the standard instructions from the HAP as to which slots in the frame it should transmit/receive. A multiple-frequency variant has also been suggested as a way of increasing the system's capacity. In this case, each cell transmits/receives using a sequence of frequencies in different parts of the frame, with each cell in a cluster starting at a different point in the sequence so as to create a hybrid time/frequency reuse plan. Again, this process remains transparent to the user, since it is assumed that each user operates on a fixed (or only long-term-varying) frequency assignment. Performance of the single-frequency-band handoff scheme was assessed using a generic pitch model. It was shown to perform robustly and perform low-latency handoffs, even with very short cell dwell times.

Furthermore, using a range of developed HAP mobility models, such as "bounce," "random walk," and "rotation," we have quantified the worst-case handoff performance for a distribution of fixed users within a coverage area. We showed that local user traffic hotspots are the major factor affecting performance. This effect is worse for rotation-type motion, with the probability of dropping dependent on the cell dwell time. Mitigation strategies include reserving channels for future handoff use, or controlling the density of admitted users within one area. The constraint on performance of the HAP system will therefore depend primarily on the resource-allocation process and on the availability of resources on the platform, and is not due to HAP motion.

6. Acknowledgement

This work was produced as part of the HeliNet Project (IST-1999-11214), which was funded under the 5th Framework Programme of the European Commission, and the CAPANINA Project (FP6-IST-2003-506745, www.capanina.org), which was funded under the 6th Framework Programme of the European Commission. The use of the OPNET Modeler by OPNET Technologies under the University Consortium license agreement is acknowledged.

7. References

1. D. Grace, N. E. Daly, T. C. Tozer, A. G. Burr, and D. A. J. Pearce, "Providing Multimedia Communications from High Altitude Platforms," Intern. J. of Sat. Comms., 19, November 2001, pp. 559-580.

2. R. Steele, "Guest Editorial – An Update on Personal Communications," IEEE Communications Magazine, 30, 12, December 1992, pp. 30-31.

3. R. Miura and M. Oodo, "Wireless Communications System Using Stratospheric Platforms," Journal of the Communication Research Laboratory, 48, 4, 2001, pp. 33-48.

4. J.-M. Park, B.-J. Ku, Y.-S. Kim, and D.-S. Ahn, "Technology Development for Wireless Communications System Using Stratospheric Platform in Korea," IEEE PIMRC 2002, 4, Lisbon, Portugal, September 15-18, 2002, pp. 1596-600.

5. J. Thornton, D. Grace, C. Spillard, T. Konefal, and T. C. Tozer, "Broadband Communications from a High Altitude Platform – The European HeliNet Programme," Electronics and Communications Engineering Journal, 13, 3, June 2001, pp. 138-144.

6. G. M. Djuknic, J. Freidenfelds, and Y. Okunev, "Establishing Wireless Communications Services via High-Altitude Aeronautical Platforms: A Concept Whose Time Has Come?," IEEE Communications Magazine, 35, 9, September 1997, pp. 128-35.

7. S. Masumura and M. Nakagawa, "Joint System of Terrestrial and High Altitude Platform Stations (HAPS) Cellular for W-CDMA Mobile Communications," IEICE Transactions on Communications, E85-B, 10, October 2002, pp. 2051-2058.

8. T. C. Tozer and D. Grace, "High-Altitude Platforms for Wireless Communications," Electronics and Communications Engineering Journal, 13, 3, June 2001, pp. 127-137.

9. Recommendation ITU-R F.1500, "Preferred Characteristics of Systems in the FS Using High Altitude Platforms Operating in the Bands 47.2-47.5 GHz and 47.9-48.2 GHz," Geneva, International Telecommunications Union, 2000.

10. Footnote 5.537A and 5.543A, Article 5, Chapter II, Radio Regulations, ITU, and "Potential Use of the Bands 27.5-28.35 GHz and 31-31.3 GHz by High Altitude Platform Stations (HAPS) in the Fixed Service," Resolution 145 (WRC-03), Radio Regulations, Geneva, International Telecommunications Unio11. Recommendation ITU-R M.1456, "Minimum Performance Characteristics and Operational Conditions for High Altitude Platform Stations Providing IMT-2000 in the Bands 1885-1980 MHz, 2010-2025 MHz and 2110-2170 MHz in the Regions 1 and 3 and 1885-1980 MHz and 2110-2160 MHz in Region 2," Geneva, International Telecommunications Union, 2000.

12. J. Thornton, D. Grace, M. H. Capstick, and T. C. Tozer, "Optimising an Array of Antennas for Cellular Coverage from a High Altitude Platform," IEEE Transactions on Wireless Communications, 2, 3, May 2003, pp. 484- 92.

13. D. Grace, C. Spillard, J. Thornton, and T. C. Tozer, "Channel Assignment Strategies for a High Altitude Platform Spot-Beam Architecture," IEEE PIMRC 2002, 4, September 2002, pp. 1586-1590.

14. D. Grace, J. Thornton, G. Chen, G. P. White, and T. C. Tozer, "Improving the System Capacity of Broadband Services Using Multiple High Altitude Platforms," IEEE Transactions on Wireless Communications, 4, 2, March 2005, pp. 700-709.

15. J. Thornton and D. Grace, "Effect of Lateral Displacement of a High Altitude Platform on Cellular Interference and Handover," IEEE Transactions on Wireless Communications, 4, 4, July 2005, pp. 1483-90.

16. B. El-Jabu and R. Steele, "Cellular Communications Using Aerial Platforms," IEEE Transactions on Vehicular Technology, 50, 5, May 2001, pp. 686-700.

17. D. I. Axiotis, M. E. Theologou, and E. D. Sykas, "The Effect of Platform Instability on the System Level Performance of HAPS UMTS," IEEE Communications Letters, 8, 2, February 2004, pp. 111-113.

18. S. Liu, Z. Niu, and Y. Wu, "Impact of Platform Motion on Soft Handover in High Altitude Platform IMT-2000 System," IEEE VTC Spring, 3, April 2003, pp. 1964-8.

19. W. L. Lim, Y. C. Foo, and R. Tafazolli, "Adaptive Softer Handover Algorithm for High Altitude Platform Station UMTS with Onboard Power Resource Sharing," Wireless Multimedia Communications 2002, 1, October 2002, pp. 52-56.

20. M. Nofal, M. Hadhood, M. Dessouky, and Y. Albagory, "A Novel Cellular Structure for Stratospheric Platform Mobile Communications," Proceedings of the Nineteenth National Radio Science Conference, NRSC 2002, pp. 354-362.

21. Y.-W. Chang and E. Geraniotis, "Optimal Policies for Handoff and Channel Assignment in Networks of LEO Satellites Using CDMA," Wireless Networks, 4, 1998, pp. 181-187.

22. S. Kalyanasundaram, E. K. P. Chong, and N. B. Shroff, "An Efficient Scheme to Reduce Handoff Dropping in LEO Satellite Systems," Wireless Networks, 7, 2001, pp. 75-85.

23. E. Papapetrou and F. N. Pavlidou, "Analytic Study of Doppler-Based Handover Management in LEO Satellite Systems," IEEE Transactions on Aerospace and Electronic Systems, 41, 3, 2005, pp. 830-839.

24. D. Grace, M. Mohorcic, M. H. Capstick, M. Bobbio Pallavicini, and M. Fitch, "Integrating Users into the Wider Broadband Network via High Altitude Platforms," IEEE Wireless Communications, 12, 5, October 2005, pp. 98-105.

25. IEEE 802.16e-2005 and IEEE 802.16-2004/Cor1-2005, Part 16, "Air Interface for Fixed and Mobile Broadband Wireless Access Systems Amendment 2: Physical and Medium Access Control Layers for Combined Fixed and Mobile Operation in Licensed Bands and Corrigendum 1," IEEE, February 28, 2006.

26. N. J. Collela, J. N. Martin, and I. F. Akyildiz, "The HALO Network," IEEE Communications Magazine, 38, 6, June 2000, pp. 142-8.

27. D. Grace, J. Thornton, T. Konefal, C. Spillard, and T. C. Tozer, "Broadband Communications from High Altitude Platforms – The HeliNet Solution," Wireless Personal Multimedia Communications, WPMC 2001, Aalborg, Denmark, August 2001.

28. Mathworld, Triangle Wave, http:// mathworld.wolfram.com/TriangleWave.html, November 2006.

29. S. P. Weber, X. Yang, J. G. Andrews, and G. de Veciana, "Transmission Capacity of Wireless Ad Hoc Networks with Outage Constraints," IEEE Transactions on Information Theory, 51, 12, December 2005, pp. 4091-4102.

WiMAX HAPS-Based Downlink Performance Employing Geometrical and Statistical Propagation-Channel Characteristics

I.R. Palma-Lázgare
J.A. Delgado-Penín

Abstract

The evolution to a well-expected technology in wireless-communications maturity is in progress. Complementary applications are being suggested for such purposes, which might be possibly effective from the already ongoing research on high-altitude-platform systems. Herein, we introduce a HAPS-based system for delivering broadband communications intended to be operational at L band. A physical-statistical channel model for the HAPS-to-fixed-terrestrial terminal provision is derived from urban geometrical radio-coverage considerations with a simple diffraction theory. The stratospheric broadband channel model is fulfilled with the two channel-state situations related to the direct and specular rays, plus multipath. The first state consists of predicting the performance for which the line-of-sight path can exist between HAPS and the still terminal at street level. The second channel state refers to modeling the statistical fading characteristics for the shadowing condition. The system implementation is approximated and analyzed by performing intensive simulation-aided modeling. The proposed hypotheses use empirical data derived from land-mobile-satellite communication-system records. Because the systems require robust, reliable, and future standardization results, IEEE 802.16™-2004 PHY-layer technical specifications are used to accomplish the WiMAX HAPS-based downlink performance evaluation.

1. Introduction

A high-altitude-platform station (HAPS) is a stand-alone airship (or an airplane) stationed in the stratosphere at about 17-25 km above the Earth's surface. The expectation is to offer an alternative or complement to terrestrial and satellite-based communication systems. HAPS is also expected to make the most advantage of aforementioned technologies. It is presumed to have the capability of carrying a large variety of wireless-communications payloads [1-4]. A viable and futuristic framework for the HAPS telecommunications network architecture is displayed in Figure 1.

Satellite systems possess many attractive features, which are moderated by their disadvantages of large propagation delays (MEO and GEO satellite cases), and the unreliability of the satellite channel. Furthermore, the LEO satellite system has a high complexity. To this end, HAPs can be employed since they represent a solution preserving most of the advantages of satellites, while avoiding some of their drawbacks [5]. Looking at the terrestrial components, it is difficult and economically inefficient to cover remote and impenetrable areas with terrestrial wireless, wired, or fiber networks. However, HAPs constitute a real asset to wireless-infrastructure operators for providing telecommunication services over such areas [5]. In addition, two other applications of the HAP in the end-to-end path can be identified [5]: HAPs can be employed in isolation from any core networks to connect private networks (such as corporate LANs), or to provide trunk connections between core networks.

We now focus on the system's performance evaluation. For this, we intended to model the signal-processing actions with a more real, reliable, and robust approach. We described the signal-processing operations through a block diagram comprising the transmitter, the channel, and the receiver. As we focused on the impairments of the signal rather

Israel R. Palma-Lázgare and José A. Delgado-Penín are with the Universitat Politècnica de Catalunya (UPC), Signal Theory and Communications Department, Campus Nord, C/Jordi Girona 1-3, Building D4, 08034 Barcelona, Spain; Tel: +34 934017214; Fax: +34 934017200; E-mail: ipalma@tsc.upc.edu; Tel: +34 934016815; Fax: +34 934016815; E-mail: delpen@tsc.upc.edu.

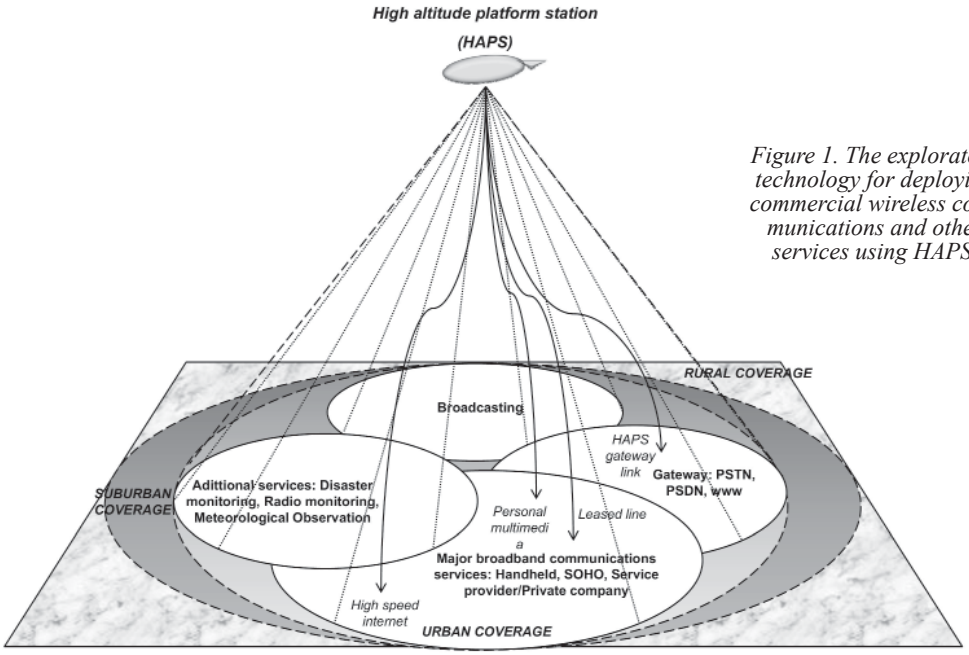

Figure 1. The exploratory technology for deploying commercial wireless communications and other services using HAPS.

than those from processing in the transceiver, the channel modeling was held as the main focus of our simulation work. The distinction we could derive here is that such signal processing was not highly precise, but it was worthwhile for the performance-evaluation and regulation issues.

We introduced the HAPS analysis with the proposal of modeling the stratospheric channel that would possibly be appropriate for a HAPS communications-link approach. For this, we required a controlled environment, in which suitable equipment and techniques may be implemented or be planned for testing. We have therefore considered the design approach referring to the propagation effects, with dependence on such a surrounding area for an end-to-end communication link. Although there are two existing impairment classes for the channel modeling, we have herein concentrated only on a specific class. In our case, the impairment class we refer to belongs to the channel and service environment that includes propagation effects of noise, fading, and shadowing. Atmospheric effects were neither considered from the stratospheric altitude nor for the considered operating frequency band. The remaining second class of impairments (i.e., phase noise and offset, channel nonlinearities, adjacent/co-channel interference, and HAPS/terminal motion) was not considered in our analysis, being considered for future analytical approaches.

Even though there are a lot of references for wireless-channel characterization dedicated to conventional terrestrial and satellite links, specific conditions in the stratospheric outdoor geometry require further investigation for the particular HAP-based system application. We state that there are a couple of radio-link types between the HAPS payload and the ground equipment: the gateway and the service link. For our case, we focused on the service link, where communications can occur between HAPS and the terrestrial still terminal in a cellular configuration mode.

The terrestrial terminals were described as being inside the urban zone, or urban area coverage (UAC) [6]. In this, we put into practice an important method of having urban coverage to the receiver antenna above, on, or below roof level. This work dealt specifically with the examination of a communication-link approach, with the physical characteristics presented in terms of the unobstructed or built-up conditions at a specific elevation angle, α , in which land-mobile satellite system (LMSS) research deployment and measurements were adopted to our HAPS proposal. The rationale behind such a proposed selection was remarked on in [7-8]. Propagation for HAPS communications behaves practically in the same manner as for the land-mobile satellite system case where similar elevation angles can be used. However, a difference is the link length, which sets the free-space loss reference level. It is also very distinctive that the land-mobile satellite system or HAPS channel was compared to the model where only a single distribution (or one single channel state) can no longer describe its behavior. HAPS and satellite communications were determined by more than two conditions of the radio link (e.g., the link being available when there was line of sight, or otherwise being in the unavailable shadowing/blockage case). Accordingly, we have also come to terms for the HAPS/satellite in which the channel model can be chiefly characterized by the geometry statistics of the terrestrial terminal environment.

We now emphasize the advantage and application for the two considered statistical and site-specific model categories. The assumed physical environment is open to reflection, scattering, and diffraction, thus path loss via base ray tracing was conceived. The case of the ray-tracing application resulted from the strategy to offer a path-loss formulation by assuming a finite number of reflectors. A reflector was considered as another source of signal, and the resultant signal at the receiver was the sum of signals

coming from all such sources with different distances and altered antenna fields. On the other hand, statistical/empirical modeling was carried out to provide an accurate formulation demanded by complex broadband communications, as well as to give an approach to low-computational-cost but robust channel modeling under urban conditions with appropriate records from the field.

Moreover, it seems that HAPS systems will operate in bands below 10 GHz, where shadowing/blockage plus multipath effects are dominant. Systems operating in these bands will most probably be based on a multi-carrier physical layer, such as that proposed in the WiMAX standard for the lower frequency bands. Hence, the pertinent HAPS-based system was evaluated under the adaptive parameters of the IEEE 802.16-2004 standard [9]. The frequency band of 1.820 GHz was used in our proposal to become the closest and a desirable approach to a representation of the 2 GHz band, over which the ITU has allocated the application of FBWA and next-generation mobile communications [6] based on a stratospheric platform using IMT-2000/IMT-Advanced technologies [10]. The thinking is to employ HAPS to supply flexible high-speed last-mile WiMAX provisions, with a rapid-deployment cost-effective wireless solution. It is also to have the HAPS application provide higher quality than satellite communications, with a lower propagation delay/distance and a more extensive area to cover than the terrestrial wireless system, the radio link of which is mostly blocked by terrestrial structures and vegetation.

Finally, the overall examined system performance was evaluated in terms of the average bit-error rate (BER), based on the proposed stratospheric-channel model and HAPS scenario. The system approach was based on computer-aided predictions (using *MATLAB*® software).

2. HAPS-Based System Scenario and Precursory Specifications

We looked at the global system geometry before its evaluation, so that the differences with respect to other radio systems could be clearly established [5, 11]. The global geometry can be represented as in Figure 2 for the HAPS-based system. This involves the Earth's curvature; a fixed position at an altitude r_{HAPS} over the point *C*; and a direct path illuminating the fixed ground terminal with an elevation angle α_{Earth}. Point *O* represents the Earth's center, and r_{Earth} is the Earth's radius. The following expression follows from the principles of trigonometry:

$$\frac{\overline{OA}}{\sin\beta_{Earth}} = \frac{\overline{OB}}{\sin(90+\alpha_{Earth})} = \frac{\overline{OB}}{\cos\alpha_{Earth}}, \quad (1)$$

so
$$\sin\beta_{Earth} = \frac{r_{Earth}}{r_{Earth}+r_{HAPS}}\cos\alpha_{Earth}. \quad (2)$$

Assuming that the Earth's surface has a perfect spherical shape, the arc *AC* indicates the radius of the coverage from the HAP on the ground, expressed by the following equation:

$$\widehat{AC} = \gamma_{Earth} r_{Earth}; \quad (3)$$

Let us consider the triangle *OAB*. The total internal angle of the triangle is 180°, so the angle γ_{Earth} satisfies the equation

$$\gamma_{Earth} = 90° - \alpha_{Earth} - \beta_{Earth}. \quad (4)$$

After substitutions, we are able to rewrite the radius of the HAPS' area coverage as follows:

$$R_{HAPS} = r_{Earth}\left[\cos^{-1}\left(\frac{r_{Earth}}{r_{Earth}+r_{HAPS}}\cos\alpha_{Earth}\right) - \alpha_{Earth}\right]. \quad (5)$$

$r_{Earth} = \frac{4}{3}6378$ km was used, instead of only the effective Earth's radius of 6378 km. This was done to consider atmospheric refraction that causes bending of the radio wave's path, and to compensate for the geometry at the time of linear propagation.

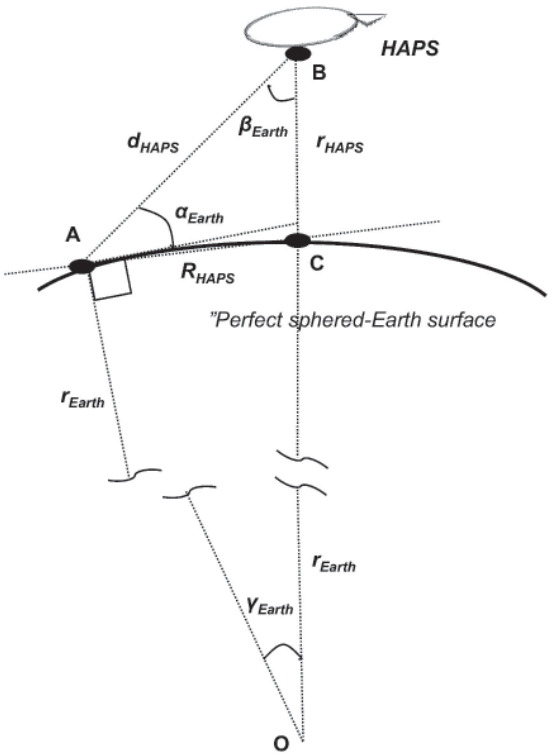

Figure 2. An early geometry of the HAPS-based proposal (not to scale) [6, 13, 14].

Regarding the above geometrical analysis, a HAPS at an altitude of 21 km has the capability of covering an area on the ground up to 419.6 km in diameter for 5° of elevation angle.

3. Performance Prediction

3.1 Preliminaries

An adequate HAPS-based radio-propagation channel model was developed. The geometry approach in Figures 1-4 was presumed, with elemental rays (or echoes) for the purpose of defining the channel conditions. At this stage, the stratospheric propagation link was established so as not to introduce other atmospheric mitigating factors, such as atmospheric refraction, precipitation (rain, fog, snow), cloud cover, and to not result in additional loss of the signal.

Two radio-propagation channel conditions were defined for the specific urban-area coverage. The first condition belongs to the line-of-sight situation, and the second belongs to the log-normal shadowing situation. For both situations, we needed to seize the pertinent propagation parameters for the "stratospheric habitat," considering the signal attenuation as a random process due to fast and slow fading variations arising from the channel's condition.

The extrapolation effort for the satellite-to-HAPS-based system scenario was assumed for the complex urban scenario, and to connect in appropriate fashion to the HAPS-to-ground design and solution. "Multi-mode channel-state modeling" in our case does not stand for the representation of the channel transitions between states (or non-stationary process). We assessed two proper single statistical processes that reviewed two independent stationary single-mode channel-state models occurring in the metropolitan scenario. For these, the state-oriented channel modeling was based on empirical land-mobile satellite system models to produce the approach to HAPS behavior. No possible extensions to an adaptable mobile scenario were used, due to the need for extensive HAPS communication measurement campaigns, or some extended approach from the satellite-based systems (e.g., by using the already proposed scheme of a multi-state chain process), referring us to mobility from the ground terminal and the platform, as well.

The HAPS-based system can have a higher line-of-sight probability because of the considerations of being an ultra-high-altitude tower, compared with a terrestrial tower. As a result, HAPS can easily provide line-of-sight communication at high α, where the links are relatively free of the influence of obstacles. Generally, the probabilities of having a line-of-sight path can be described by larger values of α ($> 40°$), and a shadowing path by lower values of α ($\leq 40°$), which would result in a high probability of the shadowing state. Nevertheless, when HAPS is used to serve an urban environmental area, buildings can stand – or even there could be skyscraper – where the condition of a line-of-sight path would be very difficult to have. In our case, since we have a heavily built-up area coverage, the shadowed region seemed large and was the most-severe attenuation factor. Shadowing-power attenuation was thus considered as another attenuation factor, in addition to the attenuation due to path loss. We remark that if a hillock appears in the radio-communication path, shadowing will be avoided and diffraction will instead appear.

Moreover, the determined signal transmission between HAPS and the ground terminal generally takes place via many paths, and the variation of α can define this. This last categorization might include one direct ray and the potential remaining multipath rays: line of sight, a single reflection from a building, a single reflection from the street, a double reflection from the building to the street, a double reflection from building to building, diffraction from the rooftop of a building, diffraction from a rooftop and a single reflection from a building, diffraction from a rooftop and a single reflection from the street, and diffraction from a rooftop and a double reflection from a building to the street. Rays outside the mentioned categories can be assumed to leave the original target. Since all surfaces in real propagation environments are finite, edges and corners also have to be considered. In our case, the situation called diffraction can occur when a large body obstructs the radio path between the transmitter and the receiver, causing secondary waves to be formed behind the obstructing body that continue to propagate towards the receiver.

The relevant model, with specific details of the building allocation, trees, etc., for the metropolitan environment, gives the signal-information approach. This sorts out an explicit ray-tracing solution for the electromagnetic wave's status that does not require a great deal of measurement data. It is a relatively generic channel model, which can be used for simulations.

The implementation of the ray-tracing algorithm in our system with relative large *d* corresponded to the two-ray model. As the stationary receiver was considered to be a gadget, station, or some small hardware for easy setup/deployment, and equipped with a low-gain antenna, the arrival rays collected by the terrestrial antenna included two coherent components. These were a direct path (a significant portion of the total energy arrives at the receiver by way of a direct wave), and a specular reflected path (the remaining power of the transmitted signal) – plus the diffuse components (many randomly scattered rays) [15]. In further detail, the frequently reflected path from the ground in satellite-based communications design was not proper in our HAPS-based communications interpretation. This was in a little contrast to the conventional non-mobile HAPS-to-ground link, carrying equipment including high-gain antennas at the receiver, which could completely reject both specular and diffuse components and collect only the direct path. The contribution of the wave reflected from building structures was considered, as well as possibly from trees nearby the receiver. Echoes that properly intersect

with the receiver were next analyzed. The power-delay profile (PDP) estimation was developed by mapping the power of the different rays with respect to the delay-time information [16, 17]. The diffuse components were considered to arrive at an elevation angle near 0° with uniformly distributed phase, with amplitude statistically described by a Rayleigh distribution, and a maximum Doppler spectrum of $2v_T/\lambda$ (denoting the small existing motion and the carrier wavelength, respectively). Thus, the approach of the aforementioned method considered the set of rays originating from the same source and reflected from the same set of surfaces to be part of the same wavefront.

We refer now to the connection of our proposed model to those with the closest relationship: the so-called (geometrical) single-bounce model, or other similar research (e.g., a circular straight cone geometry, or a three-dimensional ellipsoid propagation model). We refer specifically to distinctions for the specular reflection echo (single-bounce path) and the corresponding delay spread. We differed from those already established models by approaching the probability of the specular-ray's existence by means of the building blockage inside the impaired scatterer topography, resulting in a nonuniform coverage over the receiver. That is, we considered that the specular reflection ray came from a near scatterer with irregular environment volume, and not uniformly distributed in space to the receiver. We can add that the scattering loss that depended on the material of the structures was not totally clarified. Hence, power delay or other related angle calculations for the arrival rays were expressed differently from ours, because of different assumptions.

Eventually, we can remember that the product of the antenna fields for the corresponding peers is important in determining the received power. In the receiver's antenna, following the induction of electric currents created by the wave's arrival, the energy in our operating frequency band was directly coupled to antenna size. Equally, antenna size was directly coupled to the field's wavelength (λ), which was basically inversely proportional to the carrier frequency ($\lambda = c/f_c$). In other words, the higher the frequency, the smaller the antenna size. Hence, the antenna characteristics [11, 18] used during the analysis could have played an important role in affecting the performance outcome. Nevertheless, idealist for antennae comes for our whole analysis. Since we considered idealisms for the antenna onboard the platform, we used an ideal antenna pattern adopted for the HAPS application (denoted by the possible use of smart antennae or antenna arrays) and with a zero-dBi-gain omnidirectional antenna at the receiver terminal. Local mean received power (the local mean of the signals received) was thus directly dependent on α and on the transmitted power. Using a presumed omnidirectional antenna had the relevant aspect for our design of having the multipath power contribution be much higher than the use of a directional antenna.

3.2 Stratospheric Propagation Premises

The overall representation for the HAPS-channel modeling has been taken as the equivalent complex channel impulse response (CIR) expression [19]:

$$\tilde{c}(\tau,t) = \sqrt{Lf_{CS}(t)}\tilde{h}(\tau,t), \qquad (6)$$

where the first factor represents the long-term situation, and the second factor accounts for the short-term situation. Equation (6) is valid for values greater than 1 km, where L is the mean loss, and $f_{CS}(t)$ belongs to the channel-state situation. For example, for the shadowing state (in the locality of the receiver) through time t, the function can be modeled as a Gaussian variable with 0 dB mean and a standard deviation (the log-normal model).

In order to model the single HAPS-to-terminal channel propagation for optimization, our design was comprised of two cascaded stages (see Figure 3a). These were associated with the HAPS-to-ground path (HAP process) and with the effects surrounding the terrestrial terminal that are relative to its neighboring scatterers (terrestrial process):

$$PL = PL_{HAPS} + PL_{Terrestrial}, \qquad (7)$$

For this – and considering similarities to land-mobile satellite systems – free-space attenuation and multipath fading effects counted for the major fading factors for our proposal.

From the entire model available for propagation-loss predictions – either for terrestrial or satellite-based applications – in our case, for the HAPS-based system, a general theoretical equation can be given as

$$PL_{total} = PL_{FSPL} + PL_{shadowing} + PL_{fading}, \qquad (8)$$

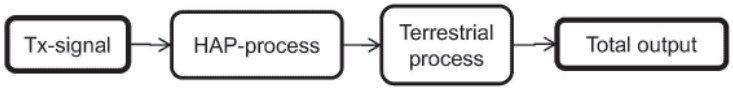

Figure 3a. A representation of stratospheric channel modeling proposal.

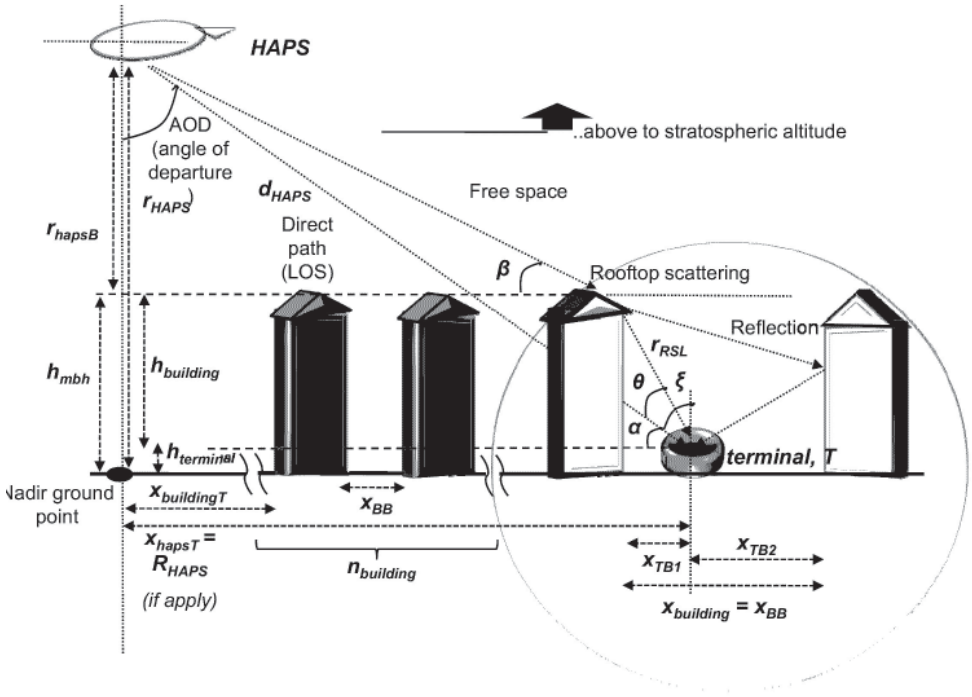

Figure 3b. An idealized urban built-up geometry for the radio-propagation model for downlink HAPS-based communications (not to scale).

where PL_{total} is the total propagation loss, PL_{FSPL} represents the free-space path loss as a function of the transmitter-receiver separation distance, $PL_{shadowing}$ denotes the shadowing loss, and PL_{fading} is the local fading loss.

HAPS has been considered to be an extremely tall base station that can present a propagation path consisting of the free-space loss, diffraction from a rooftop, and multiple reflections from nearby buildings. Thereafter, based on Equation (7) and the theoretical propagation loss, the HAPS-based communications path loss can be represented as the sum of the free-space loss (FSL), the rooftop scattering loss (RSL), and the multiple-screen diffraction loss (MSDL). We thus supposed the total propagation loss to be power-summed, since it was desired to predict the local median value. The received power can be obtained from

$$PL = PL_{HAPS,FSL} + PL_{Terrestrial,RSL} + PL_{Terrestrial,MSDL} \quad (9)$$

The formulation for the free-space path loss is dedicated to the line-of-sight (LOS) case in which there is only one direct path from transmitter to receiver. The free-space path loss depends only on the frequency and the separation distance between transceivers, as typically expressed by the fixed quantity

$$PL_{HAPS,FSL} = 10\log_{10}\left(\frac{\lambda}{4\pi \cdot d_{HAPS}}\right)^2 \text{ [dB]}, \quad (10)$$

where λ is the wavelength in meters, and d represents the transmitter-receiver distance. The free-space loss equation is only a valid predictor for values of d_{HAPS} that are in the far field of the transmitting antenna:

$$d_{HAPS} = \sqrt{R_{HAPS}^2 + r_{HAPS}^2} \,. \quad (11)$$

Now, the diffraction from the rooftop down to the street level (as shown in Figure 3b) leads to an excess loss at the ground terminal, *T*, expressed by

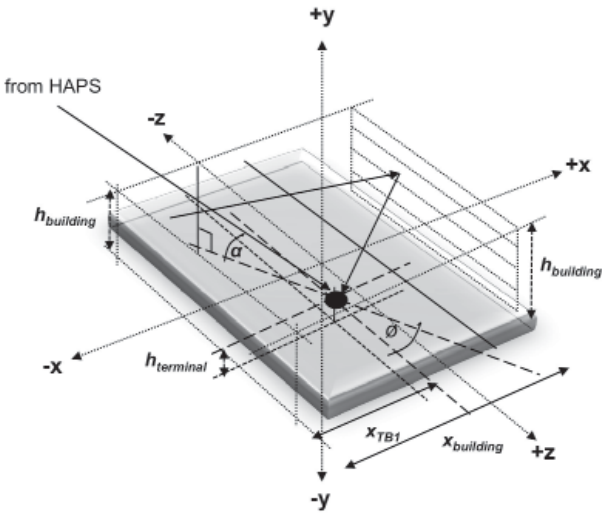

Figure 3c. The geometry for the radio propagation model at street level.

$$PL_{Terrestrial,RSL}$$

$$= \min\left\{10\log_{10}\left[\frac{\lambda}{2\pi^2 r_{RSL}}\left(\frac{1}{2\pi\theta}\right)^2\right], PL_{EPLMRB}\right\}, \quad (12)$$

where PL_{EPLMRB} is the excess propagation loss due to multiple reflections from the buildings' walls along the street and surrounding *T*. From Equation (12) and Figure (3c), it can be shown that

$$\theta = \left|\tan^{-1}\frac{h_{building}}{x1} - \alpha\right|,$$

$$r_{RSL} = \sqrt{h_{building}^2 + x_{TB1}^2}, \quad (13)$$

$$x1 = x_{TB1},\ h_{building}\cot\alpha \le x_{TB1},$$

$$x1 = 0,\ h_{building}\cot\alpha > x_{TB1},$$

where $h_{building}$ is the difference between the height of the building and the terrestrial terminal's height, x_{TB1} is the horizontal distance between the terminal and the diffraction edge (shadow), and x_{BB} is the width between the supposed buildings at both sides of the street.

For this scenario, x_{TB1} is given by

$$x_{TB1} = \min\left\{\frac{x_{BB}}{2}, h_{building}\cot\alpha\right\}, \quad (14)$$

with the second term, $h_{building}\cot\alpha$ being the width of the building's shadow cast onto the street level. When α is close to 90º, shadowing is narrow, and the rooftop diffraction loss is relatively small. In the case of a smaller α, the rooftop diffraction loss might be very high, and the user terminal would receive multiple reflection signals from the sides of nearby buildings. The condition for multiple side reflections is satisfied if

$$x_{BB} \le h_{building}\cot\alpha. \quad (15)$$

The number of reflections, N_{RB}, caused by when rooftop diffraction has occurred (from the opposite building on the other side of street) can be estimated by

$$N_{RB} = \text{int}\left(\frac{h_{building}}{x_{BB}\cot\alpha} - 1\right), \quad (16)$$

where the function $\text{int}(\ )$ means the largest integer that is smaller than or equal to the variable inside. The excess propagation loss due to reflection can thus be computed if the incident angle and the real and imaginary parts of the dielectric constant of the building material are known. However, except for "grazing" reflection, where the signal essentially propagates parallel to the building's surface, the excess loss can be taken to be ~ 10 dB. The multiple reflection loss is

$$PL_{EPLMRB} = -10N_{RB}. \quad (17)$$

Subsequently, we can speculate that the rooftop diffraction loss can be typically of the order of 10 to 40 dB, meaning that more power is needed for communications between a terminal and HAPS in the shady area. In addition to this, it is also possible to assume that at most two reflections must take place before the signal can reach the terminal (one of them must be a reflection from the ground, which is disregarded in our model). Let us take a reference from an example of a typical urban built-up situation. Both the street width and the building height are of the order of 25 m or greater. Accordingly, N_{RB} does not exceed two until α is below 19°, i.e., in an urban or suburban area with low building (building heights lower than 10 m and street widths of around 35 m), α would be less than 5.5º before N_{RB} becomes greater than two. Consequently, at different greater α values and coverage areas, the excess loss should be of the order of 20 dB or less. Moreover, we can mention that in the region of typical residential areas, outdoor radio propagation is dominated by line-of-sight propagation and rooftop diffraction. The absence of multiple reflections means that the terminal on the shady side will have to rely on rooftop diffraction to provide coverage, and it is very significant that multiple reflections could be rarely effective because of the inter-built-up distances.

Moving to the next parameter, multiple-screen diffraction loss – which differs from the multiple-screen diffraction loss of the traditional radio tower ground base station – we assumed that the data link transmission passes a row of buildings until reaching the last structure next to the terrestrial terminal. Multiple-screen diffraction loss can thus take the following general form:

$$PL_{Terrestrial,MSDL} = 10\log_{10}\left(Q^2\right), \quad (18)$$

In the HAPS case, the factor *Q* depends on α relative to the location of the terminal. For most elevation angles, $PL_{Terrestrial,MSDL}$ is essentially zero. At very small α, $PL_{Terrestrial,MSDL}$ increases rapidly. At zero elevation angle, $PL_{Terrestrial,MSDL}$ becomes arbitrarily large, so that only line-of-sight propagation is practically possible. We can examine and apply the case of multiple-screen diffraction for α with values greater than 3º. From the consideration of diffraction fringes between two successive screens, we are led to the following dimensionless variable:

$$\chi = \tan\alpha\sqrt{\frac{x_{BB}\cos\alpha}{\lambda}}\,, \qquad (19)$$

which corresponds roughly to χ being greater than one (for typical average building separations of about 50 m), and the multiple-screen diffraction loss becomes effectively zero. For this reason and because of the long coverage distance from HAPS, multiple-screen diffraction is not a significant loss factor in the main HAPS service area (we would say at values around and greater than 45º).

After these last definitions, in our case, the feasible total transmission loss becomes

$$PL\,|_{shadowing} = 10\log_{10}\left[\left(\frac{\lambda}{4\pi d_{HAPS}}\right)^2\right]$$

$$+\min\left\{10\log_{10}\left(\frac{\lambda}{2\pi^2 r_{RSL}}\left[\frac{1}{2\pi\theta}\right]^2\right),\right.$$

$$\left.10\,\mathrm{int}\left(\frac{h_{building}}{x_{BB}\tan\alpha}-1\right)\right\}, \qquad (20)$$

$$PL\,|_{LOS} = 10\log_{10}\left[\left(\frac{\lambda}{4\pi d_{HAPS}}\right)^2\right].$$

Further, we obtained further improvements in our system, covering the topic of prediction models of radio wave propagation in built-up areas, to explicitly take into account building diffraction effects to improve accuracy. At this point, we recapitulate some terminology.

The presumed built-up model has been found useful for a real-case approach where the positions of individual buildings were certainly unknown, but where some estimates of the mean building height and spacing were available. The allocation of the buildings on the ground, between the HAPS-nadir point and the receiver, were of approximately uniform height and spacing, even if there were a large number of them. It was assumed that the average building height was 20 m, having an approximation to the Rayleigh distribution. This resulted in a situation where the probability of the line-of-sight state would go down if the average building height increased. The inter-building street width was assumed to be equal to or slightly wider than a real average street width, and a constant mean inter-building spacing, $x_{building}$ (or x_{BB}) was assumed. Referring to the receiver, it was located in a position where it was surrounded by buildings on the right and left sides along the street. The receiver was assumed to be least 1 m in height. It could be located at some point across the width of the street, and not necessarily in the middle of the two surrounding buildings.

A solution for diffraction modeling purposes was therefore obtained. Buildings were conventionally viewed as parallel absorbing half planes (knife edges), located at the peak of the building's rooftop [20] (see Figure 3b). The attenuation function was provided from the complete solution to the problem of multiple collinear knife-edge diffraction with an arbitrary number of edges. The solution focused on the particular resolution for the multiple-edge diffraction integral from Vogler's model, utilizing a method of repeated approximation for the resulting integral equation [20]. The terrestrial antenna was placed at an arbitrary height, and located some distance away from the row-building's edges. The field was computed at a reference point located at the rooftop of the final building. The field strength at street level was then calculated by a simple single-plane approximation for each of the rays arriving at the receiver. The solution was uniformly valid, so that the source point could be above, level with, or below the diffraction-edge height. It was equally possible to easily apply it to a small or large number of edges.

From the shadowing attenuation theory, a more complete received power approach can be calculated. The condition is now clearly defined for a single knife-edge diffraction attenuation at the rooftop of the closest building to the ground terminal. This model, proper in the line-of-sight and shady circumstances, allowed us to make predictions where direct measurements were unavailable, and where existing land-mobile satellite system records could be adopted [8, 20].

For the obstructed condition, we assumed the attenuation from the free-space field to be determined by the two practical diffracted and reflection diffracted rays (triggered by the building opposite to the main building), which were combined with random phase at the receiver:

$$PL_{Terrestrial,DS}$$

$$= PL_{HAPS,FSL}\sqrt{A^2(\vartheta_{DLOS}) + \rho^2 A^2(\vartheta_{DSR})}\,, \quad (21)$$

where ρ is the loss because of reflection, including effects due to polarization, surface roughness, and the material's reflection coefficient. Furthermore,

$$A(\vartheta_{DLOS}) = \tfrac{1}{2}F(\vartheta_{DLOS})e^{-j\pi/4} + \tfrac{1}{2}\,, \qquad (22)$$

$$A(\vartheta_{DSR}) = \tfrac{1}{2}F(\vartheta_{DSR})e^{-j\pi/4} + \tfrac{1}{2}\,,$$

where F is the complex Fresnel integral,

$$F(\vartheta_D) = C(\vartheta_D) + jS(\vartheta_D). \quad (23)$$

The Fresnel diffraction parameters for the diffracted ray and for the reflection diffracted ray are given by

$$\vartheta_{DLOS} = -\left[\frac{\pi}{2} - \tan^{-1}\left(\frac{x_{TB1}}{h_{building}}\right) - \alpha\right]\sqrt{\frac{2x_{TB1}}{\lambda}}, \quad (24)$$

$$\vartheta_{DSR} = -\left[\frac{\pi}{2} - \tan^{-1}\left(\frac{2x_{building} - x_{TB1}}{h_{building}}\right) - \alpha\right]$$

$$\sqrt{\frac{2\left(2x_{building} - x_{TB1}\right)}{\lambda}}.$$

In due course, for the line-of-sight condition, we power-summed the respective direct and specular reflection rays:

$$PL_{Terrestrial,DD} = P(\vartheta_{LOS}) + \rho^2 P(\vartheta_{SR}), \quad (25)$$

with the diffraction parameters defined for the direct, ϑ_{LOS}, and reflected, ϑ_{SR}, rays as

$$\vartheta_{LOS} = \left(h_{building} - h_{LOS}\right)\sqrt{\frac{2}{\lambda d_{LOS}}}, \quad (26)$$

$$\vartheta_{SR} = \left(h_{building} - h_{SR}\right)\sqrt{\frac{2}{\lambda d_{SR}}}, \quad (27)$$

where

$$h_{LOS} = \begin{cases} h_{terminal} + \dfrac{x_{TB1}\tan\alpha}{\sin\phi}; & 0 < \phi \le \pi \\ h_{terminal} + \dfrac{(x_{BB} - x_{TB1})\tan\alpha}{\sin\phi}; & -\pi < \phi \le 0 \end{cases},$$

$$d_{LOS} = \begin{cases} \dfrac{x_{TB1}}{\sin\phi\cos\alpha}; & 0 < \phi \le \pi \\ \dfrac{(x_{BB} - x_{TB1})}{\sin\phi\cos\alpha}; & -\pi < \phi \le 0 \end{cases}, \quad (28)$$

$$h_{SR} = \begin{cases} h_{terminal} + \dfrac{(2x_{BB} - x_{TB1})\tan\alpha}{\sin\phi}; & 0 < \phi \le \pi \\ h_{terminal} + \dfrac{(x_{BB} + x_{TB1})\tan\alpha}{\sin\phi}; & -\pi < \phi \le 0 \end{cases},$$

$$d_{SR} = \begin{cases} \dfrac{(2x_{BB} - x_{TB1})}{\sin\phi\cos\alpha}; & 0 < \phi \le \pi \\ \dfrac{(x_{BB} + x_{TB1})}{\sin\phi\cos\alpha}; & -\pi < \phi \le 0 \end{cases}.$$

The diffracted ray power was then expressed in terms of the Fresnel cosine, $C(\vartheta)$, and sine, $S(\vartheta)$, integrals:

$$P(\vartheta) = \tfrac{1}{2}\left[\tfrac{1}{2} + C^2(\vartheta) - C(\vartheta) + S^2(\vartheta) - S(\vartheta)\right]. \quad (29)$$

The latter expressions were assumed to have HAPS-to-building distances very much greater than the building-to-terminal distances. It was also supposed that only one building contributed to the diffraction process. This meant that the higher the building height was, the more it would count for the shadowing-case attenuation.

The typical extent of vegetation areas in cities is generally too small, but realistically it exists. A similar analysis was been applied to potential shadowing by trees rather than buildings, and the explanation is as follows.

In our case, the effect of foliage was considered by adding contributions from the penetration through vegetation (empirical approach), and diffraction over vegetation effects [35]. The foliage accounted for leaves very thin from real vegetation canopies behaving like Rayleigh scatterers, without considering the influence of the stem and moisture. The diffraction over the greenery was thus specifically modeled by a single knife-edge diffraction at 1.2 m average height. Penetration through the greenery was defined to be feasible with 5 dB, by the following approach:

$$PL_{Terrestrial,foliage} = g\sum_{i=1}^{n} l_i \text{ [db]}, \quad (30)$$

where $g = 0.2$ dB/m, and l_i stands for the longitude of the ith vegetative area. This was taken as an alternate arrangement, with $n = 5$ greenery areas of 5 m in longitude for each one, and they were located through the signal transmission path.

3.3 Channel Characterization

All of these models could certainly be used to predict the narrowband characteristics. In order to acquire the right predictions for the signal for the broadband case – without requiring in-depth usage of site-specific information, and gaining time in the computation – a more promising approach of characterization of the delay spread and fading statistics must keep the system performance conjecture within a small margin error.

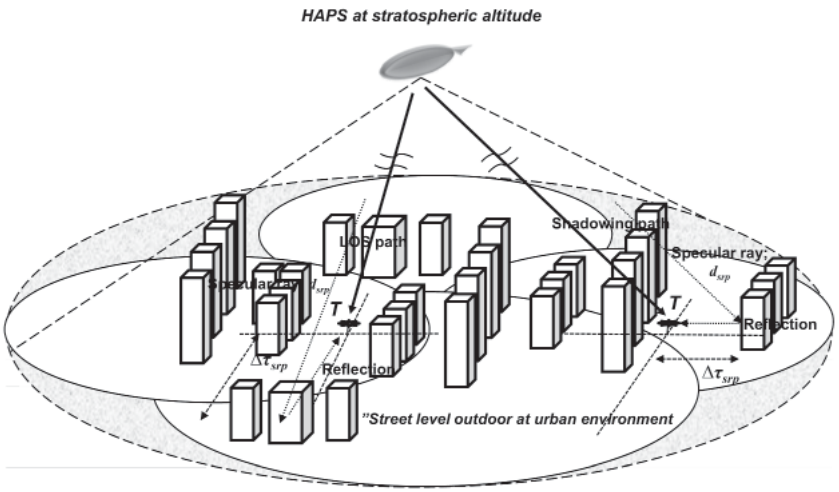

Figure 4. Based on the HAPS channel conditions and the presence or absence of smooth and rough outdoor surfaces, profiles of direct and specular reflection paths plus multipath in the urban built-up area are manifested.

In this proposal, a viable model was useful for developing the information regarding the broadband characteristics by means of the propagation prediction using the echo/ray terminology at local levels of *T* surroundings. Scattering occurred due to the radio wave infringing on a large rough surface (or on dense foliage) that caused the (reflected) rays to spread out in various directions, or due to the motion of objects nearly surrounding the terminal. The proposed propagation model was theoretically based on the geometrical features of the built-up structures surrounding the ground terminal. It was expanded with statistical estimation from the land-mobile satellite system channel model, in order to estimate the system's field capacity. The predictions were realized to be fairly different from those of the terrestrial channel, but rather similar to the satellite channel.

The evaluation of the downlink performance using the HAPS-communications channel necessarily requires a fading mitigation technique (i.e., in our analysis the use of coded orthogonal frequency-division multiplexing (COFDM) [23-24] was proposed, aiming a the standardization of the ITU administration under the IMT-2000 and IEEE frameworks) to ensure the channel quality being above a minimum level of performance. In our case, the performance evaluation was expressed in terms of the achievable bit-error rate (BER). The evaluation was able to carry broadband and other communications services at different information bit rates (allowing adaptability of the system to on-demand circumstances). It is important that we recall certain system characterizations from the research presented in [25, 26]. The channel modeling representation was treated with some similarities from these studies. The model was conformed to the hypotheses of a direct ray and a specular-reflection ray (a reflected signal caused by a "reflection body" inside the small vicinity of the receiver), plus multipath from two such main rays. These corresponded to and were added for the characterization of the already considered channel states of shadowing and unobstructed path, with a log-normal distribution [27] and a Rice distribution [28], respectively. The practical infrastructure is represented in Figures 4, 5, and 6.

Previously, we introduced that the ray components of the radio signal can establish the signal attenuation for a deterministic channel. In our case, the channel is time varying. Such statistical properties were analyzed with the Bello functions [29] as the base of our short-term-variation modeling. We reorganized the latter statistical characterization and simplified the channel to the WSSUS

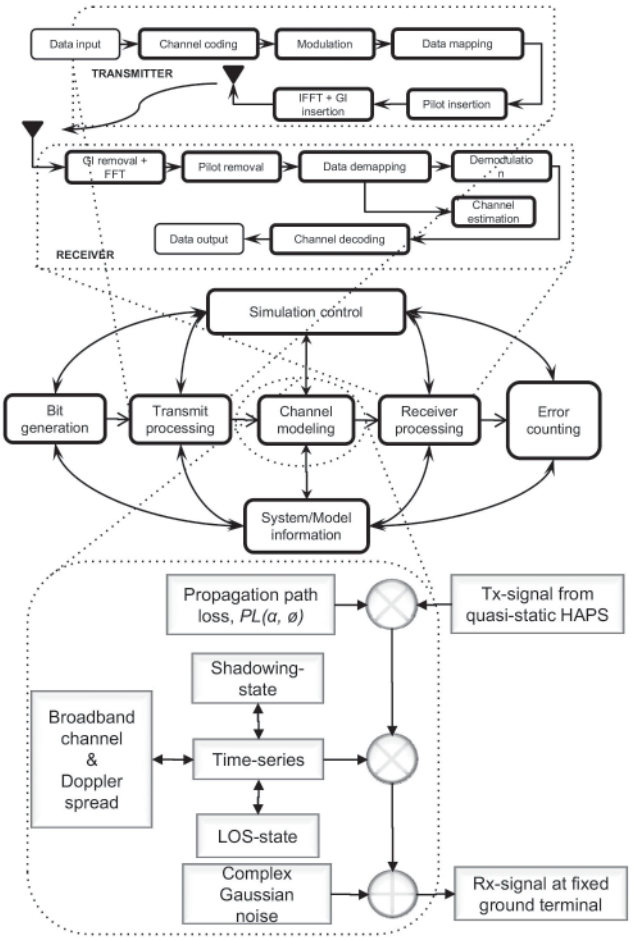

Figure 5. The simulation control for the overall stratospheric broadband channel modeling pro-

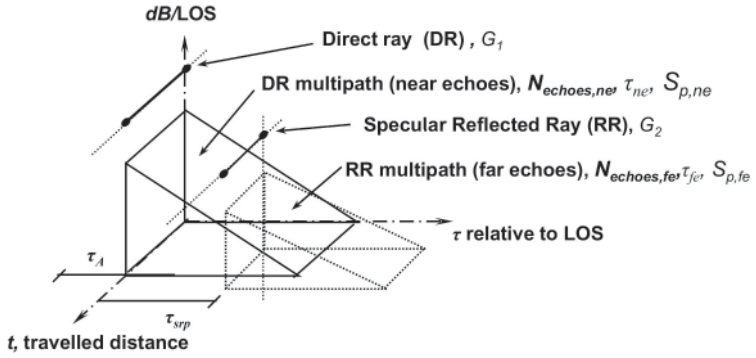

Figure 6a. An illustrative representation of the broadband channel modeling simulator for the physical echoes and multipath fading [8, 25, 26].

function, as shown in Figure 6, with a tapped-delay-line model of 11 bins.

In the last account, broadband characterization was not completely acquired, even using the characterization from [25, 26] and their references. Herein, our system exigencies claim further accurate signal predictions related to achieving a smaller margin of error.

Once we declared the major parameters and that the receiver had an elevation angle less than 45º, the significant parameter of the shadowing effect was taken to be a time sharing of shadowing of the order of 50%. Attending to this last topic, we can present one more analysis to be counted for performance in the shadowing channel condition in terms of visibility and building-height distribution.

Visibility was supposed to be the probability of the channel of having a line-of-sight situation at each elevation angle and within 360º of the azimuth angle ϕ (a variable referenced in Figure 3c). Thus, the equation for visibility was based closely on the significances of α and ϕ [13, 30]:

$$p_{vis}(\alpha,\phi) = \begin{cases} (\sin\alpha)^{0.01}; & \phi = 0^{\circ} \\ (\sin\alpha)^{\sin\phi}; & \phi = 30^{\circ}, 60^{\circ}, 90^{\circ} \end{cases}, \quad (31)$$

where ϕ was $\leq 10°$ for line of sight and $> 75°$ for shadowing. $\phi = 0°$ in the negative *z*-axis direction and $\phi = 90°$ in the negative *x*-axis direction, as shown in Figure 1. The visibility was respectively in agreement with the direct path at $\phi = 0°$ and the shadowing situation being an increasing function following high ϕ. At this point, we can say that the propagation impairments for the line-of-sight situation went along with the variations in α. In the obstructed situation, different values of ϕ resulted in different fading, because of the dominant multipath power variations, with worse effects at $\alpha < 45°$. The potentially worst case occurred when $\phi = 90°$, for which a distributed Rayleigh characterization was roughly an adequate approach.

We can state that the ray was also judged [20, 21] to be shadowed when the building height, h_{mbh}, exceeded some threshold height, $h_{threshold}$, relative to the point of the direct ray's height. The shadowing probability term, $P_{building}$, was expressed by the probability density function (PDF) of the building height, $p_{building}(h_{mbh})$:

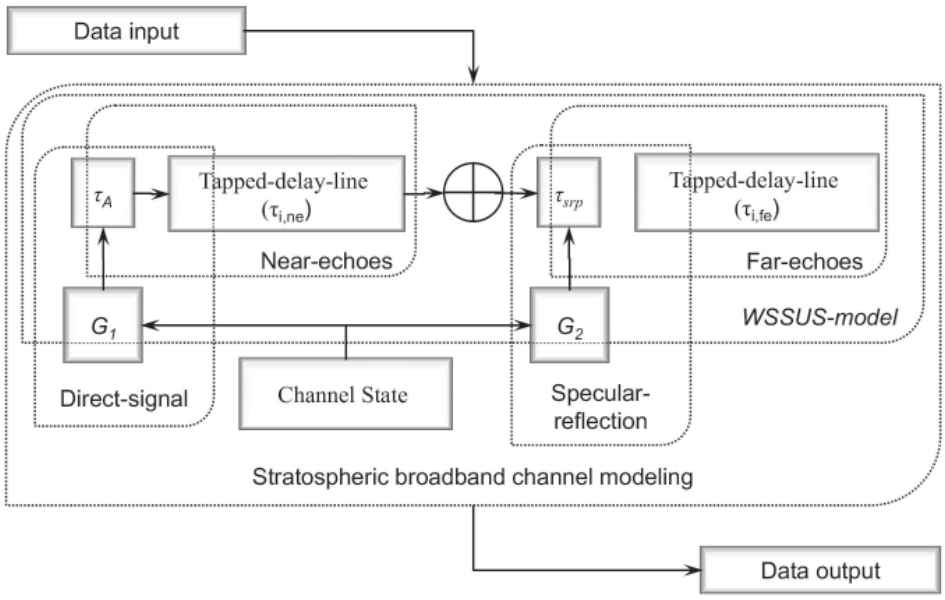

Figure 6b. A channel-state diagram of the broadband channel modeling simulator for the physical echoes and multipath fading [8, 25, 26].

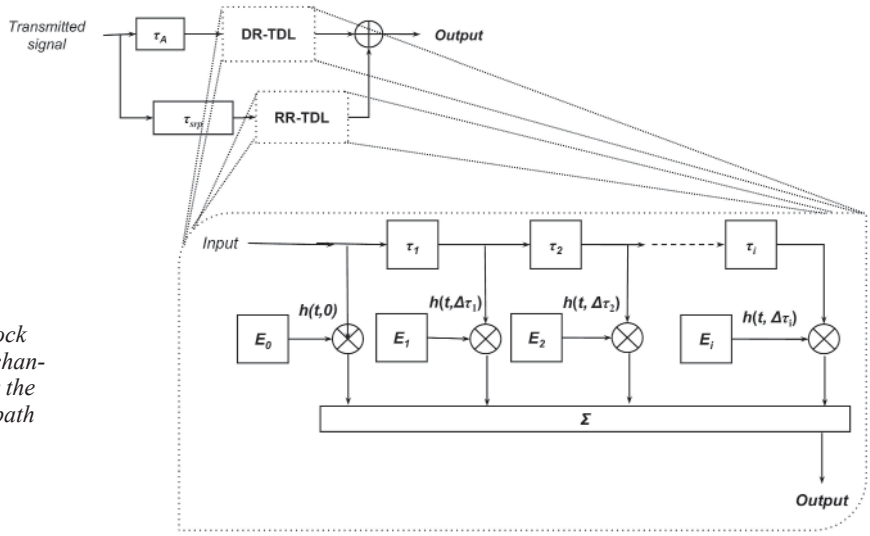

Figure 6c. A multipath block diagram of the broadband channel modeling simulator for the physical echoes and multipath fading [8, 25, 26].

$$P_{building} = P\left(h_{mbh} > h_{threshold}\right)$$

$$= \int_{h_{building}}^{\infty} p_{building}\left(h_{mbh}\right) dh_{mbh} \,. \qquad (32)$$

It was then necessary to seek a suitable form for $p_{building}\left(h_{mbh}\right)$ fitting a Rayleigh distribution with the parameter $\sigma_{building}$. The fit was acceptable, although the Rayleigh distribution tended to overemphasize the effects of the building's height. The Rayleigh distribution has the particular advantage in our scheme of being of analytic simplicity. Besides, in the cases where an explicit distribution for the building height was unavailable, the parameter $\sigma_{building}$ can be related to a qualitative classification of the environmental situation. Afterwards, $P_{building}$ is

$$P_{building} = \int_{h_{mbh}}^{\infty} \frac{h_{mbh}}{\sigma_{building}^2} e^{\left(-h_{mbh}/2\sigma_{building}^2\right)} dh_{mbh} \qquad (33)$$

$$= e^{\left(-h_{threshold}^2/2\sigma_{building}^2\right)} .$$

The simplest definition of $h_{threshold}$ was obtained by considering the geometrical block to be represented by the building's face, i.e., $h_{threshould} = h_{LOS}$, which was defined as the height of the direct ray above the building's face relative to the local ground level. In a more-sophisticated approach, the shadowing was considered to occur whenever a significant proportion (say 0.7) of the first Fresnel zone radius, $R_{FZ,LOS}$, of the direct ray was obscured by the building. This case was not considered for the specular reflected ray version. Given that the distance between the HAPS and the building was much greater than the building-to-terminal distance, $R_{FZ,LOS}$ was given by

$$R_{FZ,LOS} = \sqrt{\frac{\lambda x_{TB1}}{\sin\phi\cos\alpha}} \,. \qquad (34)$$

$h_{threshold}$ was thus obtained as

$$h_{threshold} = h_{LOS} - 0.7R_{FZ,LOS} \,. \qquad (35)$$

Subsequently, the functional approaches adopted for the shadowing and line-of-sight cases can be described as

$$f_{CS}(r)|_{shadowing} = p_{vis}(\alpha,\phi) P_{building} f_{shadowing}(r) \,,$$

$$f_{CS}(r)|_{LOS} = p_{vis}(\alpha,\phi) f_{LOS}(r) \qquad (36)$$

Furthermore, other remaining fading factors have been missed in the HAPS literature. The considerations for these significant impairments were reached as following.

In a certain manner, the multipath has a dependence on the carrier wavelength, λ. For our concise situation, the front-edge wave was contemplated as a reflection from an obstacle or object, if this was smooth and its dimension was large enough compared to λ. In other words, a smooth facade with large proportions compared to λ tends to be a specular reflector, which acts in a manner similar to a mirror. On the other hand, isolated objects with minor size or of size comparable to λ cause dispersion of the energy. Consequently, the importance of defining a smooth or rough surface was relevant to the current analysis. The Rayleigh criterion was used, interpreting a height, h_H, which should not exceed a critical height of approximately of 2 to 11 cm in our case, as a function of the angle of incidence and λ.

Accordingly, assumptions for the exterior surfaces of the buildings along the street were made. The majority were taken to consist of brick, stone, or concrete, with many glass windows. These types of surfaces have a poor reflection coefficient at normal incidence, primarily due to the surface roughness and irregularities that are sizeable relative to the RF wavelength. However, at grazing incidence, the surface appears smooth, and its reflection coefficient

becomes highest. The Rayleigh criterion, $h_H \le \lambda/8\cos(\xi)$, determined if a surface was considered smooth, with ξ being the angle of incidence, and h_H being the height of the surface irregularity. In our analysis, $\xi = 8°$ (or greater) was a realistic angle.

In addition to this last consideration, the roughness effects also had an influence on the coherent and specular paths by means of the Rayleigh factor:

$$\zeta = e\left[-\frac{1}{2}\frac{4\pi\sigma_H \cos(\xi)}{\lambda}\right], \qquad (37)$$

where σ_H is the standard deviation of the surface roughness. A major weakness in the reflection power of the specular path was deduced with such a factor.

We defined right away that signals traveled at a finite speed. Therefore, an upper limit was defined by the speed of light at the receiver sensing a time delay, Δt, related to the propagation speed and the distance, d: $\Delta t = d/c$. This was chiefly evidenced in the specular reflection path term used. This was also conditioned to the term found for the horizontal distance, Δr_{srp}, a distance from the "reflection body" to the receiver, and α. Ergo, the physical space delay of the reflection path (as shown in Figure 4) was determined by

$$\Delta\tau_{srp} = \tau_B - \tau_A$$

$$= \frac{1}{c}\left(d_{srp} - d_{HAPS}\right) \qquad (38)$$

$$= \frac{1}{c}\left\{\left[\sqrt{\left(\Delta r_{srp} + R_{HAPS}\right)^2 + r_{HAPS}^2} + \left|\Delta r_{srp}\right|\right] - \left[d_{HAPS}\right]\right\}.$$

We have that $\Delta r_{srp} < R_{HAPS}$; c is the speed of light; d_{srp} is the distance from HAPS to the "reflection body" for the specular reflection path; and τ_A and τ_B are the arrival delays from HAPS to the terminal for the direct and specular paths, respectively.

The possible attenuation for such a specular reflection path was evaluated from

$$L_{srp,FSL} = 10\log_{10}\left(\frac{d_{srp}}{d_{HAPS}}\right) \text{ [dB]}. \qquad (39)$$

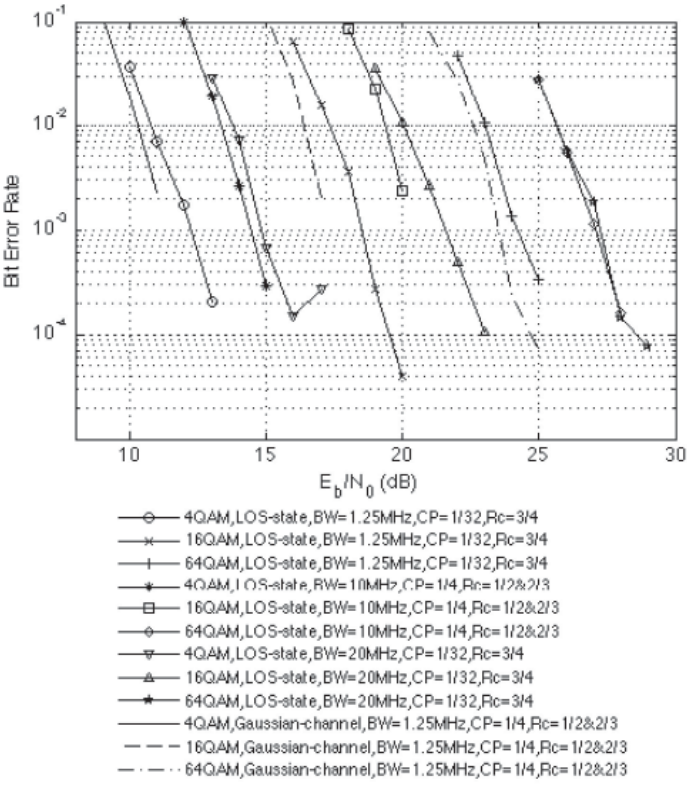

Figure 7a. As a result of intensive simulations, the WiMAX HAPS-based downlink performance evaluation approach (based on the so-called stratospheric state-oriented channel modeling) is shown for the building-shadowed path. Analyses comprise the geometrical and statistical channel propagation characteristics plus the standardization application by means of the IEEE Std 802.16 WirelessMAN-OFDM air-interface (Fixed-WiMAX).

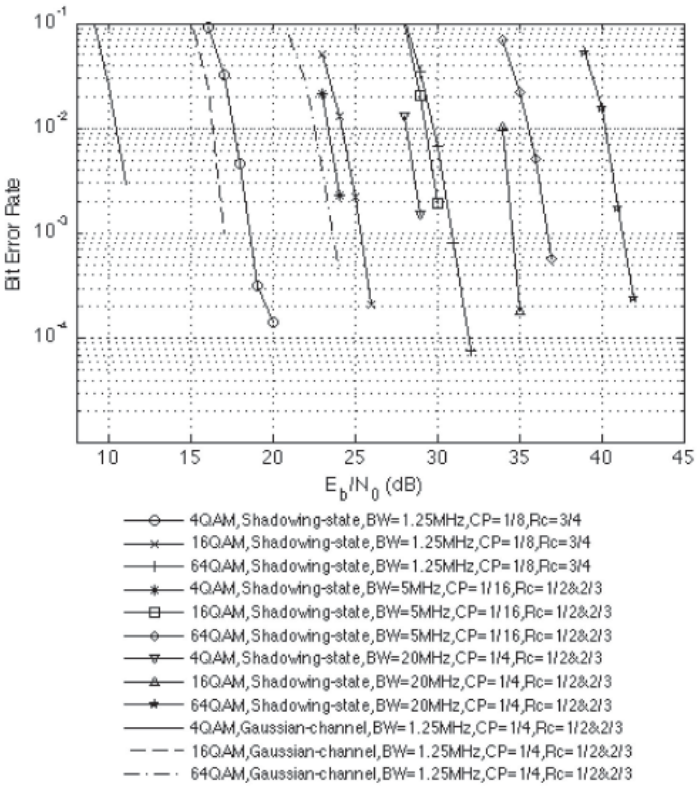

Figure 7b. As a result of intensive simulations, the WiMAX HAPS-based downlink performance evaluation approach (based on the so-called stratospheric state-oriented channel modeling) is shown for the built-up environment direct path. Analyses comprise the geometrical and statistical channel propagation characteristics plus the standardization application by means of the IEEE Std 802.16 WirelessMAN-OFDM air-interface (Fixed-WiMAX).

4. Performance Results and Discussion

The HAPS-based model was analyzed by means of intensive *MATLAB*-based simulations [31] in the frequency band of 1.820 GHz, following the considerations of IEEE Std 802.16-2004 for the IMT-2000 agenda. We considered a realistic situation, where HAPS provides broadband communications as a fixed wireless-access alternative for the standardization regime. The performance achieved results were qualitatively reasonable, as illustrated in Figure 7 for the specific HAPS-to-terminal elevation angle of 43º (almost at the edge of the defined circular urban-zone coverage of 30º), plus all possible parameters established in the preceding sections. Tables 1 and 2 set for the remaining parameters for usage at the transceiver and the channel-propagation approach. Hence, the results illustrated the outcome for the overall software-aided proposal founded on our analysis hypotheses. Projections of the performance variations under different conditions of modulation (4QAM, 16QAM, 64QAM), coding (Reed-Solomon convolutional coder), and channel characteristics are displayed by means of the bit-error rate (BER) as a function of $E_b/N_{0.}$

The transceiver components (as displayed in Figure 6) were designed around the principles of COFDM. Together with the IEEE standards, this technique supported us with a wide range of operating bandwidths to flexibly address the need for various spectrum-allocation and application requirements, as the alternative outcomes in [25, 26] have already clarified this situation. A brief description of the transmitter block is given, conforming to the main tasks.

Channel coding: The channel-coding stage includes randomization, coding, and puncturing. The input data was randomized in order to avoid long runs of ones and zeros. The output of the data randomizer was encoded with a block of a Reed-Solomon-convolutional coder (RS-CC). The convolutional coder constraint length was seven, and its native code rate was one-half. The puncturing block punctured the output of the concatenated encoder to produce variable higher code rates.

Interleaving: This block mapped adjacent encoded bits into separated subcarriers, thus minimizing the impact of burst errors caused by spectral nulls.

Modulation: The modulation block converted the sequence of interleaved bits into the sequence of complex symbols, depending on the chosen M-QAM modulation scheme (BPSK, QAM, 16QAM, and 64QAM).

Data mapping: The data were introduced to mapping into blocks/frames.

Pilot insertion: Pilots were inserted at this point. In addition, at this stage all data symbols were mapped to the data region and their corresponding logical subcarriers.

IFFT: The final stage converted the data into the time domain for use at the radio front end, and a guard interval (GI) was inserted after this step.

Table 1 gives the relevant parameters utilized in the transceiver under the standards. The last tasks were applied essentially in order to have a robust and power-spectral-efficient communication outcome, aiming to the alternative of adaptive coding modulation (ACM).

The transceiver parameters were modified into the diverse current system characteristics according to the propagation-channel conditions. Once the time-varying stratospheric channel was estimated, the transmitter was adapted to the new conditions by varying the coding-modulation type, conditioned to maintain a constant error rate. The values of *M*-QAM and RS-CC coding were

Parameter	Value
FFT size	256
Channel bandwidth, BW [MHz]	5, 10, 20
Sampling frequency, F_s [MHz] = nBW 8000/8000 ; $n = 8/7$(5 MHz) at licensed band, $n = 57/50$ (10 & 20 MHz) at licensed band	5.71 (5 MHz), 11.4, 22.8 (10 MHz, 20 MHz)
Sampling period, $1/F_s$ [µs]	0.175, 0.087, 0.043
Subcarrier frequency spacing, $\Delta f = F_s/N_{FFT}$ [kHz]	22.31, 44.5, 89.03
Useful symbol period, $T_b = 1/\Delta f$ [µs]	44.81, 22.47, 11.23
Guard time, $T_g = T_b CP$ [µs]; $CP = 1/4$ and $CP = 1/32$ (cyclic prefix ratio)	11.2, 5.61, 2.8; 1.4, 0.07, 0.035
OFDM symbol duration, $T_s = T_b + T_g$ [µs]; $CP = 1/4$ and $CP = 1/32$ (cyclic prefix ratio)	56.01, 28.08, 14.03; 46.21, 22.54, 11.265
No. of used subcarriers	200
No. of pilot subcarriers	8
No. of data subcarriers	192
No. of null subcarriers, and dc subcarriers	55, 1

Table 1. The parameters in downlink mode for the PHY-layer, IEEE 802.16-2004 [9, 26]

manually varied. However, they were theoretically related to a switching process, depending on the estimation process controlled by the value of the predicted signal-to-noise ratio. Furthermore, we selected the same modulation case scheme in the way that was applied to all subcarriers. Different modulation was not considered for any group of subcarriers (as possibly carried out by OFDM access, OFDMA).

Two scenes were assumed, according to the surrounding situation at the outdoor terrestrial receiver (as is shown in Figure 5). We contemplated the digital signal scheme consisting of the two main direct and specular reflected rays, which determined the respective fading effect for the short-term set. The objective of this was to quantify the needs of a more-complex channel model, considering real situations that account for the environment and broadband channel characterization. The settled behavior of the whole system clearly developed and differentiated the explicit state-oriented model, where a direct path (Loo's representation) and a shadowing path (Lutz's representation) arose, with the option to be compared to that obtained for the Gaussian case.

Parameter		
f_c = 1820 MHz, λ = 0.1647 m	r_{HAPS} = 21 km, R_{HAPS} = 0-36.15 km (urban area, α = 90º-30º); d_{HAPS} = 30.72 km, $d_{srp,LOS}$ = 66.14 km, $d_{srp,shadowing}$ = 66.11 km	α = 43º; R_{HAPS} = 22.43 km $\varnothing_{LOS} \leq 10º$, $\varnothing_{shadowing} > 75º$, ξ = 47º
h_{mbh} = 20 m, $h_{terminal}$ = 1.5 m, x_{TB1} = 5 m, x_{BB} = 25 m = $x_{building}$, $h_{building}$ = 18.5 m, $\Delta r_{srp,LOS} \leq$ 30 m, $\Delta r_{srp,shadowing} \leq$ 15 m	L_{LOS} = 131.48 dB: $PL_{HAPS,FSL}$ = 127.4 dB, $PL_{Terrestrial,RSL}$ = 0 dB (N_{RB} = 0), PL_{EPLMRB} = 0 dB, $PL_{Terrestrial,DD}$ = 4.08 dB; $L_{srp,FSL}$ = 0.0073 dB	$L_{shadowing}$ = 198.91 dB: $PL_{HAPS,FSL}$ = 127.4 dB, $PL_{Terrestrial,RSL}$ = 8.43 dB (N_{RB} = 1), PL_{EPLMRB} = 10 dB, $PL_{Terrestrial,DS}$ = 53.08 dB, $L_{srp,FSL}$ = 0.0048 dB
A_{tss} = 54%, Shadowing time percentage	K = 5.5 dB Rice-factor	μ = –13.6 dB , Mean power relative to LOS under shadowing condition
σ = 2.9 dB, Standard deviation of lognormal fading	τ_A = 102.5 µs, $\tau_{B.LOS}$ = 102.67 µs, $\tau_{B,shadowing}$ = 102.58 µs, $\Delta\tau_{srp,LOS}$ = 0.17 µs, $\Delta\tau_{srp,shadowing}$ = 0.097 µs	$N_{echoes,ne} > 50$, $N_{echoes,fe} > 50$ No. of multipath echoes at receiver for the diffuse component
i = 11 taps (WSSUS tapped-delay-line representation): 6 taps at near-echoes, and 5 taps at far-echoes	$\tau_{echoes,ne}$ = [0 0.6) µs, $\tau_{echoes,fe}$ = [0.6-1.2) µs Time duration of near- and far-echoes	$\Delta\tau_i$ = 0.1 µs Equally spaced tap delay
Average power of *i-th* tap [μs]: $MP_{1,ne}$=–24.49, $MP_{2,ne}$=–31.67, $MP_{3,ne}$=–39.21, $MP_{4,ne}$=–49.03, $MP_{5,ne}$=–59.40, $MP_{6,ne}$=–50.40, $MP_{7,fe}$=–51.66, $MP_{8,fe}$=–57.71, $MP_{9,fe}$=–63.49, $MP_{10,fe}$=–69.11, $MP_{11,fe}$=–73.47.	A_1 = 0 dB (level power of the direct-signal), MP = –23.6 dB	A_2 = –10 dB (level power of the specular reflection signal), MP = –26.8 dB
$S_{p,ne}$ = 10 dB/µs, $S_{p,fe}$ = 10 dB/µs Multipath power slope decay	$\tau_{e,ne}$ = 0.069 µs, $\tau_{e,fe}$ = 0.091 µs Average distribution for excess delay (near- and far-echoes)	$\tau_{m,ne}$ = 0.6 µs, $\tau_{m,fe}$ = 1.2 µs Maximum excess delay (near- and far-echoes)
$f_{D,max}$ of ~2.4 Hz, Maximum Doppler shift	$T_{coherence} \approx 1/f_{D,max}$ = 0.416 s, Coherence time	$BW_{coherence} \approx 1/\tau_m$ = 833.33 kHz, Coherence bandwidth

Table 2. Radio propagation and channel-fading characteristics.

The analysis processes given in the previous sections have provided a practical means of incorporating the shadowing case for a built-up area, and the unobstructed-path situation, for an accurate HAPS-based transmission link prediction. Environmental situations have been successfully applied to predict the median field strength and fading over the received signal with good accuracy. We prevented the transmission system from counteracting against the signal attenuation and variations with low computational complexity and simple physical data. We can note that the result might particularly have been a worse outcome for the shadowing case (Figure 7a), which effect should not have had a high impact on the system's performance, in spite of the high elevation-angle value of 43º. However, within the built-up environment influenced by the visibility and building heights, plus a low code rate, low cyclic prefix ratio, and high nominal bandwidth usage, the signal underwent low performance (Figure 7a). The complete calculations also showed that the performance got better for the direct path (Figure 7b), because of the existence of the line-of-sight situation, and less impact from the built-up structures.

Moreover, the owned application and simulation have been virtually required that one can have line of sight state communications much of the time given the power limited nature of the actual surreal HAPS-based system. The concept of the combination of the shadowed and un-shadowed cases (i.e., the state-oriented model) was performed, but without the actions to introduce it into a single-channel simulation run. Rather, it was compared with the two possible scenarios existing within the urban-area coverage. We assumed that the channel was in each of the states for a certain percentage of time (with help from the land-mobile satellite system empirical approaches). Separate simulations were then conducted, using each of the models. The outcomes were then combined in a uniform manner according to the suppositions of the percentage of time spent in each state.

The implementation of this last approach has limitations based on neglecting the channel state's transition effects, where the communication condition would be changing from one state to another. The fading-mitigation techniques may be sensitive to such changes for each case.

Correspondingly, we can remark that singularly, very little measured and other advanced theoretical data exist nowadays to use as references for comparison to our model, specifically with the specifications used for performance evaluation. Hence, worth limitations for our HAPS-based proposal where presumed in order to reflect the real application as a wireless access system. However, on the positive side for the broadband application, we had an approximation to the fading countermeasures with the technology used. These can possibly be compared with the general and real performance predictions from wireless terrestrial studies; shadowing and direct conditions could be included.

The system demonstrated in this case is an ongoing work. Based on simulations, it has been proven that the HAPS-based approach model can be an alternative and supportive system to those wireless systems already defined for practical real applications, based on data primarily obtained from terrestrial and satellite campaign research. In the interim, the utilization of channel coding and OFDM techniques were sufficient requirements to realize palpable, reliable, and robust communications based on a stratospheric platform for the metropolitan coverage service area.

5. Conclusions

This paper has presented a WiMAX HAPS-based downlink performance analysis, using a proposal for the HAPS-to-fixed terminal channel at L band. Free-space loss plus deterministic ray tracing and statistical approaches have been used to provide more realistic predictions of the HAPS service coverage sector for a stipulated building grouping and position. Miscellaneous simulations by means of bit-error rate as a function of E_b/N_o were achieved for the performance of the system, using the air-interface scheme proposed in fixed WiMAX. The COFDM technique offered advantages for our specific conditions of channel modeling and environment. Finally, it was observed that additional work is also needed to determine methods to open the fixed condition to mobility of both the receiver and the platform.

6. Acknowledgements

The authors would like to thank the anonymous reviewers for their helpful comments and suggestions, which have significantly improved this paper. This work was partially supported by the EU under IST Project Capanina (FP6 IST-2003-506745) and the Spanish Government Project TEC2004-0136-E. The authors were members of COST297-High Altitude Platforms for Communications and Other Services (HAPCOS) (European Action ending by 2009). Thanks to the CONACyT Program (National Financial Resource in Mexico for Science and Technology) for corresponding to the financial support.

7. References

1. G. M. Djuknic and Y. Okunev, "Establishing Wireless Communications Services via High-Altitude Aeronautical Platforms – A Concept Whose Time Has Come?," *IEEE Communications Magazine*, **35**, 9, 1997, pp. 128-35.
2. Y. Hase, R. Miura, and S. Ohmori, "A Novel Broadband All-Wireless Access Network Using Stratospheric Platforms," The 48th IEEE Semi-annual Vehicular Technology Conference (VTC-1998 Spring), 2, 1998, pp. 1191-94.
3. T. C. Tozer and D. Grace, "High-Altitude Platforms for Wireless Communications," *Electronics & Communication Engineering Journal*, **13**, 3, 2001, pp. 127-37.
4. A. K. Widiawan and R. Tafazolli, "High Altitude Platform Station (HAPS): A Review of New Infrastructure Development for Future Wireless Communications," *Wireless Personal Communications*, **42**, 3, 2007, pp. 387-404.

5. Stylianos Karapantazis and Fotini-Niovi Pavlidou, "Broadband Communications via High-Altitude Platforms: A Survey," *IEEE Communications Surveys & Tutorials*, **7**, 1, 2005, pp. 2-31.

6. International Telecommunication Union, Radiocommunications Sector, "Minimum Performance Characteristics and Operational Conditions for High Altitude Platform Stations Providing IMT-2000 in the Bands 1885-1980 MHz, 2010-2025 MHz, and 2110-2170 MHz in the Regions 1 & 3, and 1885-1980 MHz and 2110-2160 MHz in Region 2," ITU-R M.1456, 2000.

7. M. A. Vázquez-Castro, D. Belay-Zeleke, and A. Curieses-Guerrero, "Availability of Systems Based on Satellites with Spatial Diversity and HAPS," *IEE Electronics Letters*, **38**, 6, 2002, pp. 286-88.

8. María Vázquez-Castro and Fernando Pérez-Fontán, "Channel Modeling for Satellite and HAPS System Design," *Wireless Communications and Mobile computing*, **2**, 3, 2002, pp. 285-300.

9. IEEE, "802.16™ – IEEE Standard for Local and Metropolitan Area Networks, Part 16: Air Interface for Broadband Wireless Access Systems," IEEE Std 802.16™-2009 (Revision of IEEE Std 802.16-2004).

10. International Telecommunication Union, Radiocommunication Sector, "Detailed Specifications of the Radio Interfaces of International Mobile Telecommunications – 2000 (IMT-2000)," ITU-R M.1457, 2001-2007.

11. S. Karapantazis and F. N. Pavlidou, "Broadband from Heaven [High Altitude Platforms]," *IEE Communications Engineer*, 2004, pp. 18-24.

12. A. Aragón-Zavala, Cuevas-Ruíz, and J. A. Delgado-Penín, *High-Altitude Platform Systems for Wireless Communications*, New York, John Wiley & Sons, 2008, p. 256.

13. M. Iskandar and Shigueru Shimamoto, "On the Performance of IMT-2000 Communication Link based on Stratospheric Platforms," *Makara, Teknologi (Fakultas Teknik Universitas Indonesia)*, **10,** 1, 2006, pp. 1-10.

14. Marina Mondin, Favio Dovis, and P. Mulassano, "On the Use of HALE Platforms as GSM Base Stations," *IEEE Personal Communications*, **8**, 2, 2001, pp. 37-44.

15. F. Davarian, "Channel Simulation to Facilitate Mobile-Satellite Communications Research," *IEEE Transactions on Communications*, **35**, 1, 1987, pp. 47-56.

16. A. Jahn, "Propagation Data and Channel Model for LMS Systems," European Space Agency Final Report (DLR German Aerospace Research Establishment Institute for Communications Technology, Institut Für Nachrichtentechnik), 1994.

17. M. A. N. Parks, S. R. Saunders, and B. G. Evans, "A Wideband Channel Model Applicable to Mobile Satellite Systems at L- and S-Band," IEE Colloquium on Propagation Aspects of Future Mobile Systems, Digest No. 1996/220 (12), 1996, pp. 1-6.

18. Riu Miura and Mikio Suzuki, "Preliminary Flight Test Program on Telecom and Broadcasting Using High Altitude Platform Stations," *Wireless Personal Communications*, **24**, 2, 2003, pp. 341-61.

19. Matthias Pätzold, *Mobile Fading Channels*, New York, John Wiley & Sons, 2002.

20. S. R. Saunders and F. R. Bonar, "Prediction of Mobile Radio Wave Propagation Over Buildings of Irregular Heights and Spacings," *IEEE Transactions on Antennas and Propagation*, **AP-42**, 2, 1994, pp. 137-44.

21. S. R. Saunders and B. G. Evans, "A Physical-Statistical Model for Land Mobile Satellite Propagation in Built-Up Areas," 10th International Conference on Antennas and Propagation (IEE), 1997, pp. 44-47.

22. D. M. Le Vine and M. A. Karam, "Dependence of Attenuation in a Vegetation Canopy on Frequency and Plant Water Content," *IEEE Transactions on Geoscience Remote Sensing*, **34**, 1996, pp. 1090-96.

23. A. Czylwik, "OFDM and Related Methods for Broadband Mobile Radio Channels," Proceedings of International Zürich Seminar on Broadband Communications. Accessing, Transmission, Networking, Zürich, Switzerland, 1998, pp. 91-98.

24. E. Falletti, M. Laddomada, M. Mondin, and F. Sellone, "Integrated Services from High-Altitude Platforms: A Flexible Communication System," *IEEE Communications Magazine*, **44**, 2, 2006, pp. 85-94.

25. I. R. Palma-Lazgare, J. A. Delgado-Penin, and F. Perez-Fontan, "An Advance in Wireless Broadband Communications Based on a WiMAX-HAPS Architecture," 26th International Communications Satellite Systems Conference (ICSSC'2008), San Diego, CA, 2008.

26. I. R. Palma-Lazgare and J. A. Delgado-Penin, "Fixed Broadband Wireless Access Based on HAPS Using COFDM Schemes: Channel Modelling and Performance Evaluation," Australasian Telecommunication Networks and Applications Conference (ATNAC 2008), Adelaide, SA, Australia, pp. 62-66.

27. Erich Lutz, D. Cygan, M. Dippold, and W. Panke, "The Land Mobile Satellite Communication Channel –Recording, Statistics, and Channel Model," *IEEE Transactions on Vehicular Technology*, **40**, 2, 1991, pp. 375-93.

28. C. Loo and J. S. Butterworth, "Land Mobile Satellite Channel, Measurements and Modeling," *Proceedings of the IEE*, **86**, 7, 1998, pp. 1442-63.

29. P. A. Bello, "Characterization of Randomly Time-Variant Linear Channels," *IEEE Transactions on Communications Systems*, **11**, 4, 1993, pp. 360-93.

30. M. Iskandar and Shigeru Shimamoto, "On the Downlink Performance of Stratospheric Platform Mobile Communications Channel," The 49th Annual IEEE GLOBECOM, San Francisco, CA, 2006.

31. Fernando Pérez Fontán and P. Mariño Espiñeira, *Modeling the Wireless Propagation Channel, A Simulation Approach with Matlab®*, 2008.

ITU's Regulatory Framework, Technical Studies in ITU-R, and Future Activities in Relation to High-Altitude-Platform Stations (HAPS)

Ph. Aubineau
S. Buonomo
W. Frank
K.A. Hughes

Abstract

As early as in 1996, the ITU-R Study Groups and the Radiocommunication Bureau [1-3], as well as the Radio Regulations Board in 1997 and the World Radiocommunication Conference 1997 (WRC-97), started considerations of a newly emerging technology: high-altitude-platform stations (HAPS), or stratospheric stations, as they were mainly called in the early studies. This article presents an overview of the developments during the study periods in ITU-R and the phases between WRCs, including the WRC process. In particular, it presents the radio-regulatory aspects as they are reflected in the ITU Radio Regulations and in Conference Resolutions. The various ITU-R Recommendations developed during the last and current study periods dealing with HAPS are also summarized. Since developments on HAPS and associated frequency-sharing studies are still going on, an overview of the current situation in preparation for agenda item 1.20 of WRC-12 (consider the results of ITU-R studies and spectrum identification for gateway links for HAPS in the range 5850-7075 MHz in order to support operations in the fixed and mobile services, in accordance with Resolution 734 (Rev.WRC-07)) is also provided.

1. Introduction

In 1996, the ITU's Radiocommunication Bureau (BR) received a first request to consider the advance registration in the Master International Frequency Register (MIFR), and the publication of particulars of frequency assignments to stratospheric stations in the relevant publications of the Radiocommunication Bureau, in accordance with the provisions of the Radio Regulations (RR).

Stratospheric stations were considered as stations in the terrestrial radiocommunication services. As such, they should – according to the Radio Regulations – be brought into operation within three months of their publication. However, this caused a serious problem for an emerging technology. Pending discussion of the matter by the next World Radiocommunication Conference in 1997 (WRC-97) and in response to an urgent request by the Administration of the USA, the Radiocommunication Bureau developed a draft Rule of Procedure on the appropriate provisions of the Radio Regulations. This introduced interim measures, allowing recording and publication of stratospheric stations more than three months before their entry into operation. This draft Rule of Procedure was presented in 1997 to the Radio Regulations Board (RRB). The interim measures showed that the Radiocommunication Bureau and Radio Regulations Board were receptive to new technology. It also permitted the notification of the stratospheric stations by granting an extended period for notification prior to the bringing into service of the frequency assignments in question, subject to confirmation by the following WRC. In parallel, appropriate studies were initiated within relevant Study Groups of the Radiocommunication Sector (ITU-R), the results of which were also made available to WRC-97.

The new technology that was envisaged to provide fixed services to high-density regions operating in the 47.2-47.5 GHz and 47.9-48.2 GHz bands utilized stations located at fixed points in the stratosphere. Figure 1 shows an average wind profile in the upper atmosphere. Recommendation ITU-R F.1569 indicates that the wind speed has a local minimum around the altitude of 20-25 km. To keep the position of the airship at a nominal fixed point against the wind, adequate propulsion power is necessary, which also requires heavy batteries for night operation. From this standpoint, the operation of an airship at an altitude less than 25 km is feasible in the light of current technology.

Ph. Aubineau, S. Buonomo, W. Frank, and K. A. Hughes are with the Radiocommunication Bureau of the International Telecommunication Union, Geneva, Switzerland (http://www.itu.int); e-mail: Philippe.Aubineau@itu.int; Sergio.Buonomo@itu.int; Wolfgang.Frank@itu.int; kevin.hughes@itu.int

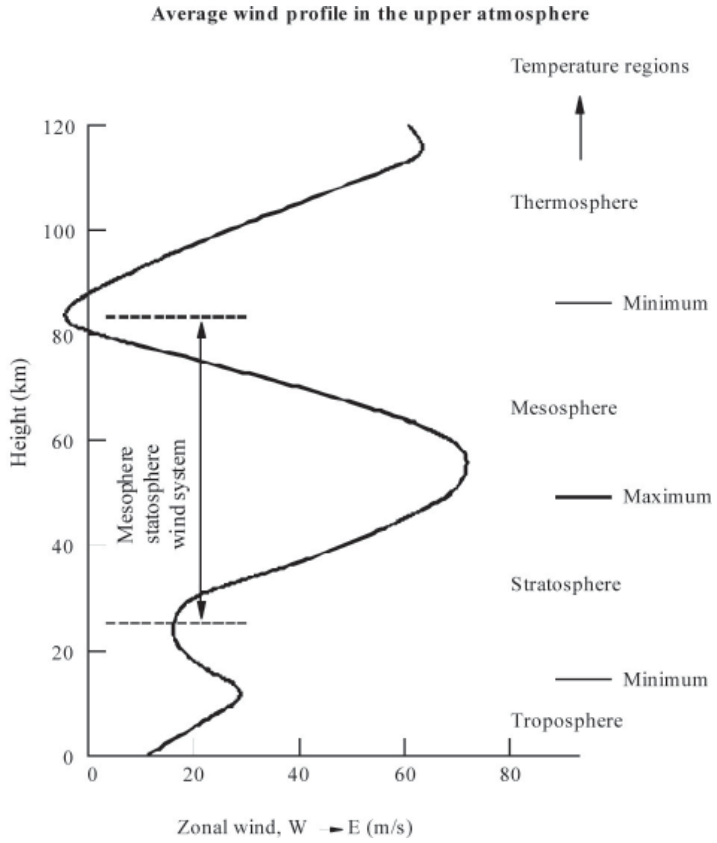

Figure 1. The general magnitude of zonal winds in the upper atmosphere, illustrated by a height profile for 45° N in January [4].

The use of such stratospheric stations located above major metropolitan regions would enable applications such as interactive video and Internet services. The 1997 World Radiocommunication Conference (WRC-97), through one of its agenda items, considered the identification of suitable frequency bands above 30 GHz for use by the fixed service for high-density applications. Fixed-service systems utilizing relays at fixed points in the stratosphere, operating in the 47.2-47.5 GHz and 47.9-48.2 GHz bands over metropolitan regions, were found to be a suitable candidate for providing high-density applications for the purpose of the relevant WRC agenda item. Figure 2 illustrates the concept of a communication system using HAPS with a minimum elevation angle of 20° or 40º.

2. Regulatory Issues Related to HAPS

In the early stages, from a regulatory perspective, it was concluded that stratospheric services are best defined as a high-density fixed service using stations located in the stratosphere (high-altitude-platform stations: HAPS). The service is high density because of the extraordinarily high number of communication circuits it can provide in a fairly small, urban area. The technology was considered a fixed service because most user terminals will be accessed through a fixed antenna. Another reason that HAPS has been considered a fixed service is because the platforms do not meet the definition of a space service (stations on an object beyond the major portion of the Earth's atmosphere), and consequently must be a terrestrial service.

In order for HAPS to be economically feasible on a global scale, stratospheric systems require an international designation to enable worldwide compatibility of components and systems, as well as investor confidence that is necessary for the rapid growth of such a service.

2.1 WRC-97

Based on contributions from the various regional groups. such as from the Americas, Europe, and the Asia-Pacific Region, as well as from individual administrations like Japan and Canada, WRC-97 considered under its agenda item 1.9.6 the introduction of HAPS applications in certain parts of the frequency spectrum. This resulted in an update of the international regulatory framework (Radio Regulations).

A *high-altitude-platform station* was defined as

> A station located on an object at an altitude of 20 to 50 km and at a specified, nominal, fixed point relative to the Earth.

The Conference resolved, *inter alia*, to urge administrations to facilitate coordination between high-altitude-platform stations in the fixed service operating in the bands 47.2-

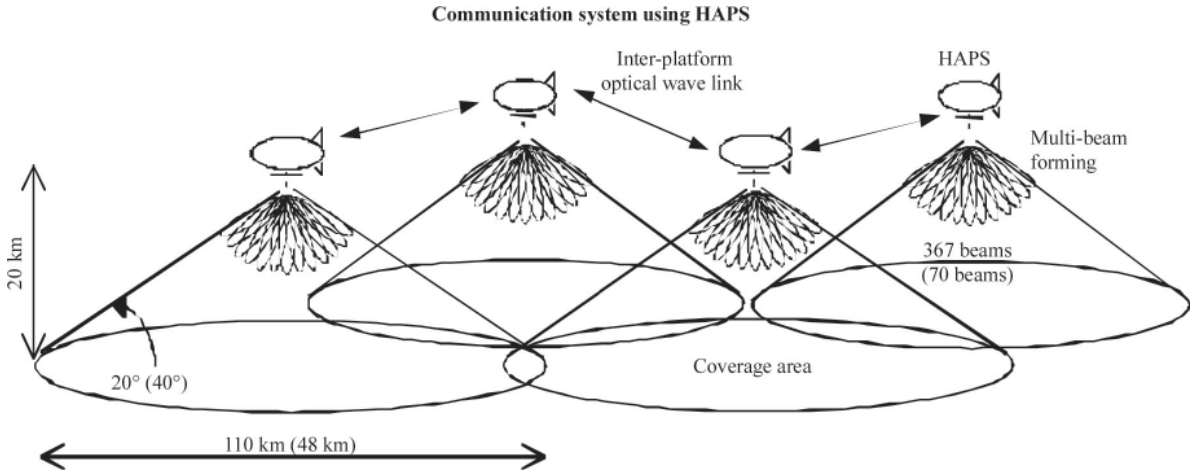

Figure 2. The concept of a communication system using HAPS.

47.5 GHz and 47.9-48.2 GHz and other co-primary services in their territory and adjacent territories. It also resolved that the existing coordination procedures, on a provisional basis, shall also be used for coordination between satellite systems and high-altitude-platform systems. It also decided that notices relating to assignments for high-altitude-platform stations in the fixed service in the bands 47.2-47.5 GHz and 47.9-48.2 GHz should reach the Bureau no earlier than five years before the assignments would be brought into use, and that transmissions to or from high-altitude-platform stations shall be limited to bands specifically identified in the Radio Regulations.

2.2 WRC-2000

One of the important topics considered at the World Radiocommunication Conference 2000 (WRC-2000) was the use of high-altitude-platform stations to provide International Mobile Telecommunications-2000 (IMT-2000) in the bands 1885-1980 MHz, 2010-2025 MHz, and 2110-2170 MHz in Regions 1 and 3, and 1885-1980 MHz and 2110-2160 MHz in Region 2. It should be noted that the use of these frequency bands by high-altitude-platform stations as base stations to provide IMT-2000 does not preclude the use of these bands by any station in the services to which they are allocated, and does not establish priority in the Radio Regulations.

In addition, for a number of countries, it was decided that the allocation to the fixed service in the band 27.5-28.35 GHz may also be used by HAPS. The use of this band by HAPS is limited to operation in the HAPS-to-ground direction, and shall not cause harmful interference to, nor claim protection from, other types of fixed-service systems or other co-primary services. Furthermore, the allocation to the fixed service in the band 31.0-31.3 GHz may also be used by HAPS in the ground-to-HAPS direction, subject to further restrictions.

2.3 WRC-03

The issue of HAPS, again being on the agenda of a WRC in 2003, was debated at length and resulted in a number of further updates to the regulatory provisions. Firstly, Resolution 734 ("Feasibility of Use of High-Altitude-Platform Stations in the Fixed and Mobile Services in the Frequency Bands Above 3 GHz Allocated Exclusively For Terrestrial Radiocommunication") and Resolution 221 ("Use of High-Altitude-Platform Stations Providing IMT-2000 in the Bands 1885-1980 MHz, 2010-2025 MHz, and 2110-2170 MHz in Regions 1 and 3 and 1885-1980 MHz and 2110-2160 MHz in Region 2") were revised. A new Resolution 145 on the "Potential Use of the Bands 27.5-28.35 GHz and 31-31.3 GHz by High-Altitude-Platform Stations (HAPS) in the Fixed Service" was agreed upon. Secondly, existing regulatory provisions dealing with HAPS were accordingly aligned.

2.4 WRC-07

The most-recent World Radiocommunication Conference in 2007 (WRC-07) significantly updated the radio-regulatory framework by refining current frequency-allocation provisions of the Radio Regulations (RR) and by updating the various Resolutions dealing with HAPS. It also defined a new part in Appendix 4 to the Radio Regulations describing a full set of "Characteristics for High-Altitude-Platform Stations (HAPS) Frequency Assignments in the Terrestrial Services." This data set in Appendix 4 to the Radio Regulations comprises elements listed in Table 1. From then on, the development of this internationally agreed upon data set enabled administrations to perform their coordination activities for new frequency assignments, and if they so wish, to notify them to the ITU for recording in the Master International Frequency Register (MIFR).

It is worthwhile mentioning that WRC-07 decided to maintain, under certain conditions, previously notified and

Table 1. Characteristics for high-altitude-platform station (HAPS) frequency assignments in the terrestrial services (extract from Table 2 of Annex 1 of Appendix 4 to the Radio Regulations)

.

Item identifier	Characteristics for high-altitude-platform stations (HAPS) frequency assignments
1.B	the symbol of the notifying administration
1.D	the provision code of the Radio Regulations under which the notice has been submitted
1.ID1	the unique identifier given by the administration to the station
	LOCATION OF THE STATION
1.4.a	the name by which the station is known
1.4.b	the code of the geographical area, above which the station is located
1.4.c	the nominal geographical coordinates of the station Latitude and longitude are provided in degrees, minutes and seconds
1.4.h	the nominal altitude of the station above mean sea level, in metres
1.4.t	Station location tolerances:
1.4.t.1.a	the planned latitudinal tolerance northerly limit, using d.m.s units
1.4.t.1.b	the planned latitudinal tolerance southerly limit, using d.m.s units
1.4.t.2.a	the planned longitudinal tolerance easterly limit, using d.m.s units
1.4.t.2.b	the planned longitudinal tolerance westerly limit, using d.m.s units
1.4.t.3	the planned altitudinal tolerance, in metres
	COMPLIANCE WITH TECHNICAL OR OPERATIONAL LIMITS
1.14.b	a commitment that the HAPS does not exceed an out-of-band pfd of –165 dB(W/(m^2 · 4 kHz)) at the Earth's surface in the bands 2160-2200 MHz in Region 2 and 2170-2200 MHz in Regions 1 and 3 (see Resolution 221 (Rev.WRC-07))
1.14.c	a commitment that the HAPS does not exceed the out-of-band pfd limits of –165 dB(W/(m^2 · MHz)) for angles of arrival (θ) less than 5° above the horizontal plane, –165 + 1.75 (θ – 5) dB(W/(m^2 · MHz)) for angles of arrival between 5° and 25° and –130 dB(W/(m^2 · MHz)) for angles of arrival between 25° and 90° (see Resolution 221 (Rev.WRC-07))
1.14.d	a commitment that the unwanted power density into the HAPS ground station antenna in the band 31.3-31.8 GHz shall not exceed –106 dB(W/MHz) under clear-sky conditions and –100 dB(W/MHz) under rainy conditions (see Resolution 145 (Rev.WRC-07)) Required in the band 31-31.3 GHz
1.14.e	a commitment that the maximum power density into an ubiquitous HAPS ground station antenna in the Urban Area Coverage (UAC) shall not exceed 6.4 dB(W/MHz) for elevation angles of ground station antenna greater than 30° and less than or equal to 90° (see Resolution 122 (Rev.WRC-07)) Required in the bands 47.2-47.5 GHz and 47.9-48.2 GHz
1.14.f	a commitment that the maximum power density into an ubiquitous HAPS ground station antenna in the Suburban Area Coverage (SAC) shall not exceed 22.57 dB(W/MHz) for elevation angles of ground station antenna greater than 15° and less than or equal to 30° (see Resolution 122 (Rev.WRC-07)) Required in the bands 47.2-47.5 GHz and 47.9-48.2 GHz
1.14.g	a commitment that the maximum power density into an ubiquitous HAPS ground station antenna in the Rural Area Coverage (RAC) shall not exceed 28 dB(W/MHz) for elevation angles of ground station antenna greater than 5° and less than or equal to 15° (see Resolution 122 (Rev.WRC-07)) Required in the bands 47.2-47.5 GHz and 47.9-48.2 GHz
1.14.h	a commitment that the separation distance between the nadir of the HAPS and a radio astronomy station operating in the band 48.94-49.04 GHz within the territory of another administration shall exceed 50 km (see Resolution 122 (Rev.WRC-07)) Required in the bands 47.2-47.5 GHz and 47.9-48.2 GHz
	COORDINATION AND AGREEMENT
1.11.a	the symbol of each administration with which coordination has been successfully effected, including where the agreement is to exceed the limits prescribed in the Radio Regulations Required if coordination is necessary and has been obtained pursuant to the relevant provisions of the Radio Regulations
	OPERATING ADMINISTRATION OR AGENCY
1.12.a	the symbol for the operating agency
1.12.b	the symbol for the address of the administration responsible for the station and to which communication should be sent on urgent matters regarding interference, quality of emissions and questions referring to the technical operation of the circuit (see Article 15)

	REMARKS
1.13.c	Remarks for assisting the Bureau in processing the notice
	IDENTIFICATION AND DIRECTION OF THE HAPS ANTENNA BEAM
2.1.a	the designation of the HAPS antenna beam
2.1.b	an indicator showing whether the antenna beam, under 2.1.a, is fixed or whether it is steerable and/or reconfigurable
2.1.c	an indicator showing whether the HAPS antenna tracks the service area
2.1.d	an indicator showing whether the antenna beam is individual or composite beam
	ANTENNA CHARACTERISTICS
2.9.g	the maximum co-polar isotropic gain
2.9.j	the measured radiation pattern of the antenna, the reference radiation pattern or the symbols in standard references to be used for coordination
2.9.gp	the co-polar antenna gain contours plotted on a map of the Earth's surface, preferably in a radial projection from the HAPS onto a plane perpendicular to the axis from the centre of the Earth to the HAPS The HAPS antenna gain contours shall be drawn as isolines of the isotropic gain, relative to the maximum antenna gain, when any of these contours is located either totally or partially outside the territory of the notifying administration
	The antenna gain contours shall include the effects of the planned longitudinal and latitudinal tolerance, planned altitudinal tolerance and the pointing accuracy of the antenna, taking into consideration the movement of the HAPS antenna boresight around the effective boresight area
	ASSIGNED FREQUENCY
3.1.a	the assigned frequency, as defined in No. 1.148
3.1.b	the reference frequency, as defined in Article 1 Required if the modulation envelope is asymmetric
	DATE OF OPERATION
3.2.c	the date (actual or foreseen, as appropriate) of bringing the frequency assignment (new or modified) into use
	LOCATION OF THE ASSOCIATED ANTENNA(S)
	For an area in which associated transmitting/receiving ground station(s) operate:
3.5.c.a	the geographical coordinates of a given zone A minimum of six geographical coordinates are required, in degrees, minutes and seconds NOTE – For the fixed service in the bands 47.2-47.5 GHz and 47.9-48.2 GHz the geographical coordinates are provided for each of the UAC, SAC and if applicable RAC (see the most recent version of Recommendation ITU-R F.1500) Required if neither a circular area (3.5.e and 3.5.f) nor a geographical area (3.5.d) are provided
3.5.d	the code of the geographical area (see the Preface) NOTE – For the fixed service in the bands 47.2-47.5 GHz and 47.9-48.2 GHz separate geographical areas are provided for each of the UAC, SAC and if applicable RAC (see the most recent version of Recommendation ITU-R F.1500) Required if neither a circular area (3.5.e and 3.5.f) nor the geographical coordinates of a given zone (3.5.c.a) are provided
3.5.e	the geographical coordinates of the centre of the circular area in which the associated ground station(s) are operating The latitude and longitude are provided in degrees, minutes and seconds NOTE – For the fixed service in the bands 47.2-47.5 GHz and 47.9-48.2 GHz different centres of the circular area may be provided for the UAC, SAC and if applicable RAC (see the most recent version of Recommendation ITU-R F.1500) Required if neither a geographical area (3.5.d) or geographical coordinates of a given zone (3.5.c.a) are provided
3.5.f	the radius, in km, of the circular area NOTE – For the fixed service in the bands 47.2-47.5 GHz and 47.9-48.2 GHz, a separate radius is provided for each of the UAC, SAC and if applicable RAC (see the most recent version of Recommendation ITU-R F.1500) Required if neither a geographical area (3.5.d) nor geographical coordinates of a given zone (3.5.c.a) are provided
	CLASS OF STATION AND NATURE OF SERVICE

3.6.a	the class of station, using the symbols from the Preface
3.6.b	the nature of service, using the symbols from the Preface
	CLASS OF EMISSION AND NECESSARY BANDWIDTH *(in accordance with Article 2 and Appendix 1)*
3.7.a	the class of emission
3.7.b	the necessary bandwidth
	POWER CHARACTERISTICS OF THE TRANSMISSION
3.8.	the symbol (X, Y or Z, as appropriate) describing the type of power (see Article 1) corresponding to the class of emission
3.8.aa	the power delivered to the antenna, in dBW, including the level of power control in 3.8.BA NOTE – For a receiving HAPS, the power delivered to the antenna refers to the associated transmitting ground station(s)
3.8AB	the maximum power density[1] averaged over the worst 1 MHz band delivered to the antenna
3.8.BA	the range of power control, in dB NOTE – For a receiving HAPS, the power control refers to its use by the associated transmitting ground station(s) In the case of a receiving HAPS, required in the bands 47.2-47.5 GHz and 47.9-48.2 GHz
	POLARIZATION AND RECEIVING SYSTEM NOISE TEMPERATURE
3.9.d	the code indicating the type of polarization (see the Preface)
3.9.j	the reference radiation pattern of the associated ground station(s) Required in the bands 47.2-47.5 GHz and 47.9-48.2 GHz
3.9.k	the lowest total receiving system noise temperature, in Kelvin, referred to the output of the receiving antenna
	HOURS OF OPERATION
3.10.b	the regular hours of operation (in hours and minutes from ... to ...) of the frequency assignment, in UTC

recorded frequency assignments to HAPS (140 assignments from eight administrations), contained in the Master International Frequency Register, although none of them had been brought into use. These conditions were specified in Resolution 122 (Rev.WRC-07) ("Use of the Bands 47.2-47.5 GHz and 47.9-48.2 GHz by High-Altitude-Platform Stations in the Fixed Service and by other Services"). This stipulated that the Radiocommunication Bureau shall maintain and process notices concerning HAPS that were received by the Bureau prior to October 20, 2007, and provisionally recorded in the Master International Frequency Register, only until January 1, 2012. Notifying administrations are invited to inform the Bureau before that date of the bringing into use of particular assignments, and to provide the complete set of data elements of Appendix 4**.** The Bureau shall then examine all assignments to HAPS in the fixed service notified prior to October 20, 2007, and apply the relevant provisions of Resolution 122 (Rev. WRC-07) and the respective calculation methodologies in Recommendations ITU-R F.1820 and ITU-R SF.1843. However, since WRC-07, the Bureau has not received any new submission of frequency assignments to HAPS.

A revision to Resolution 734 undertaken at WRC-07 now serves as a basis for the studies being currently carried out by in preparation for the forthcoming World Radiocommunication Conference (WRC-12), which will be held in Geneva from January 23 to February 17, 2012 (see http://www.itu.int/ITU-R/go/wrc-12), as described in Section 4.

3. Studies and Recommendations by ITU-R

ITU-R Study Group 5 (Terrestrial Services) and, in particular, its Working Party 5C (Fixed Wireless Systems; HF and Other Systems Below 30 MHz in the Fixed and Land Mobile Services) studies the characteristics of systems using HAPS. Working Party 5C also studies the interference between HAPS and other systems, in both the 47/48 GHz and 27/31 GHz frequency bands, in coordination with other Study Groups. Moreover, ITU-R Study Group 3 (Radiowave Propagation), already in 1999 approved a Recommendation dealing with propagation data and prediction methods required for the design of HAPS.

A list of current ITU-R Recommendations related to HAPS can be found in Table 2. In particular, further to the approval of Resolution 734 at WRC-2000 and in preparation for WRC-03 agenda item 1.13, preliminary studies on the interference evaluation from HAPS in the fixed service into radio-relay stations, which widely use the frequency range 3-18 GHz, have been conducted in former ITU-R Working Party 9B since 2001. The completion of these ITU-R studies after WRC-03 resulted in the approval of Recommendation ITU-R F.1764 which provides a "Methodology to evaluate interference from fixed service systems using high-altitude-platform stations to fixed wireless systems in the bands above 3 GHz."

New Recommendations that are in preparation and could be published before WRC-12 are described in Section 4.

4. Topics for Consideration by WRC-12

As a result of the consideration of a proposal from the Asia-Pacific Region, WRC-07 approved a new revision of Resolution 734 and decided to include item 1.20 on the WRC-12 Agenda, "to consider the results of ITU-R studies and spectrum identification for gateway links for high-altitude-platform stations (HAPS) in the range 5850-7075 MHz in order to support operations in the fixed and mobile services, in accordance with Resolution 734 (Rev.WRC-07)."

In taking these decisions, it was considered that systems based on new technologies using HAPS can potentially be used for various applications, such as the provision of high-capacity services to urban and rural areas. It was also considered that while provision has been made in the Radio Regulations for the deployment of HAPS in specific bands, including their use as base stations to serve IMT-2000 networks, it is desirable to have adequate provision for gateway links to serve HAPS operations (Figure 3).

To that aim, it was agreed that additional studies are needed to identify potential scenarios and conditions of sharing with other services using the above-mentioned frequency band, with the view to an appropriate spectrum allocation of two channels of 80 MHz each for gateway links for HAPS base stations in the range from 5850 to 7500 MHz, in bands already allocated to the fixed service, while ensuring the protection of existing services. These studies would be based on existing ITU-R studies of spectrum sharing between HAPS as a fixed service and other terrestrial and space services, as well as the regulatory considerations to avoid interference to services in neighboring countries. These additional ITU-R studies in preparation for WRC-12 agenda item 1.20 are carried out within ITU-R Working Party 5C.

As no formal definition for the term *HAPS gateway links* exists, for the purpose of clarity for the ongoing studies it is assumed that this term would have a similar meaning to the term *feeder link* in the context of satellite communications.

As of June 2009, a new Recommendation ITU-R F.[HAPS CHAR] is under development to describe the "Technical and operational characteristics of gateway links in the fixed service using high-altitude-platform stations to be used in sharing studies in the band 5850-7075 MHz," and in the assessment of sharing feasibilities with the systems of other services in that band and in adjacent bands. It is expected that this new Recommendation would also describe the use of multiple gateway stations providing multiple gateway links to multiple HAPS stations.

Another new Recommendation ITU-R F.[HAPS Modelling] is also under development, and in addition to the information already included in Recommendation ITU-R F.1764, it would describe the "Interference analysis modeling for sharing between HAPS gateway links in the range 5850-7075 MHz and other services." This Recommendation will provide general consideration for sharing studies between HAPS gateway links and conventional station types of fixed service systems and with other services (fixed-satellite service, NGSO mobile-satellite service feeder links, and passive microwave sensors), as well as interference modeling and analysis methodologies for the sharing studies. The sharing studies will cover both directions, thereby addressing the potential interference from existing services to and from HAPS, with the understanding that conventional systems in existing services are ensured appropriate protection.

References to the latest information regarding ongoing ITU-R studies on WRC-12 agenda item 1.20, as well as on other WRC-12 agenda items, are provided on the following ITU Web page: http://www.itu.int/ITU-R/go/rcpm-wrc-12-studies.

Based on these studies, Working Party 5C will develop draft method(s) to satisfy WRC-12 agenda item 1.20. This (these) draft method(s), accompanied by possible examples of draft changes to the Radio Regulations, will be considered

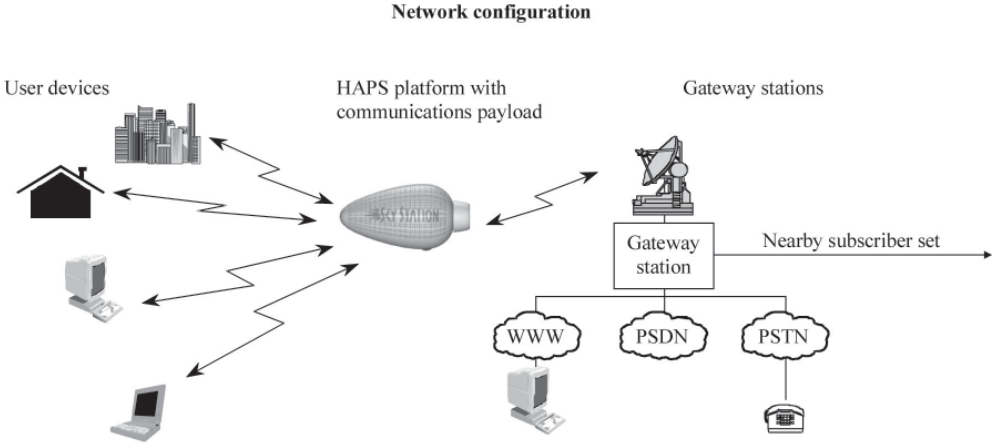

Figure 3. A HAPS network configuration.

Table 2. A list of current ITU-R Recommendations related to HAPS.

ITU-R Rec.	Title
M.1456	Minimum performance characteristics and operational conditions for high altitude platform stations providing IMT-2000 in the bands 1885-1980 MHz, 2010-2025 MHz and 2110-2170 MHz in Regions 1 and 3 and 1885-1980 MHz and 2110-2160 MHz in Region 2
SF.1481-1	Frequency sharing between systems in the fixed service using high-altitude platform stations and satellite systems in the geostationary orbit in the fixed-satellite service in the bands 47.2-47.5 and 47.9-48.2 GHz
F-1500	Preferred characteristics of systems in the fixed service using high altitude platforms operating in the bands 47.2-47.5 GHz and 47.9-48.2 GHz
F.1501	Coordination distance for systems in the fixed service (FS) involving high-altitude platform stations (HAPSs) sharing the frequency bands 47.2-47.5 GHz and 47.9-48.2 GHz with other systems in the fixed service
F.1569	Technical and operational characteristics for the fixed service using high altitude platform stations in the bands 27.5-28.35 GHz and 31-31.3 GHz
F.1570-1	Impact of uplink transmission in the fixed service using high altitude platform stations on the Earth exploration-satellite service (passive) in the 31.3-31.8 GHz band
SF.1601-2	Methodologies for interference evaluation from the downlink of the fixed service using high altitude platform stations to the uplink of the fixed-satellite service using the geostationary satellites within the band 27.5-28.35 GHz
F.1607	Interference mitigation techniques for use by high altitude platform stations (HAPS) in the 27.5-28.35 GHz and 31.0-31.3 GHz bands
F.1608	Frequency sharing between systems in the fixed service using high altitude platform stations and conventional systems in the fixed service in the bands 47.2-47.5 and 47.9-48.2 GHz
F.1609-1	Interference evaluation from fixed service systems using high altitude platform stations to conventional fixed service systems in the bands 27.5-28.35 and 31.0-31.3 GHz
F.1612	Interference evaluation of the fixed service using high altitude platform stations to protect the radio astronomy service from uplink transmission in HAPS systems in the 31.3-31.8 GHz band
M.1641-1	A methodology for co-channel interference evaluation to determine separation distance from a system using high-altitude platform stations to a cellular system to provide IMT-2000 service
F.1764	Methodology to evaluate interference from fixed service systems using high altitude platform stations (HAPS) to fixed wireless systems in the bands above 3 GHz
P.1409	Propagation data and prediction methods required for the design of systems using high altitude platform stations at about 47 GHz

by the ITU Member States and Sector Members during the second session of the Conference Preparatory Meeting for WRC-12 (CPM11-2), to be held in Geneva from February 14 to 25, 2011 (see http://www.itu.int/ITU-R/go/rcpm).

As a result of CPM11-2, the agreed possible method(s) and examples of changes to the Radio Regulations to satisfy WRC-12 agenda item 1.20 will be included in the CPM Report to WRC-12. Armed with this information, the ITU Member States will then finalize their individual and/or common proposals to WRC-12 on this and other agenda items.

5. Conclusion

High-altitude-platform stations (HAPS) represent a new technology having great potential for future broadband radio communications. The nature of the system dictates that it falls within the fixed service (FS) as defined by the ITU Radio Regulations. As for most radio-communication systems, it is required to conform to regulatory procedures and technical specifications that allow it to coexist with other services and systems using the radio spectrum.

This article traced the treatment of HAPS at past World Radiocommunication Conferences (WRC) of the ITU, with mention of the regulatory procedures subsequently adopted. Such procedures are underpinned by technical studies that have led to, or are leading to, the development of ITU-R Recommendations within the ITU-R Study Groups. Finally, the current status of studies on HAPS relating to Agenda Item 1.20 of WRC-12 has been addressed, with indications as to the expected outcome.

6. References

1. ITU Radiocommunication Bureau, Study Group Department: http://www.itu.int/ITU-R/index.asp?category=study-groups&link=rsg&lang=en
2. ITU-R Conferences and Meetings: http://www.itu.int/ITU-R/index.asp?category=conferences&rlink=rconf&lang=en
3. ITU Publications: http://www.itu.int/publications/sector.aspx?sector=1&lang=en
4. Committee on Space Research (COSPAR) International Reference Atmosphere, Berlin, Akademie-Verlag, 1972.

EISCAT_3D: A Next-Generation European Radar System for Upper-Atmosphere and Geospace Research

U.G. Wannberg et al.

Abstract

The EISCAT Scientific Association, together with a number of collaborating institutions, has recently completed a feasibility and design study for an enhanced performance research radar facility to replace the existing EISCAT UHF and VHF systems. This study was supported by EU Sixth-Framework funding. The new radar retains the powerful multi-static geometry of the EISCAT UHF, but will employ phased arrays, direct-sampling receivers, and digital beamforming and beam steering. Design goals include, inter alia, a tenfold improvement in temporal and spatial resolution, an extension of the instantaneous measurement of full-vector ionospheric drift velocities from a single point to the entire altitude range of the radar, and an imaging capability to resolve small-scale structures. Prototype receivers and beamformers are currently being tested on a 48-element, 224 MHz array (the "Demonstrator") erected at the Kiruna EISCAT site, using the EISCAT VHF transmitter as an illuminator.

1. Introduction

The radar systems of the European Incoherent Scatter Association (EISCAT) have provided the scientific community with outstanding high-latitude data for more than 25 years. Observations made during this time have contributed to the opening of several new fields of research, e.g., the study of transient coherent echoes from the ionosphere, polar mesospheric summer echoes (PMSE), extremely narrow natural layers of ionization in the E region, and observations of micro-meteors interacting with the atmosphere. Many of these phenomena are spatially compact and of very short duration (tens of milliseconds or less), while others tend to occur under conditions of low electron density and/or very high electron-to-ion temperature ratio. Radar returns from these processes also frequently show a significant degree of coherence.

The present EISCAT UHF and VHF systems, having been designed for incoherent-scatter conditions, are not really optimized for addressing these scientific challenges. In addition, the frequency band currently used by the multi-static UHF radar will soon be claimed by the UMTS900 third-generation mobile phone service in all the three EISCAT host countries, forcing the gradual closing down of the UHF system over a three-year period. There is thus a strong case for a new research radar system in the auroral zone.

In 2005, the EISCAT Association, Luleå University of Technology, Tromsø University, and the Rutherford

Correspondence should be directed to U. G. Wannberg via e-mail: ugw@irf.se. U. G. Wannberg, L. Eliasson, J. Johansson, and I. Wolf are with the Swedish Institute of Space Physics, Box 812, SE-981 28 Kiruna, Sweden. H. Andersson, P. Bergqvist, I. Häggström, T. Iinatti, T. Laakso, R. Larsen, J. Markkanen, I. Marttala, M. Postila, E. Turunen, A. van Eyken, L.-G. Vanhainen, and A. Westman are with the EISCAT Scientific Association, Box 812, SE-981 28 Kiruna, Sweden. R. Behlke, V. Belyey, T. Grydeland, B. Gustavsson, and C. La Hoz are with the Auroral Observatory, University of Tromsø, N-9037, Tromsø, Norway. J. Borg, J. Delsing, J. Johansson, M. Larsmark, T. Lindgren, and M. Lundberg are with EISLAB, Luleå University of Technology, SE-971 87, Luleå, Sweden. I. Finch, R. A. Harrison, and D. McKay are with the Space Science and Technology Department, Rutherford Appleton Laboratory, Chilton, Oxfordshire OX11 0QX, UK. W. Puccio is with the Swedish Institute of Space Physics, Box 537, SE-751 21 Uppsala, Sweden. T. Renkwitz is with the Institut für Atmosphärenphysik, D-18225, Kuhlungsborn, Germany. T. Grydeland is now at Discover Petroleum, Roald Amundsens Plass 1B, 9008 Tromsø, Norway. B. Gustavsson is now at the Department of Communication Systems, University of Lancaster, Lancaster LA1 4YR, UK. M. Postila is now at Sodankylä Geophysical Observatory, Tähteläntie 62, FIN-99600 Sodankylä, Finland. A. van Eyken is now at SRI International, 333 Ravenswood Avenue, Menlo Park, CA 94025, USA.

This is one of the invited *Reviews of Radio Science* from Commission G

Appleton Laboratory (joined in 2008 by the Swedish Institute of Space Physics) therefore embarked on a four-year design and feasibility study for a new research radar facility with greatly enhanced performance. This was supported by European Union funding under the Sixth Framework Initiative. This facility would be capable of providing high-quality ionospheric and atmospheric parameters on an essentially continuous basis, as well as near-instantaneous response capabilities for users needing data to study unusual and unpredicted disturbances and phenomena in the high-latitude ionosphere and atmosphere. The study period ended on April 30, 2009. The present paper is a condensed summary of the results and recommendations from the study. A comprehensive report [1] was submitted to the EU FP6 Project Office on June 14, 2009.

2. EISCAT_3D Performance Targets

Design targets for the new EISCAT_3D system [1] include:

- A tenfold improvement in temporal and spatial resolution relative to the current EISCAT systems. It will be possible to measure electron densities to better than 10% accuracy over the 100 to 300 km range in one second or less, even at 100 m altitude resolution.
- An extension of the instantaneous measurement of full-vector ionospheric drift velocities from a single point to the entire altitude range of the radar. It is planned to have at least five beamformers running concurrently at the receive-only sites.
- Beam-pointing resolution of better than 0.625° in two orthogonal planes, with 10% (0.06°) pointing accuracy.
- Built-in imaging capabilities, offering a horizontal resolution of better than 20 m at 100 km altitude.

The transmitter system will be designed to provide better than 100 m line-of-sight resolution along the transmitted beam. The antenna arrays at the receiving sites will be designed to provide better than 150 m horizontal −3 dB resolution at 100 km altitude everywhere in the multi-static field of view.

3. System Configuration

The EISCAT_3D system will retain and expand on the unique and powerful multi-static configuration of the mainland EISCAT UHF system. A central transmitting/receiving site (the "core"), located not far from the present EISCAT Tromsø radar site at Ramfjordmoen, Norway, will be augmented by at least two receiver facilities. These will be located at ground distances of ~220-280 km roughly

Figure 1. A map of the deployment area of the projected EISCAT_3D radar system, showing the locations of the antenna sites. The dashed circle indicates the approximate extent of the common field of view at 300 km altitude.

System	Frequency (MHz)	Power (MW)	Quoted Gain (dBi)	Aperture (m^2)	Duty Cycle (%)	System Noise Temperature (K)	PA (GWm^2)	FOM
EISCAT VHF (1 klystron	224	1.5		3110	12.5	300	4.67	1.00
EISCAT VHF (2 klystrons)	224	3		3110	12.5	300	9.33	2.00
EISCAT UHF	930	2	48	522	12.5	120	1.04	0.13
EISCAT Svalbard	500	1	45	905	25	65	0.90	0.57
Sondrestrom	1290	3.5	49	341	3	85	1.19	0.08
PFISR	449	2	43	708	10	120	1.42	0.34
EISCAT_3D Core	233	9		10000	20	190	90.00	37.04
Jicamarca	50	4.5		75000.0	6	3000	337.50	22.46
Arecibo	430	2.5		55000.0	6	90	137.50	35.46

Table 1. The parameters of some current incoherent-scatter radar systems and the planned EISCAT_3D core site. The figure-of-merit (FOM) is defined as $FOM = \frac{PA\sqrt{D}}{T_{sys} f}$, *where* PA *is the power-aperture product,* D *is the transmitter duty cycle,* T_{sys} *is the system noise temperature, and* f *is the radar frequency. For comparison purposes, all FOMs were normalized to that of the two-klystron EISCAT VHF. The FOM of the EISCAT_3D core is seen to fall in the same range as those of the Arecibo and Jicamarca systems.*

south and east of the core site, respectively (see Figure 1). Each receiving site will be equipped with a phased-array antenna and its associated receivers. These will be followed by a beamformer system capable of generating several simultaneous, independently steerable receiving beams that can intersect the beam from the central core at arbitrary altitudes between 200 and 800 km. Two additional receiving facilities, located at ground distances of ~90-120 km from the core on the same north-south and east-west baselines, will deliver three-dimensional data from the 70-250 km altitude range. This will thus provide truly simultaneous three-dimensional measurements over the entire vertical extent of the ionosphere for the first time in the history of incoherent-scatter diagnostics. In addition, the transmitting/receiving site will also provide monostatic coverage into the ionospheric topside to beyond 2000 km altitude, where three-dimensional coverage is not required.

For optimum performance in low-electron-density conditions, i.e., primarily at mesospheric and ionosphere topside altitudes, the EISCAT_3D system will use an operating frequency in the high VHF range. However, obtaining a coordinated allocation for a scientific radar system in this part of the spectrum has turned out to be a very nontrivial problem. In the ITU Radio Regulations, the entire 174-230 MHz frequency range is allocated to the Broadcasting Service on a primary basis and to various communication services on a secondary basis. The 230-240 MHz range is allocated to the fixed and mobile services on a primary basis. In Europe, a slightly different scheme (the so-called Wiesbaden Agreement, WI95), based on proposals from CEPT and its subsidiary, the European Telecommunications Standards Institute (ETSI), has been adopted. Under WI95, the entire 174-240 MHz range is allocated to broadcasting. Frequencies above 235 MHz are shared with the military.

Following the transition from analog to digital terrestrial TV broadcasting in Europe, the 174-240 MHz range is now gradually being taken into use for digital audio broadcasting (T-DAB). The WI95 plan allocates one or more frequency blocks for T-DAB to each European country. However, the actual implementation of the spectrum at the national level is delegated to the respective frequency administrations. This is fortunate, as the administrations are in fact free to also allocate spectrum to services other than those having a recognized status in a specific band, as long as this causes no interference to the primary service(s). In early 2008, the EISCAT_3D design study team therefore approached all three Nordic frequency administrations with a request to have 10 MHz of contiguous, coordinated bandwidth in the 225-240 MHz range allocated to the project. The Norwegian administration eventually responded by offering to allocate T-DAB blocks 13A-13D (229.928-236.632 MHz) for active use by the future EISCAT_3D core site on a noninterference basis, these blocks being unallocated in northern Norway. This offer was gratefully accepted by the EISCAT Scientific Association on December 17, 2008.

The spectrum slot proposed by the Norwegian administration also turned out to be essentially unallocated in northern Sweden and northern Finland. Negotiations are currently in progress with the respective administrations, with the aim to obtain Nordic-wide protection of at least 230.0-236.5 MHz for reception.

The fully populated core array will contain about 16000 elements, each equipped with a dual (300 + 300) watt solid-state power amplifier, a short X-Yagi antenna, and a direct-sampling receiver. With an effective aperture of the order of 10000 m^2, this array will deliver a main-beam half-power beamwidth of $\approx 0.75°$, i.e., comparable to that of the EISCAT UHF; a power-aperture product exceeding 90 GW m^2, i.e., about an order of magnitude greater than that of the EISCAT VHF operating in single-beam, dual-klystron mode; and an overall figure of merit of the same order as that of the Arecibo and Jicamarca ISR systems (see Table 1). The power-amplifier system will be designed for an instantaneous −1 dB power bandwidth of more than 5 MHz, corresponding to about 60 m range resolution. Pulse lengths from 0.2 to 2000 μs, and PRFs between essentially zero

and 3000 Hz, can be accommodated. A reduced-power CW mode, mainly intended for active space-plasma experiments, is also being considered. The drive signals will be generated by digital arbitrary-waveform RF generators, receiving their baseband data containing both the radar waveform information, any desired aperture-tapering, and the time-delay information required to steer the transmitted beam into the desired direction, from large RAM banks. This will allow a fully flexible choice of transmission, limited only by power bandwidth and permissible pulse length.

It will be possible to steer the beam generated by the core array out to a zenith angle approaching 40° in all azimuth directions. At 300 km altitude, the radius of the resulting field of view is approximately 200 km, corresponding to a latitudinal coverage of ±1.80° relative to the transmitter site.

In the receiving mode, the core array will be configured as approximately 50 19-m diameter modules of 343-element antennas. Each module will be made up from 7 × 7 close-packed hexagonal seven-element cells (Figure 2), and equipped with a fully capable digital beamformer. To form a single beam, the digital data streams from all modules will simply be added. In imaging mode, any two modules can be selected to form the endpoints of a baseline. Depending on the module and array layout, between 20 and 40 unique baselines can be formed, covering the 10λ to 60λ length interval (see Section 4). Since the ultimate transverse resolution requirement (150 m at 100 km altitude) demands even longer baselines, at least six small outlier receive-only arrays, spaced up to 750λ away from the center of the core array, will also be installed.

Considering the size, complexity, and cost of the proposed EISCAT_3D system, it is not unlikely that the construction will have to proceed in phases, similar to the construction of the EISCAT Svalbard Radar in the 1990s. In this case, the core array would initially be populated with about 5000 elements, sufficient to deliver a power-aperture product equal to that of the existing EISCAT VHF radar, while offering greatly increased performance in almost all other respects. A basic set of imaging outlier arrays (at least three) would also be installed right from the start. Such a system could profitably take over most of the tasks of the VHF immediately upon commissioning. The core could then be expanded up to the target size of »16000 elements as resources become available. Provisions for this expansion (e.g., civil works, access points for power and data, etc.) will be designed-in from the beginning.

The arrays at the receive-only sites will provide fields of view matching that of the central core as seen from the respective site. It has been determined that this can be most economically achieved through the use of multi-element X-Yagi antennas with about 10 dBi gain, allowing up to one-wavelength element-to-element spacing without running into severe grating-lobe problems. All receivers will employ bandpass sampling [2]. The received signal is bandlimited by a 30 MHz-wide bandpass filter centered on »233 MHz

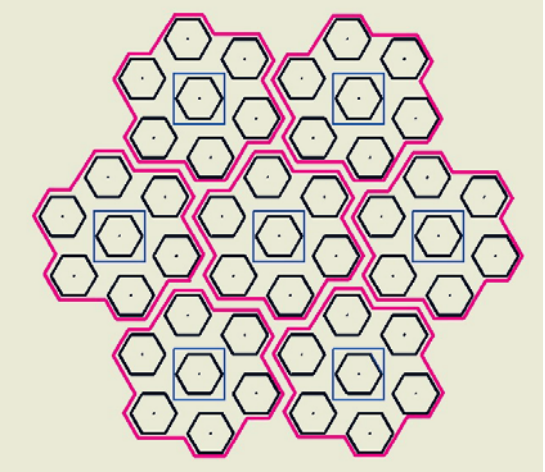

Figure 2. A top view of a EISCAT_3D core array 343-element, 19-m diameter array module, formed from seven sub-groups (outlined in red), each of which is composed of seven seven-element hexagonal cells. Each sub-group is served by a common, approximately 2-m by 2-m equipment container (indicated by a blue square at the center of each sub-group) containing all RF, signal-processing, and control and monitoring electronics.

and sampled at an »85 MHz sampling rate, without any preceding down-conversion. This scheme centers the signal spectrum in the sixth Nyqvist zone while providing a 6 MHz transition band at either end. The signals from the two orthogonal linear polarizations will be processed independently, all the way from the antennas to the output of the digital beamformers (see Section 9).

4. Imaging Capabilities

Numerous dynamic phenomena at high latitudes are characterized by small-scale structures produced by non-thermal processes (such as plasma instability) not resolved by conventional radar techniques. The imaging capability of the EISCAT_3D will enable the measurement of these structures, in most cases fully resolved. Some examples of non-thermal small-scale structure include polar mesospheric summer and winter echoes (PMSE and PMWE), atmospheric turbulence in the upper troposphere and lower stratosphere, numerous small-scale structures induced by artificial RF heating of the ionosphere, naturally enhanced ion-acoustic lines (NEIALs), space debris, meteors, and possibly others. A special case is provided by the small-electron-density structures produced by auroral precipitation [3], where filaments with scales of tens of metres have been resolved by optical means. The signals arising from these structures (in the absence of naturally enhanced ion-acoustic lines) are produced by conventional incoherent scattering, that is, by the thermal fluctuations of electron density at a scale equal to half the radar wavelength (Bragg scattering). The possibility of radar imaging such features is helped by the fact that the electron density can be strongly enhanced inside the bright structures of aurora.

The built-in imaging capabilities of the EISCAT_3D system – complemented with multiple beams and rapid beam scanning – will make the new radar truly three-dimensional and justify its name. A work package of the design study was therefore dedicated to establishing the basic conditions under which these imaging capabilities could be implemented.

The fully populated core array will be subdivided into »47 modules of 343 (7 x 49) antenna elements. Each module can be used as the endpoint of one or several baselines. To comply with the resolution requirements, some six to 10 outlying receive-only 343-element modules will be deployed along three log-spiral baselines, extending out to about 2000 m from the core center. The result is an optimum and flexible antenna layout, from which favorable configurations can be quickly implemented to obtain the resolution and bandwidth of the required image. A simple calculation shows that the figure-of-merit of a single imaging module paired with the full core is approximately equal to 0.8 times that of the present EISCAT VHF radar with one klystron. It is much better than the EISCAT UHF and Svalbard radars, and the PFISR radar (see Table 1). It will thus be possible to image radar auroral structures, although time variability may limit the sharpness of the obtained images. Even the modules of a reduced core of 5000 elements might be able to perform imaging, especially under strong aurora, as the module's figure of merit in this case is about 0.05, not much less than the Sondrestrom radar, which has a figure of merit of 0.08.

The accuracy of the timing system has been specified to fulfill the desired image resolution (see Section 7). A novel way to calibrate the imaging system has been proposed, using the phases obtained from measurements of the usual incoherent-scattering signals. An inversion algorithm based on the Maximum Entropy Method (MEM) has been implemented and tested on simulated and real data obtained with the imaging-capable radar at Jicamarca. Methods to visually represent a function of five independent variables – with various degrees of completeness and compression – have also been investigated and tested with simulated and real-world data.

The technology employed is aperture-synthesis imaging radar (ASIR). This is closer to the technology used by radio astronomers to image stellar objects than to the SAR (synthetic-aperture radar) technique used to map the Earth's surface. In the radio-astronomy case, the source emits radiation collected by a number of passive antennas. In the radar case, the transmitter illuminates the ionosphere or atmosphere, and a number of antennas collect the scattered radiation. From this point on, the two cases are essentially identical (although the Earth's motion is an important difference).

The image of the target is constructed by calculating the spatial autocorrelation of the diffraction pattern on the plane of measurement, called the visibility function. This is accomplished using a number of receivers, from which all the different signal-pair cross-correlations are calculated. These values represent samples of the visibility function. The spatial dimensions of the visibility are defined by the baselines between each pair of receivers. The imaging inversion problem consists of obtaining the image from the visibility, which is a two-dimensional Fourier transform. However, in virtually all cases, the visibility samples are uneven, truncated, and sparse, leading to a highly singular inversion problem requiring carefully crafted algorithms.

The image obtained from the inversion is called the brightness distribution, and (for each range) represents the angular distribution of the target intensity. In the radar application, it is advantageous to decompose the receiver signals into their frequency components and separately apply the imaging inversion to each spectral component. Since the mathematical relationship between the visibility and the image is a simple (two-dimensional) Fourier transform, the accumulated knowledge of Fourier transforms in other domains can be applied to imaging. For instance, the resolution of the image is determined by the longest baseline, the largest structures are determined by the shortest baseline, resolution and bandwidth are related by the Nyqvist theorem, and so on.

It is a nontrivial task to express the image as a function of five variables (three spatial dimensions, frequency, and time). The time variable can be taken care of by displaying images in the form of an animation or movie. There still remain four independent variables, of which only two can be represented by conventional plotting techniques. The other two can be codified using two of the three color-space variables, of which the hue, saturation and value (or brightness) or HSV space seems to perform more satisfactorily.

The required instantaneous timing accuracy is about 100 ps at 250 MHz, equivalent to an error of 10° in phase, or 1/40th of a (fringe) period. When accounting for beamforming, which is a weighted average operation, the accuracy can be reduced in proportion to the square root of the average length. For instance, the allowed time jitter for a 343-element module after beamforming is reduced by a factor equal to $\sqrt{343} \approx 20$, to 2 ns.

The image bandwidth and resolution follow from Nyqvist's theorem. For an assumed module length of 16λ, the angular coverage is 1/16 radians or 3.16°, which maps into a horizontal extent of 6 km at 100 km range. Assuming a target resolution of 20 m at 100 km range, subtending an angle of 2×10^{-4} radians, results in a longest baseline length of 5000λ or 6000 m for a radar frequency of 250 MHz. Appealing to superresolution concepts, this baseline can be reduced to 750λ or 900 m. Some additional outlier antennas are thus needed to obtain this resolution.

The incoherent-scatter capability of the radar affords a novel and convenient phase-calibration procedure. Under

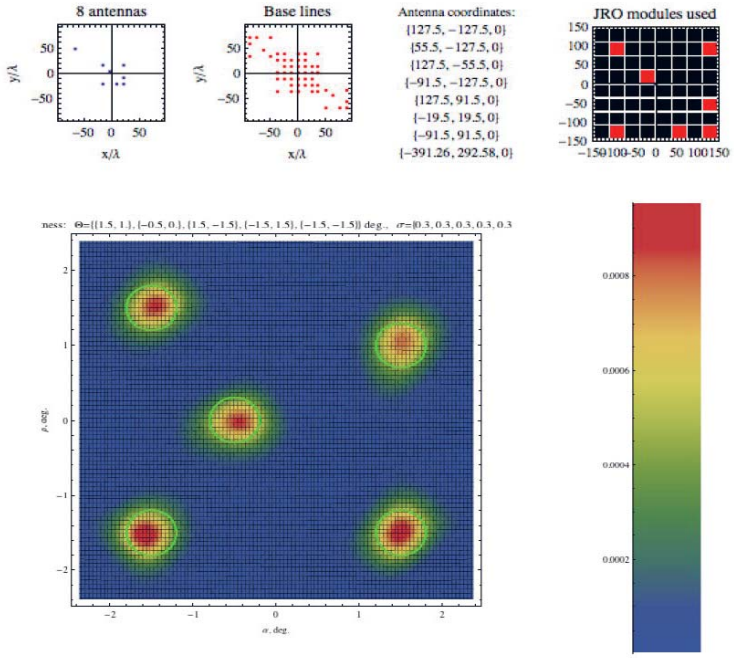

Figure 3. A five-blob image reconstructed from the visibility measured with the eight-antenna configuration with seven core antennas of the Jicamarca array and one outlier, shown in the upper-left panel. The second upper-left panel shows the baselines generated by the configuration. The rightmost upper panel shows the core antennas used in the configuration in red, and their coordinates alongside. It is a remarkably optimum configuration that produces an excellent reconstruction.

quiet conditions, the illuminated volume is homogeneous, which implies that the brightness is constant with a visibility function that is purely real, that is, the visibility phase is constant and is equal to zero. Measurement of the visibility function in a quiescent ionosphere thus directly produces the calibration phases.

The number of visibility function samples that can be measured is equal to the number of different receiving antenna pairs, or $n(n-2)/2$, where n is the number of receivers. A good configuration of receiving antennas is one in which the baseline space is maximally and evenly filled, although in practice, gaps will occur. Heuristic search procedures have been devised and used to produce simulations of the adopted image-restoration algorithm, such as that given in Figure 3.

Among the many image-inversion/restoration algorithms employed by the radio astronomy community, two stand out: namely, the CLEAN procedure and the Maximum Entropy Method (MEM) [4]. The CLEAN procedure assumes that the image is composed of a small number of point sources, often the case in astrophysical situations but not generally in radar applications. MEM has a more mature mathematical foundation and is effective and robust, as shown by its implementation at Jicamarca [5]. The numerical problem is to find an extremum of the following function:

$$E\left[f\left(e_j,\lambda_j,\Lambda,L\right)\right]=S+\lambda_j\left(g_j+e_j-f_i h_{ij}\right)$$

$$+\Lambda\left(e_j^2\sigma_j^{-2}-\Sigma\right)+L\left(I_i f_i-F\right), \qquad (1)$$

where f is the sought-after brightness distribution, $S=-f_i\ln\left(f_i/F\right)$ is the entropy, I_i is a vector of ones, $F=I_i f_i$ is the integrated (total) brightness, g_j is the measured visibility, h_{ij} is the point-spread function containing the Fourier kernel, e_j are the random errors, σ_j^2 are the (theoretical) expected error variances, and Σ parameterizes the error norm, effectively constraining it. The remaining quantities are Lagrange multipliers: the λ_j relate the measured visibility (including the random errors) to the brightness that makes the entropy function an extremum. The other Lagrange multipliers impose additional constraints to ensure an improvement of the final solution Λ puts a bound on the error norm equal to a preset value equal to S. L constrains the total brightness, ensuring that the solution will be nonnegative.

An implementation of the algorithm has been tested on simulated data and on data taken with the Jicamarca Radar. An interesting configuration of seven core modules and one outlier was found that produces an even distribution of baseline coordinates with a minimum of gaps. Figure 3 shows the configuration, and the results of inverting the visibility produced by five Gaussian blobs. The $1-\sigma$ contours of the assumed Gaussian blobs are represented by the thick circular rings in green.

5. Faraday Rotation and Adaptive Polarization Matching

Primarily for technical convenience, the transmitting/receiving core will employ circular LHC/RHC polarization. Signals scattered from the ionosphere above the core site toward the receiving sites will therefore be elliptically polarized and subject to Faraday rotation.

At 240 MHz, the total rotation from a scattering point at 300 km altitude above Tromsø, Norway, to a receiver at Kiruna can be anywhere in the range $\pi/2$ to $3\pi/2$ radians, assuming typical ionospheric conditions. Since the propagation path from the scattering region is partially outside the core site's field of view, and therefore through an unknown and time-varying amount of plasma, the total Faraday rotation along the path cannot be predicted a priori with any degree of confidence. Instead, the receiver system must continually track the polarization of the received signal.

The noise-corrupted signals received on the two orthogonal sets of element antennas are first beam-formed. To generate a single data stream with maximum signal-to-noise (SNR) ratio (important because the signal-to-noise ratio at the receiver site will often be very low), the two beam-formed data streams should then be recombined in such a way as to cause the signal components to be added in-phase in proportion to their respective amplitudes.

Faraday rotation leaves the shape of the polarization ellipse unchanged, to first order. Therefore, its spatial orientation at the receiver site, and consequently the optimum way to recombine the two noisy component signals, can be estimated from their average amplitude ratio and relative phase angle as received. A more powerful tool to track the polarization state of the backscattered signal can be obtained by observing that the polarization vector constitutes the principal eigenvector of the measurement covariance matrix [6]. Using this observation, low-complex strategies to tune to the unknown polarization can be found within the rich literature on subspace tracking [7-9]. In principle, such procedures will locate that subspace in complex two-dimensional space which inherits most energy. In order for such an approach to function properly, especially at low signal-to-noise ratios, the noise components must be independent and identically distributed to high accuracy. Since this is unlikely to be the case in the target system – e.g., due to mutual coupling between elements and unequal gains and noise temperatures of the two signal channels – the data should be pre-whitened, using noise-only data collected when the target is not illuminated [10].

A study of how to extend the above strategy using a Bayesian approach is currently underway. In such a scheme, prior knowledge regarding the Faraday rotation can be incorporated. This could be useful, especially in extremely difficult (e.g., low-SNR) scenarios. In a later phase, the study will also be expanded to include a feed-forward element, using available observational data on the electron density along the propagation path as a function of time of year, time of day, phase of the solar cycle and solar activity, etc., to improve the a priori knowledge. Since the total Faraday rotation is proportional to the number of plasma electrons along the propagation path, everything else being equal, the latter quantity (previously unobservable) will become continually available as a byproduct of the polarization tracking.

6. Fractional Sample Delay Beam-Steering

The beam-pointing resolution requirement of 0.06° puts unusually demanding requirements on the beam-steering system and the beamformers. The combination of large aperture size, large steering angle, and short pulse length creates a situation where true time-delay steering – i.e., steering by delaying the signal from each element in time before summation – is the only viable alternative. A drawback of this technique is that the maximum delay length is determined by the physical size of the array, rather than by the operating frequency. Implementing the beam steering in analog technology would have required the length of the longest delay lines to be of the same order as the array size, but the construction of thousands of analog delay lines with electrical lengths of 100 m or more is clearly impractical. Instead, post-ADC beam-forming, using digital fractional-sample delay techniques, has been selected. As far as we have been able to determine, this is the first time that this technique is being proposed for use in a large research radar system, although it has earlier been used, e.g., in sonar [11].

To achieve the required pointing resolution, the minimum delay increment must be shorter than 15 ps. For a 100-by-100-element array with an inter-element distance of 1.68 m, the total delay can be as long as 550 ns, i.e., about 50 sampling intervals. Any delay value in this range can be realized by first delaying the sample stream by a number of samples equal to the integer part of (delay/sampling interval) and then handling the remainder in a fractional delay filter, an all-pass FIR filter designed to have exactly the required group delay [12, 13].

FIR filters are easy to design, characterize, and implement in hardware. FPGAs are available today with 18-bit hardware multipliers, giving a natural limit of 18-bit resolution for the filter coefficients. Several different design approaches have been used to synthesize almost perfectly phase-linear FIR filters. Extensive MATLAB simulations have been performed to verify the validity of the approach [13]. 36-tap filters have been shown to provide the required delay accuracy over the 30 MHz baseband, while introducing very little amplitude ripple. The filters add a timing error to each antenna with a maximum error of ~5 ps and 0.8% of amplitude error. Multiple simultaneous beams can be generated from the same set of input data streams merely by feeding these into multiple sets of digital delay lines in parallel.

During the winter season, snow, ice, and hoarfrost will accumulate on the element antennas and change their group-delay characteristics: see Figure 4. Adaptive calibration and correction software will be installed at each receiving array to counteract the resulting unpredictable and potentially large pointing and beam-forming errors. Under normal operating conditions, one of the available beams will be dedicated to tracking one or more of the strongest

Figure 4. The 48-element Demonstrator array at the Kiruna EISCAT site in typical winter conditions, November 2007.

circumpolar celestial calibrator sources (e.g., Cas-A and Cyg-A) whenever these are in the array's field of view. Pointing corrections will be continually computed from the measured data and fed back into the beamformer control system. When no calibrator source is visible, feed-forward corrections using a priori information will be employed.

7. Timing System

The performance of the EISCAT_3D radar timing system is critical to achieving the stated beam-pointing resolution and accuracy. Since a delay-and-sum type of beamformer is used, the shape and direction of the formed

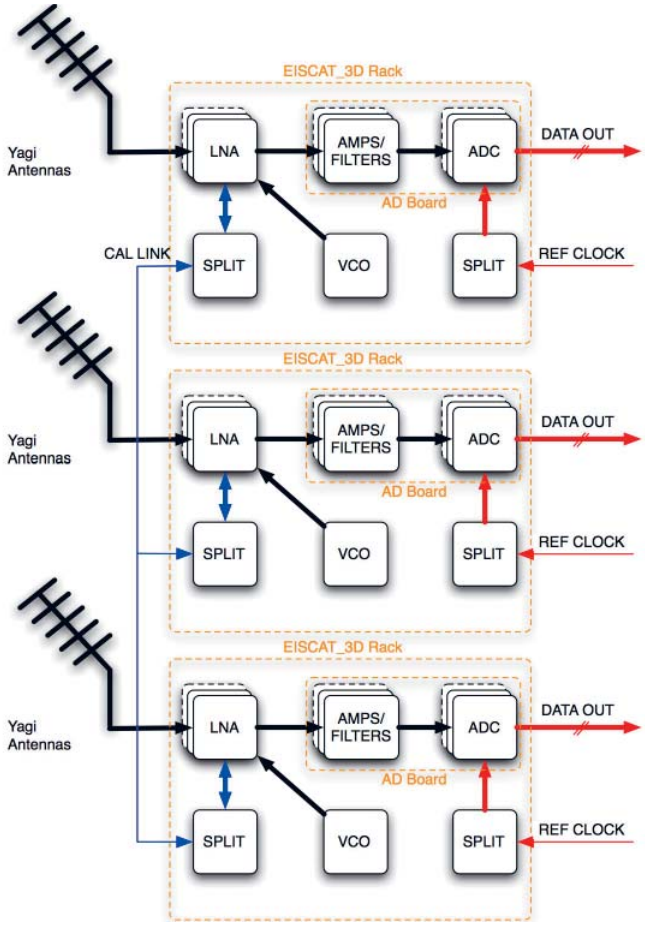

Figure 5. A diagram of the EISCAT_3D LAAR racks containing the cable calibration system. Each low-noise amplifier (LNA) is connected to every other low-noise amplifier in the array via the passive cable net, CAL LINK, to allow calibration of the different units to each other. Thick connection lines indicate that there is more than one physical cable connection for each component.

beams are strongly dependent on the timing accuracy. As stated in Section 6, the resolution required in the beamforming filters is as small as 15 ps, but, as it turns out, the standard deviation of the overall timing system can be allowed to be quite a bit larger.

An extensive examination of the necessary timing performance has been made [13]. The results showed that a timing-error standard deviation of less than 120 ps over the array is necessary for incoherent scatter, while for imaging applications the accuracy requirement is 100 ps (see Section 4). This includes error contributions from the timing distribution system, phase shifts of the antenna phase centers due to icing, etc., and antenna movement due to wind and weather conditions. A reasonable target for the timing-distribution system has thus been set to better than 40 ps standard deviation. From these numbers, it is apparent that a non-calibrated timing system would not perform well enough. Over an array of hundreds of meters, heating by unevenly distributed sunlight would seriously affect the performance of such a system.

Two different approaches have been taken to solve the timing-distribution problem. The first was to design a cable calibration system that connects all antennas in the array to each other [e.g., 14]. The second was to develop a Global Navigation Satellite System (GNSS) receiver that provides high-accuracy timing to small groups of antennas throughout the array [15].

Preliminary findings for both methods showed that the 40-ps standard-deviation goal is within reach for either. The cable calibration system and the GNSS system both reach about 20 ps. The main difference between the two is that the cable calibration system requires more hardware, but the GNSS system is dependent on satellite coverage. Since the GNSS system was explored at later date than was the cable calibration system, it had already been decided that the cable-based system was to be installed in the Demonstrator array (see Section 9), and thus further investigation of the GNSS system, although promising, was deferred.

The cable calibration system works by signal injection through directional couplers in the low-noise amplifier (LNA) system, located in the signal path between each antenna element and its associated low-noise amplifier input. The injection can be directed either into the antenna, to measure its reflection coefficient; into the signal path; or out onto an external cable connection connecting each low-noise amplifier to all of the others in the array (see Figure 5). In this setup, a signal generated at one low-noise amplifier can be routed to all antennas in the array and measured. Both the timing between the antennas and the amplitude differences can be resolved.

With the low tolerances on timing that apply to the timing system, simulations have been made to evaluate how large errors arise due to component mismatch between each manufactured low-noise amplifier. It will not be possible to compensate for the errors in timing and amplitude due to this mismatch with the calibration system. However, as seen in Figure 6, the simulations showed that even for increasing array sizes, the errors do not significantly increase.

Initial measurements in the test array in Kiruna showed that the standard deviations between antenna pairs in the array were all within 5 ps. When adding this to the uncertainty from the component-mismatch simulations and the errors added by the beamforming filters, a total error from the timing system of about 20-25 ps can be expected.

While the amplitude uncertainty is relatively large due to the component mismatch, the largest part of it originates from differences in the directional coupler in the low-noise amplifiers. This mismatch is measured during the production stage of the low-noise amplifiers and can subsequently be compensated for. Amplitude measurements in the test array yielded a standard deviation of less than 0.1% of antenna-pair amplitude difference as a worst case.

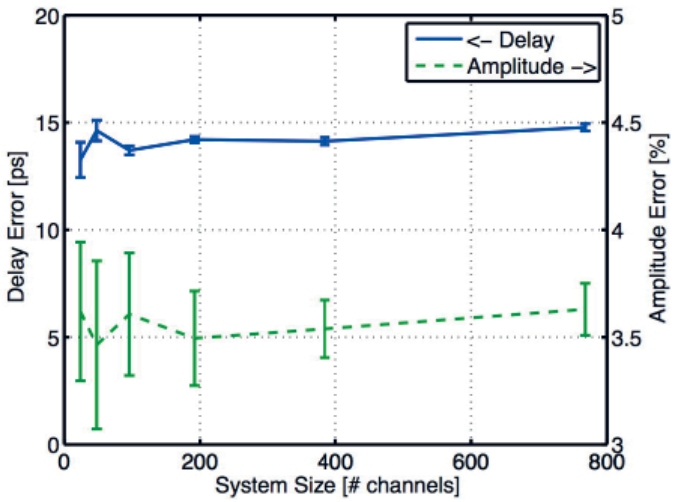

Figure 6. The simulated performance of the proposed system for increasing array sizes. The standard-deviation delay errors are on the left axis, and the amplitude errors are on the right axis. As seen, increasing the number of channels in the calibration net does not significantly increase the errors.

8. Data Recording, Storage, and Access

Each element antenna in the array will be generating about 180 MB/s amplitude-domain data per polarization, or 360 MB/s for the two polarizations. This corresponds to a frighteningly large total array data rate of 5.76 TB/s, which clearly cannot be recorded for permanent storage. Instead, the normal approach will be to combine the data streams from all elements in real time into a relatively small number of simultaneously beam-formed data streams (a maximum of three at the core site, and four to five at each receiver site). After scaling, this brings the data rate back to the element rate of 180 MB/s per polarization, corresponding to 1.3 TB/h/beam, or 31 TB/day/beam.

Even though archiving data at this rate is now feasible using off-the-shelf technology, it is still expensive, and requires a non-negligible amount of electrical power. The standard archiving policy foreseen for the operational EISCAT_3D system will therefore be to buffer the beam-formed data in hard-disk ring-buffers at each site for a limited time (about 24 hours), thus providing users needing the raw data with a time window in which to access the buffers and download interesting data records to their own storage. The ring buffers will be continually overwritten from the beginning.

A coherency detector will monitor the partially beam-formed data at the module level (before beamforming). Whenever a preset coherency threshold is exceeded, module-level data will be saved to the ring buffers for brief intervals, to allow later offline signal processing for the imaging applications.

The primary archived data product will be profiles of target autocorrelation values at different time lags (so-called "lag profiles"). These will be continually computed from each beam at the radar pulse-repetition rate, and averaged to a time resolution of the order of one second. The lag profile data will be fitted for physical parameters (density, temperature, etc.), and the results will also be archived. A petabyte-scale central data archive, accessible via the Internet, will be established close to the core site.

9. The Demonstrator Array

Since several of the design concepts envisaged for full-scale use in the EISCAT_3D system have not been applied in a research radar context before, it was decided to construct a small, 224-MHz, receive-only phased array (the "Demonstrator") at the Kiruna EISCAT site [1]. Operating together with the EISCAT 224-MHz VHF and HF heating systems in Tromsø, the Demonstrator is being used as a test bed, where mission-critical hardware and software (direct-sampling receivers, digital real-time multi-beaming, adaptive polarization coherency triggering, etc.) can be debugged and validated on real radar returns from the ionosphere. Figure 4 shows the array in a winter setting.

The Demonstrator design is a compromise among effective aperture, construction cost, flexibility, and ease of use. For an overview, see Figure 7. Elevating the individual Yagis to 55° causes their beams to intersect a vertically pointing beam from the VHF system at approximately 300 km altitude above Tromsø, that is, close to the peak of the ionospheric F region, where the incoherent-scatter signal-to-noise ratio is maximum.

The basic array was completed in October 2007. For the initial tests, the VHF transmitter was programmed to illuminate the ionosphere with 2 ms coded pulses, radiated vertically at about 1.5 MW. Because only two receiver channels were available, the signals from all twelve rows were phased and combined, using coaxial-cable delay lines and three-port power combiners, to generate two beams at 55° elevation, one for each polarization.

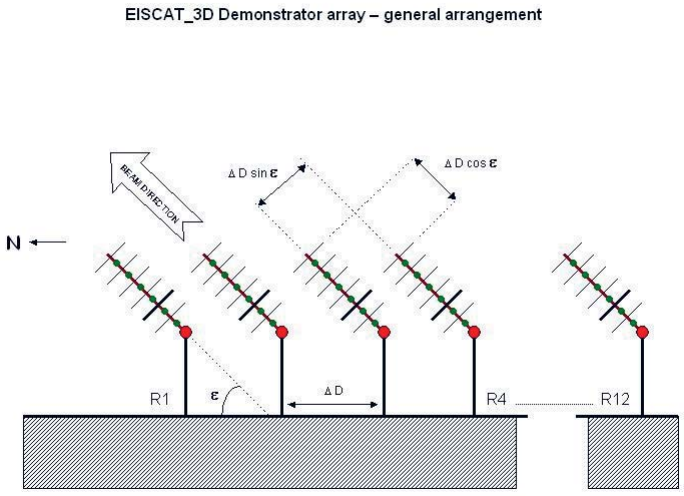

Figure 7. The 224 MHz Demonstrator array at the Kiruna EISCAT site is a rectangular, 12 × 4 array of (6 + 6) element X-Yagis, with its major axis aligned in the Kiruna-Tromsø plane. Each row (R1…R12) comprises four 6 + 6 element X-Yagis, stacked broadside at 1.60 m (1.2l) spacing, and combined in-phase in two four-port power combiners, one for each polarization. The individual Yagis are elevated to $\varepsilon = 55°$. The row-to-row distance, ΔD, is 1.95 m.

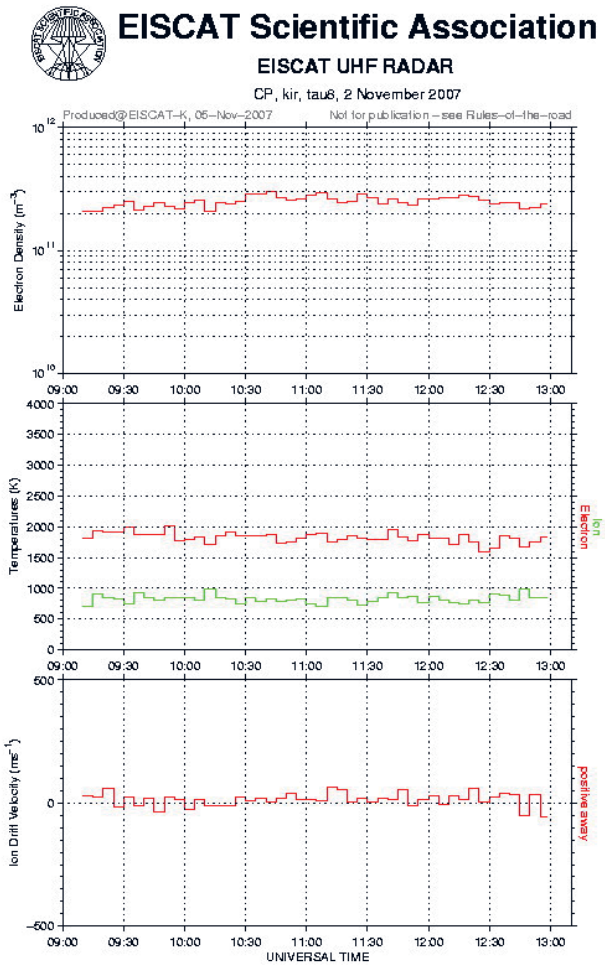

Figure 8. The electron density, electron and ion temperatures, and ion drift velocity at 290 km altitude above Tromsø, derived from 224 MHz incoherent-scatter signals received by the Demonstrator array on November 2, 2007. The signal-to-noise ratio during this observation varied between 4% and 6 %.

At the prevailing daytime electron density of $\approx 2\times10^{11}$ m^{-3}, the resulting projected aperture of 95 m^2 delivered a signal-to-noise ratio of about 4%. Figure 8 shows the physical parameter values obtained by running the standard GUISDAP analysis program on the recorded data, integrated to five minutes time resolution.

During the second half of 2008, 24 direct-digitizing receiver front ends, meeting the full EISCAT_3D target performance specifications but designed for a center frequency of 224 MHz, were installed in the array. A detailed description of these units and the challenges encountered during their design is given in Section 10.

Snapshots of the data generated by the full digital-receiver complement will eventually be input to the EISCAT UHF receiver system for recording and post-processing in the familiar EROS environment. However, since the 1.92 Gsamples/s aggregate output data rate is vastly greater than what the EISCAT receiver can presently accommodate, a system of digital down-converters, low-pass filters, and re-samplers is used to band-limit and decimate the data by a factor of sixteen, bringing the data rate down to a more manageable 6 × 20 Msamples/s.

These data streams are then converted to serial format, and piped from the array into the EISCAT control room via optical fiber. At the receiving end, the data are presently converted back to parallel format and dumped into a bank of dual-page buffer memories belonging to the EISCAT receiver back-end. A prototype digital beam-former, implemented in FPGA, is running on the bench, and will soon replace the serial-to-parallel converter. The beam-former will delay and add the signal streams from the twelve rows to simultaneously generate at least two beams at different elevations in the vertical plane.

An extensive test program will follow the completion and installation of the beamformers. The timing and beam-pointing systems will be validated through a series of observations of Cas-A under all possible weather conditions. The coherency trigger software will be tested on heating-induced artificial ionospheric echoes. Complex amplitude data from the two polarizations will be collected to provide a test database for the adaptive-polarization sub-project. The finished polarizer algorithms will be installed and validated on real-time incoherent-scatter signals.

10. Demonstrator Front-End Design

The two primary active subsystems in the Demonstrator receiver front end are the low-noise amplifier (LNA) and the dual-channel A/D converter board. One antenna polarization is served by one low-noise amplifier and half of one A/D converter board. An overview of the receiver chain is shown in Figure 9. All control signals and switches in the receiver electronics are connected to a microcontroller. This gives the possibility of controlling power-supply outputs, the coupler modes for signal injection, signal-injection frequency, low-noise amplifiers, A/D converter boards, and temperature stabilization of the low-noise amplifier boxes.

The target requirements for the low-noise amplifier were:

- A bandwidth of 30 MHz
- A system noise temperature of 50 K
- A spurious-free dynamic range of 70 dB
- A return loss of 17 dB.

The applications for very-low-noise-figure (NF) amplifiers operating at VHF frequencies are limited, and so is the number of available semiconductor devices. The device with the best specified performance at a frequency not too different from the intended frequency range was the ATF-541M4 E-HEMT from Avago, with a specified noise

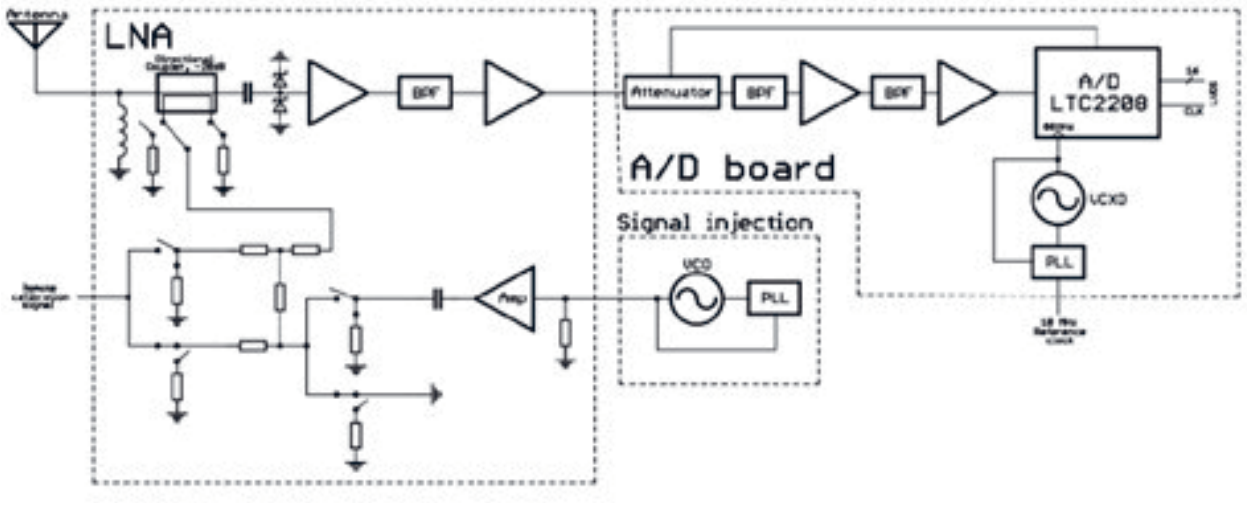

Figure 9. An overview of the receiver front end.

figure at optimal noise match of 0.1 dB (7 K) at 500 MHz. This device was selected for the first gain stage. To arrive at a model for system design, a thorough characterization of the device at 224 MHz was performed. The E-HEMT stage is followed by a bandpass filter and a monolithic gain block (RFMD RF3376). Each low-noise amplifier board also includes one directional coupler and a number of semiconductor switches for routing of calibration signals into the receiver path.

A MATLAB tool for simulating noisy two-ports was implemented. This tool was used together with a particle-swarm optimizer to find an "optimal" low-noise amplifier, given a number of constraints on noise figure, return loss, bandwidth, frequency selectivity, and stability margin. The requirement of high return loss (−17 dB) over a large bandwidth (30 MHz) led to a significant tradeoff in achievable noise figure due to suboptimal (from a noise perspective) input matching and losses in the matching network. This results in a noise figure in the range of 40-50 K, as opposed to the theoretical sub-10 K at optimal noise match.

The manufactured low-noise amplifier boards shown in Figure 9 include various voltage-regulation and bias-regulation circuits. To arrive at the stringent requirements for the timing synchronization, the low-noise amplifiers are built into temperature stabilized boxes with a precision of 0.1° C.

The A/D converter board contains additional filters and two additional gain stages for each signal channel. After amplification and bandpass filtering, the signal is digitized by a 16-bit LTC2208 ADC, clocked at 80 MHz. This device was selected mainly on the basis of its low distortion when under-sampling a 200-240MHz signal, combined with moderate power consumption. As the last gain stages are capable of producing signal levels exceeding the permissible A/D converter input voltage range, a protection circuit consisting of a Schottky diode limiter and a programmable attenuator is included in the signal path, immediately preceding the ADC.

A challenge in the design of the under-sampling A/D converter board was the problem of how to keep the sampling clock phase noise down. In an ADC, clock noise is transferred to the digital output signal with a scaling factor of $20\log_{10}\left(F_{sig}/F_{clk}\right)$, i.e., the clock noise is about 20 dB more prominent when sampling a 224 MHz signal at 80MHz than it would have been if the 224 MHz signal had been down-converted to, say, 24 MHz before sampling. Even for the lowest-noise VCXOs (voltage-controlled crystal oscillator) currently available, this will result in a larger noise contribution from the sampling clock than from the signal quantization. In practice, it was found that this limits the maximum-achievable SNR over a 40 MHz bandwidth centered on 224 MHz to no better than 65 dB, which is 8 dB or more inferior to the theoretically achievable SNR when using a good ADC with a noise-free sampling clock.

In the present design, both channels are clocked by a common on-board Crystek CVHD-950 VCXO, phase-locked to a 10 MHz reference clock derived from the EISCAT time and frequency system, and distributed array-wide. As the ADC noise (both clock-induced noise and quantization noise) will increase the system noise temperature by an amount equal to the equivalent ADC noise temperature divided by the total gain of the analog stages preceding the ADC, the noise contribution from the ADC must be balanced against the maximum SNR by adjusting the pre-ADC gain. In the current system, the gain is somewhat too high, resulting in about 2.9 K noise temperature contribution. Of course, this is very low, but comes at the cost of reducing the maximum system SNR to only about 45 dB. In the current Demonstrator context this is of no consequence, but for a final system it would probably be desirable to reduce the gain preceding the ADC by about 6 dB, thus increasing the system SNR to 51 dB at the cost of increasing the noise contribution to 12 K.

11. Antenna Measurement System

Antennas operating in an Arctic environment may have their performance degraded significantly due to snow and hoarfrost sticking to the antennas. This has been shown to be a problem affecting both the impedance of the antenna elements in an array [16], and the beam shape and pointing direction of large telescopes [17]. In the EISCAT_3D system, it is particularly important to assess the climatic effects, since the shape and pointing direction of the main beam must be quantitatively known.

The performance of the element antennas used in the Demonstrator array during snowfall has been studied [18]. The return loss, $|S_{11}|$, was measured continuously during a 48-hour period with significant precipitation in the form of a snow/rain mixture. At the onset of the snowfall, the whole pass band of the antenna is shifted downwards and the bandwidth was reduced. On some occasions, the useable pass band of the antenna fell entirely outside the desired frequency band. This behavior agreed with results from simulations of a crossed Yagi antenna covered with a dielectric medium.

Simulations have also shown that there can be significant distortion of both the amplitude and the phase of the far-field pattern. Due to the stringent requirements of the relative timing between elements in the array, even a small shift in the far-field phase could cause unacceptable errors in the beamforming process.

A popular technique for mitigating the effects of climate on large antennas is to place the whole antenna inside a radome. However, this is not practical in the EISCAT_3D case, due to the sheer physical size of the antenna arrays. For the same reason, deicing by heating the antennas is not a realistic option. A possible partial solution is to place only the driven elements of the crossed Yagi antennas inside a radome. The drawback is that the gain of the antennas would be reduced during snowfall. Ideally, the antennas should also be designed with a larger bandwidth than needed in order to be able to handle both the shift in frequency and the narrowing of the band. That this is possible is evidenced by, e.g., the results obtained in controlled tests of the "Renkwitz Yagi," proposed as the element antenna for the core array [19]. A good compromise would likely include both of the solutions mentioned above.

The phase and amplitude of the far-field pattern during snowfall are more difficult to control, and should therefore ideally be monitored. When the system is in actual operation, this can probably best be done by a near-field measurement system, such as, e.g., the one presented in [20]. This system used probes located in the near field of the antenna array to estimate the electric-current distribution on the antenna elements. The electric-current distribution can then be transformed into a complex far-field pattern. The technique has the advantage of using relatively few probes that can be located at varying distances from the antenna elements, which is necessary in an antenna array of the size considered here. Also, the whole far-field pattern can be estimated without having probes in the main beam of the antenna, which minimizes the interference and diffraction effects that could degrade the performance of the radar.

12. Summary and Next Steps

In this paper, we have presented the results of an EU-funded study conducted into the design of the EISCAT_3D system, a next-generation incoherent-scatter radar to be deployed for atmospheric and geospace studies in the Scandinavian Arctic. As well as describing the novel elements in this new multi-static phased-array radar, we have drawn attention to some of the new scientific areas that the new facility will open up to its users, and outlined the principles under which it will operate (essentially continuous operation with un-staffed remote sites). While the concepts behind the design have been firmly established, some important details at the hardware level have still not been finally specified, because of the speed at which cheaper and more effective signal-processing solutions are currently emerging. The final choice of hardware in this area will only be made closer to the time of system construction.

The design study the results of which were presented here is only the first of three development phases that will lead to the eventual realization of EISCAT_3D. In December 2008, the project was added to the ESFRI European roadmap for research infrastructures [21], which identifies future programs and facilities corresponding to the long-term needs of the European research community. Acceptance into the roadmap is seen as an important recognition of the EISCAT_3D concept, which will lead to further opportunities to take the project forward within the context of future EU Framework Programmes.

It should be noted that although the design exercise reported here has produced a specification for a radar facility with one active central site and four passive remote receivers, the finally constructed system may have a very different configuration. Given the availability of sufficient funding, it would be simple to scale up from the present design into a system with multiple active sites, offering unparalleled coverage of the upper atmosphere and geospace region above northern Scandinavia, and providing an unprecedentedly detailed data set to scientists in this important research area.

The next phase of EISCAT_3D development is likely to be a three-year preparatory study, hopefully beginning early in 2010, again using EU funding (this time under the Seventh Framework). In this phase, some remaining technical issues, including the choice of DSP and beam-forming hardware, will be finalized; frequency clearances will be confirmed; site-selection issues will be resolved and construction permissions obtained; manufacturing

questions relating to the mass-production of thousands of antennas, transmitters, and signal-processing units will be clarified; and a consortium will be established to fund the construction phase. It is anticipated that construction will begin around 2013, with first operations around 2015. This will provide a state-of-the-art research radar with a nominal operating lifetime of 30 years, to yield top-quality data for the next generation of researchers in upper-atmospheric physics and geospace science.

13. Acknowledgements

The authors gratefully acknowledge the financial support of the EU under its Sixth Framework Programme, which made this study possible. Financial and staffing commitments from each of the five participating institutes, and the assistance of IAP Kühlungsborn and the University of Rostock in the antenna-design exercise, are also gratefully acknowledged.

14. References

1. EISCAT_3D Design Study Team, "EISCAT_3D: The Next Generation European Incoherent Scatter Radar, Final Design Study Report (D11.1)," available at http://e7.eiscat.se/groups/EISCAT_3D_info.

2. C. Ackerman, C. Miller, and J. Brown, "Theoretical Basis and Practical Implications of Band-Pass Sampling," Proceedings of the National Electronics Conference, 18, 1962, pp. 1-9

3. T. Grydeland, C. la Hoz, T. Hagfors, E. M. Blixt, S. Saito, A. Strømme and A. Brekke, "Interferometric Observations of Filamentary Structures Associated with Plasma Instability in the Auroral Ionosphere," Geophysical Research Letters, 30, 2003, pp. 1338-1348 (doi:10.1029/2002-GL016362).

4. T. Cornwell, "Deconvolution," in G. B. Taylor, C. L. Carilli, and R. A. Perley (eds.), Synthesis Imaging in Radio Astronomy II, (ASP Conference Series, 180, xxxiii, 1999, ISBN No. 1583810056), pp. 167-184.

5. D. L. Hysell and J. L. Chau, "Optimal Aperture Synthesis Radar Imaging," Radio Science, 41, 2006, (doi: 10.1029/2005RS003383).

6. P. Comon and G. H. Golub, "Tracking a Few Extreme Singular Values and Vectors in Signal Processing," Proceedings of the IEEE, 78, 8, August 1990, pp. 1327-1343.

7. B. Yang, "Projection Approximation for Subspace Tracking," IEEE Transactions on Signal Processing, 43, 1, 1995, pp. 95-107.

8. R. Badeau, B. David, and G. Richard, "Fast Approximated Power Iteration Subspace Tracking," IEEE Transactions on Signal Processing, 53, 8, August 2005, pp. 2931-2941.

9. X. Doukopoulos and G. V. Moustakides, "Fast and Stable Subspace Tracking," IEEE Transactions on Signal Processing, 56, 4, April 2008, pp. 1452-1465.

10. H. Krim and M. Viberg, "Two Decades of Array Signal Processing Research: The Parametric Approach," IEEE Signal Processing Magazine, 13, 4, April 1996, pp. 67-94.

11. P. Murphy, A. Krukowski, and A. Tarczynski, "An Efficient Fractional Sample Delayer for Digital Beam Steering," IEEE International Conference on Acoustics, Speech, and Signal Processing (Cat.No.97CB36052), 3, 1997, pp. 2245-2248.

12. V. Välimäki and T. Laakso, "Principles of Fractional Delay Filters," Proceedings of the IEEE International Conference on Acoustics, Speech, and Signal Processing, 6, 2000, pp. 3870-3873.

13. G. Johansson, J. Borg, J. Johansson, M. Lundberg-Nordenvaad and G. Wannberg, "Simulation of Post-ADC Digital Beam-Forming for Large Aperture Array Radars," Radio Science, 2010 (in press).

14. W. Grover, "A New Method for Clock Distribution," IEEE Transactions on Circuits and Systems: I, Fundamental Theory and Applications, 41, 2, February 1994, pp. 149-160.

15. G. Stenberg, T. Lindgren and J. Johansson, "A Picosecond Accuracy Timing System Based on L1-Only GNSS Receivers for a Large Aperture Array Radar," Proceedings of the Twenty-first International Technical Meeting of the Satellite Division of the Institute of Navigation: ION GNSS 2008, Institute of Navigation, 2008, pp. 112-116.

16. L. D. Poles, J. P. Kenney and E. Martin, "UHF Phased Array Measurements in Snow," IEEE Antennas and Propagation Magazine, 46, 5, October 2004, pp. 181-184.

17. E. Salonen and P. Jokela, "The Effects of Dry Snow on Reflector Antennas," Proceedings of the Seventh International Conference on Antennas and Propagation, 1, 1991, pp. 17-20.

18. T. Lindgren, Characterization Problems in Radio Measurement Systems, Doctoral Thesis, Luleå University of Technology, Sweden, 2009, ISBN 978-91-7439-034-6.

19. EISCAT_3D Design Study Team, "EISCAT_3D: Options for the Active Element (D3.2)," available at http://e7.eiscat.se/groups/EISCAT_3D_info.

20. T. Lindgren and J. Ekman, "A Measurement System for the Complex Far-Field of Physically Large Antenna Arrays under Noisy Conditions Utilizing the Equivalent Electric Current Method," submitted to IEEE Transactions on Antennas and Propagation, 2010.

21. ESFRI, European Strategy Forum on Research Infrastructures, Roadmap Update 2008, available at ftp://ftp.cordis.europa.eu/pub/esfri/docs/esfri_roadmap_2008_update_20090123.pdf.

The Virtual Wave Observatory (VWO): A Portal to Heliophysics Wave Data

Shing F. Fung

Abstract

The Virtual Wave Observatory (VWO) is one of the discipline-oriented virtual observatories that help form the nascent NASA Heliophysics Data environment to support heliophysics research. It focuses on supporting the searching and accessing of distributed heliophysics wave data and information that are available online. Since the occurrence of a natural wave phenomenon often depends on the underlying geophysical – i.e., context – conditions under which the waves are generated and propagate, and the observed wave characteristics can also depend on the location of observation, VWO will implement wave-data search-by-context conditions and location, in addition to searching by time and observing platforms (both space-based and ground-based). This paper describes the VWO goals, the basic design objectives, and the key VWO functionality to be expected. Members of the heliophysics community are invited to participate in VWO development in order to ensure its usefulness and success.

1. Introduction

The Virtual Wave Observatory (VWO) is the latest heliophysics virtual observatory selected by NASA to help form the Heliophysics Data Environment (HPDE [1]). The primary audience of VWO is the heliophysics wave research community, the main scientific interests of which are in wave phenomena, such as wave excitation, reception, and propagation; wave-particle interactions; and nonlinear wave phenomena. URSI is thus a major constituent of this community. This article introduces and describes VWO, and invites the wave research community to take part in and contribute to VWO development, thus ensuring the usefulness and success of VWO in supporting research into the exciting science involving the wide variety of heliophysics wave phenomena.

Wave phenomena are ubiquitous throughout the heliosphere (Figure 1). The primary objective of VWO is to provide basic wave data and information services to

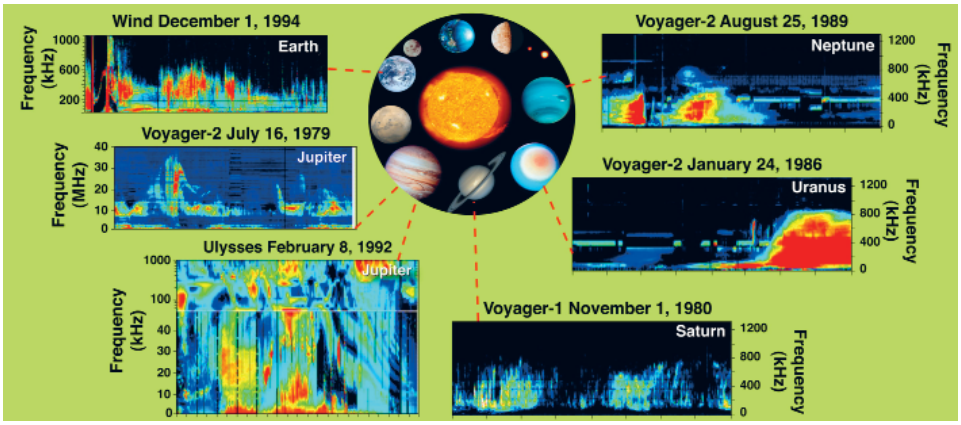

Figure 1. The Virtual Wave Observatory will enable cross-comparison of wave phenomena throughout the heliosphere.

Shing F. Fung is with the Geospace Physics Laboratory, Code 673, NASA Goddard Space Flight Center, Greenbelt, Maryland 20771, USA; Tel: +1-301-286-6301; E-mail: shing.f.fung@nasa.gov.

This is one of the invited *Reviews of Radio* Science from Commission H

facilitate wave research in all heliophysics domains: the sun, heliosphere, magnetosphere, ionosphere, atmosphere, and planetary magnetospheres. Like other heliophysics domain-oriented virtual observatories (VxOs), VWO will (1) work with the SPASE [Space Physics Archive Search and Extract] Consortium to develop the SPASE data model and provide wave data terms to the SPASE data dictionary; (2) describe the metadata of heliophysics (space-based and ground-based) wave data sets using SPASE; (3) develop a heliophysics wave data registry; and (4) develop a Web interface for searching, sub-setting, and retrieving distributed wave data. VWO differs from other domain-oriented VxOs in that the defining theme for VWO is the common interest in heliophysics wave phenomena, irrespective of domains. VWO thus aims to promote and facilitate interdisciplinary research that can lead to new and deeper understanding of wave processes and their relations to the structures and dynamics of various heliophysics domains. To that end, the VWO goal is to make all online-accessible heliophysics wave data searchable, understandable, and usable by the heliophysics community.

In the following sections, we describe the challenges confronting researchers (particularly non-wave experts and students) in finding the relevant wave data to support their research. We discuss how VWO might facilitate data search and promote the use of wave data in heliophysics studies.

1.1 Why Develop the VWO?

Heliophysics plasma wave and radiation data are currently not easily computer-searchable, making the identification of pertinent wave data features for analyses and cross comparisons difficult and laborious. Since wave studies span the spectrum of microphysics (kinetic scales) to macrophysics (MHD scales or larger), researchers and students with varied training or expertise may not feel at ease at using wave data. In order to resolve these difficulties, and to allow wave data to contribute more fully to heliophysics research, we are creating VWO *to make all online-accessible heliophysics wave data searchable, understandable, and usable by the heliophysics community*.

1.1.1 Unique Characteristics of Wave Data

Wave phenomena, ranging from freely propagating electromagnetic radiation (e.g., solar radio bursts, AKR) to plasma-wave modes trapped in various plasma regimes (e.g., whistlers, Langmuir, and ULF waves) and atmospheric gravity waves, are ubiquitous in the heliosphere. Because waves can propagate, wave data obtained at a given observing location may belong to wave oscillations generated locally or from afar. Each panel in Figure 1 was obtained from a passive wave receiver. The individual frequency-time records are called dynamic spectrograms. A dynamic spectrogram recorded in the Earth's magnetosphere, with many emissions identified, is presented in Figure 2.

Since most wave data are recorded in the spectral domain (e.g., frequency) as well as in the time domain, and because wave data taken at a location (and time) can either be generated locally or from a remote source, searching wave data by time or location alone, as is traditionally the case for in situ particle and field data, is thus not always meaningful. As shown in Figure 2, RPI [the radio plasma imager] aboard the IMAGE satellite detected different electromagnetic emissions in the frequency range of 50-500 kHz at different times (different orbital locations), such as the Earth's intense auroral kilometric radiation (AKR), kilometric continuum (KC) radiation, and solar Type III radio bursts. At lower frequencies, RPI detected in situ electrostatic plasma waves below the local electron gyrofrequency during its passage within the Earth's plasmasphere. A wave dynamic spectrogram can contain a wealth of different plasma and electromagnetic wave phenomena, covering a large spatial volume that may include vastly different heliophysics domains. Hence, tools developed primarily for time-series particle and field data do not work well in serving the needs for searching wave data.

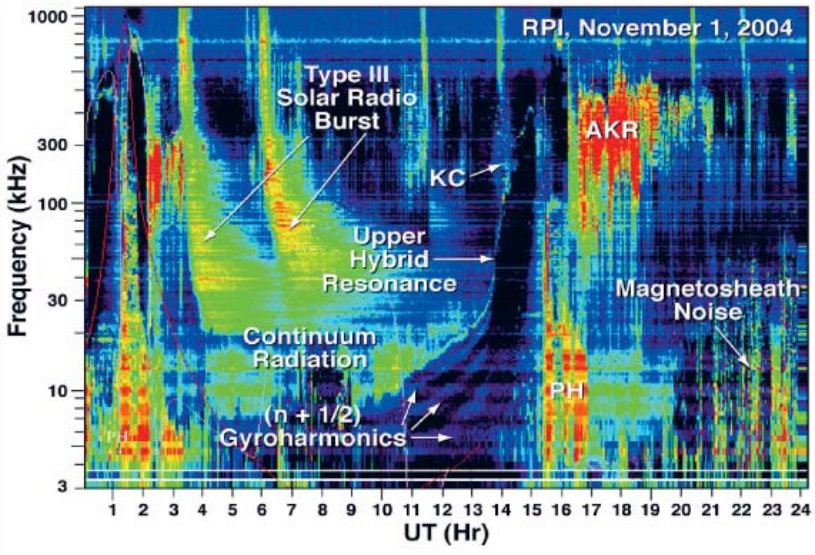

Figure 2. Wave data are often displayed in a dynamic spectrogram. This IMAGE/RPI example shows different electromagnetic free-space mode wave components: type III solar radio burst, auroral kilometric radiation (AKR), kilometric continuum (KC), and non-thermal continuum radiation; as well as a number of localized plasma wave components: plasmaspheric hiss (PH), $(n+1/2)$ gyroharmonic and upper hybrid resonances, and magnetosheath noise, observed inside and outside the Earth's magnetosphere.

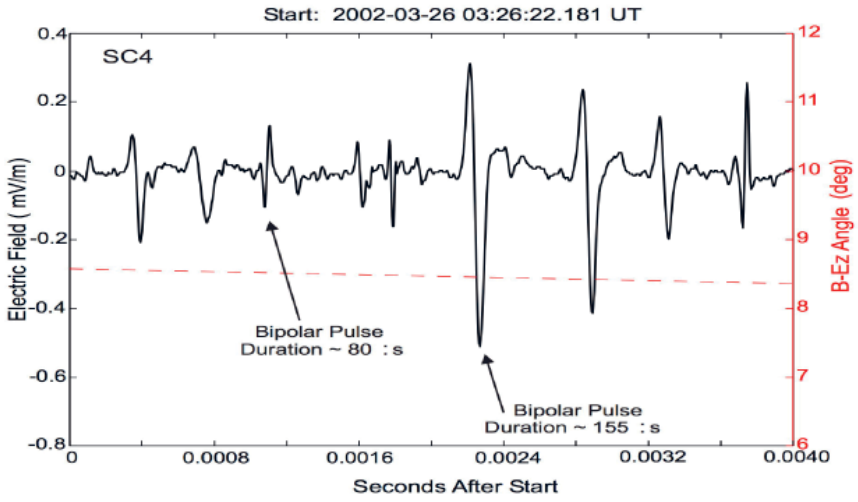

Figure 3a. An example of a high-time-resolution 4 ms sample of waveforms by Cluster Spacecraft 4, showing the isolated, short duration bipolar pulses in broadband electrostatic noise (BEN) observed during bow shock crossings and well into the magnetosheath [5].

In order to serve wave research effectively, we need to devise and implement data-search mechanisms that cater to searching and obtaining pertinent wave and ancillary data sets.

As shown by the example in Figure 2, wave data cannot be selected by frequency alone, in the same way particle data are selected by energy. Data tools for particle and field data must be suitably modified in order to be applicable to wave data. Because of the context-dependent nature of wave observations, it is desirable to be able to select wave data based on geophysical conditions (solar wind, IMF, geomagnetic activity, etc.) and wave phenomena.

In addition to dynamic spectrogram data (e.g., Figure 2), Figure 3 illustrates other wave data types in the forms of time series (A) and a wave map (B). Active sounding measurements can also yield multidimensional wave data on plasma resonances and echo signals in different wave modes (e.g., [2-4]). Figure 3c presents an example of a plasmagram resulting from radio sounding in the Earth's magnetosphere. Figure 3 thus illustrates the cross-domain nature and the unique multidimensional characteristics of wave data (frequency, time, location, multi-component intensities, etc.). The diverse wave data types suggest the need for a cross-disciplinary virtual wave observatory to support wave research, and the heliophysics research community in general. The emerging VWO will require close collaboration with all existing and future heliophysics virtual observatories.

A unique aspect of active wave data (e.g., Figure 3c) is that of its complex, discipline-specific metadata. For example, active radio sounding IMAGE/RPI data have extensive metadata associated with each sounding measurement regarding radiated power, frequency range, frequency step size, time per measurement, minimum and maximum virtual range, range increments, pulse repetition rate, pulse width, receiver bandwidth, receiver sensitivity, coherent integration time, Doppler resolution, receiver saturation recovery, Doppler range, amplitude resolution,

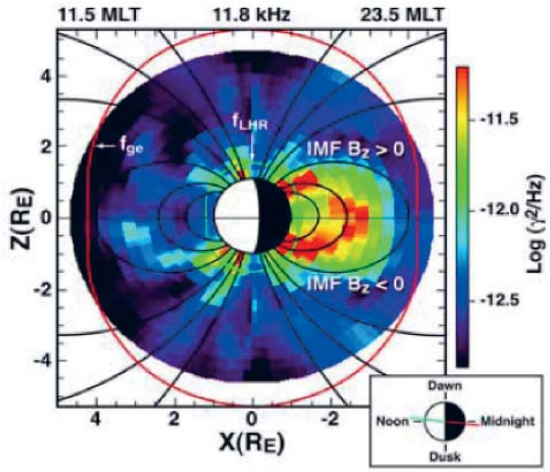

Figure 3b. An example of a wave map of the spatial distribution of wave electric field intensity at 11.8 kHz taken from DE1 observations near the noon-midnight meridian plane [6].

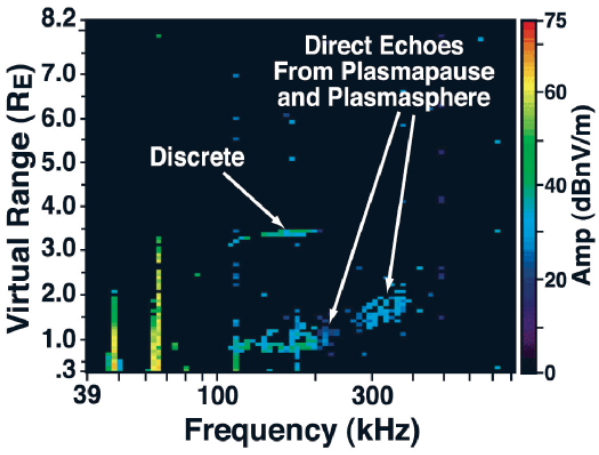

Figure 3c. An example of active radio sounding data from IMAGE /RPI showing plasma resonance (e.g., vertical traces at lower left), discrete guided echoes, and diffuse direct plasmapause echoes [2].

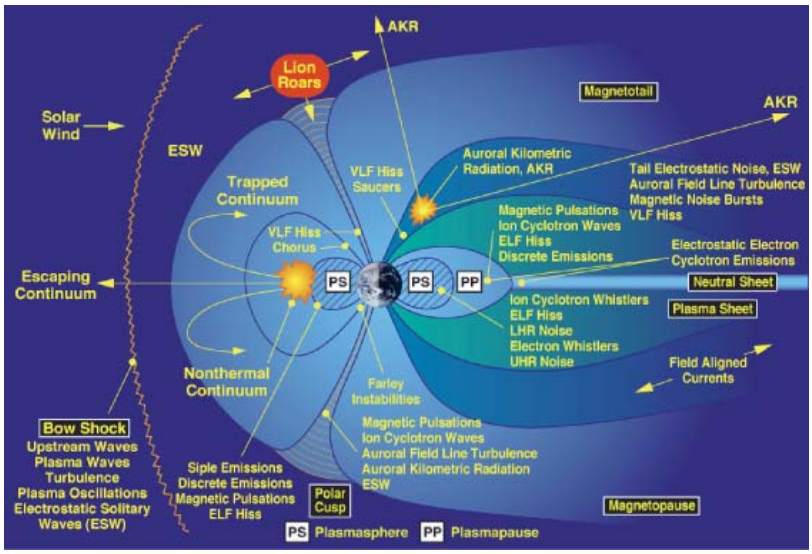

Figure 4. The VWO will provide researchers with sophisticated query tools tailored to this complex environment to better enable science discovery, as illustrated by the abundance of distinct wave phenomena observed in the Earth's magnetosphere (adapted from [8])

angle-of-arrival resolution, antenna length, and processing gain [7]. This uniqueness, and the lack of a metadata standard description within the wave community, warrants a separate focal point to develop SPASE descriptions (Section 1.3) for active and passive wave data.

1.1.2 Wave Research and Heliophysics Science

Heliophysics wave data span most heliophysics domains: solar wind, interplanetary space, Earth's ionosphere and magnetosphere, and planetary magnetospheres. They are thus of multidisciplinary interest. Figure 1 shows observations of radio emissions from different planetary magnetospheres. Cross comparisons of these datasets will help determine, for example, which radio emissions have common emission mechanisms. Wave-propagation studies are also important for elucidating plasma structures in various planetary magnetospheres.

Wave data analysis often requires specialized knowledge of different wave phenomena (e.g., see Figure 4) and the associated physics, such as the propagation characteristics of different wave modes. This specialized expertise requirement can be a hindrance to wider use of heliophysics wave data by non-wave researchers and students, despite the important information wave data can contribute to understanding many heliophysical processes. In addition to the basic data and information services, the VWO will endeavor to enhance the understandability and usability of heliophysics wave data by developing data annotation and tutorial services for describing the data content and illustrating how wave data can be used. Data annotations by expert users will be collected and organized into a searchable database, so that wave data can eventually be organized and searched for specific features and used for comparisons with other heliophysics data sets.

Search for appropriate data for heliophysics wave studies also requires knowledge of wave phenomena. In addition to deciding whether the wave activity of interest is electrostatic (i.e., locally trapped) or electromagnetic (with propagation over distances), considerations must be given to the dependence of the wave activity on the observer's location or viewing geometry, propagating frequency range, and whether the wave data were acquired by passive or active observations. Occurrences of natural wave emissions in the magnetosphere (e.g., auroral kilometric radiation) are often also dependent on the state (i.e., context) of the magnetosphere, which varies with the changing solar wind, IMF, and geomagnetic conditions. Fung and Shao [9] showed recently that magnetospheric state can be specified by a set of suitably time-shifted solar wind, IMF, and the multi-scale geomagnetic response parameters. These parameters form a magnetospheric state vector that provides the basis for searching magnetospheric wave data by their context conditions. Innovative context and content data search capabilities will make VWO a very useful tool for heliophysics research.

1.2 New NASA Heliophysics Data Environment

As described in the recently released NASA Heliophysics Science Data Management Policy [10], the Heliophysics Data and Model Consortium (HDMC) is a project established by NASA to provide *open, easy, uniform, and scientifically meaningful* access to its heliophysics mission data and models. The HDMC oversees all heliophysics mission-resident archives, data recovery and upgrade projects, and discipline (x)-oriented Virtual Observatories (VxOs). It leads the SPASE consortium [11] in developing the heliophysics data model used for describing heliophysics metadata.

VWO [12] is one of the latest VxOs selected to complement the overall heliophysics data environment. In addition to VWO, the current suite of VxOs includes:

- Virtual Solar Observatory (VSO, [13])
- Virtual Heliospheric Observatory (VHO, [14])
- Virtual Energetic Particle Observatory (VEPO, [15])
- Virtual Magnetospheric Observatory (VMO, [16])
- Virtual Radiation Belt Observatory (VIRBO, [17])
- Virtual Ionosphere, Thermosphere and Mesosphere Observatory (VITMO, [18])
- Virtual Modeling Repository (VMR, [19])

As suggested by their names, each of the VxOs is identified by its respective domain or associated domain science, and is expected to (1) serve its respective discipline community and the heliophysics community as a whole; and (2) enable effective use of discipline data sets (e.g., to enhance scientific returns of the data), likely in accordance with how the discipline/domain science is practiced.

1.3 SPASE

In order to support wave research across different heliophysics domains, there needs to be ready availability and accessibility of wide varieties of wave and ancillary data, and effective data search and retrieval mechanisms to handle the selection and retrieval of diverse wave-data products, as illustrated in Figures 2 and 3. The wave-research community already has made available heterogeneous (instrument-specific) metadata and data for many of its publicly available, distributed datasets (e.g., in NASA's CDAWeb [20] and Planetary Data System [21]). However, there exists no metadata standards to enable effective searches across distributed archives and inter-comparisons of the data. Although wave data providers have made great strides in documenting their data sets and storing many of them online or near-online in self-describing data formats (e.g., the NASA Common Data Format, CDF), the lack of metadata standards hinders our ability to effectively draw together diverse data sets, including those from particle and field instruments, for analyses.

SPASE, which stands for Space Physics Archive Search and Extract, is now the recognized standard data model adopted by the VxO community to facilitate data searches between members. It is an open activity, involving an international team of solar, heliospheric, and space physicists and information scientists engaged in the process of defining standards for data descriptions and archive interoperability. The SPASE development effort is under the oversight of the SPASE Group Consortium [11], which is responsible for official release and documentation of the SPASE data model. The VWO has been working with the SPASE Group Consortium to develop SPASE terms for describing active and passive wave data. This effort has contributed to the release of SPASE 2.0. The wave-research community is invited to contribute to this effort so that all wave data can be effectively described.

2. VWO Description

2.1 VWO Goal

The VWO is a data service dedicated to serving the wave-research community having primary scientific interest in wave phenomena and how they relate to processes in the heliosphere. Its aim is to provide access to wave and ancillary data to support wave research. The VWO is thus especially suited to serve the science goals of Commission H of the International Union of Radio Science (URSI) [22]:

(a) to study waves in plasmas in the broadest sense, and in particular in: (i) the generation (i.e., plasma instabilities) and propagation of waves in plasmas, (ii) the interaction between these waves, and wave-particle interactions, (iii) plasma turbulence and chaos, and (iv) spacecraft-plasma interaction, and (b) to encourage the applications of these studies, particularly to solar/planetary plasma interactions, space weather, and the exploitation of space as a research laboratory.

Also of interest are nonlinear wave phenomena, such as solitary waves, ponderomotive forces, and nonlinear wave-particle interactions. To accomplish its goal, the VWO endeavors to make all online-accessible heliophysics wave data searchable, understandable, and usable.

2.2 VWO Design Objectives

The development of VWO as a data service is guided by the desire for VWO to offer *ease of use* and *efficacy* in satisfying users' requests. To that end, the VWO will strive to:

(1) Have a simple but functional user interface;

(2) Provide data search options (in addition searching data by time, spectral range, and observing platform) to satisfy needs for data in different contexts, such as spatial location, solar, solar-wind and magnetospheric conditions, etc.

(3) Be interoperable with other VxOs and data services in order to locate and provide access to all online heliophysics discipline data and information;

(4) Provide tutorial and educational materials to explain heliophysics wave data and to illustrate how they may

be utilized more broadly in heliophysics research; and

(5) Develop a wave-data annotation service with which data-feature annotation by expert users can be captured and organized into a searchable database.

2.3 VWO Architecture

Like most VxOs, the VWO functions as "middleware" between users and distributed data sources. It accepts users' input queries, and then locates (and delivers when feasible) data granules and information available from appropriate data sources to support heliophysics research. Successful VWO operations require seamless handshake for information exchange between different components: end users, middleware, and data sources. The schematic in Figure 5 shows the relationships between VWO middleware and other HDMC components.

In order to limit development cost and minimize duplication of effort, the VWO middleware will be based largely on the existing VHO and VMO architecture. However, the existing virtual observatories are geared toward providing primarily time-ordered data, because time is traditionally the key organizing parameter for most space-physics data. In addition, the VHO and VMO also provide statistical summaries of magnetic-field and plasma data. These tools are not applicable to finding and accessing wave data organized in the spectral domain. The VWO middleware will thus need to provide data-search mechanisms and an interface catered to wave studies.

As shown in Figure 5, central to VWO middleware is the VWO Query Manager (VQM) the primary function of which is to decipher users' queries and determine appropriate resources that satisfy the queries. Figure 6 shows a more-detailed view of the various query types and services that the VQM will have to manage and be accessed by other services via Web services or application programming interfaces (API).

The middleware will store and have access to context (such as solar wind, IMF, and geomagnetic indices information) and orbit information, and event catalogs from which appropriate time and spatial constraints can be determined. Queries to VWO will result in the appropriate restrictions being determined from user queries. These restrictions will be sent as appropriate to domain virtual observatories (VHO, VMO or VITMO) to query for data availability.

In order to implement this architecture, we have identified five tasks as well as the overarching needs to work with other VxOs and the SPASE community. These detailed tasks and our plan to implement them are discussed in the following subsections.

2.4 VWO User Interface

The VWO aims to serve different user categories: scientists (both wave experts and non-experts), data providers, students, and educators. A research scientist may look for data to perform scientific analysis, a data provider may need information about how to contribute to the VWO

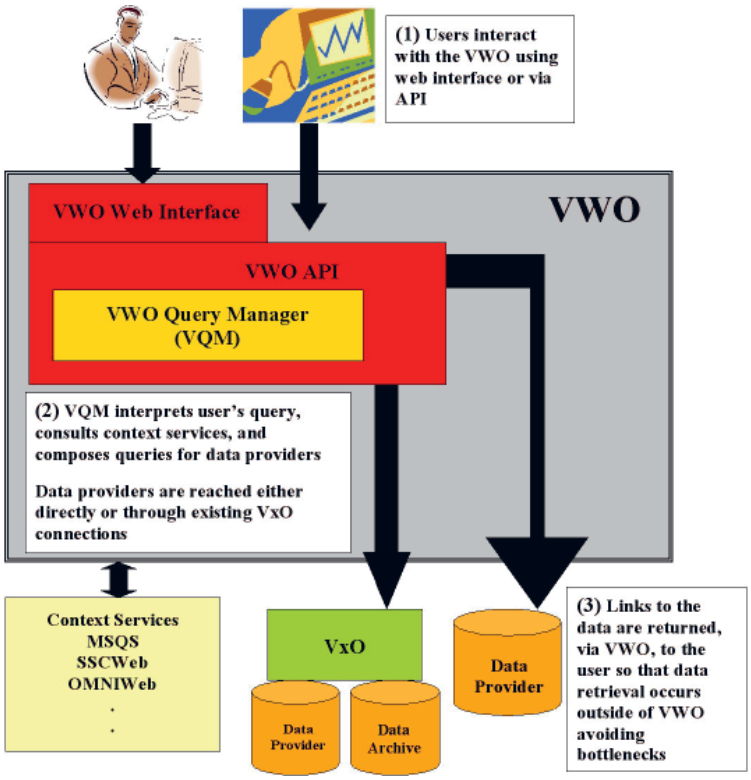

Figure 5. A schematic of the VWO architecture. The VWO middleware (grey shaded box) will contain a complete set of tools to provide both context and content-based searches for the wave research community. In addition to its own data providers, the VWO will leverage existing VxOs and their data providers whenever applicable.

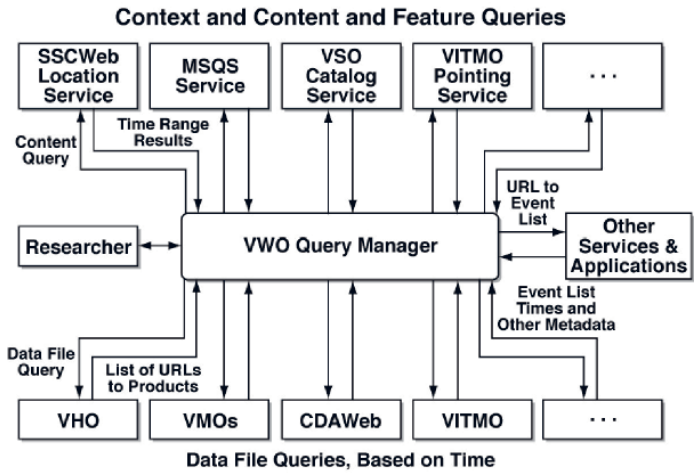

Figure 6. A schematic of VWO's Query Manager system, interacting with various VxOs and distributed data services, to enable content and context queries (top) as well as queries for data files (bottom).

data registry, while an educator or student may need mission information and explanations on wave phenomena and data examples. Since the data needs of different users vary with their interests, background, and expertise, VWO will work toward providing a user-oriented Web interface through which queries posed by different category users can all be effectively answered.

Searching for appropriate data for wave studies can be a daunting task, particularly for non-expert users. A scientist may wish to search for wave data by frequency and observing location, or by wave phenomena, rather than by time and missions, as has been the case traditionally, and may not want data from pre-sorted mission-centric data catalogs. The goal of the VWO user interface is to offer a common yet flexible data-discovery and access tool, i.e., a data-query builder [23], that saves users from having to use many distinct tools and spending an inordinate amount of time to hunt for wave data sources, documentation, and analysis tools. The query builder will be useful for handling complex data queries. Since wave data do not naturally come with identities of wave phenomena, wave data tend to be used less by non-wave experts. VWO will develop tutorial and annotation services to promote understandability and usability of heliophysics wave data.

Since observations of wave phenomena depend largely on observing locations, geophysical conditions, and the pertinent wave modes being observed, it will be convenient to have data-search options based on the contexts in which data are sought. While the VWO interface will allow users to perform traditional search for data by missions and time, it will also support search options according to contextual conditions: magnetospheric state, observing location, measurement types (e.g., active or passive), and wave phenomena.

As indicated in Figure 5, VWO will also develop appropriate APIs suitable for power users who may wish to access VWO services as behind-the-scene users, such as a data provider or a VxO. Since metadata are generally stored in Extensible Markup Language (*XML*) documents, the most commonly suited APIs are Web services using, for example, Web Services Description Language (*WSDL*) [24] or REpresentational State Transfer (*REST*) [25]. Other API types for call routines in *IDL*, *MATLAB*, or *Java* can also be supported as needed and as resources permit.

2.5 VWO Functions

As stated in the "VO Framework" document [26], "a Virtual Observatory (VO) is a suite of software applications... that allows users to uniformly find, access, and use resources (data, software, document, and image products and services using these) from a collection of distributed product repositories and service providers. A VO is a service that unites services and/or multiple repositories." To effectively serve various user categories, the VWO will provide five core services: (1) data query, (2) data registry, (3) accessing other data services, (4) annotation and education, and (5) tools.

2.5.1 Data Query

Providing access to heliophysics wave data is a primary VWO function. As such, the VWO seeks to become a major portal to both space-based and ground-based heliophysics wave data sources. As mentioned above, the VWO middleware and interface will provide different data-query options. In addition to supporting traditional data search by time, spectral range, and observing platform, the VWO will implement context data search mechanisms [23] with which *multiple* and *distributed* wave data sets can be searched by:

- Location: this option allows users to specify an observing location, such as a ground station, a local time zone, or a spatial region, at which the desired data were taken;

- Magnetospheric state: this option, applicable particularly to magnetospheric wave phenomena,

allows users to specify the solar activity, solar wind, interplanetary magnetic field, and geomagnetic conditions under which the desired data were taken; and

- Wave phenomena: this option, when implemented eventually (see Section 2.5.4), will be useful for obtaining data pertaining to a given wave phenomenon.

Like most heliophysics studies, investigations of wave phenomena will often require using ancillary data sets, such as solar wind or other in situ particle and field measurements. In the current heliophysics data environment (HPDE, Section 1.2) under HDMC oversight, it is envisioned that all data sets registered with VxOs should be accessible from any one VxO (see Section 2.5.3). SPASE (Section 1.3) is being developed to provide the *lingua franca* between VxOs from which all VxO-registered data sets can be queried and accessed without further user intervention.

2.5.2 Data Registry

Registration of a data set with a VxO is the key step by which the data and metadata of the data set become accessible to and searchable by VxOs. Data-set registration means that all relevant metadata pertaining to the data set are described by a set of *XML* documents that conform to the SPASE data model. The responsible VxO then maintains the *XML* documents of all the data sets registered with it in a database, and makes it searchable by other VxOs. Since the selection of the VWO for development, the VWO team has been working with the SPASE Group Consortium [11] to define wave-data terms to be added to the SPASE data dictionary, which will facilitate registering wave data sets at the VWO. This effort has contributed to the formal release of version 2.0 of the SPASE data model.

Tables 1 and 2 respectively list a number of space-based and ground-based wave data sets relevant to the VWO. The data sets in bold lettering are the data sets being targeted initially for registration with the VWO. In fact, the IMAGE RPI data, consisting of *both* active radio-sounding and passive wave measurements, have been used to aid with defining wave data terms for the SPASE data model. We expect the VWO data registry to grow in time with the inclusion of additional national and international space missions, as well as ground-based data sets.

VWO will work closely with other VxOs (last column in Table 1) and other data providers (e.g., the NASA CDAWeb system [20]) to ensure interoperability, so that users can seamlessly access the data sets registered at those facilities. The VWO will work with current and upcoming missions (e.g., THEMIS, RBSP) in order to have those data served within the Heliophysics Data Environment. As the VWO registry matures, we will reach out to the international space-based and ground-based heliophysics community to register additional heliophysics wave data sets.

Mission (Experiment/Data Types)	Time Span	VxO Cross Reference
Alouette 2 (Sounder/digital ionograms)	1965 – 1975	VITMO
ISIS 1 (Sounder/digital ionograms)	1969 – 1984	VITMO
ISIS 2 (Sounder/digital ionograms)	1971 – 1984	VITMO
Hawkeye (ELF-VLF/spectrogram)	1974 – 1978	
ISEE 1 & 2 (Plasma wave, VLF)	1977 – 1987	
Voyager 1 & 2 (PRA/spectrogram)	1977 – 1989	
Voyager 1 & 2 (PWS/spectrogram)	1978 – 2000	
ISEE 3/ICE (Plasma waves spectrum analyzer)	1978 – 1997	
ISEE3/ICE (Radio Mapping of solar wind disturbances)	1978 – 1997	
DE 1 (PWI/spectrogram)	1981 – 1990	
Galileo (PWS/spectrogram)	1989 – 2003	
CRRES (Plasma wave)	1990 – 1991	
Ulysses (URAP/spectrogram, waveform, direction)	1990 – present	
Geotail (PWI)	**1992 – present**	
Wind (Waves/spectrogram)	1994 – present	VHO
Polar (PWI/waveform, spectrogram)	**1996 – 1997**	
Cassini (RPWS/spectrogram)	1997 – present	
IMAGE (RPI/spectrogram, plasmagram)	**2000 – 2005**	
Cluster (DWP, EFW, STAFF, WHISPER/spectrogram)	**2001 – present**	
Cluster (WBD/waveform, spectrogram)	**2001 – present**	
STEREO (SWaves/spectrogram)	2006 – present	VHO
THEMIS (EFI, SCM/waveform, spectrogram)	**2007 – present**	

Table 1. VWO-relevant space-based data sets.

Ground Observatory (Experiment/Data types)	Time Span	VxO Cross Reference
Augsburg College AGO (Search coil Magnetometer/spectrograms)	1993 – 2008	
U. Maryland AGO (Magnetometer, Riometer & VLF/Survey plots)	1986 – 2005	
Augsburg College Svalbard (Search coil Magnetometer/spectrograms)	2006 – 2008	
NCAR Svalbard (Search coil Magnetometer/daily data files)	2006 – 2008	

Table 2. VWO-relevant ground-based data sets.

2.5.3 Accessing Other Data Services

As a VxO, VWO supports the overall HDMC goal to enable researchers and students to search and access heliophysics wave data *without* having to contact multiple data providers and data centers separately, although it may still be necessary to obtain guidance on the proper use of data from instrument teams. In order to locate and provide access to all heliophysics online data and information resources, VWO will work closely with existing VxOs. It will leverage the tools and middleware being developed by those VxOs in order to economize on development effort and cost, and to avoid duplication of effort. In particular, VWO will rely on close collaboration with Goddard's VMO and VHO. These two VxOs share a common architecture. As such, they allow us to work with two diverse heliophysics sub-disciplines while minimizing technical implementation challenges. In particular, both VHO and VMO plan to offer data searching based on user-contributed event lists. This capability fits naturally with the VWO plan to convert context queries into lists of times suitable for other VxOs.

As mentioned in Section 2.5.1, SPASE is the basis of the *lingua franca* between VxOs. Efforts are now underway to develop *SPASEQL* [27] within the HPDE to use the SPASE data model and associated terminology to create a standardized communication language for HPDE Virtual Observatories. *SPASEQL* defines *XML*-based standards for query and response message construction such that VxOs can have a common language for communication [28]. With *SPASEQL* or a similar language in place, software tools can be rapidly developed and used throughout the HPDE. The VWO will work with our collaborating data providers and VxO partners, the SPASE consortium, and community wave researchers to define the standard SPASE terms to describe wave metadata.

2.5.4 Annotation, Tutorial and Education Services

As illustrated by Figures 1-4, there exist numerous wave phenomena throughout the heliosphere. They appear in different portions of the frequency spectrum, can be electromagnetic or electrostatic, and can have natural or artificial sources. Although wave experts often can identify the wave features in which they are interested relatively easily, it can sometimes be a challenge for non-wave experts to identify a wave phenomenon from data, because wave measurements do not always come with wave-mode identifications, which are critical for understanding the data. For example, in contrast with particle data, electron/ion measurements at different energies are still electron/ion measurements, even though details of the phase-space distributions in different energy regimes may differ.

To make wave data more understandable and usable by the broader heliophysics community, VWO will endeavor to develop capabilities to search wave data by *context conditions* (Section 2.5.1) and *wave phenomena.* In the latter case, it is required not only that data be described by their appropriate metadata (in SPASE), but also identified by their associated phenomena. To that end, VWO plans to develop an annotation service that will capture the data annotations to be provided by wave experts as they analyze the data. The captured information will then be collected, organized, and stored in the VWO searchable metadata database. We hope that the annotation service will become a useful tool that can also help broaden the VWO user base to non-wave experts.

However, in order to develop a successful annotation service, it is important for domain experts to actively contribute to the annotation database. To ensure quality of the captured information, the annotation-gathering procedure has to be an iterative process. A similar "expert rating service" has already been implemented for expert users to identify, rate the quality of, and describe the data features in the IMAGE/RPI radio-sounding observations [29]. With a simple interface as part of the IMAGE/RPI data visualization and analysis software, users can seamlessly submit annotations (and revisions) to a master database over the Internet as they work with the data from their remote workstations. With some organization of the submitted information, the annotations can be used as additional constraints in data queries. The development of the VWO annotation service will thus be based upon the IMAGE/RPI "expert rating service."

While the VWO annotation service should provide value-added data-search capability, to perform wave data analysis effectively, users still need to possess basic knowledge of wave phenomena and physics of wave propagation, particularly regarding the specific wave mode of interest. To help increase usability of wave data, the VWO will provide on its Web site tutorial materials on how wave

data might be used in heliophysics studies, and educational materials on basic wave physics to introduce students to the exciting science of wave phenomena.

2.5.5 Tools for Users and Data Providers

To promote utilization of heliophysics wave data, VWO aims to augment users' analysis capabilities by providing a set of uniform and robust tools to access and use distributed heliophysics-relevant wave data, metadata, and services. In addition, we plan to provide an assortment of basic data visualization and processing tools to aid in browsing and selecting data for further studies. Hyperlinks for accessing these tools and information will be collected and made available on the VWO website. For example, to assist data providers with data registration, members of the SPASE and VxO community are developing SPASE-related tools [30], including SPASE description editors, which data providers can use to produce SPASE-compliant metadata layers at their sites.

3. Science Examples Illustrating the Potential Use of VWO

A few examples of use cases may help illustrate how VWO can be put into practical use. For example, in studying how the Earth's auroral kilometric radiation (AKR, Figure 2) may depend on solar activity, solar wind, and geomagnetic conditions, a scientist may wish to compare AKR observations taken at different magnetic local times and latitudes under various conditions. This task can be facilitated by using VWO's context search capability based on the Magnetospheric-State Query System (MSQS) [31] to search for time intervals when a particular set of space environment conditions or magnetospheric state [9] occurs, including when solar activity is high (and low, for comparison). Additionally, the scientist can use VWO's location search capability, which is based on NASA's SSCWeb [32], to search for times when, for example, the Cluster, Geotail and Polar/IMAGE spacecraft were in specific locations to observe AKR in order to determine the variations of AKR emission patterns under different conditions. The user may also need to find times when polar and ground magnetometer stations are in magnetic conjunction in order to correlate space-based and ground-based observations. Each of these queries produces an event list at VQM (Figures 5 and 6), which can then determine the intersections between event lists to find the appropriate time intervals for further analysis. Using the resultant times from the VQM, VWO will then identify and retrieve the pertinent data granules from wave data sources such as CDAWeb and other VxOs, and return them to the scientist. Similarly, upstream solar wind data from Wind and ACE can also be obtained, so the user can identify possible inter-planetary shock precursors of AKR events.

Another example of a possible application of the VWO can be illustrated by recent research on kilometric continuum (KC) radiation (e.g., [3]). This radiation is shown in Figure 7a as the nearly horizontal filaments that increase slowly in frequency with increasing UT. (The term "continuum" is a carryover from earlier research using receivers that lacked the frequency resolution to detect the fine frequency structure visible in Figure 7a.) The more intense (nearly vertical) emission features in Figure 7a with rapidly decreasing frequency with increasing UT are solar type III radio bursts. Kilometric radiation has been investigated for more than three decades, has been observed in every planetary magnetosphere visited by spacecraft with plasma-wave detectors, and has been the subject of several review articles [3, 33-35]. It has long been believed that KC is generated in regions of sharp density gradients, such as in the plasmapause, and that it occurs at all local times. Recent work [36] indicates that it originates in density bite-outs in the equatorial plasmasphere, called notches, as illustrated in Figure 7b. This conclusion was possible because IMAGE/EUV data defined the notch (see insert in Figure 7b) and allowed the plasmapause boundary to be displayed in equatorial distance as a function of magnetic local time, so as to be compared with the track of Geotail during the KC reception in Figure 7b. Ray-tracing calculations indicated that the KC was generated deep within the notch, and that the radiation beam was constrained by the notch structure in a manner consistent with the Geotail observations. To further understand the KC emission pattern and occurrences, a user may use the VWO to (1) locate KC observations by Geotail and Cluster, based on frequency range and spacecraft locations during times when notches appeared in IMAGE/EUV imaging observations; or (2) query other VxOs to locate possible notch observations during KC events; and/or (3) locate simultaneous multi-satellite KC observations of emissions from the same source region. Such capabilities will greatly facilitate the investigation of long-standing questions concerning all aspects of a wave research problem, i.e., wave generation, propagation, and reception, that is of fundamental importance to the wider heliophysics community as well as to the wave community. This is because information concerning the KC fine structure will also provide information on the dynamics and structure of the plasmapause source region.

The third example is inspired by a recent study by Muldrew [37]. As discussed by Benson and Fung [38], Muldrew [37] presented a theoretical model to explain the ionospheric-sounder-stimulated fundamental gyroharmonic emission that has defied satisfactory explanation for four decades. The confirmation of the model depended crucially on analyzing topside-sounder data obtained when the instrument was operating in an extended fixed-frequency sounding mode, *and* where the local gyro frequency (at the satellite location) matched the sounding frequency. The ISIS/Alouette data-restoration project [39] provided the pertinent topside-sounder data. Because the digital ISIS-2 sounder data include the metadata containing the

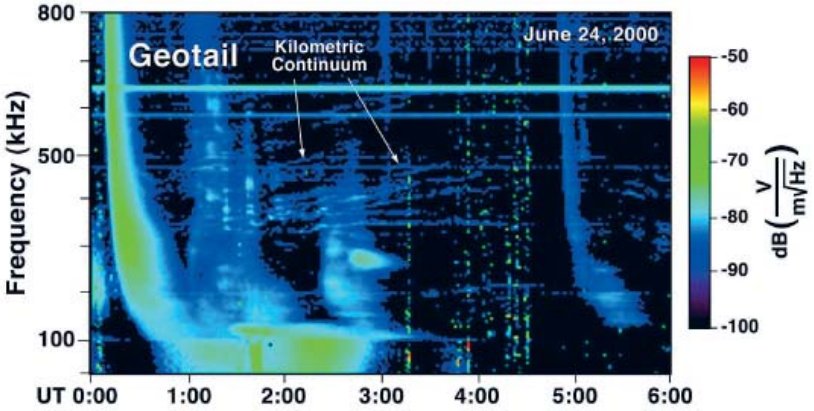

Figure 7a. The KC wave observations from Geotail/PWI (adapted from [2]).

local gyro frequencies at the satellite positions (based on a magnetic-field model), it was relatively straightforward to search [40] through more than 300,000 ISIS-2 digital topside ionograms to identify the data intervals satisfying the complex data-query conditions required by Muldrew's study. This example illustrates the benefit of the availability of *both* pertinent metadata and support for complex query for locating desired data granules for analysis. However, generally speaking, not all data sets will include specialized metadata. We expect that by using the SPASE data model for metadata descriptions, the query builder (Section 2.4) and the VQM (Figures 5 and 6), the VWO will be able to handle a variety of complex queries to effectively support heliophysics research.

4. Community Participation

The VWO is a discipline-oriented data service with the objective of supporting heliophysics wave research. Its development is guided by (i) the data needs of the wave-research community, (ii) the best practices adopted by the heliophysics VxOs for interoperability (e.g., the use of SPASE and *SPASEQL*), and (iii) feedback from VWO users. To help make the VWO a successful research tool, active community involvement and input are therefore needed to:

(1) Define community data needs,

(2) Support the VxO framework and SPASE standards,

(3) Make wave data sets available,

(4) Annotate data, and

(5) Provide user feedback.

5. Summary

We have introduced the Virtual Wave Observatory (VWO) as one of the VxOs forming the nascent heliophysics data environment. While most VxOs serve specific domains of interest (Section 1.2), the VWO caters to supporting

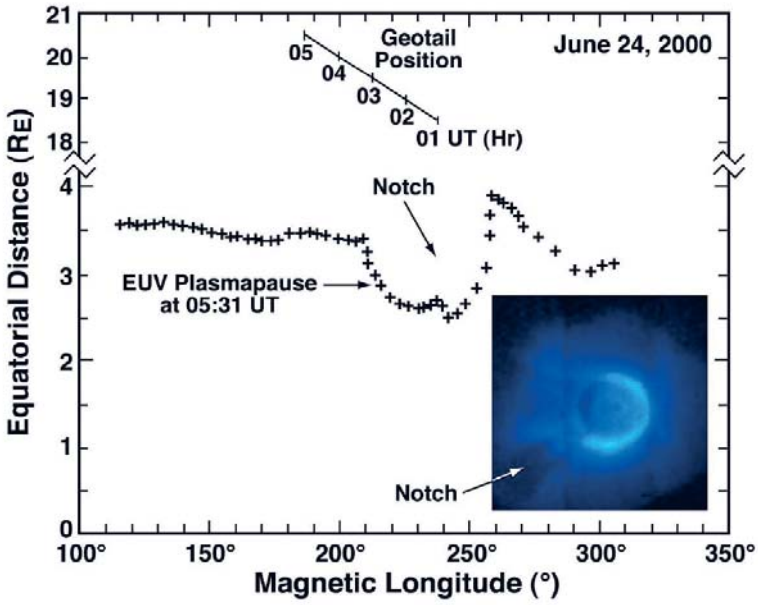

Figure 7b. The KC wave observations from Geotail/PWI (Figure 7a) map to a plasmaspheric notch structure as observed by IMAGE/EUV (adapted from [2]).

wave research using wave data obtained by sounding rockets, satellites, and ground stations in all heliophysics domains (e.g., Tables 1 and 2). Being a portal to such rich data contents, the VWO can benefit not only wave research, but also other heliophysics studies by enabling data comparisons, complex searches, and other services.

The VWO will provide unique data-search capabilities (Section 2.5.1) to support queries for heliophysics wave data. Such capabilities are ideal for conducting context searches for data obtained under the geophysical conditions (e.g., solar wind, magnetospheric state, etc.) and/or locations specified by the users [11]. With the support of SPASE-compliant metadata and *SPASEQL*, the same search capabilities can be applied to access data registered at other VxOs and distributed archives.

With the variety of heliophysics wave phenomena (electromagnetic, electrostatic, high and low frequency, trapped and freely-propagating, etc.), identifying a given set of observations with a particular phenomenon can sometimes be challenging to non-specialists. In order to increase the appreciation and use of wave data, the VWO will develop and post on its Web site [12] educational and tutorial materials to introduce the exciting science of waves, and to illustrate how wave data may be used in heliophysics studies. More importantly, VWO plans to develop an annotation service (Section 2.5.4) which will make searching for heliophysics wave data by phenomena possible, and more efficient and productive. Final success of VWO will depend on close collaboration between the VWO team and the wave researchers, whose input to the VWO (Section 4) will be highly valued.

Finally, it may be appropriate to give a few comments on the status of VWO development to date, and to provide an outlook of what is to come. Presently, about halfway into the three-year initial VWO development, the VWO team has helped develop the SPASE data model to enable basic descriptions of heliophysics wave data, although describing more-specialized wave data products may still require further data-model development. Using experience gained from applying SPASE to initially describe a few data sets (Table 1), we plan to develop a SPASE descriptor template for wave data. This template will be useful for constructing the VWO metadata database. A query builder with user interface, a part of the VQM (Figures 5 and 6), is being developed to support data search by context and location [11], as well as by time and platform. The VQM will be complemented by the development of SPASE-based search algorithms for locating, retrieving, and delivering data and information from data sources. As described in Section 2.5.4, VWO also plans to develop an annotation service patterned after the IMAGE RPI Expert Rating Service [12]. Although current VWO funding does not permit full annotation service development, we hope that in time it will become a key VWO feature that enables data search by phenomena.

6. Acknowledgements

The author gratefully acknowledges the VWO team for their critical roles in supporting VWO development. We especially thank T. King (UCLA) and the SPASE Consortium for their assistance in clarifying and resolving SPASE-related issues.

The VWO team members are:

Co-Investigators

R. F. Benson (NASA Goddard Space Flight Center, Greenbelt, MD)

T. E. Eastman (Wyle/GSFC, Greenbelt, MD)

I. A. Galkin (University of Massachusetts Lowell, MA)

L. N. Garcia (Wyle/GSFC, Greenbelt, MD)

J. Merka (University of Maryland Baltimore County, MD)

T. W. Narock (University of Maryland Baltimore County, MD)

B. W. Reinisch (University of Massachusetts Lowell, MA)

X. Shao (University of Maryland College Park, MD)

Collaborators

R. R. Anderson (University of Iowa, Iowa City, Iowa)

R. M. Candey (NASA Goddard Space Flight Center, Greenbelt, MD)

M. L. Kaiser (NASA Goddard Space Flight Center, Greenbelt, MD)

R. J. MacDowall (NASA Goddard Space Flight Center, Greenbelt, MD)

R. E. McGuire (NASA Goddard Space Flight Center, Greenbelt, MD)

J. D. Menietti (University of Iowa, Iowa City, Iowa)

D. Morrison (Johns Hopkins University, Applied Physics Laboratory)

J. S. Pickett (University of Iowa, Iowa City, Iowa)

A. Szabo (NASA Goddard Space Flight Center, Greenbelt, MD)

R. J. Walker (University of California Los Angeles)

R. S. Weigel (George Mason University, Fairfax, VA)

The Commission H Editor thanks the reviewers, Andris Vaivads and Jan Soucek, for their assistance in evaluating this paper.

7. References

1. "NASA Heliophysics Data Environment (HPDE):" http:// hpde.gsfc.nasa.gov

2. S. Fung, et al., "Guided Echoes in the Magnetosphere: Observations by Radio Plasma Imager on IMAGE," *Geophys. Res. Lett.*, **30**, 11, 1589, 2003, doi:10.1029/2002GL016531.

3. James L. Green and Shing F. Fung, "Advances in Inner Magnetosphere Passive and Active Wave Research," in Tuija I. Pulkkinen, Nikolai A. Tsyganenko, and Reiner H. W. Friedel (eds.), *The Inner Magnetosphere: Physics and Modeling*, (Geophysical Monograph Series, Volume 155), Washington, DC, American Geophysical Union, 2005, pp. 181-202.

4. J. W. LaBelle and R. A. Treumann (eds.), *Geospace Electromagnetic Waves and Radiation*, Berlin, Springer-Verlag, 2006.

5. J. S. Pickett, L.-J. Chen, S. W. Kahler, O. Santolík, M. L. Goldstein, B. Lavraud, P. M. E. Décréau, R. Kessel, E. Lucek, G. S. Lakhina, B. T. Tsurutani, D. A. Gurnett, N. Cornilleau-Wehrlin, A. Fazakerley, H. Rème, and A. Balogh, "On the Generation of Solitary Waves Observed by Cluster in the Near-Earth Magnetosheath," *Nonlinear Processes in Geophysics*, **12**, 2005, pp. 181-193, SRef-ID: 1607-7946/npg/2005-12-181.

6. J. L. Green, S. Boardsen, L. Garcia, W. W. L. Taylor, S. F. Fung, and B. W. Reinisch, "On the Origin of Whistler Mode Radiation in the Plasmasphere," *J. Geophys. Res*., **110**, 2005, A03201, doi:10.1029/2004JA010495.

7. B. W. Reinisch, D. M. Haines, K. Bibl, G. Cheney, I. A. Galkan, X. Huang, S. H. Myers, G. S. Sales, R. F. Benson, S. F. Fung, J. L. Green, W. W. L. Taylor, J.-L. Bougeret, R. Manning, N. Meyer-Vernet, M. Moncuquet, D. L. Carpenter, D. L. Gallagher, and P. H. Reiff, "The Radio Plasma Imager Investigation on the IMAGE Spacecraft," *Space Science Reviews*, **91**, 2000, pp. 319-359.

8. S. D. Shawhan, "Magnetospheric Plasma Wave Research 1975-1978," *Reviews of Geophysics and Space Physics*, **17**, 1979.

9. S. F. Fung and X. Shao, "Specification of Multiple Geomagnetic Responses to Variable Solar Wind and IMF Input," *Ann. Geophys*., **26**, 2008, pp. 639-652.

10. "NASA Heliophysics Science Data Management Policy:" http://lwsde.gsfc.nasa.gov/ Heliophysics_Data_ Policy_2009Apr12.html.

11. "SPASE Group Consortium:" http:// www.spase-group.org.

12. "Virtual Wave Observatory (VWO):" http:// vwo.nasa.gov.

13. "Virtual Solar Observatory (VSO):" http:// sdac.virtualsolar.org.

14. "Virtual Heliospheric Observatory (VHO):" http://vho.nasa.gov.

15. "Virtual Energetic Particle Observatory (VEPO):" http:// vepo.gsfc.nasa.gov.

16. "Virtual Magnetospheric Observatory (VMO):" http://vmo.nasa.gov.

17. "Virtual Radiation Belt Observatory (VIRBO):" http://virbo.org.

18. "Virtual Ionosphere, Thermosphere and Mesosphere Observatory (VITMO):" http:// vitmo.jhuapl.edu.

19. "Virtual Modeling Repository (VMR):" http:// vmr.engin.umich.edu.

20. "NASA's CDAWeb Data System:" http:// cdaweb.gsfc.nasa.gov.

21. "Planetary Data System (PDS):" http:// pds.nasa.gov.

22. "URSI Commission H Terms of Reference:" http://www.ursi.org/H/hterms.html.

23. S. F. Fung, X. Shao, L. N. Garcia, I. A. Galkin, R. F. Benson, "Facilitating Heliophysics Research by the Virtual Wave Observatory (VWO) Context Data Search Capability," *Eos Trans. AGU, Fall Meet. Suppl.,* **90***, 52*, 2009, (Abstract SH51B-1274) (presentation available at http://vwo.nasa.gov).

24. "W3C Recommendation on Web Services Description Language (WSDL):" http:// www.w3.org/TR/wsdl20/.

25. R. T. Fielding, *Architectural Styles and the Design of Network-based Software Architectures*, PhD Dissertation, University of California, Irvine, 2000 (see http://www.ics.uci.edu/~fielding/pubs/ dissertation/top.htm).

26. A. Roberts, "VO Framework," Virtual Observatories in Space and Solar Physics Workshop, Greenbelt, Maryland, October 27, 2004 (http://hpde.gsfc.nasa.gov/VO_Framework_7_Jan_05.doc).

27. "SPASE Query Language (*SPASEQL*):" http:// spaseql.gsfc.nasa.gov/.

28. T. W. Narock and T. King, "Developing a SPASE Query Language," SPASE Meeting, July 2007, Rutherford Appleton Laboratory, Abingdon, England; presentation available at http:// www.SPASE-group.org/meetings/Jul2007/ presentations/SPASEQueryLanguage.pdf.

29. I. A. Galkin, A. V. Kozlov, G. M. Khmyrov, and B. W. Reinisch, "Intelligent Resident Archive for RPI Level 2 Data," in P. Song, J. Foster, M. Mendillo, and D. Bilitza (eds.), *Radio Sounding and Plasma Physics, AIP Conference Proceedings 974*, Melville, NY, American Institute of Physics, 2008, pp. 111-117.

30. "SPASE-Related Tools:" http://www.spase-group.org/tools.

31. S. F. Fung, "Announcement of a 'Magnetospheric-State Query System,' *SPA Sect. Newsl.*, **XI**, Washington, DC, American Geophysical Union, 2004 (available at ftp:// igpp.ucla.edu/scratch/aguspa/volume11_2004/vol11no009).

32. "NASA's Satellite Situation Center Web Site (SSCWeb):" http://sscweb.gsfc.nasa.gov.

33. M. L. Kaiser, "Observations of Non-Thermal Radiation from Planets," in B. Tsurutani and H. Oya (eds.), *Plasma Waves and Instabilities at Comets and in Magnetospheres*, Washington, DC, American Geophysical Union, 1989, p. 221.

34. J. L. Green and S. A. Boardsen, "Kilometric Continuum Radiation," *Radio Science Bulletin*, No. 318, 2006, pp. 34-42.

35. K. Hashimoto, et al., "Review of Kilometric Continuum," in J. W. LaBelle and R. A. Treumann (eds.), *Lecture Notes in Physics 687: Geospace Electromagnetic Waves and Radiation*, New York, Springer, 2006, pp. 37-54.

36. J. L. Green, et al., "Association of Kilometric Continuum Radiation with Plasmaspheric Structures," *J. Geophys. Res*., **109**, 2004, A03203, doi:10.1029/2003JA010093.

37. D. B. Muldrew, "The Poynting Vector Applied to the Complex Refractive Index in a Hot Plasma Near the Electron Cyclotron Frequency and to the Cyclotron Resonance Observed on Topside Ionograms," *Radio Sci*., **41**, 2006, RS6006, doi:10.1029/2006RS003496.

38. R. F. Benson and S. F. Fung, "ISIS Topside-Sounder Plasma-Wave Investigations as Guides to Desired Virtual Wave Observatory (VWO) Data Search Capabilities," *Eos Trans. AGU, Fall Meeting Supplement,* **89**, 53, 2008 (Abstract SA51B-07); presentation available at http:// vwo.nasa.gov.

39. "ISIS/Alouette Data Restoration Project:" http://nssdc.gsfc.nasa.gov/space/isis/isis-status.html.

40. "ISIS-2 Topside Sounder Digital Data Search:" http://nssdc.gsfc.nasa.gov/space/isis/isis_menu4.html.

Radio Science Doctoral Abstract

Aaron Paul Chippendale, ***Detecting Cosmological Reionization on Large Scales through the 21 cm HI Line,*** the Sydney Institute for Astronomy, the University of Sydney, Sydney, Australia, December 2009; E-mail: Aaron.Chippendale@csiro.au.
Relevant Commission: J.

Abstract

This thesis presents the development of new techniques for measuring the mean redshifted 21 cm line of neutral hydrogen during reionization. This is called the 21 cm cosmological reionization monopole. Successful observations could identify the nature of the first stars, and test theories of galaxy and large-scale structure formation.

The goal was to specify, construct, and calibrate a portable radio telescope to measure the 21 cm monopole in the frequency range 114 MHz to 228 MHz, which corresponds to the redshift range $11:5 > z > 5:2$. The chosen approach combined a frequency-independent antenna with a digital correlation spectrometer to form a correlation radiometer. The system was calibrated against injected noise and against a modeled galactic foreground.

Components were specified for calibration of the sky spectrum to 1 mK/MHz relative accuracy. Comparing simulated and measured spectra showed that bandpass calibration was limited to 11 K, that is, 1% of the foreground emission, due to larger than expected frequency dependence of the antenna's pattern. Overall calibration, including additive contributions from the system and the radio foreground, was limited to 60 K. This was 160 times larger than the maximum possible monopole amplitude at redshift eight. Future work will refine and extend the system, known as the Cosmological Reionization Experiment Mark I (CoRE Mk I).

Radio-Frequency Radiation Safety and Health

James C. Lin

Frequent Exposure to Mobile Phones Changes Cognitive Behavior in Children

Issues of mobile phone use still are of interest to people, although money for biological or health-effects research has become increasingly more scarce worldwide. It is estimated that more than 90% of youngsters between the ages of 10 to 14 years have mobile phones or routine access to them in many countries.

A recent research paper on young adolescents' use of mobile phones in the *Bioelectromagnetics* journal [1] has picked up a considerable amount of media coverage. **M**edia outlets, including ABC News, *The Telegraph*, and *Brisbane Times*, among many others, reported on findings of the article with headlines of "Texting Changes Children's Brains," "Texting Makes Kids Faster and Dumber," "Text Messaging Trains Kids to be Fast But Inaccurate," and "Cell Phones May Make Children Impulsive."

The study examining cognitive functions in secondary-school children was part of the Mobile Radiofrequency Phone Exposed Users' Study in Australia. It included 317 seventh graders (145 boys, 172 girls, median age 13 years, range 11-14 years) from 20 schools around Melbourne, Australia. Most (299) of the 317 students had used a mobile phone, and 243 had their own phones.

The median reported duration of mobile-phone use was 1.74 years, with an inter-quartile range (IQR: 25th percentile - 75th percentile) from 0.89 to 2.63 years. The median total number of reported phone calls per week was eight (IQR four to 15 calls). The median number of reported short-message service (SMS) or text messages was also eight (IQR 2.5 to 20) per week.

This study is of interest for several reasons. The number of subjects involved is by far the largest of its kind to date, and it studied prolonged effects of mobile phones on a battery of cognitive functions of adolescents. It should be noted that acute, short-term effects of mobile phones on cognitive functions of children have previously been reported [2, 3]. However, the numbers of subjects were small in those preliminary studies. The limitations of acute effects on a small number of subjects made it difficult to draw any firm conclusions concerning the sensitivity of young children to radio-frequency radiation from mobile phones.

Specifically, one cognitive-function study of young users of standard 902 MHz GSM mobile phones found some trends toward faster reaction times, higher accuracy, and higher sensitivity in the presence of radio-frequency energy from mobile-phone exposure than under sham-exposure conditions [2]. However, none of these effects reached statistical significance. Moreover, the other study did not detect any change in cognitive functions [3].

In the recent Australian study [1], cognitive function was assessed with a computerized psychometric test battery and the color-word test. The cognitive function involved very basic information-processing tasks, such as signal detection, short-term memory or working memory, simple learning, associative learning, movement monitoring, and a color-word test.

The subjects wore headphones to present auditory cues, went through a training session of all tasks to standardize learning effects, and completed all tasks in succession, while a computer recorded their response times and accuracies. The signal-detection test consisted of simple reaction time, which measured the time taken to detect the presence of and perform a motor response to a stimulus; and choice reaction time, which had the added cognitive requirement of discriminating between two stimuli. These are used to assess possible impacts on neural function, as was the case for acute mobile-phone exposure [2].

The possible effects of mobile-phone exposure on short-term memory were assessed using one-back and two-back tasks, which tested the ability to flexibly hold information in working memory. It required the student to keep an object in memory for a short period so that it could be compared to another object, and then the first object

---

James C. Lin is with the University of Illinois-Chicago, 851 South Morgan Street, M/C 154, Chicago, IL 60607-7053 USA; Tel: +1 (312) 413-1052 (direct); +1 (312) 996-3423 (main office); Fax: +1 (312) 996-6465; E-mail: lin@ece.uic.edu.

[A version of this article appeared as J. C. Lin, "Cognitive Changes in Children from Frequency Use of Cell Phones," *IEEE Antennas and Propagation Magazine*, **52**, 1, February 2010, pp. 232-234; copyright 2010 by the IEEE.]

was discarded from memory and the latter one stored in its place. The two-back task required the student to keep an object in memory to compare with another object, following an intervening object that was then discarded. The tasks were assessed in terms of reaction time and accuracy, and required strong attention and mnemonic processes.

The simple learning test was a continuous visual-recognition task that examined visual-recognition memory and attention. Subjects were presented with an image of a playing card, and had to respond "Yes" or "No," depending on whether the card had previously been displayed. The associative learning test assessed the subject's ability to learn associations between images of playing cards, unlike the simple learning task, which required subjects to remember previously displayed cards.

The moving-card monitoring or movement-monitoring task evaluated the ability to track and correctly predict the motion of an object. The color-word test involved reading words representing the names of colors. One task directed the subject to read 50 words printed in black ink. The subject was also asked to name each of four colors presented in 50 meaningless symbols. An interference task called for the subject to read the word or identify the color in which it was printed, respectively, where the word and color were incongruous.

The study showed that children who reported more phone calls per week demonstrated shorter response times for the simple and associative learning tasks. More-frequent mobile-phone users also performed less accurately on working memory tests and the associative learning task. Simple and choice reaction times and movement monitoring were not related to the total number of phone calls per week. Interference by words printed in an incongruous color was greater among children who reported making and receiving more phone calls per week. Putting it another way, the completion time for word-naming tasks was longer for those reporting more mobile-phone calls.

Students who made and received more SMS messages exhibited shorter response times to the simple learning task, but less accurate responses to the working memory and associative learning tasks. Signal detection and movement monitoring were not related to total SMS messages. There were also no significant relationships between total SMS messages and interference by words printed in an incongruous color. Thus, there were no significant relationships between total SMS messages and word-naming completion time ratios

Overall, for both mobile-phone calls and SMS, simple learning-task reaction times and associative learning response times were shorter, but the accuracy of working memory and associative learning response were poorer for those reporting more mobile-phone use. There were no significant relationships between mobile-phone use and signal detection (simple and choice reaction times) and movement monitoring. However, the completion time for word-naming tasks was longer, indicating interference by words printed in an incongruous color was greater among children who reported making and receiving more phone calls per week

These findings are intriguing. In common usage, radio-frequency energy to the human head is minimal when the phone is held at a distance from the body during SMS. In contrast, a handset may be next to the head in making a phone call, with nearly 50% of the radio-frequency energy emitted from the mobile phone directed toward it.

In summary, it is interesting to note that apparently mobile-phone use was associated with faster but less accurate response in cognitive-function tasks. With the exception of the complex word-naming tasks, results were similar for children reporting more mobile-phone calls or a greater total number of SMS or text messages per week, suggesting that these cognitive changes were not due to radio-frequency exposure, if confirmed by subsequent experiments. Instead, the behavior may have resulted from more-frequent use of mobile phones and acquired cognitive skills.

References

1. M. J. Abramson, G. P. Benke, C. Dimitriadis, I. O. Inyang, M. R. Sim, R. S. Wolfe, and R. J. Croft, "**Mobile Telephone Use is Associated with Changes in Cognitive Function in Young Adolescents,"** *Bioelectromagnetics*, **30**, 2009, pp. 678-686.

2. A. W. Preece, S. Goodfellow, M. G. Wright, S. R. Butler, E. J. Dunn, Y. Johnson, T. C. Manktelow, and K. Wesnes, "Effect of 902 MHz Mobile Phone Transmission on Cognitive Function in Children," *Bioelectromagnetics Supplement*, **7**, 2005, pp. S138-S143.

3. C. Haarala, M. Bergman, M. Laine, A. Revonsuo, M. Koivisto, and H. Hämäläinen, "Electromagnetic Field Emitted by 902 MHz Mobile Phones Shows no Effects on Children's Cognitive Function," *Bioelectromagnetics Supplement*, **7**, 2005, pp. S144-S150.

Conferences

CONFERENCE REPORT

International Reference Ionosphere Workshop 2009

Kagoshima, Japan, November 2-7, 2009

The 2009 URSI/COSPAR Workshop on the International Reference Ionosphere (IRI) was held at Kagoshima University in Kagoshima, Japan, from November 2-7, 2009. IRI is a joint project of the International Union of Radio Science (URSI) and the Committee on Space Research (COSPAR). Annual meetings are the primary venue for the improvement of the IRI representation of ionospheric parameters, such as electron density, electron temperature, ion composition, ion temperatures, and total electron content (TEC). The special emphasis of the 2009 Workshop was on (1) regional modeling of the ionosphere, and (2) ionosphere/atmosphere/geosphere coupling studies for improvement of IRI. Other topics of interest for the workshop included comparisons of IRI with other models and with satellite/ground observations, proposed changes to the IRI models for improved performance and accuracy, and applications of the model in the many areas of interest. The workshop home page with more information and workshop details is at http://www.ep.sci.hokudai.ac.jp/ ~iri2009/.

The workshop received financial support from the following sponsors: COSPAR, URSI, Kagoshima Prefecture, Kagoshima City, Hokkaido University, Japan Aerospace Exploration Agency (JAXA), Kagoshima University, National Institute of Information and Communications Technology (NICT), Air Force Office of Scientific Research, Society of Geomagnetism and Earth, Planetary and Space Sciences, Society for Promotion of Space Science, Hombo Shoten Company Ltd., Keirinkan Company Ltd., AD Company Ltd., and Elm Company Ltd.

The workshop was a great success, with 113 participants from 20 countries, including many students and several first-time IRI contributors from Japan, China, Taiwan, Thailand, Malaysia, and Philippines. The 117 presentations were grouped into one poster session and three oral sessions covering the topics "Structure and Dynamics of the Ionosphere," "Solar and Geomagnetic Variability of the Ionosphere," and "Ionosphere-Thermosphere Coupling." A final discussion session reviewed the presented results, and came up with proposals for future improvements of IRI.

Papers presented at the workshop were based on data from many ground stations and satellites, including ionosonde stations, incoherent-scatter radars, and the satellites Alouette, ISIS, AE-C, Akebono, CHAMP, GPS, ROCSAT-1, Demeter, DMSP, TIMED, IMAGE, COSMIC, and TOPEX/Jason. Radio-occultation measurements from the COSMIC constellation are a promising new data source for improvements of the global representation of the topside and plasmaspheric electron density in IRI, and were extensively discussed during the meeting. Comparisons with ionosonde and incoherent-scatter radar data are helping to correct and improve the COSMIC data-analysis scheme. Test computations in an IRI ionosphere were also used to evaluate the density reconstruction technique. Differences with ionosonde bottomside profiles are generally below the 10% level, but larger discrepancies are found in the topside when comparing with incoherent-scatter radar measurements. Demeter, launched in 2004 and still operating, is another global data source for IRI, covering the recent extended low solar minimum. First comparisons presented at the meeting show that IRI electron densities are higher than the Demeter measurements, whereas electron temperatures are lower. Data from several new ionosonde stations were presented at the meeting and compared with IRI. This included the Korean Anyang station (geographic latitude 37.4°N, longitude 127°E; geomagnetic latitude 27.7°N); the Thai Chumphon station (10.7°N, 99.4°E; 3.2°S); the Thai Chiang Mai station (18.8°N, 98.9°E; 13.2°N); and the Indonesian Katotabang station (0.2°S, 100.3°E; 10.1°S). The latter three are aligned along the 100° meridian, and they are part of the South East Asian Low-latitude IOnospheric Network (SEALION), which also includes the Vietnamese stations in Phu Thuy (21.03°N, 105.96°E) and Bac Lieu (9.30°N, 105.71°E). Data from these stations are of particular interest for modeling the equatorial anomaly in the Asian sector.

During the final-discussion session, the Working Group decided on several improvements for the next release of the model. Most importantly, the improved representation of the seasonal and solar-cycle variations of the bottomside electron-density profile as modeled by Altadill et al. (Ebro Observatory, Spain), based on ionosonde data, will be introduced into IRI. For the F peak, the goal is to introduce the neural-network models of McKinnell (South Africa) and Oyeyemi (Nigeria) into IRI. These models are based on a much larger volume of

data than the original CCIR and URSI models, and they have proven to be superior to the older models. At auroral latitudes, IRI-2010 will benefit from the efforts of two groups using TIMED data. Mertens et al. (NASA Langley, USA) have used SABER data for the development of an E-peak storm model, and Zhang and Paxton (APL/JHU, USA) have developed a model for the auroral particle energies and fluxes and the auroral boundaries based on GUVI data. With the inclusion of auroral boundaries and the description of the expansion of the oval with magnetic activity, the IRI team can now focus on the representation of characteristic structures such as the sub-auroral Ne depletion (trough) and Te enhancement. In the topside, the Vary-Chap approach of Reinisch and Huang (UML, USA) for Ne has reached a high degree of maturity, but still needs a global study of the relationship between the topside and bottomside scale heights. Several presentations during the workshop reported on sporadic-E occurrence statistics, a parameter not yet included in IRI. This information would be important for HF communication, especially over long distances. A good approach would be to model the occurrence probability at different frequencies.

For the electron temperature, IRI-2010 will include the new model that Truhlik et al. (IAP, Czech Republic) presented at the meeting. The model is based on a large volume of in-situ measurements from different satellites. The main improvement over its predecessor is the inclusion of the solar-activity dependence of Te. The same now needs also to be done for the ion temperature. A better model is also scheduled to be included for the molecular ion densities in the bottomside ionosphere. This has long been a weak point of IRI, because of the limited availability of reliable data for these parameters. The new model is based on the well-established photochemistry in this region, and on normalizing the chemical-equilibrium calculation to the IRI electron density (Richards and Bilitza, George Mason University, USA). In the D-region, the model of Friedrich (TH Graz, Austria) for the transition height from molecular to cluster ions will be a new addition to IRI.

The meeting program and logistics were expertly handled by the Local Organization Committee, chaired by Prof. Shigeto Watanabe (Hokkaido University, Japan). The LOC also organized a very informative scientific excursion to the Yamagawa Radio Observatory of the National Institute of Information and Communication Technology (NICT), with a visit and luncheon at the Ibusuki hot sand resort. A new feature during this IRI workshop was the awarding of Best Student Paper Awards. The first recipients were Y. Y. Sun (National Central University, Taiwan) for "The Comparison of Low Latitude Spread-F Measured by IRI2007, FORMOSAT-1 and GPS Ground-Based Receivers During Solar Maximum;" A. Ichihara (Nagoya University, Japan) for "Nighttime Medium-Scale Traveling Ionospheric Disturbances Propagating Northward Observed by the SuperDARN Hokkaido HF Radar and GEONET;" T. Kondo (Hokkaido University, Japan) for "Thermospheric Zonal Neutral Wind and Zonal Plasma Drift Controlled by F-Region Dynamo;" and N. Kitamura (Tohoku University, Japan) for "Solar Zenith Angle Dependence of the Electron Density Profile in the Polar Topside Ionosphere During Geomagnetically Quiet Periods in the Solar Maximum."

The workshop website is at http:// www.ep.sci.hokudai.ac.jp/~iri2009/.

Papers from the 2007 IRI Workshop have now been published in two issues of *Advances in Space Research*: D. Bilitza, Jan Laštovička, B. Reinisch (eds.), "Ionosphere – Modeling, Forecasting, and Telecommunications I," *Advances in Space Research*, **43**, 11, June 2, 2009, pp. 1595-1846; and B. Reinisch, D. Bilitza, and Jan Laštovička (eds.), "Ionosphere – Modeling, Forecasting, and Telecommunications II," *Advances in Space Research*, **44**, 6, June 2, 2009, pp. 641-774. The papers from the Kagoshima Workshop will be published in a special issue of *Earth, Planet, Space*.

The next IRI meetings are planned as follows:

2010 : COSPAR Scientific Assembly, Bremen, Germany, July 18-25, 2010: two-day session on IRI in the auroral and polar ionosphere (MSO: Bilitza)

2011 : one-week workshop at the Hermanus Observatory in Hermanus, South-Africa (MSO: McKinnell)

2013 : one-week workshop at the University of Warmia and Mazury in Olsztyn, Poland (MSO: Krankowski)

Dieter Bilitza
E-mail: dieter.bilitza-1@nasa.gov

CONFERENCE ANNOUNCEMENT

NORDIC HF CONFERENCE
HF 10 WITH LONGWAVE SYMPOSIUM LW 10

Fårö, Sweden, August 17-19, 2010

General

HF, LF, and VLF systems are fields of increasing importance. NRS, the Nordic Radio Society, is a foundation cooperating with SNRV, the Swedish National Committee of URSI. They invite you to the ninth Nordic HF conference, combined with an integrated long-wave symposium, LW 10. Nowadays, HF 10 is one of the very few HF conferences, and LW 10 is the only one on VLF/LF.

VLF, LF, and HF communications technology has advanced significantly over the last few years, with trends towards a higher degree of automation, and signal processing that can be cost-effectively implemented to achieve affordable performance, even in small systems. Topics focus on communications beyond the horizon with emphasis on HF, LF, and VLF radio, but include these as information bearers for other applications.

Since the first conference in 1986, each Nordic HF conference has gathered around 150 participants. These have enjoyed the relaxed atmosphere and stimulating company of colleagues in the informal setting provided by the unique nature of Fårö and the Fårö Training Camp on the Baltic Sea. The triennial Nordic HF conferences are always at Fårö, and always in week 33.

We are happy to announce two well-known invited speakers: Prof. L. W. (Les) Barclay, OBE, and Thormod Bøe, former director of ERO, the European Radio Office (now ECO, the European Communication Office).

Call for Papers

The second invitation with preliminary program is available for downloading from the HF 10 Web site: http://www.nordichf.org. There you will find further information, such how to submit an abstract, the conference fee, with generous discounts for students and pensioners, scholarship grants, the step-by-step registration procedure, the conference organization, as well as travel and lodging. Industry will have the opportunity to display their products, no costs incurred.

Further Information

The conference will open on Tuesday morning and close on Thursday afternoon. Please schedule arrival for Monday afternoon or evening on August 16, and departure on Friday, August 20. At a nominal charge, the camp will be open for families and on adjoining weekends.

Please register no later than May 30 on the Web site, or using the form available there by letter or fax to HF 10, Saab, SE-581 82 Linköping, Sweden (Fax: +46-13-299235). For further information, please e-mail to info@nordichf.org.

The conference venue is the Fårö kursgård camp. The camp is comfortable but Spartan, and shared quarters will allow attendees to meet new friends. Authors, participants, exhibitors, and family members are welcome to meet in an excellent conference theater, in an interesting exhibition area, and in a camp near Mother Nature, well suited to participants and their families.

URSI CONFERENCE CALENDAR

March 2010

MicroRad 2010
Washington, DC, USA, 1-4 March 2010
Web: http://www.microrad2010.org/

8th International Nonlinear Waves Workshop
La Jolla, CA, USA, 1-5 March 2010
Contact: William E. Amatucci, Plasma Physics Division, Code 6755, Naval Research Laboratory, Washington, DC 20375, USA, Fax : 202-767-3553, E-mail : bill.amatucci@nrl.navy.mil

3rd Workshop on RFI Mitigation in Radio Astronomy
Groningen, The Netherlands, 29-31 March 2010
Contact: Prof. W.A. BAAN, Netherlands Foundation for Research, in Astronomy - Westerbork Observatory, P.O. Box 2, NL-7990 AA DWINGELOO, NETHERLANDS, Fax : +31 521-595 101, E-mail: baan@astron.nl

April 2010

AP-EMC 2010 - Asia-Pacific EMC Symposium
Beijing, China, 12-16 April 2010
Contact: Web: http://www.apemc2010.org

May 2010

EMF Bordeaux Event, including the URSI Commission K midterm meeting
Bordeaux, France, 26-29 May 2010
Contact : Web : http://ebea.org/menu.html

June 2010

CROWNCOM - 5th Int. Conference on Cognitive Radio Oriented Wireless Networks and Communications
Cannes, France, 16-18 June 2010
Contact : Jacques Palicot, SUPELEC, Avenue de la Bulaie, 53576 Cesson-Sévigné, France, Fax +33 299-844599, E-mail: jacques.palicot at supelec.fr

OCOSS 2010 - Ocean and Coastal Observation: sensors and observing systems, numerical models and information systems
Brest, France, 21-23 June 2010
Contact: jisnard-isti at club-internet.fr

MSMW 2010
Kharkov, Ukraine, 21-26 June 2010
Contact : Alexei Kostenko, IRE NASU, ul. Proskura 12, Kharkov 61085, Ukraine, Fax: +380(57)3152105, E-mail:kostenko at ire.kharkov.ua

July 2010

SCOSTEP - STP12
Berlin, Germany, 12-16 July 2010
Contact: Prof. Dr. Franz-Josef Lübken, Leibniz Institute of Atmospheric Physics, Schloss-Straße 6, 18225 Kühlungsborn, Germany, Fax: +49-38293-6850, E-Mail: luebken@iap-kborn.de, http://www.iap-kborn.de/SCOSTEP2010/

COSPAR 2010 - 38th Scientific Assembly of the Committee on Space Research (COSPAR) and Associated Events
Bremen, Germany, 18 - 25 July 2010
cf. Announcement in the Radio Science Bulletin of December 2008, p. 73.
Contact: COSPAR Secretariat, c/o CNES, 2 place Maurice Quentin, 75039 Paris Cedex 01, France, Fax: +33 1 44 76 74 37, E-mail: cospar@cosparhq.cnes.fr, Web: http://www.cospar2010.org/ or http://www.cospar-assembly.org

August 2010

EMTS 2010 - International Symposium on Electromagnetic Theory (Commission B Open Symposium)
Berlin, Germany, 16-19 August 2010
Contact: EMTS 2010, Prof. Karl J. Langenberg, Universität Kassel, D-34109 Kassel, Germany, E-mail: info@emts2010.de , Web: http://www.emts2010.de

Nordic Shortwave Conference HF10 and Longwave Symposium LW10
Farö, North of the Island of Gotland in the Baltic, 17-19 August 2010
Contact : Saab Aerotech, Nobymalmsvägen, SE- 58182 Linköping, Sweden, Phone : +46 13 23 13 21, Fax : +46 13 29 92 35, E-mail : margareta.samuelsson@saabgroup.com, Web : http://www.nordichf.org

3rd International Communications in Underground and Confined Areas
Val d'Or, Québec, Canada, 23-25 August 2010
Contact: Paule Authier, Secrétaire, LRTCS-UQAT, Laboratoire de recherche Télébec en communications souterraines de l'UQAT, 450, 3e Avenue, local 103, Val-d'Or,Québec J9P 1S2, Fax: (1)(819) 874-7166, E-mail: lrcs@uqat.ca, Web: http://www.icwcuca.ca/welcome.asp

ISRSSP'10 - 2nd International Symposium on Radio Systems and Space Plama
Sofia, Bulgaria, 25-27 August 2010
Contact : E-mail: Blagovest Shishkov - bshishkov at math.bas.bg, Web: http://www.isrssp.org
cf. Announcement in the Radio Science Bulletin of December 2009, p.33-34 .

September 2010

ISTC2010 - International Symposium on Turbo Codes
Brest, France, 6-10 September 2010
cf. Announcement in the Radio Science Bulletin of December 2009, p. 34-36.
Contact: Télécom Bretagne, International Symposium on Turbo Codes, Département: Électronique, Technopôle Brest Iroise, CS83818, 29238 BREST Cedex, FRANCE, Tel: +33 2 98 00 10 28, Fax : +33 2 98 00 11 84, Email : istc at mlistes.telecom-bretagne.eu, Web: http://conferences.telecom-bretagne.eu/turbocodes/

Metamaterials 2010 - The Fourth International Congress on Advanced Electromagnetic Materials in Microwaves and Optics
Karlsruhe, Germany, 13-16 September 2010
Contact : Web: http://congress2010.metamorphose-vi.org/

ISSSE 2010
Nanjing, China, 16-19 September 2010

ICEAA 2010 - International Conference on Electromagnetics in Advanced Applications
Sydney, Australia, 20-24 September 2010
cf. Announcement in the Radio Science Bulletin of September 2009, p. 62-63.
E-mail: Roberto.Graglia@polito.it, Web: http://www.iceaa-offshore.org/

AP-RASC - 2010 Asia-Pacific Radio Science Conference
Toyama, Japan, 22-26 September 2010
cf. Announcement in the Radio Science Bulletin of December 2009, p. 6-8.
Contact: Prof. K. Kobayashi, Vice President for International Affairs, Chuo University, 1-13-27 Kasuga, Bunkyo-ku, Tokyo 112-8551, JAPAN, Fax: +81-3-3817-1847, E-mail: kazuya@tamacc.chuo-u.ac.jp

URSI cannot be held responsible for any errors contained in this list of meetings.

October 2010

Commission F Microwave Signatures Symposium
Florence, Italy, 4-8 October 2010
Contact: Prof. P. Pampaloni, IFAC/CNR, Florence, Italy, Fax +390 555 226434, E-mail: p.pampaloni@ifac.cnr.it

December 2010

2010 Asia-Pacific Microwave Conference
Yokohama, Japan, 7-10 December 2010
Contact: Prof. Kiyomichi Araki, Chair, Steering Committee, c/o Real Communications Corp., 3F Shinmatsudo, Matsudo 270-0034, Japan, Tel. +81 47-309-3616, Fax +81 47-309-3617, E-mai: nweapmc at io.ocn.ne.jp, Web: www.apmc2010.org

An up-to-date version of this Conference Calendar, with links to various conference web sites can be found at www.ursi.org/Calendar of supported meetings

News from the URSI Community

NEWS FROM A MEMBER COMMITTEE

France
Médaille du CNFRS

La Médaille du Comité National Français de Radioélectricité Scientifique (CNFRS) section française de l'Union Radio Scientifique Internationale (URSI) a été décernée le 16 mars 2010 à Pierre-Noël Favennec.

Le CNFRS (URSI-France) souhaite, par cette médaille, souligner tant l'importance des contributions de Pierre-Noël Favennec au développement des radiosciences et de la physique des composants hyperfréquences et optoélectroniques que son rôle majeur dans l'animation des communautés scientifiques de ces domaines, dans la diffusion des connaissances et dans la promotion de l'édition scientifique, en particulier comme directeur de la Collection Télécom.

La Médaille du CNFRS/URSI est « destinée à honorer des personnes qui ont œuvré pour le renom de la Science en Radioélectricité et/ou participé d'une manière très significative à la vie et au renom du CNFRS/URSI »

Pierre-Noël Favennec, né en 1943 à Quimper, docteur ès sciences physiques (Faculté des sciences de Rennes), intègre en 1967 le Centre national des études et des télécommunications (CNET), à Lannion, et le laboratoire « Études sur les Radiations des Matériaux », nouvellement créé, dirigé par Gérard Pelous, laboratoire qui s'est par la suite orienté vers les technologies d'implantation ionique puis, plus largement, vers la physique et technologies des composants et dispositifs nécessaires aux télécommunications.

Il y a plus particulièrement étudié les matériaux III-V tels que le GaAs et l'InP. Ses travaux sur les composants hyperfréquences (Transistors MESFET, circuits intégrés) et optoélectroniques (lasers, DEL, afficheurs, photodétecteurs) ont donné lieu à douze brevets, une centaine de publications, une cinquantaine de conférences, des enseignements spécialisés de 3ème cycle, et deux ouvrages. Ces dispositifs ayant donné lieu à applications industrielles, il s'est orienté par la suite vers l'étude du dopage de l'erbium dans divers matériaux dans l'objectif de concevoir des composants de télécommunications optiques émettant à 1,56 µm. Travail qui a abouti à une première DEL en silicium et à la démonstration que tout matériau dopé à l'erbium, ayant un gap plus grand que 0,8 eV, émettait à 1,56 µm et était potentiellement applicable pour les télécommunications optiques.

En 1992, il est nommé à la Direction scientifique du CNET et est chargé des domaines de la microélectronique, des télécommunications hertziennes et optiques. Sous l'impulsion de Jeannine Hénaff, il coordonne et engage des actions propres à investir des domaines innovants en mettant en réseau laboratoires du CNET et laboratoires académiques. C'est ainsi que des thématiques telles que les fonctions opto-hyper, les antennes millimétriques, les nouvelles fonctions optiques, les communications quantiques (1996), le millimétrique, santé et téléphonie mobile (action lancée en 1994) etc. ont été explorées et ont données lieu à publications, séminaires et conférences etc. Parallèlement, Pierre-Noël Favennec a continué à prospecter de nouveaux thèmes de recherche comme les liaisons à peu de photons (co-brevet), les liaisons optiques sans fil, les objets communicants, les écrans souples, le GTTH (Gigabits To The Home)… En 1994, il prend en charge la Collection technique et scientifique des télécommunications (CTST). Sous son impulsion, 60 livres ont, à ce jour, été édités. La CTST, collection en français et pour une plus grande reconnaissance des auteurs français, il favorise, en partenariat avec les grands éditeurs internationaux, des traductions d'ouvrages (18 ouvrages à ce jour).

En 2003, il devient consultant à la Direction scientifique de l'Institut Télécom, tout en continuant à diriger la CTST, renommée Collection Télécom. Il prend alors une part encore plus active dans l'édition scientifique et notamment en prenant des responsabilités dans des comités de rédaction (Annales des télécommunications, I2M, Radio Science Bulletin), en étant rédacteur en chef invité dans Comptes Rendus Physique (2 numéros thématiques) ou rédigeant des articles de synthèse sur la mesure de l'environnement radioélectrique.

Il prend, de même, une part très active dans la vie d'URSI-France, officiellement le Comité national français de radioélectricité scientifique, où, après avoir été président de la commission « Électronique et optique », il en assume la Présidence de 2003 à 2006 et depuis il continue d'y être très présent.

En 2005, premier Président de la Fondation de recherche « Santé et radiofréquences », il met en place celle-ci, en veillant à un dialogue exigeant entre associations-industriels-scientifiques-représentants de l'État…

Face à la nécessité de développer la communication scientifique à l'attention du grand public, il crée, en collaboration avec l'Association bretonne pour la recherche et la technologie (ABRET) une exposition itinérante « Un monde sans fil – les ondes en questions ? ». De même face aux nouvelles avancées technologiques et au besoin du public de comprendre et de recevoir une information objective, Pierre-Noël Favennec s'est fortement investit dans l'animation des associations bretonnes de culture et de diffusion scientifique que sont l'ABRET et l'APAST (Association Pour l'Animation Scientifique du Trégor).

BOOKS PUBLISHED FOR URSI RADIOSCIENTISTS

The Earth's Ionosphere: Plasma Physics and Electrodynamics, Second Edition

by Michael C. Kelly; San Diego, Academic Press, 2009, ISBN 13:978-0-12-088425-4; hardcover, 577 pp., USD 89.95.

Following the success of the first edition, in this second edition the author has extended the scope of the book by introducing many of the recent advances in the lower D-region of the ionosphere, and by emphasizing the importance of the coupling of the ionosphere to the neutral atmosphere. The book covers all aspects of the Earth's ionosphere, and is divided into 10 chapters.

The first chapter provides a historical overview of ionospheric research. The second chapter gives a detailed description of ionospheric and magnetospheric plasma, and provides a graduate-level text on magnetohydrodynamics. Chapter 3 is devoted to the electrodynamics of the equatorial zone. Because of the horizontal nature of the Earth's magnetic field, this region exhibits a number of unique phenomena. Thermospheric winds in the equatorial region are explained to be the source of energy that maintains the electric field. Direct measurements of such winds by the Fabrey-Perot technique are presented. The dynamics of the F and E regions are discussed both theoretically and

experimentally, with reference to results from incoherent-scatter radar measurements made at Jicamarca Radio Observatory, in Peru. Chapter 4 provides a comprehensive review of equatorial plasma instabilities, starting with F-region instabilities "convective equatorial ionospheric storms (CEIS)," and followed by E-region plasma instabilities. The author's expertise in this area means there is a good in-depth discussion of contributing processes, namely gravity waves, shear effects, the generalized Rayleigh-Taylor instability, and diffusive damping by wave-wave coupling. The nonlinear theories of electrojet instabilities in the E-region (i.e., the gradient drift and Farley Buneman) are presented in good detail, together with numerical simulations. In Chapter 5, the focus shifts away from the equator to the mid-latitude ionosphere. The complex coupled electrodynamic system of the ionosphere is detailed by considering the outflow of plasma along magnetic field lines during the day, and low-altitude recombination and inflow of plasma at night, with the contribution of neutral wind and electric field in the movement of plasma. A strength of the text is that the theoretical considerations of these processes are accompanied by appropriate observations from incoherent-scatter radar.

Chapter 6 continues at mid-latitudes by addressing waves and instabilities in this region. Since the neutral-wind effects are important at mid-latitude, the role of gravity waves and tides in creating vertical structure have been examined in detail. The role of horizontal structure and the need for an elongated sporadic-E layer for the existence of two-stream instabilities are also illustrated. Most of the theoretical developments are based on explaining the observed layered structures. This chapter concludes with a recent theory of wind-driven thermal instabilities, in support of recent radar observations demonstrating the constant evolution of our knowledge of the ionosphere.

Continuing the theme of new knowledge, Chapter 7 is devoted to a new area of scientific interest in the mesosphere, namely the polar summer mesosphere and noctilucent clouds. This interesting and poorly understood region of the upper atmosphere is associated with dusty or icy plasmas. The scientific interest in this area has grown with the idea of a link between polar mesospheric summer echoes (PMSE), noctilucent clouds, and atmospheric changes. This chapter also discusses a growing area of interest, that of upward-propagating lightning and accompanying phenomena, such as "sprites," elves, and "blue jets."

The last three chapters, Chapters 8, 9, and 10, cover the high-latitude ionosphere, starting with the coupling between ionosphere, magnetosphere, and solar wind. Chapter 8 discusses the relationship between the electric field and currents that are present in the coupled system. It sets the scene for the more-complex high-latitude ionospheric phenomena, such as electrodynamic forcing of the neutral atmosphere, particle acceleration, and ion outflows, all of which are discussed in Chapter 9. The final chapter focuses on high-latitude instabilities and waves and E-region irregularities. The author does excellent work in covering more than 40 years of theoretical and observational studies of high-latitude ionospheric instabilities.

In summary, this book is an excellent source of information on ionospheric structures and instabilities. It does not cover all aspects of ionospheric science. However, the physical and chemical processes controlling the behavior of the ionosphere, including reaction rates and transport equations, are well documented in other text books, such as the book on the ionosphere by Schunk and Nagy (2000), or a classic text book by Rishbeth and Garriott (1969). This text also does not cover the recent advances in global ionospheric morphology, despite the trend in global studies of ionospheric phenomena with advances in space and ground-based instrumentations (e.g., SuperDARN radars).

In the first edition, Chapter 4 included a section on future directions. There it was mentioned that future advances in space research will come from direct comparison between experimental results and numerical simulation. It is unfortunate that no discussion of recent modeling efforts have been included in this current edition.

Although I suspect that this book will be most useful for graduate-level students and researchers, each chapter has some material for use in undergraduate courses on the Earth's ionosphere, or as an introduction to space plasmas. The accompanying Web site is a very useful teaching aid, with a large number of problems and their associated solutions. There are two online appendices on ionospheric measurement techniques (Appendix A) and magnetic indices and basic formulas (Appendix B). It is unfortunate that these appendices are only available on the accompanying Web site, as they would have been a valuable addition to the printed book, if only as a matter of completeness.

Farideh Honary
Lancaster University, UK
E-mail: f.honary@lancaster.ac.uk

Information for authors

Content

The *Radio Science Bulletin* is published four times per year by the Radio Science Press on behalf of URSI, the International Union of Radio Science. The content of the *Bulletin* falls into three categories: peer-reviewed scientific papers, correspondence items (short technical notes, letters to the editor, reports on meetings, and reviews), and general and administrative information issued by the URSI Secretariat. Scientific papers may be invited (such as papers in the *Reviews of Radio Science* series, from the Commissions of URSI) or contributed. Papers may include original contributions, but should preferably also be of a sufficiently tutorial or review nature to be of interest to a wide range of radio scientists. The *Radio Science Bulletin* is indexed and abstracted by INSPEC.

Scientific papers are subjected to peer review. The content should be original and should not duplicate information or material that has been previously published (if use is made of previously published material, this must be identified to the Editor at the time of submission). Submission of a manuscript constitutes an implicit statement by the author(s) that it has not been submitted, accepted for publication, published, or copyrighted elsewhere, unless stated differently by the author(s) at time of submission. Accepted material will not be returned unless requested by the author(s) at time of submission.

Submissions

Material submitted for publication in the scientific section of the *Bulletin* should be addressed to the Editor, whereas administrative material is handled directly with the Secretariat. Submission in electronic format according to the instructions below is preferred. There are typically no page charges for contributions following the guidelines. No free reprints are provided.

Style and Format

There are no set limits on the length of papers, but they typically range from three to 15 published pages including figures. The official languages of URSI are French and English: contributions in either language are acceptable. No specific style for the manuscript is required as the final layout of the material is done by the URSI Secretariat. Manuscripts should generally be prepared in one column for printing on one side of the paper, with as little use of automatic formatting features of word processors as possible. A complete style guide for the *Reviews of Radio Science* can be downloaded from http://www.ips.gov.au/IPSHosted/NCRS/reviews/. The style instructions in this can be followed for all other *Bulletin* contributions, as well. The name, affiliation, address, telephone and fax numbers, and e-mail address for all authors must be included with

All papers accepted for publication are subject to editing to provide uniformity of style and clarity of language. The publication schedule does not usually permit providing galleys to the author.

Figure captions should be on a separate page in proper style; see the above guide or any issue for examples. All lettering on figures must be of sufficient size to be at least 9 pt in size after reduction to column width. Each illustration should be identified on the back or at the bottom of the sheet with the figure number and name of author(s). If possible, the figures should also be provided in electronic format. TIF is preferred, although other formats are possible as well: please contact the Editor. Electronic versions of figures *must* be of sufficient resolution to permit good quality in print. As a rough guideline, when sized to column width, line art should have a minimum resolution of 300 dpi; color photographs should have a minimum resolution of 150 dpi with a color depth of 24 bits. 72 dpi images intended for the Web are generally *not* acceptable. Contact the Editor for further information.

Electronic Submission

A version of Microsoft *Word* is the preferred format for submissions. Submissions in versions of T_EX can be accepted in some circumstances: please contact the Editor before submitting. *A paper copy of all electronic submissions must be mailed to the Editor, including originals of all figures.* Please do *not* include figures in the same file as the text of a contribution. Electronic files can be send to the Editor in three ways: (1) By sending a floppy diskette or CD-R; (2) By attachment to an e-mail message to the Editor (the maximum size for attachments *after* MIME encoding is about 7 MB); (3) By e-mailing the Editor instructions for downloading the material from an ftp site.

Review Process

The review process usually requires about three months. Authors may be asked to modify the manuscript if it is not accepted in its original form. The elapsed time between receipt of a manuscript and publication is usually less than twelve months.

Copyright

Submission of a contribution to the *Radio Science Bulletin* will be interpreted as assignment and release of copyright and any and all other rights to the Radio Science Press, acting as agent and trustee for URSI. Submission for publication implicitly indicates the author(s) agreement with such assignment, and certification that publication will not violate any other copyrights or other rights associated with the submitted material.

APPLICATION FOR AN URSI RADIOSCIENTIST

I have not attended the last URSI General Assembly, and I wish to remain/become an URSI Radioscientist in the 2009-2011 triennium. Subscription to *The Radio Science Bulletin* is included in the fee.

(please type or print in BLOCK LETTERS)

Name : Prof./Dr./Mr./Mrs./Ms. _____
Family Name First Name Middle Initials

Present job title: _____

Years of professional experience: _____

Professional affiliation: _____

I request that all information be sent to my ☐ home ☐ business address, i.e.:

Company name: _____

Department: _____

Street address: _____

City and postal/zip code: _____

Province/State: _____ Country: _____

Phone: _____ ext._____ Fax: _____

E-mail: _____

Areas of interest (Please tick)

☐ A Electromagnetic Metrology
☐ B Fields and Waves
☐ C Radio-Communication Systems & Signal Processing
☐ D Electronics and Photonics
☐ E Electromagnetic Environment & Interference
☐ F Wave Propagation & Remote Sensing
☐ G Ionospheric Radio and Propagation
☐ H Waves in Plasmas
☐ J Radio Astronomy
☐ K Electromagnetics in Biology & Medicine

I prefer (Please tick)

☐ An electronic version of the RSB downloadable from the URSI web site
(The URSI Board of Officers will consider waiving the fee if a case is made to them in writing.) 40 Euro

☐ A hard copy of the RSB sent to the above address 100 Euro

Method of payment : VISA / MASTERCARD (we do not accept cheques)

Credit card No ☐☐☐☐ ☐☐☐☐ ☐☐☐☐ ☐☐☐☐ Exp. date _____

CVC Code: _____ Date : _____ Signed _____

Please return this signed form to :

The URSI Secretariat
c/o Ghent University / INTEC
Sint-Pietersnieuwstraat 41
B-9000 GHENT, BELGIUM
fax (32) 9-264.42.88